Jet Energy Scale at DØ

DØNOTE # 3287

August 28th, 1997

Brad Abbott[1]
Emanuela Barberis[2]
Mrinmoy Bhattacharjee[3]
Linda Coney[4]
Gian Di Loreto[5]
V.Daniel Elvira[6]
Robert Hirosky[7]
Bob Kehoe[4]
Freedy Nang[8]
Harry Weerts[5]

New York University[1]
Lawrence Berkeley Laboratory[2]
Delhi University, India[3]
University of Notre Dame[4]
Michigan State University[5]
SUNY at Stony Brook[6]
S.C.R.I., Florida State University[7]
University of Arizona[8]

Abstract

The DØ detector is used to study $p\overline{p}$ collisions at the 1.8 TeV center of mass energies available at the Fermilab Tevatron. The heart of the detector is a hermetic calorimeter made of uranium and liquid argon as the passive and active mediums respectively. The dominant physics process at the Tevatron is jet production. The understanding of the jet energy calibration is not only important for precision tests of QCD, but also in the measurement of particle masses and the determination of physics backgrounds associated with new phenomena. This note describes the methods developed at the DØ experiment to determine and verify the jet energy calibration.

Contents

List of Figures

List of Tables

Chapter 1

Introduction

The DØ Uranuim-Liquid Argon Sampling Calorimeters [1] are hermetic, uniform and provide a full solid angle coverage. The Central (CC) and End (EC) Calorimeters contain 7-8 and 8-10 interaction lengths of material respectively, ensuring containment of most particles except high p_T muons and neutrinos. The intercryostat region (ICR), between the CC and the EC calorimeters, is covered by the intercryostat detector (ICD) and the massless gaps (MG). The ICD consists of an array of scintillator tiles located on the EC cryostat wall. The MG are separate single-cell structures installed in the CC and EC calorimeters between the module endplates and the cryostat wall. The characteristics described above, together with a fine segmentation and excellent energy resolution for electrons and pions ($15\%/\sqrt{E(GeV)}$) and $50\%/\sqrt{E(GeV)}$), make the DØ calorimeters especially suited to jet and missing transverse energy ($\not{E}_T$) measurements.

The calorimeter readout pads provide an electronic signal which is proportional to the energy of particles entering each unit cell. The relative sampling weights of the different sections and the conversions from ADC counts to energy are obtained from Test Beam data [2]. A general view of the DØ calorimeters, with their different electromagnetic and hadronic sections is displayed in Figure 1.1. Figure 1.2 describes a unit cell, which consists of Uranium absorber plates and liquid argon gaps as the passive and active medium, respectively. A side view of the calorimeters is displayed in Figure 1.3. We define a coordinate system with the origin in the geometric center of the detector and the z axis pointing towards the direction of the proton beam. The transverse plane is generated by the cartesian axes x and y. In spherical coordinates, the three degrees of freedom are described by $|\vec{r}|$, the azimuthal angle φ and the polar angle θ. Pseudorapidity is defined as $\eta = -\ln[\tan(\theta/2)]$. The advantage of using η instead of θ is that pseudorapidity transforms under Lorenz rotations like η plus a term that depends only on the boost of the parton-parton system.

The Tevatron[1] produces hard $p\overline{p}$ collisions ($\sqrt{s}$ =1.8 TeV) which uncover the composite structure of the proton. The parton-parton (quarks or gluons) interactions are described by Quantum Field Theories. The evolution of the outgoing partons after the hard scattering is described by Quantum Chromodynamics (QCD). The color interactions between final state partons produce a shower of more partons which, as a result of color confinement, reorganize into colorless hadrons. The latter process, known as hadronization, is a non-perturbative process that yields the production of collimated beams of particles (mostly photons, pions and kaons) called jets. Jet production is a common process in hadron collisions with a center of mass energy greater than 10 GeV.

The jet energy measured in the calorimeters is distorted by response effects, uranium noise, spectator interactions, reconstruction and resolution effects. The calorimeter response to the different types of particles is the most important aspect of the jet energy scale cor-

[1] proton-antiproton collider at Fermilab

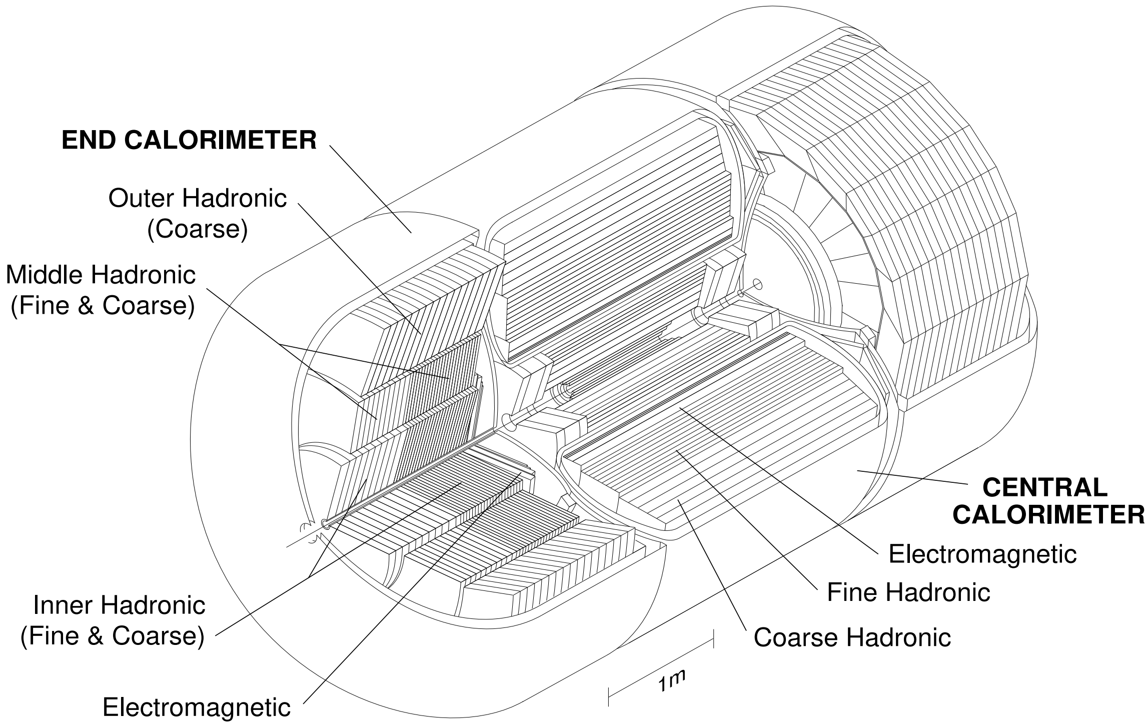

Figure 1.1: General view of DØ calorimeters.

rection. Most of the electromagnetically interacting particles (γ,e) deposit all their energy in the electromagnetic (EM) section of the calorimeters ($\sim$20 radiation lengths thick). Since the mechanism of energy loss for hadrons is through nuclear interactions, their associated shower develops through the three sections of the calorimeter: EM, fine hadronic (FH) and coarse hadronic (CH). The calorimeter response to the EM (e) and non-EM (h) components of hadron showers is different because there are different physics processes involved in the energy loss process ($\frac{e}{h}$ >1). There are large and non-gaussian event-to-event fluctuations in the fraction of the energy lost on π° production (f_{em}). In addition, the fraction $\langle f_{em} \rangle$ increases logarithmically with energy. Therefore, *non-compensating* calorimeters ($\frac{e}{h} \neq 1$) give non-gaussian signals distributions for monoenergetic hadrons. Moreover, the signals are not proportional to the hadron energy (*non-linearities*) and e/π (electron to pion response) is energy dependent[3].

The DØ calorimeters are compensating, with an e/π ratio less than 1.05 above 30 GeV. Figure 1.4 shows a linear dependence of measured energy versus Test Beam energy for pions and electrons using the DØ calorimeters. Monoenergetic jets are represented by a delta function (Figure 1.5a). In a non-hermetic or non-linear calorimeter their energy distribution will have a finite width and a low energy tail (Figure 1.5b). Figure 1.5c shows the general shape of jet energy distributions in a hermetic and compensating calorimeter. Figure 1.5d shows a gaussian behavior of the asymmetry variable $(E_{T1} - E_{T2})/(E_{T1} + E_{T2})$ for 140 GeV dijet events observed with the DØ calorimeters, where E_{T1} and E_{T2} are randomly one of the pair of leading transverse energy jets.

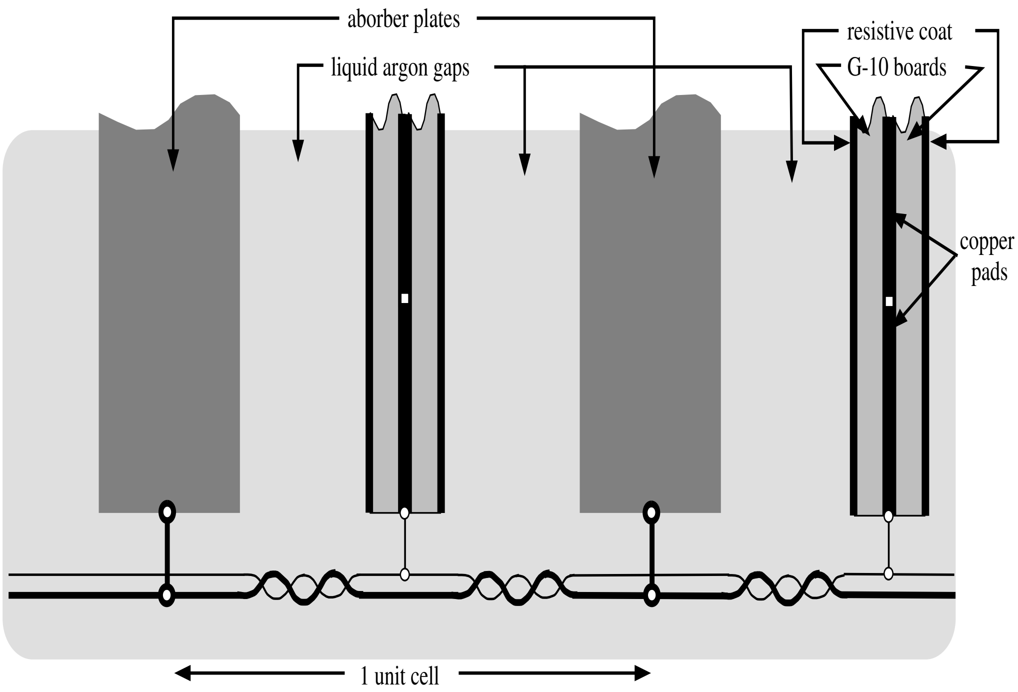

Figure 1.2: Diagram of a Calorimeter unit cell.

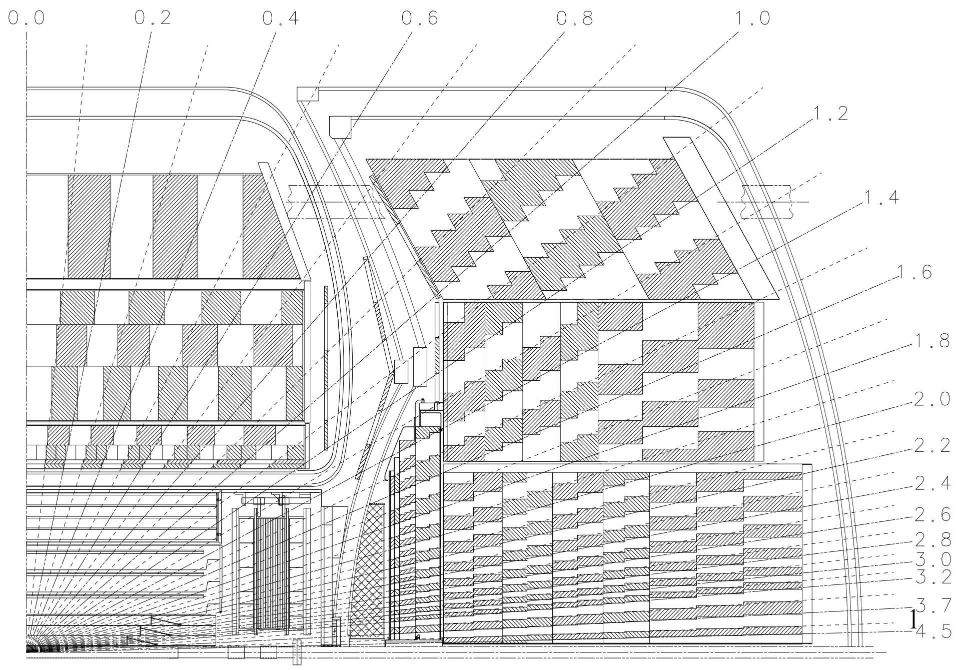

Figure 1.3: Side view of the DØ Calorimeters. The numbers indicate position in units of pseudorapidity.

The purpose of this work is to obtain the energy correction to scale the measured jet energy, on average, back to the energy of the final state particle level jet. The linearity and hermeticity of the DØ calorimeters allows separation of the jet energy resolution from the scale corrections. Here, we only focus on the scale correction and leave aside resolution effects. The lack of a central magnetic field, which would provide an independent measurement of charged hadron energies, moved DØ to derive a jet energy calibration based almost entirely on data measurements, using conservation of transverse momentum through an accurate determination of the event $\not\!\!E_T$. The jet energy scale correction is measured as a function of a number of variables, and is provided as an average correction for jets with similar characteristics.

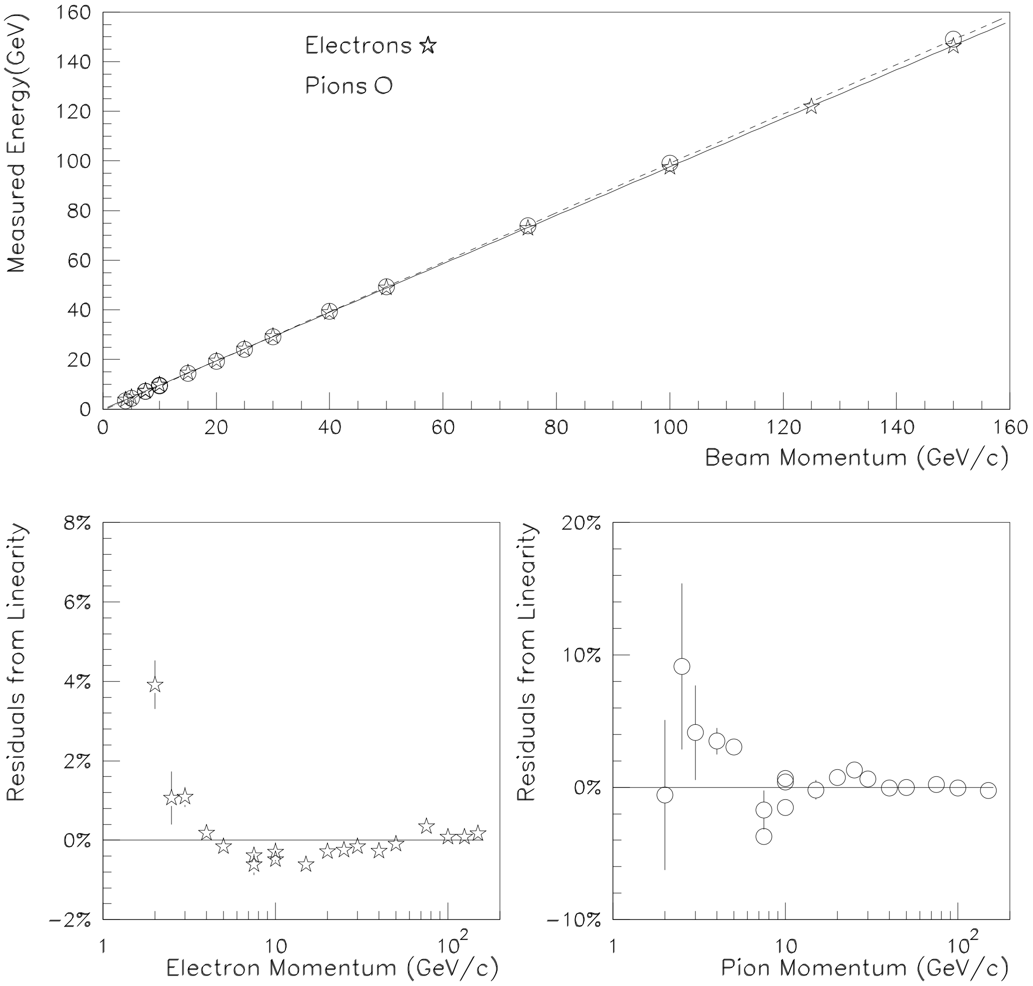

Figure 1.4: Measured energy versus Test Beam energy for electrons and pions. Good linearity between signal and energy is achieved with the DØ calorimeters.

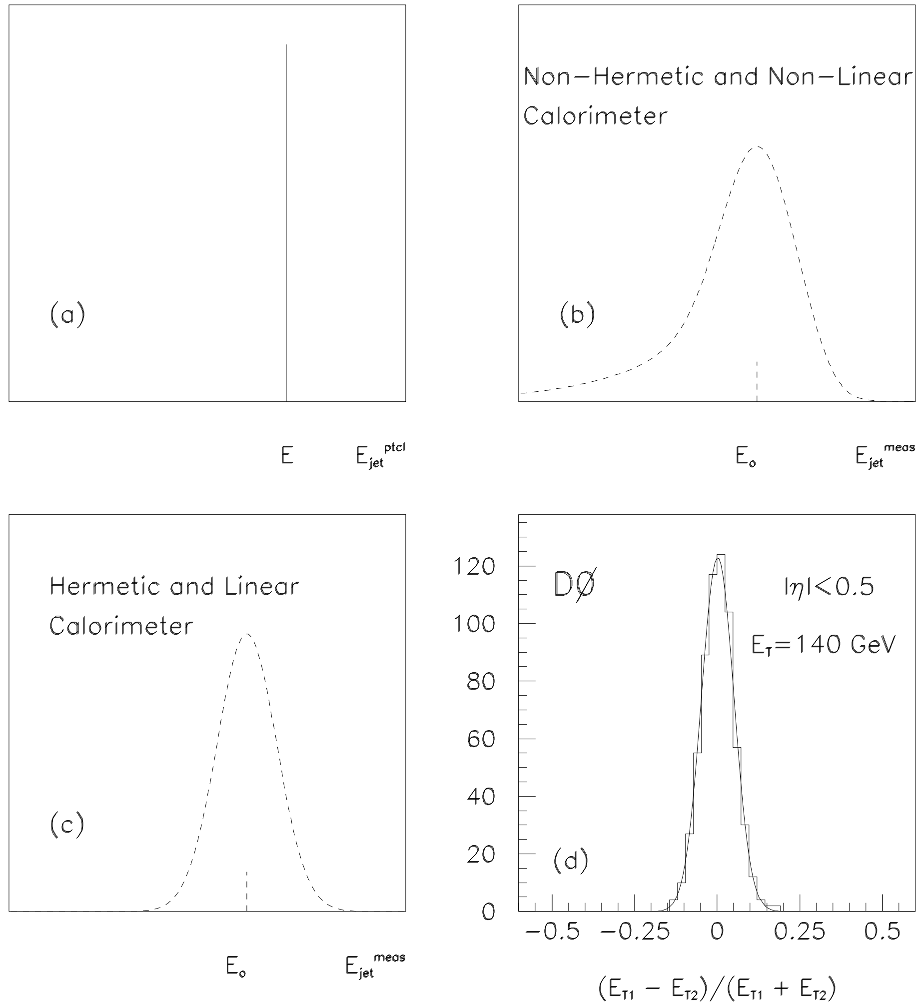

Figure 1.5: (a): Energy distribution of monoenergetic jets before the calorimeter. (b): Illustration of a typical jet energy distribution in non-hermetic or non-linear calorimeters (height and width are arbitrary). The distribution peaks at $E_o < E$, and includes a low energy tail. (c): Illustration of jet energy distribution in a hermetic and linear calorimeter (height and width are arbitrary). (d): Real asymmetry distributions $(E_{T1} - E_{T2})/(E_{T1} + E_{T2})$ from dijet events observed in the DØ central calorimeter.

1.1 Jet Definition

The fact that most events display a dijet structure intuitively connects the observed jets to a simple picture of the parton interaction. However, it is not easy to associate the jet energy measured in the calorimeter with a specific underlying parton energy. Partons radiate gluons, fragment into hadrons and are color connected to each other. On the other hand, the jets that emerge from the hard interaction produce energy depositions in an array of cells in the calorimeter. To determine the jet energy, an algorithm is needed which assigns calorimeter cells to jets. The final measured jet energy is dependent on this algorithm or jet definition.

Figure 1.6 illustrates the evolution from *parton* through *particle* to *calorimeter* jets. In Figure 1.6a, the quark radiates a gluon which may be merged with the quark into a single *parton* jet depending on the jet finding algorithm. Further evolution, through parton showering and hadronization, yields a *particle* jet. After hadronization, the distinction between quark and gluon is blurred. Figure 1.6b shows a diagram of a jet as it enters the calorimeter. Three charged hadrons produce wide showers, while photons from π°'s and η°'s leave narrower showers confined to the EM portion of the calorimeter. The lightest shower in the figure shows that a fraction of the energy from a particle emitted inside the jet, is showered outside the *calorimeter* jet. *Calorimeter* jet is defined as the object reconstructed with a given algorithm from energy depositions in calorimeter cells. A fixed cone algorithm is always used in this note [4].

The jet calibration must compensate for detector effects, thereby correcting the measured jet energy, E_{jet}^{meas}, to the *particle* level energy, E_{jet}^{ptcl}. This *particle* level energy is defined as the energy of a jet found from final state particles using a similar algorithm to that used at the *calorimeter* level. The *particle* jet includes only particles arising from partons participating in the hard scatter. We do not attempt to correct the jet energy to the *parton* level.

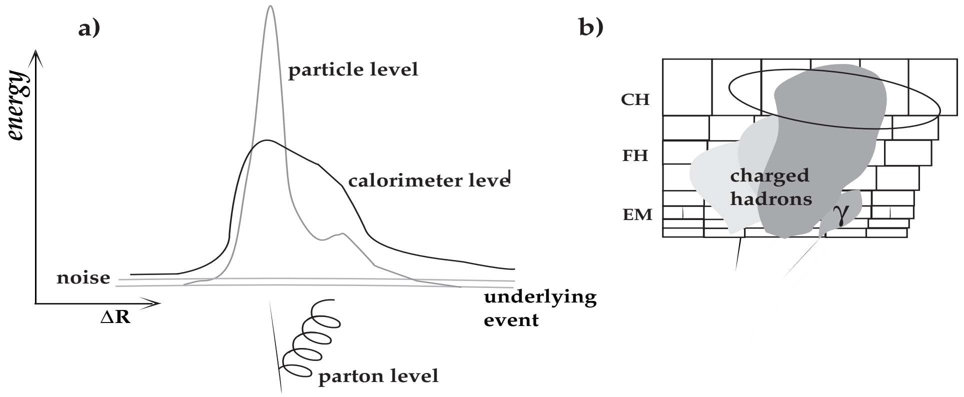

Figure 1.6: Jet evolution. (a): Jets at *parton*, *particle* and *calorimeter* levels. (b): Section of the calorimeter with individual particle showers.

1.2 Jet Energy Scale

The true jet energy E_{jet}^{ptcl} is obtained from E_{jet}^{meas} using the following relation:

$$E_{jet}^{ptcl} = \frac{E_{jet}^{meas} - E_O(\mathcal{R}, \eta, \mathcal{L})}{R_{jet}(\mathcal{R}, \eta, E) R_{cone}(\mathcal{R}, \eta, E)},$$

where:

- $E_O(\mathcal{R}, \eta, \mathcal{L})$ is an energy offset, which includes the underlying event, uranium noise, energy from previous crossings (pile-up) and the underlying event contribution of extra $p\overline{p}$ interactions.
- $R_{jet}(\mathcal{R}, \eta, E)$ is the calorimeter response.
- $R_{cone}(\mathcal{R}, \eta, E)$ is the fraction of the jet calorimeter shower contained in the algorithm cone.

The underlying event is defined as the energy contributed by spectators of the hard collision which resulted in the high E_T event. This quantity may or may not be included in the energy offset, depending on the physics under study. The offset depends on the cone size $\mathcal{R}$, if using a fixed cone algorithm and the jet pseudorapidity. A luminosity dependence arises due to the contribution of extra interactions. We assume that the offset does not depend on the azimuth or the jet energy.

The energy response is never perfect in a real calorimeter, and is typically less than one. This is due to energy lost in uninstrumented regions between modules, differences between electromagnetic and nuclear interacting particles ($\frac{e}{h}$ >1) and module to module inhomogenities. The response is independent of the cone size; however, its parametrization versus E_{jet}^{meas} is cone size dependent since larger cones encompass a larger fraction of the energy of the cluster. The response is η dependent because the various detector components are not the same. For example, the effective absorber plate and gap thicknesses depend on η. Jets with the same calorimeter energy and pseudorapidity may require different response corrections depending on the type and energy spectrum of constituent particles, particle multiplicity, and width in $\eta - \varphi$ space. The response measurement presented here is averaged over these characteristics in the γ-jet sample. The assumption is that jet characteristics in a γ-jet sample used to derive the response are similar to those in an inclusive jet sample.

R_{cone} is the ratio of the energy contained by the calorimeter fixed cone algorithm to the energy contained by the *particle* level algorithm. It is computed after the offset and response corrections, and is less than one due to leakage of shower energy out of the cone as the shower develops.

This note describes the underlying philosophy, the structure and the different pieces of the jet energy scale correction. It is a continuation of earlier work [5, 8]. The implementation of the correction, a description of the associated computer program (CAFIX) and usage warnings are also included. The analysis and code described in this note corresponds to CAFIX5.1, CAFIX from now on, except when we want to distinguish between different versions.

Chapter 2

Offset Correction

The offset correction involves subtracting the fraction of the measured jet energy which does not belong to the hard collision. A hard collision is a non-diffractive $p\overline{p}$ interaction where both the proton and the antiproton break into partons. This excess energy includes the contributions of uranium noise, pile-up and energy from additional $p\overline{p}$ interactions. Pile-up is the residual energy from previous $p\overline{p}$ crossings as a result of the long shaping time associated with the preamplification stage. Therefore, pile-up energy depends on the number of interactions in the previous bunch crossings, which is luminosity dependent. There is also the choice of including in the offset correction the energy associated with the physics underlying event (E_{ue}). This is the energy from soft interactions between spectator partons which composed the colliding $p\overline{p}$ pair. If the underlying event is subtracted, only the energy associated with the parton-parton scattering remains. The offset subtraction is performed before the response correction, since it is measured from uncorrected samples.

At DØ, a crossing triggered as a high p_T event can be modelled as the sum of a hard parton scattering and a zero bias event (ZB) at the same luminosity. A ZB event has no trigger requirement other than a $p\overline{p}$ crossing. The average number of hard interactions in a high p_T event, $\langle N_{High\,p_T}\rangle$, may be written as:

$$\langle N_{High\,p_T}\rangle = 1 + \langle N_{ZB}\rangle \, .$$

Here, $\langle N_{ZB}\rangle$ is the average number of hard interactions in a ZB event and can be expressed as:

$$\langle N_{ZB}\rangle = 0 \times P(0) + 1 \times P(1) + \cdots + n \times P(n) \, ,$$

where the probability of having n hard collisions at a given luminosity, $P(n)$, follows a Poisson distribution.

The total offset correction is factorized as:

$$E_O = E_{ue}(1 + \langle N_{ZB}\rangle) + E_{nse} + E_{pile} \Rightarrow$$

$$E_O = E_{ue} + \langle N_{ZB}\rangle E_{ue} + E_{nse} + E_{pile} \Rightarrow$$

$$E_O = E_{ue} + E_{\Theta} \, ,$$

where the first term, E_{ue}, is the energy associated with the physics underlying event, $\langle N_{ZB}\rangle E_{ue}$ is the contribution to the underlying event from additional $p\overline{p}$ interactions, E_{nse} is the energy associated with radiation from uranium decay, and E_{pile} is the pile up energy. We measure E_{ue} and E_{Θ} separately, as described in the following sections.

2.1 Physics Underlying Event

The energy associated with the spectator partons in a high p_T event may or may not be subtracted from the measured jet energy, depending on the details of the particular physics analysis. Therefore, it is provided as a separate and optional correction. The correction was measured in a minimum bias (MB) low luminosity sample, $\mathcal{L}$=0.1 $\times$ 10^{30} cm^{-1}sec^{-1} ($\mathcal{L}$=0.1 for simplicity of notation). An event is called minimum bias if it passes the Level Ø trigger condition, that is a crossing with a hard collision. The E_T density, D_{MB}, in MB events is measured as a function of pseudorapidity by dividing the average energy in a calorimeter tower (generally a 0.1 $\times$ 0.1 volume in η-φ space) by the η-φ area of the tower. This density is averaged over φ. D_{MB} is a measure of the transverse $E_{ue} + E_{nse} + E_{pile}$ density. The contribution of uranium noise and pile-up, $D_{ZB}^{no\,L\emptyset}$, is measured in a low luminosity ZB sample with the requirement that the events do not pass the Level Ø trigger (no hard interaction). D_{ue} is obtained subtracting the latter density from the former:

$$D_{ue} = D_{MB} - D_{ZB}^{no\,L\emptyset} \,.$$

The energy subtracted from the jet, E_{ue}, is calculated as $D_{ue} \times A_{\eta,\varphi}$, where $A_{\eta,\varphi}$ is the area of the jet in η-φ space. Figures 2.1, 2.2, and 2.3 show D_{MB}, $D_{ZB}^{no\,L\emptyset}$ and D_{ue} as a function of pseudorapidity, respectively. D_{ue} is fairly flat except in the intercryostat region. In the range 0.7$<|\eta|<$1.2, there is a peak attributed to mis-calibration of the intercryostat detector. The dip above η =1.2 is located in a range where the electromagnetic coverage is very poor. Even though the energy density in real space increases towards the beam pipe, D_{ue} falls fairly quickly with η at high pseudorapidities. This is because D_{ue} is the transverse energy density in $\eta - \varphi$ space, which shrinks as a function of pseudorapidity. Since the physics underlying event is associated with the soft interactions of the debris in a single $p\overline{p}$ collision, it does not depend on the luminosity or the number of $p\overline{p}$ interactions in the event.

2.2 Uranium Noise, Pile-up and Extra Interactions

Since a high p_T event is a sum of a hard $p\overline{p}$ collision and a zero bias event, we can measure E_Θ from a zero bias sample.

The average energy of the individual cells is not zero in the absence of the beam. This is due to radiation from uranium decay and electronic noise. The initial electronic calibration shifts the average energy to zero. However, the cell energy distribution peaks at a negative value, is non-symmetric, and has a finite width σ, as shown in Figure 2.4. Cells with an energy within 2σ of zero are considered empty and are not read out. This process is called zero suppression and saves a significant amount of storage space per event. The noise distribution is asymmetric towards a larger high energy tail. Therefore, the symmetric 2σ zero suppression cut leaves, on average, some positive energy in each cell. The dotted vertical lines in Figure 2.4 illustrate the effect of the zero suppression cut in an empty cell. The magnitude of E_{nse}, which is due to the zero suppression effect rather than uranium noise contamination, depends on the number of cells suppressed in an event.

The occupancy factor, $\mathcal{F}$, is defined as the fraction of cells read out in a given volume. This factor is different within a jet, in a MB event and in a ZB event. It also depends on the size of the jet algorithm cone because a smaller cone has a higher fraction of its cells read out. Since the contribution of E_Θ to the offset correction is measured in a zero suppressed (ZS) zero bias sample, the energy associated with the zero suppression cut is already included. However, since the offset subtraction is applied to jets reconstructed from a ZB sample, there has to be a correction for the difference between the suppression contribution within a jet and the analog in a ZB event.

The E_T density contribution to the offset from uranium noise, pile-up and additional $p\overline{p}$ interactions is:

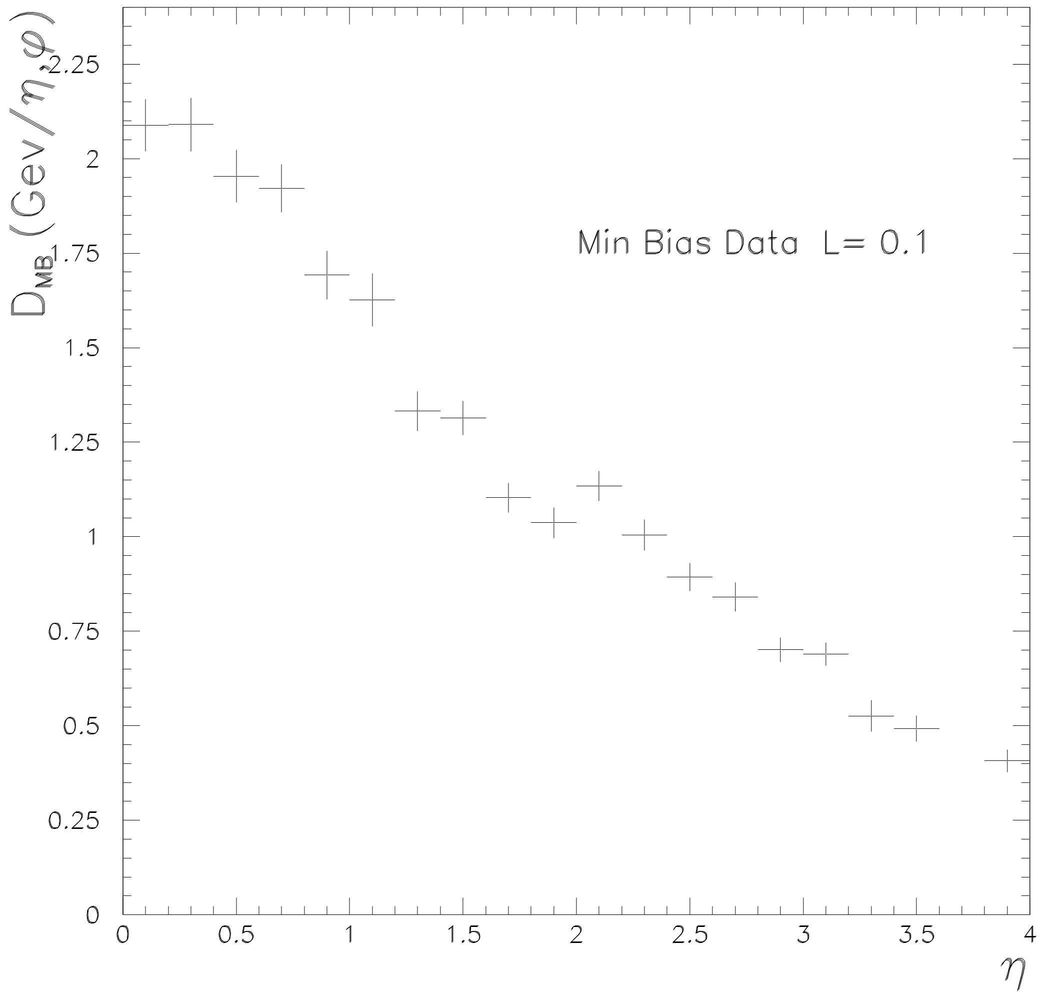

Figure 2.1: E_T density, D_{MB}, measured from minimum bias data at low luminosity. Uranium noise is not subtracted.

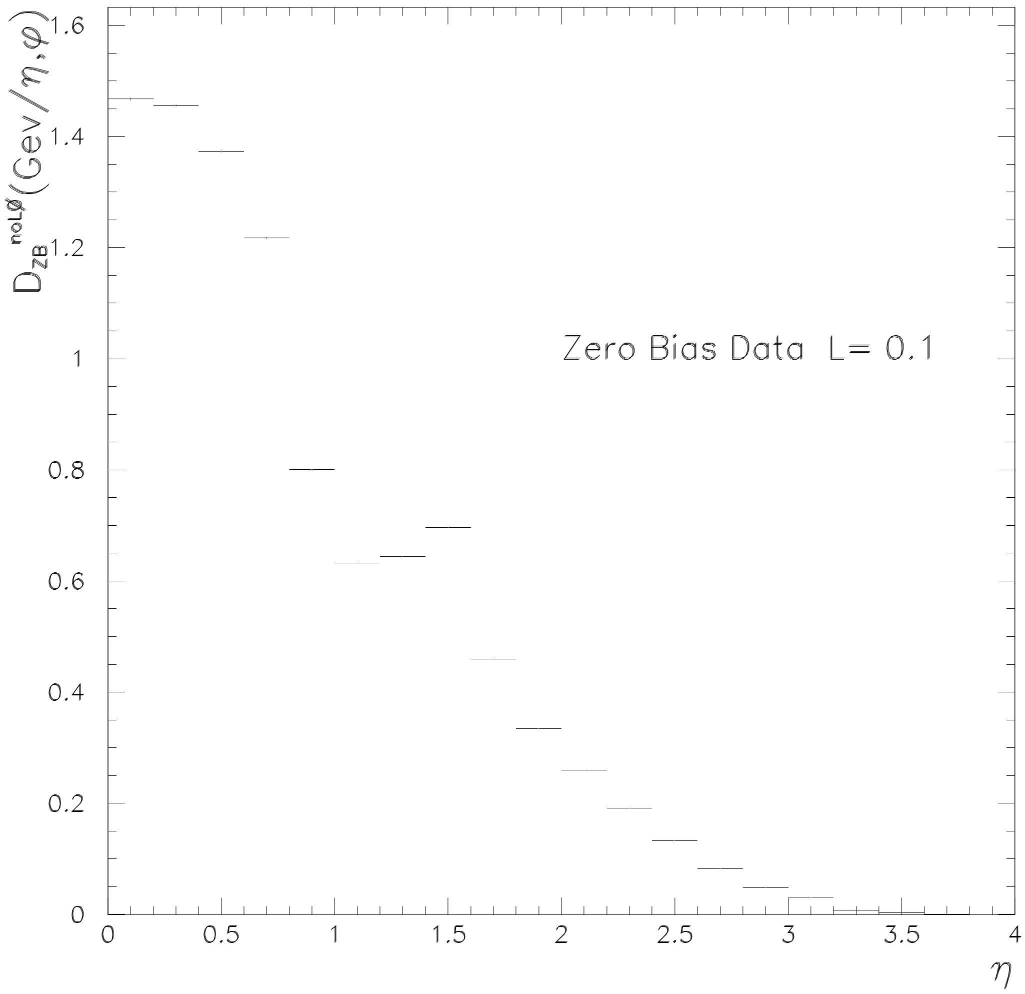

Figure 2.2: E_T density, $D_{ZB}^{no\,L\emptyset}$, measured from zero bias data at low luminosity. Uranium noise is not subtracted.

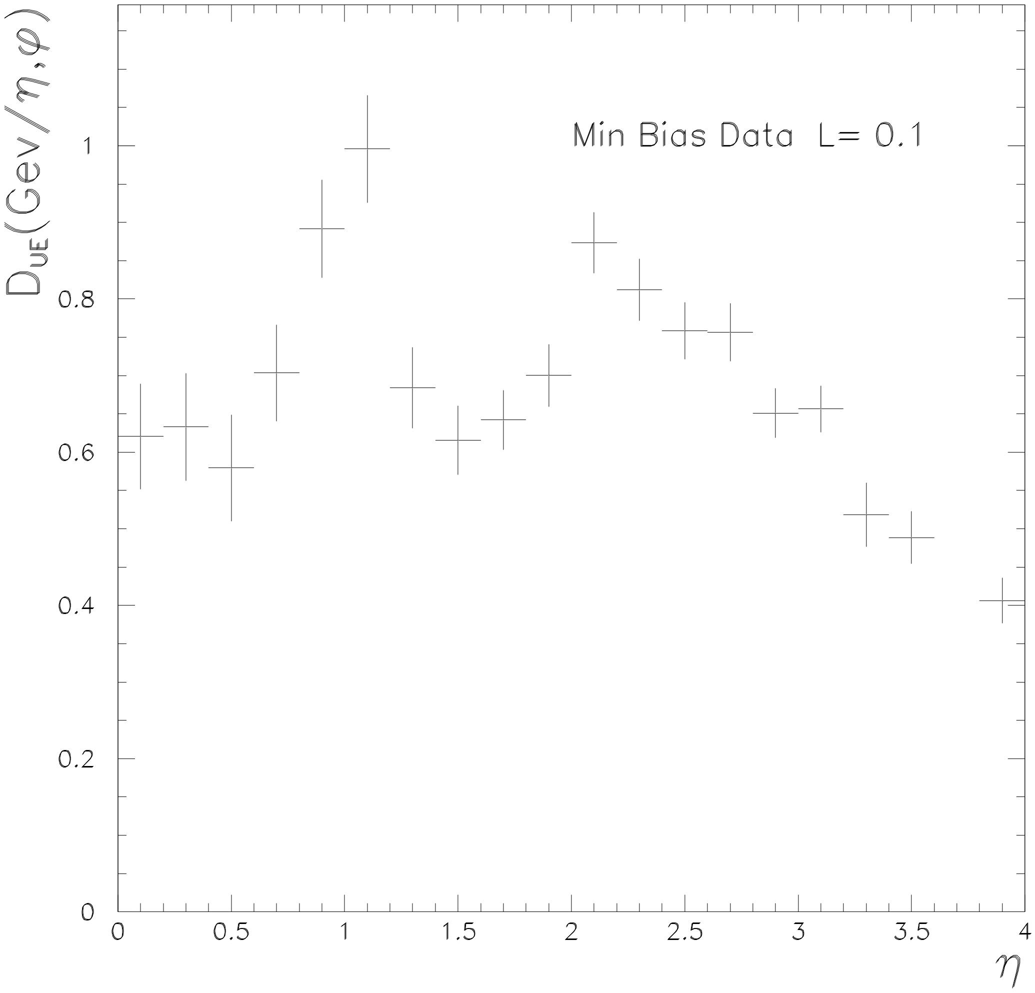

Figure 2.3: Physics underlying event density, D_{ue}.

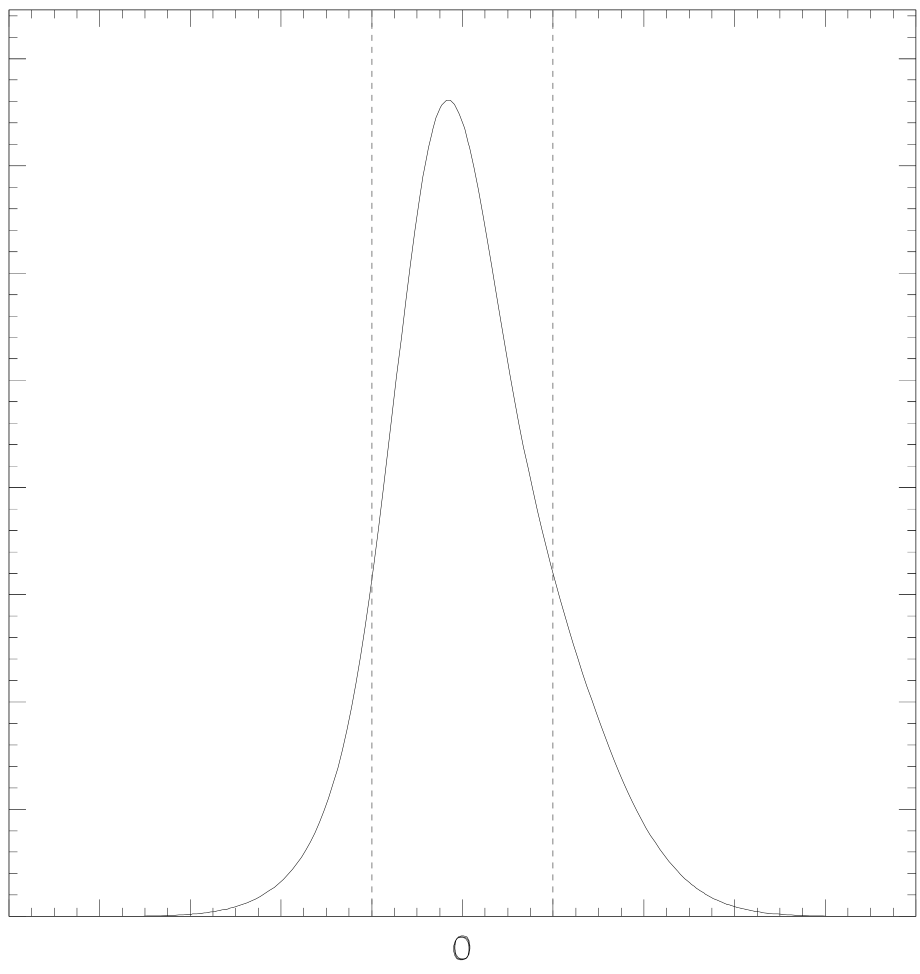

Figure 2.4: Illustration of the energy distribution in a calorimeter cell (solid line). Note that the net result of the 2σ cut (vertical dashed lines) is to cause the average of the distribution to be positive.

$$D_\Theta = D_{ZB}^{ZS} - \delta_{ZB} + \delta_{jet}\,,$$

where D_{ZB}^{ZS} is the measured density in a ZB sample, δ_{ZB} is the E_T density contribution of the ZS cut in a ZB sample, and δ_{jet} is the E_T density contribution of the ZS cut within a jet. The contribution of the ZS cut is measured as:

$$\delta_{ZB} = D_{ZB}^{ZS} - D_{ZB}^{NZS}$$
$$\delta_{jet} = D_{jet}^{ZS} - D_{jet}^{NZS}\,,$$

where D_{ZB}^{ZS} and D_{ZB}^{NZS} are measured as a function of pseudorapidity in a zero suppressed and a non-zero suppressed sample respectively. δ_{ZB} is shown is Figure 2.5. Since there were no jet triggers defined in the non-zero suppressed sample, D_{jet}^{NZS} is measured in the few MB events ($\sim$ 5,000) where jets were reconstructed. The density is measured only within the limits of the jet cone and assigned to the pseudorapidity bin associated with its centroid.

The limited number of jet events in non-zero suppressed MB data introduces a large statistical error on the suppression correction. Since we know that the difference between δ_{ZB} and δ_{jet} is due to different occupancy factors, we measured $\mathcal{F}_{ZB}$ and $\mathcal{F}_{jet}$ in order to derive a prediction for δ_{jet} from δ_{ZB}. $\mathcal{F}_{ZB}$ is determined as the number of cells read out in a particular η-φ bin, and then dividing by the total number of cells in that area. $\mathcal{F}_{ZB}$ is determined as the number of cells read out within a jet divided by the total number of cells in the jet.

Figure 2.6 shows the zero suppression corrections for both ZB and MB jet data. The zero suppression correction from jet data is in general agreement with a prediction from ZB data assuming that δ_{ZB} and δ_{jet} satisfy the relation:

$$\delta_{jet} = \delta_{ZB} \times \frac{\mathcal{F}_{ZB}}{\mathcal{F}_{jet}}\,.$$

Fewer cells are suppressed in a jet than in a zero bias event. Therefore, the amount of positive energy introduced by the zero suppression cut is smaller in a jet than in a zero bias event. Figure 2.7 shows that there is some dependence of $\mathcal{F}_{ZB}$ on luminosity. There is also a dependence on the number of $p\overline{p}$ interactions, which is studied with a software tool (MITOOL). MITOOL distinguishes between single and multiple interaction events using Level Ø trigger, tracking and calorimeter information. An MITOOL value of 1 or 2 means it is very likely that the event is a single interaction. MITOOL>2 implies that there is a high probability of having more than one hard interaction in the event. $\mathcal{F}_{ZB}$ is measured for different luminosities and the two MITOOL bins are indicated in Figure 2.7. It is also shown in the same plot that the $\mathcal{F}_{jet}$ dependence on jet energy and luminosity is not significant enough to require separate parametrizations.

The D_Θ measurement is fit to an eight-parameter function:

$$D_\Theta = a_1 + a_2\eta + a_3[sin(a_4\eta + a_5)] + a_6[sin(a_7\eta + a_8)]\,.$$

Figure 2.8 shows parametrizations of D_Θ as a function of η for different luminosities (averaged over MITOOL). Parametrizations of D_Θ for events with MITOOL=1 or 2 and for MITOOL>2 are also provided (averaged over luminosity). At very low luminosities, $\sim$0.1, the zero bias sample always returns MITOOL=0, since it is unlikely to have a hard interaction. No MITOOL binning is made in this case.

This functional form for D_Θ fits the data very well, with an average error of approximately 5%. Statistical errors are of the order of 8%. The disagreement between the predicted and the observed value of δ_{jets} contributes an uncertainty of 0.25 GeV.

In the case of the physics underlying event, E_{ue}, the correction is taken directly from the histogram in Figure 2.3. Pseudorapidities in between the bin center values are obtained using linear interpolations.

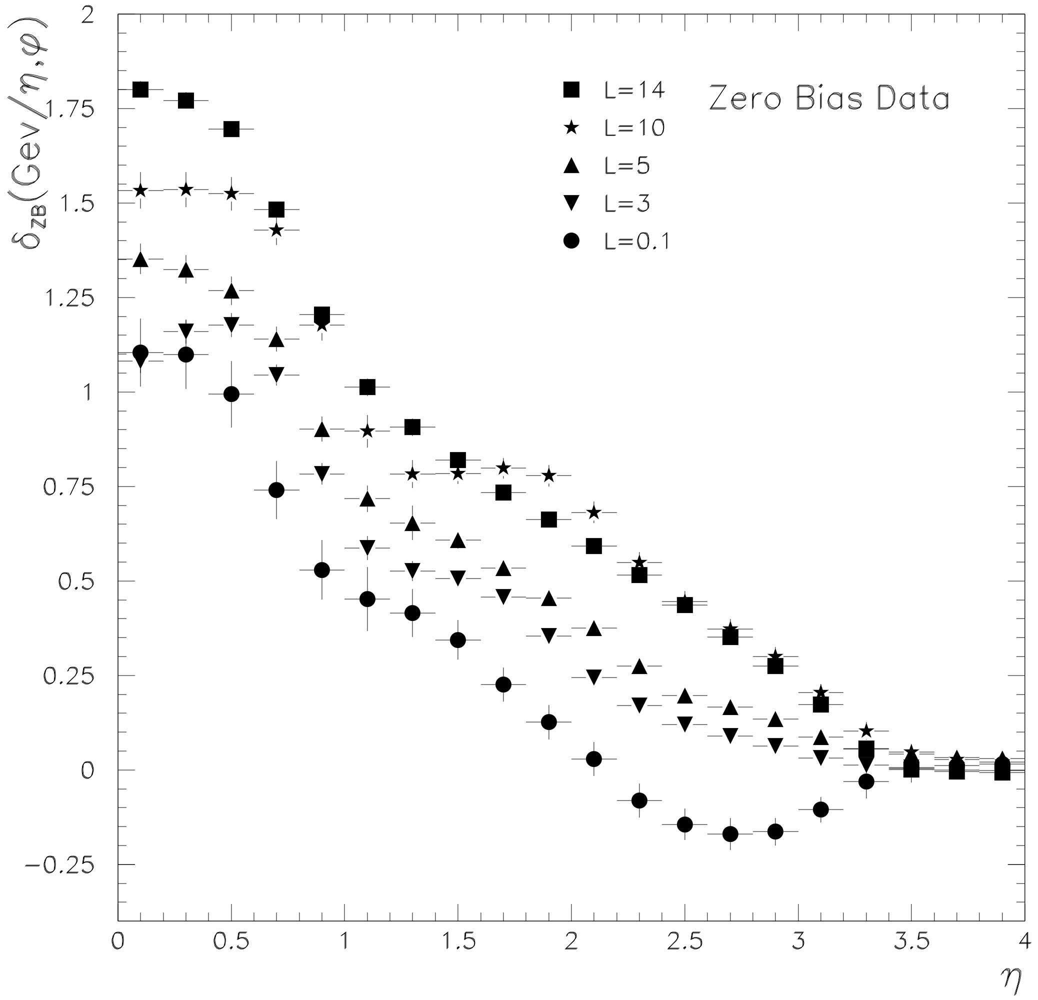

Figure 2.5: E_T density, δ_{ZB}, contributed to zero bias events by the zero suppression cut. δ_{ZB} is luminosity dependent.

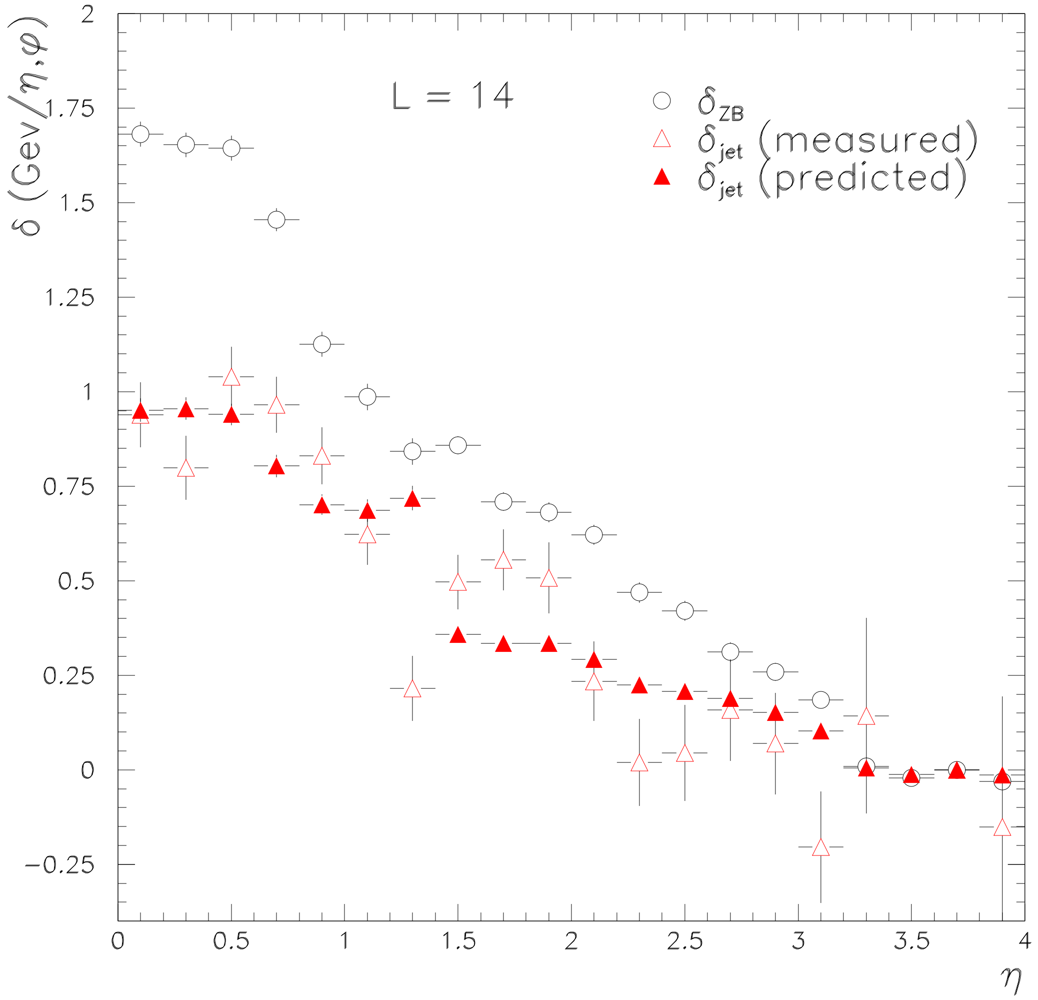

Figure 2.6: E_T densities, δ_{ZB} and δ_{jet}, contributed to zero bias and jet data by the zero suppression cut. The prediction of δ_{jet} from δ_{ZB} based on occupancy measurements is also included.

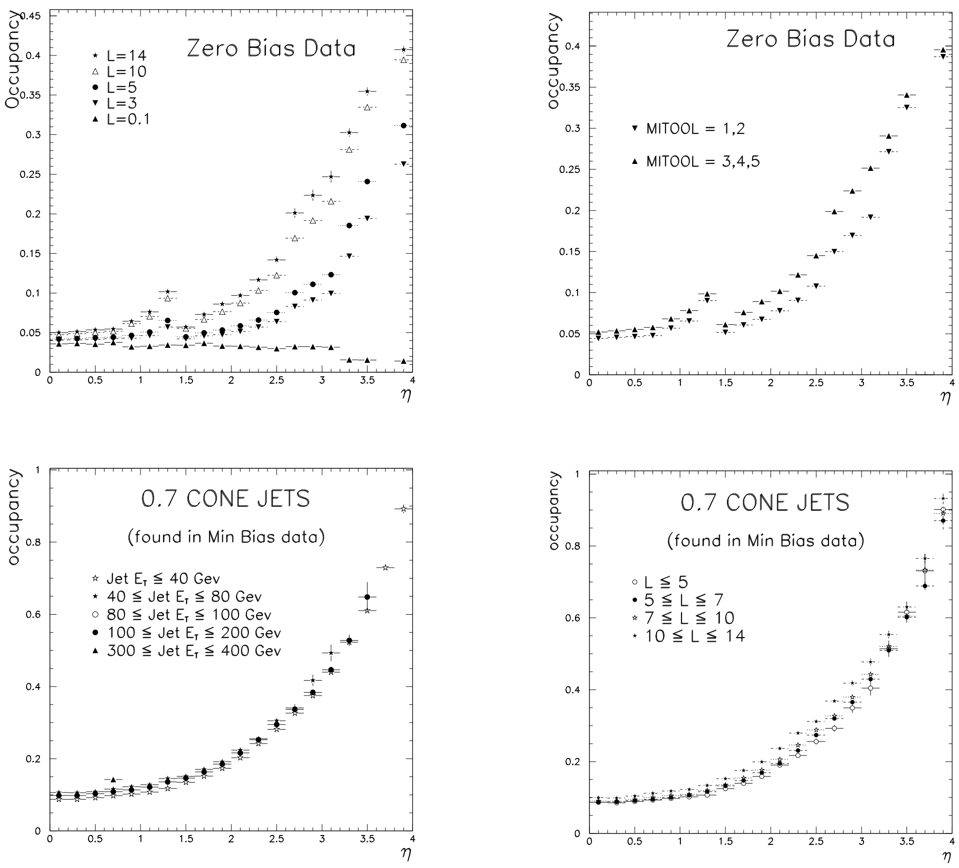

Figure 2.7: Luminosity, MITOOL and jet energy dependence of occupancy for both zero bias and $\mathcal{R}$=0.7 cone jets.

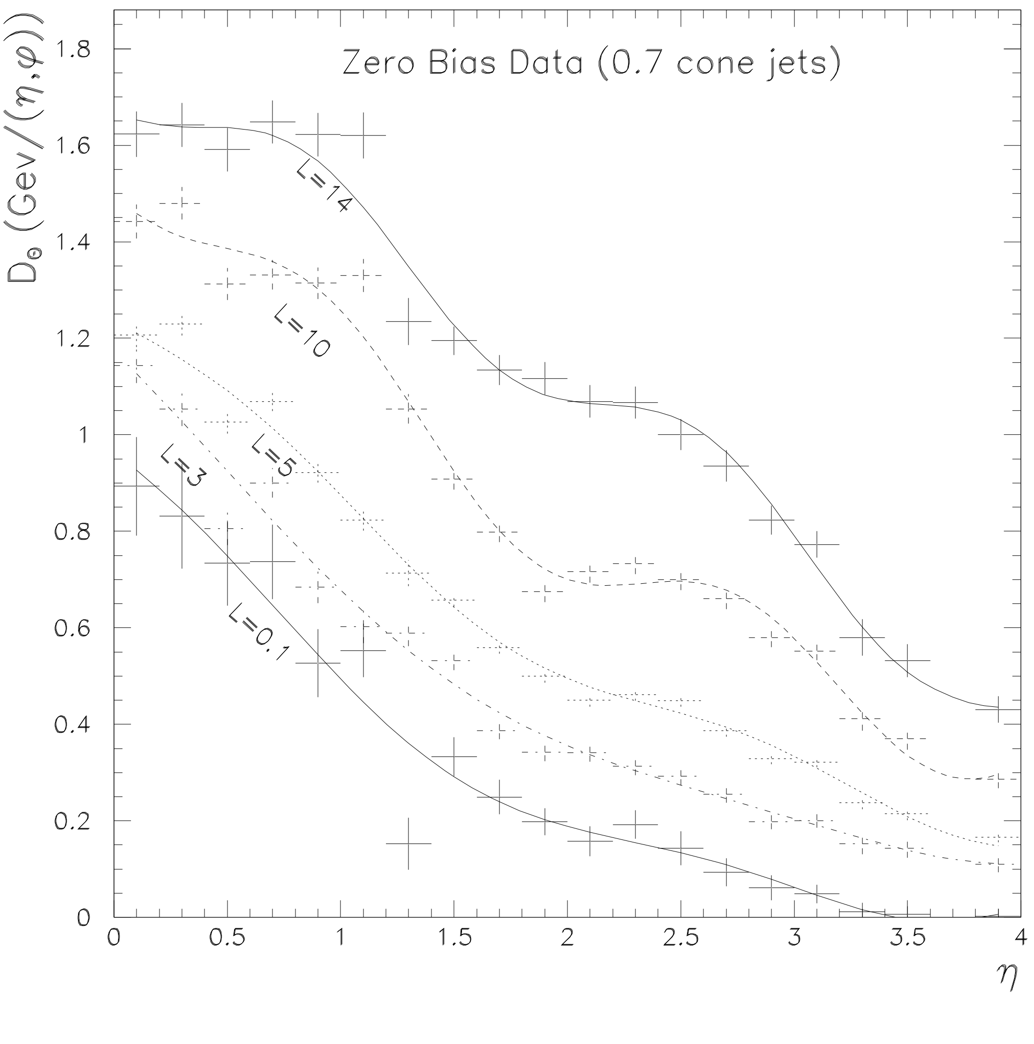

Figure 2.8: Energy density, D_Θ, contributed by uranium noise, pile-up and additional hard interactions (physics underlying event not included). The parametrizations correspond to $\mathcal{R}$=0.7 cone jets, and the density is averaged over all values of MITOOL.

Chapter 3

Response: The Missing E_T Projection Fraction Method

Measured jet energies are degraded due to the response of the calorimeter to the single particles which comprise a jet. Initially, the jet energy is derived solely from calibrations made from Test Beam data, based on charge deposition in the liquid argon, and the assumptions of linearity and no dead material. In reality, these assumptions are not precisely met and the cumulative effect is a lower jet response from unity, even for high energy jets. Several effects make the energy response to jets different from one:

- Test Beam studies indicate that e/π varies between 1.15 and 1.03 for particles of energies between 10 GeV and 150 GeV.
- Jets are extended objects which can deposit energy in poorly instrumented regions not well represented in the Test Beam calibration. These include the cryostat walls, the inter-cryostat regions and cracks between modules.
- The average response of each cryostat may be different from the corresponding test-module used to obtain its sampling weight. Studies of $Z \rightarrow e^+e^-$ events and other resonances show that the EM modules have a scale shifted relative to that measured in the Test Beam [2, 9, 10].

3.1 MPF Definition

At DØ, we make a direct measurement of the jet energy response, using conservation of p_T in γ-jet events. The event missing transverse energy ($\not{E}_T$) is defined as:

$$\not{E}_T = \sqrt{\left(\sum_i E_x^{(i)}\right)^2 + \left(\sum_i E_y^{(i)}\right)^2},$$

where the sum is over all calorimeter cells. This definition implies we assign zero mass to the energy observed in each cell, so that $\not{E}_T = \not{p}_T$. The $\not{E}_T$ resolution, as measured in minimum bias events with the DØ detector, is shown in Figure 3.1. In a perfect calorimeter, a non-zero $\not{E}_T$ indicates the presence of a neutrino and/or a high p_T muon (p_T>3 GeV) in the event. In real γ-jet events, $\not{E}_T$ also measures the overall imbalance of transverse energy in the calorimeter due to differences in response to photons and jets. Therefore, we use this feature to measure the response to jets, R_{jet}.

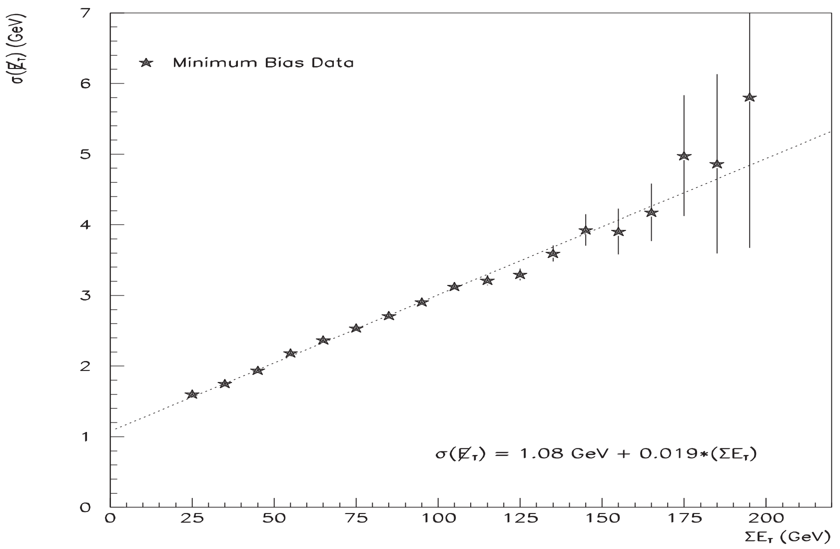

Figure 3.1: $\not{E}_T$ resolution ($\sigma(\not{E}_T)$ in GeV) versus total scalar E_T (scalar sum of E_T of the event) in events taken with a Minimum Bias trigger.

In a sample of γ-jet events in an ideal calorimeter, the photon transverse energy $E_{T\gamma}$ and the transverse energy of the hadronic recoil E_T^{had}, satisfy:

$$\vec{E}_{T\gamma} + \vec{E}_T^{had} = 0\,.$$

However, in a real calorimeter the electromagnetic and hadronic responses are not equal to one and the equation is modified to:

$$R_{em}\vec{E}_{T\gamma} + R_{had}\vec{E}_T^{had} = -\vec{\not{E}}_T\,,$$

where $\vec{\not{E}}_T$ can be measured. The electromagnetic scale was measured from the Z, J/ψ and π° data samples [2, 9, 10]. In this way, the response in the EM section of the calorimeters, where photons and electrons deposit all their energy, is determined very accurately. Therefore, after the photons are calibrated, $R_{em} = 1$, and we can write:

$$\vec{E}_{T\gamma} + R_{had}\vec{E}_T^{had} = -\vec{\not{E}}_T \Rightarrow$$

$$E_{T\gamma} + R_{had}\hat{n}_{T\gamma}\cdot\vec{E}_T^{had} = -\hat{n}_{T\gamma}\vec{\not{E}}_T \Rightarrow$$

$$1 + R_{had}\frac{\hat{n}_{T\gamma}\cdot\vec{E}_T^{had}}{E_{T\gamma}} = -\frac{\hat{n}_{T\gamma}\vec{\not{E}}_T}{E_{T\gamma}}\,.$$

By definition $E_{T\gamma} = -\hat{n}_{T\gamma}\cdot\vec{E}_T^{had}$, and R_{had} is expressed as:

$$R_{had} \equiv 1 + MPF = 1 + \frac{\vec{\not{E}}_T\cdot\hat{n}_{T\gamma}}{E_{T\gamma}}\,,$$

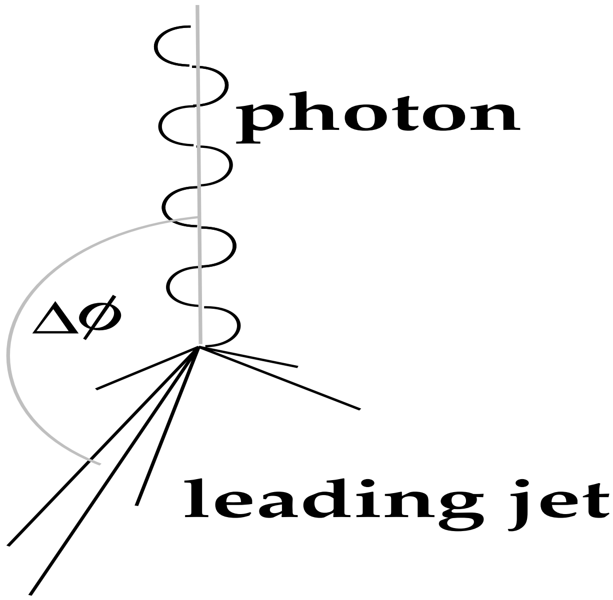

Figure 3.2: Sketch of a γ-jet event in the transverse plane. The response is measured for the leading jet.

where MPF is the Missing E_T Projection Fraction and $\hat{n}_{T\gamma}$ is the direction of the photon. In the case of a γ-jet two body process, $R_{had} = R_{jet}$; otherwise, R_{had} is an approximation to R_{jet}. If there were no offset and no showering effects, R_{had} would become $E_{Tjet}^{meas}/E_{Tjet}^{ptcl}$. To first order, R_{jet} is independent of the jet algorithm since MPF is a function of $\vec{\not{E}}_T$ and $\vec{E}_{T\gamma}$ only. Figure 3.2 illustrates the MPF method with a sketch of a γ-jet event. The hadronic response measured in a given event is assigned to the leading jet (probe jet with E_T^{probe}) and in this simple case is equal to R_{jet}.

3.2 Resolution Bias

Although R_{jet} is measured using transverse quantities, the fundamental dependence of the response is on jet energy. This is because e/π and the particle composition of jets is energy dependent. Therefore, we measure the response as a function of energy.

The MPF measurement of R_{jet} in terms of E_{jet}^{meas} is affected by a number of biases. The combination of finite jet and photon energy resolutions, the steeply falling photon cross section, the trigger and reconstruction thresholds, and the event topology contribute potential biases which must be removed. The event topology and the reconstruction threshold biases will be discussed in chapters 4 and 6, respectively.

The photon and jet fractional E_T resolutions are parametrized by the function:

$$\left(\frac{\sigma_{E_T}}{E_T}\right)^2 = \frac{N^2}{E_T^2} + \frac{S^2}{E_T} + C^2 \,.$$

In the CC, $N = 0.39$, $S = 0.135$, $C = 0.005$ for photons [7], and $N = 3.85$, $S = 0.54$, $C = 0.03$ for $\mathcal{R}$=0.7 jets [6]. The photon resolution is much better than the jet resolution. Figure 3.3 is an illustration of the photon and jet calorimeter energy distributions associated with an ensemble of 40 GeV photons in one photon plus one jet events (R_{jet} is set to 0.8

for 40 GeV particle jets). In this example, the width of the distributions is a measure of the fractional resolution for 40 GeV particle photons and jets. $R_{jet} = E_{Tjet}^{meas}/E_{T\gamma}$ is a measure of the energy response for jets with $E_{Tjet}^{meas} = 32$ GeV.

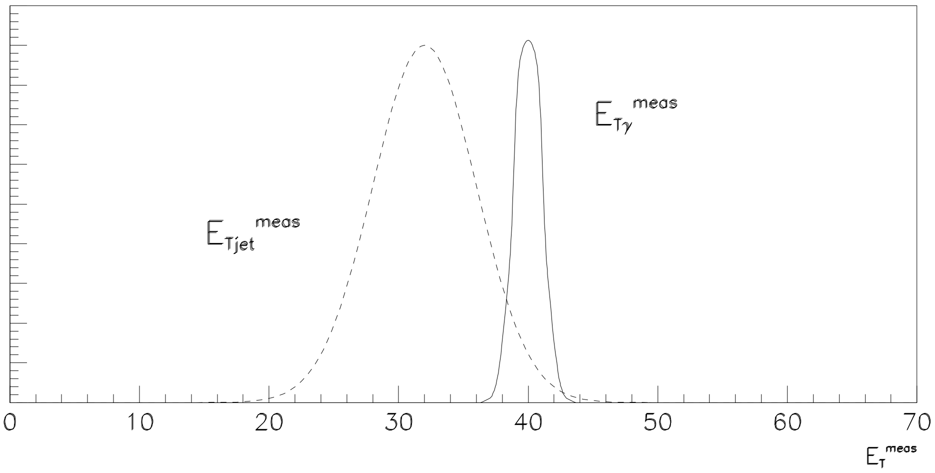

Figure 3.3: Illustration of the Photon and jet calorimeter E_T distributions for an ensemble of 40 GeV photons in one photon plus one jet events.

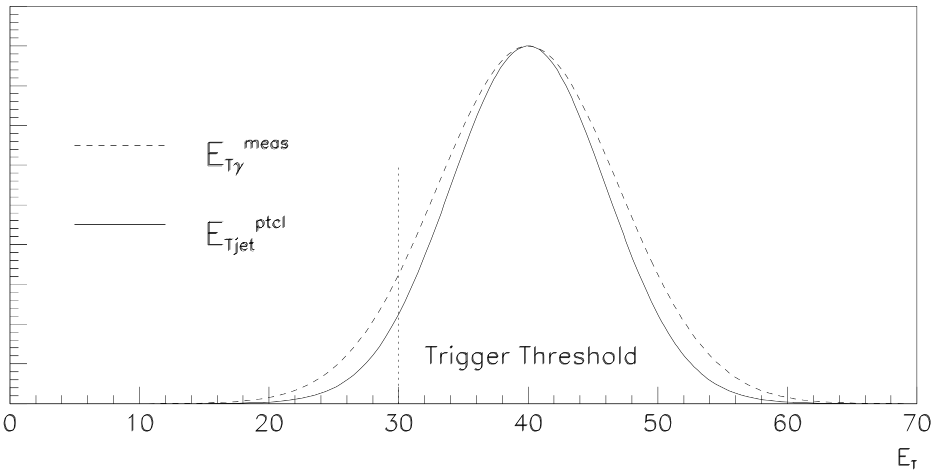

Figure 3.4: E_T spectra of calorimeter photons and particle level jets associated with a bin defined by E_{Tjet}^{meas}. The contribution of the photon energy resolution makes the photon spectrum a little bit wider than the particle level jet spectrum.

3.2.1 Trigger Effect

In the real data analysis, the energy of the particle jet is not known. If R_{jet} is binned in terms of E_{Tjet}^{meas}, and a bin with an average $E_{Tjet}^{meas} = 32$ GeV is selected, the associated particle level E_T will not be a delta function at 40 GeV. The photon energy distribution in the calorimeter is a little wider than the jet particle level distribution, since it includes the convolution of the jet and the photon energy resolutions (Figure 3.4).

If we applied a trigger cut on $E_{T\gamma}$ at 30 GeV, the average $E_{T\gamma}$ would shift from 40 GeV to $\sim$ 44 GeV and R_{jet} would be measured as 0.73 instead of 0.8. Such a trigger bias is a direct consequence of binning in terms of a poorly measured quantity, E_{Tjet}^{meas}.

3.2.2 Photon Cross Section Effect

In a given E_{Tjet}^{meas} bin, the lower E_T particle level events are much more likely to contribute than higher E_T events, since the photon cross section is a rapidly falling function of $E_{T\gamma}$. For a fixed bin, this shifts the mean of the $E_{T\gamma}$ distribution to a lower value. The shift is worse as the photon cross section becomes steeper or as the jet resolution worsens.

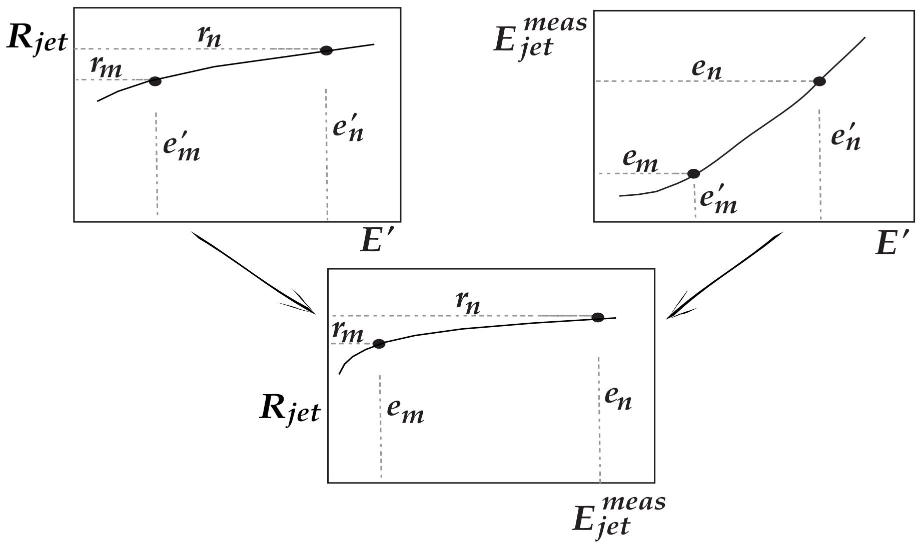

Figure 3.5: Derivation of R_{jet} versus E_{jet}^{meas} using the energy estimator E'.

3.3 The Energy Estimator E'

All the biases and smearing effects that depend on the jet energy resolution may be eliminated by binning the response in terms of a well measured quantity, strongly correlated with E^{ptcl}_{Tjet}. After the EM response correction, $E^{meas}_{T\gamma}$ is a good representation of its parent parton transverse energy. We define the jet energy estimator, E', as:

$$E' = E^{meas}_{T\gamma} \cdot \cosh(\eta_{jet}),$$

where both $E^{meas}_{T\gamma}$ and the jet pseudorapidity η_{jet} are very well measured quantities. E' would be the particle energy of the jet in the case of a two body γ-jet process. After binning the response in terms of a good representation of the particle jet energy, E', the dependence of R_{jet} on E^{meas}_{jet} is obtained as a second step by measuring the average E^{meas}_{jet} in each E' bin. Figure 3.5 illustrates the $E' \rightarrow E^{meas}_{jet}$ mapping procedure.

3.4 Tests of MPF Method

The MPF method was tested using collider γ-jet data and a parametric simulation. The simulation generates direct photon events according to a cross-section with a given E_T dependence. A parton jet is then added at $\Delta\varphi = \pi$ with respect to the photon. Finally, both the photon and the jet are smeared with energy resolutions and scaled with the energy responses. Figure 3.6 shows the E_T distributions in the simulated data for nine $E_{T\gamma}$ bins from 30 GeV to 120 GeV. The bin size is 10 GeV. E_{Tjet} is uncorrected. The mean and σ of the distributions are controlled with the offset, response and resolution parameters in the simulation.

Figure 3.7c shows a comparison between R_{jet} determined from the simulation directly as a function of E^{meas}_{jet} (open circles), and the same quantity binned in terms of E' and then mapped onto E^{meas}_{jet} (closed circles). While the closed circles are in very good agreement with the input response (solid line), the open circles show the smearing effect that comes from a finite jet energy resolution and a steeply falling photon cross section. No photon trigger or jet reconstruction thresholds are modelled in the simulation illustrated in Figure 3.7.

The simulation is also used to investigate the effect of the photon cross section on the measurement of R_{jet}. Figure 3.8a is binned in terms of E^{meas}_{jet} and shows the change in the measured response for different E_T dependences of the photon cross section. The differences are particularly large at low energies. Figure 3.8b is binned in terms of E' and therefore shows unbiased measurements of the jet energy response. The dashed line is a fit to the response obtained for a E_T^{-5} dependence of the photon cross section, which is the most realistic of the three examples shown. The agreement between the fit and the input response is excellent.

Finally, we illustrate the trigger threshold bias on the response, using direct photon collider data. Figure 3.9a shows the different responses binned in terms of E^{meas}_{jet} for three different photon triggers, requesting photons above 25, 40 and 60 GeV respectively. Figure 3.9b is binned in terms of E', and shows no bias. Again, we see that the use of E' produces the desired result.

In conclusion, the method developed to measure R_{jet} removes the instrumental biases arising from the use of measured quantities in γ-jet events.

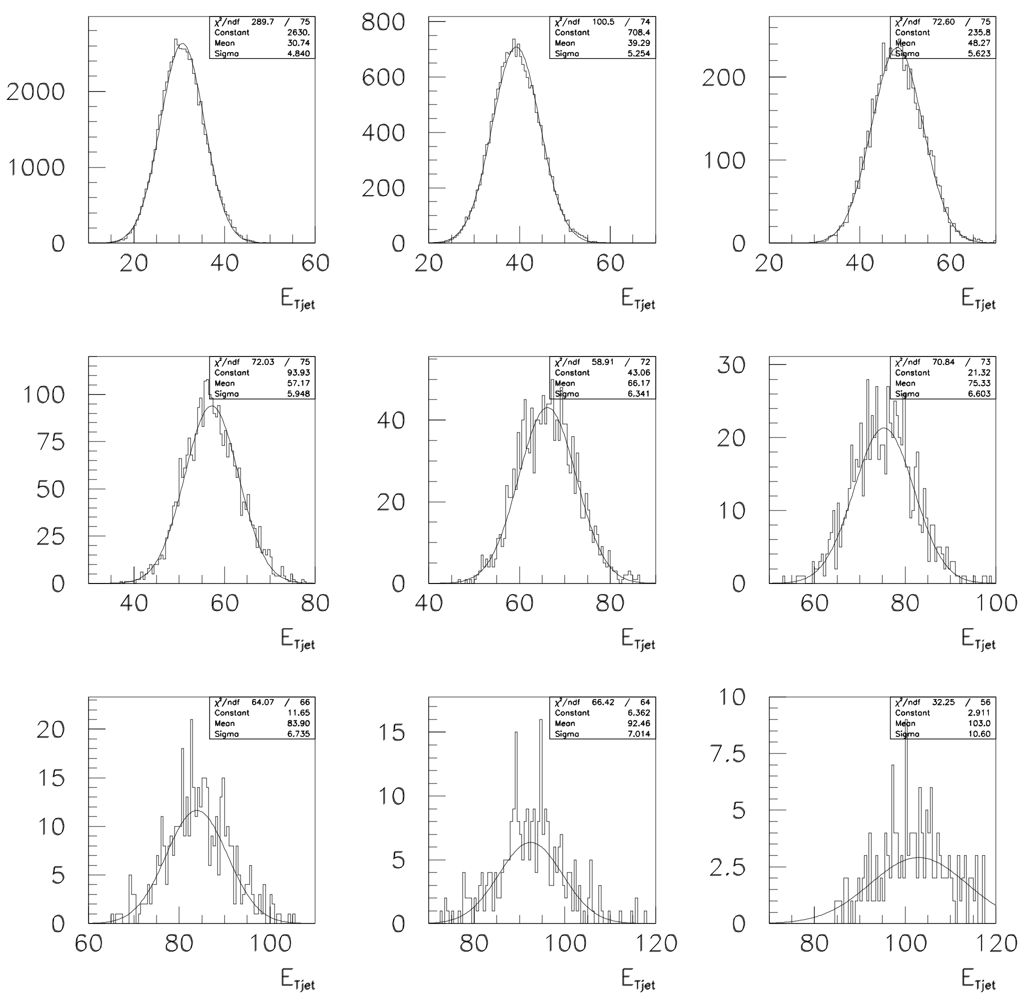

Figure 3.6: Jet E_T distributions for simulated γ-jet events. The nine plots correspond to different $E_{T\gamma}$ bins from 30 GeV to 120 GeV. The bin size is 10 GeV. E_{Tjet} is uncorrected.

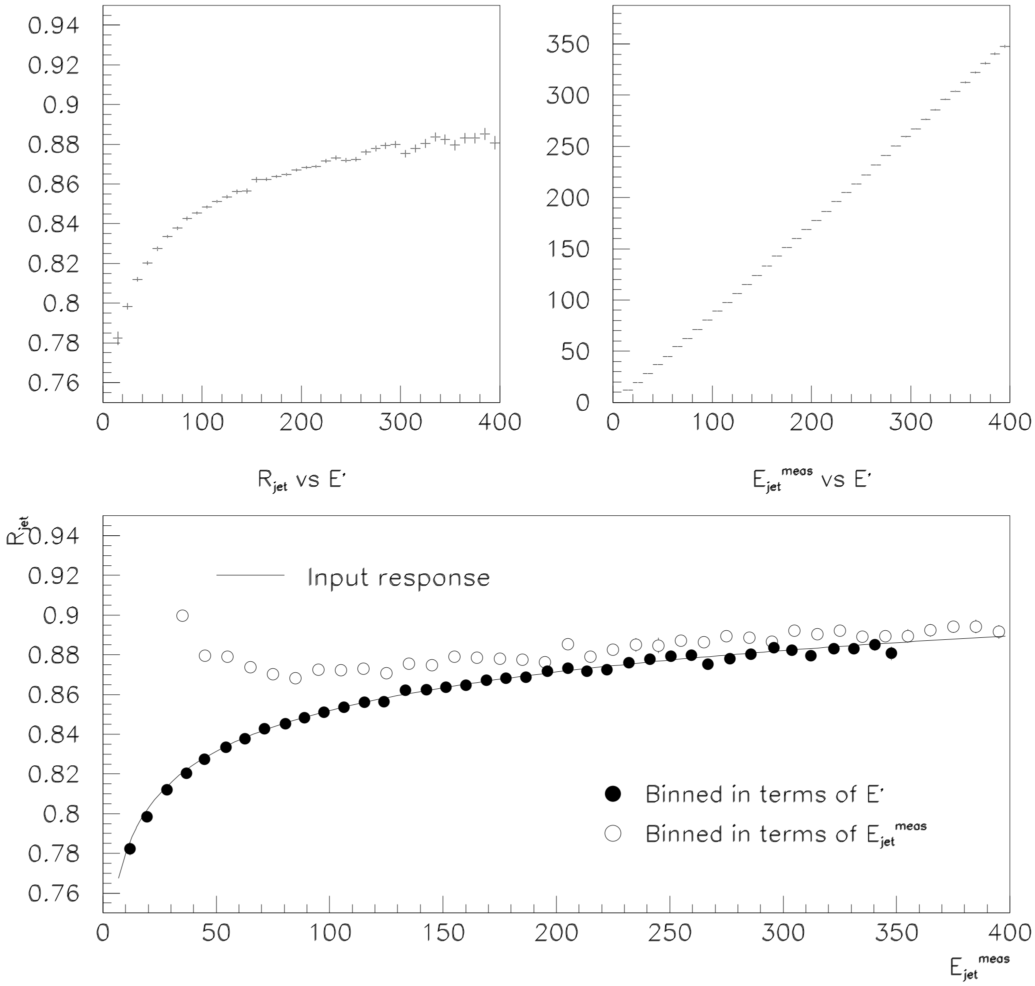

Figure 3.7: Parametric simulation of the R_{jet} measurement. The bottom plot shows a comparison of R_{jet} determined directly as a function of E_{jet}^{meas} (open circles) and the same quantity binned in terms of E' and then mapped onto E_{jet}^{meas} (closed circles).

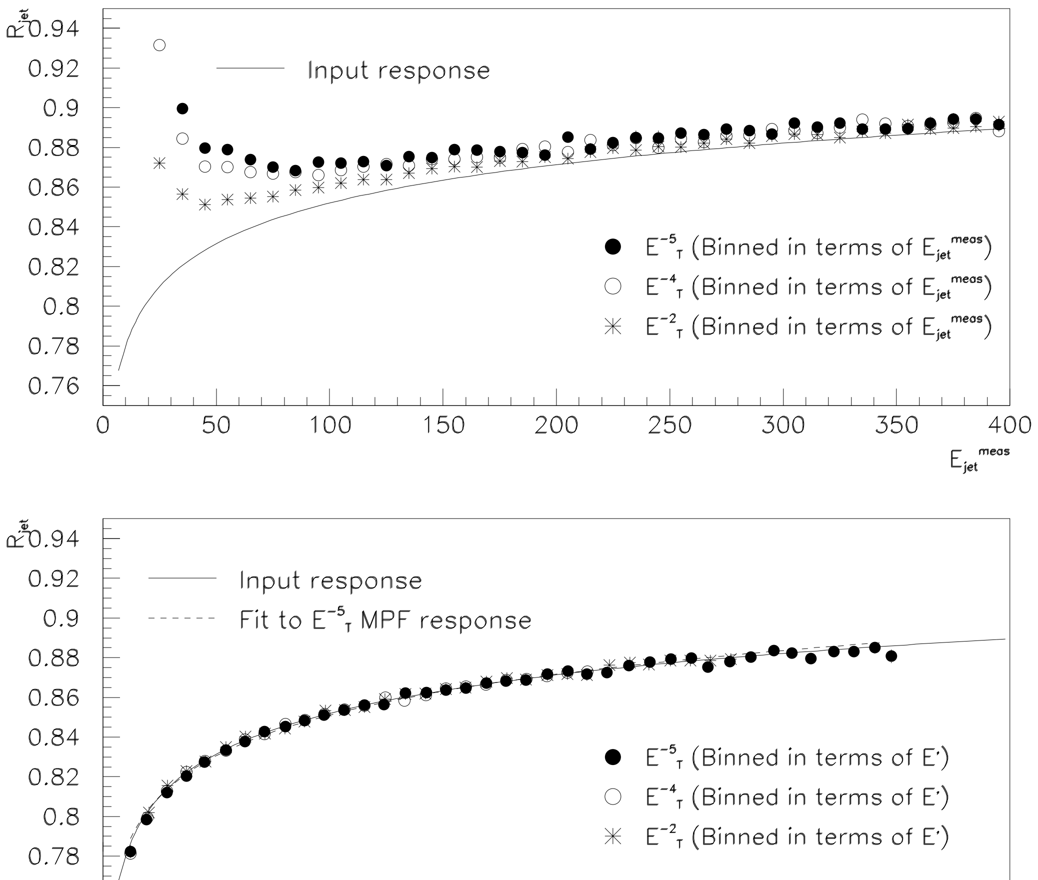

Figure 3.8: Parametric simulation of the R_{jet} measurement. The top plot shows the bias in R_{jet} for different E_T dependences of the photon cross section. The bottom plot shows the unbiased response, binned in terms of E'.

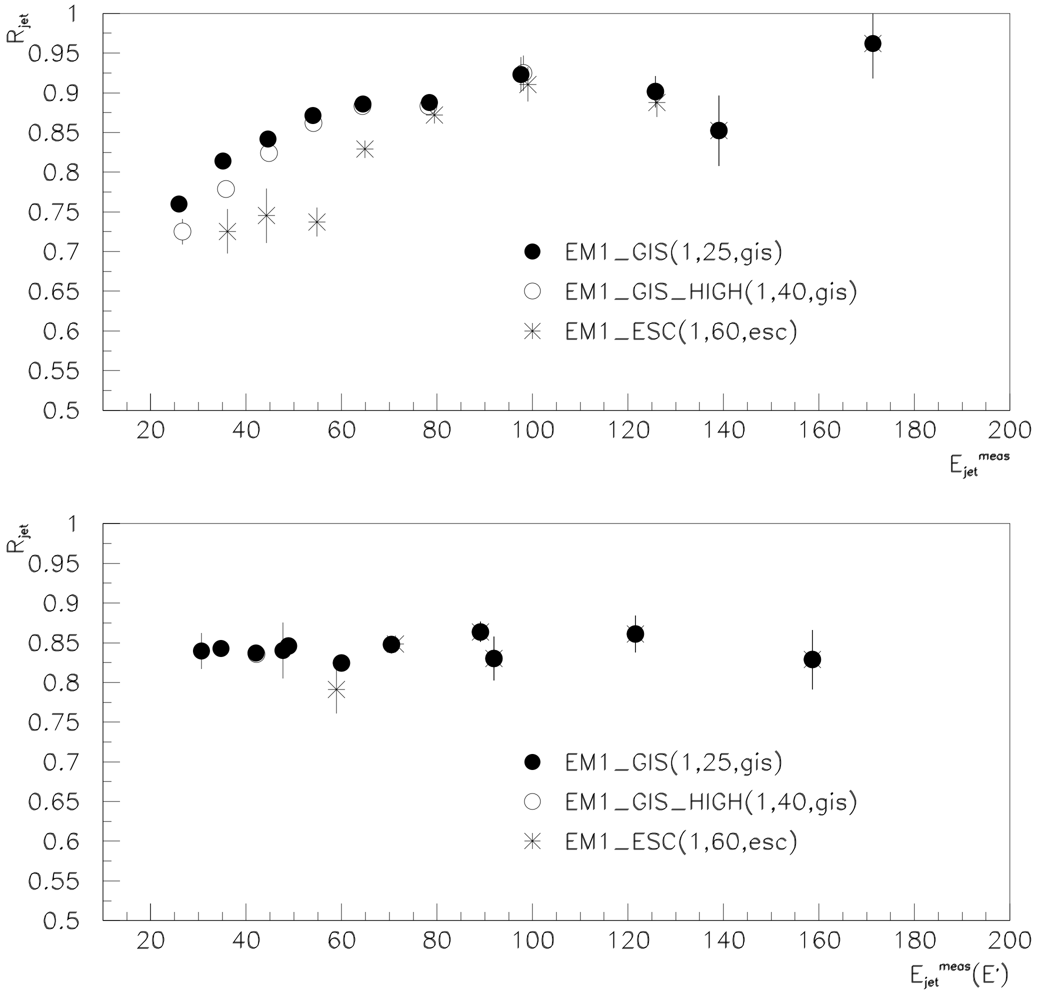

Figure 3.9: Parametric simulation of the R_{jet} measurement. The top plot shows the trigger threshold bias on R_{jet}. The bottom plot is binned in terms of E' and shows no bias.

Chapter 4

Response: Photon Sample Selection

The selection of a sample of pure direct photon events is not a trivial exercise. In addition, we need the largest possible sample in order to measure the jet response of each calorimeter with a reasonable uncertainty over a large range of energies. Therefore, R_{jet} was measured from a collider data sample obtained by applying a set of cuts which retain the most events while limiting the systematic errors. These cuts are not tuned to give a pure sample of direct photon events but rather to give a sample of events with one isolated photon or electromagnetic (EM) cluster.

4.1 Triggering

The triggers employed in this analysis were designed for the Run I direct photon measurements and span the E_T range from 4 GeV through 60 GeV. Two less restrictive triggers, GAM_LOW (Run Ia) and EM1_ESC (Run Ib), improve the sample statistics in the low and high energy range respectively. Aside from these two triggers, the Level 2 filters (software triggers) required at least one isolated electromagnetic cluster with shower shape consistent with a photon ("gis"). The triggers are described in Table 4.1.

The events are included in the sample only if the $E_{T\gamma}$ is greater than the trigger threshold plus one $\sigma_{E_{T\gamma}}$, where $\sigma_{E_{T\gamma}}$ is the photon energy resolution. This offline cut avoids biased photon candidates. In cases in which multiple photon triggers were running at once, a high E_T threshold cut prevents a photon event to pass a lower threshold trigger and fail a higher threshold trigger, if the reconstructed $E_{T\gamma}$ is higher than the higher trigger threshold. This removes rare events with photons which fluctuated to a very high energy in the calorimeter.

4.2 General Offline Cuts

From the events that passed the triggers and the $E_{T\gamma}$ threshold cuts, we used only those events with one or more PPHO objects (EM clusters without a track, mostly photons) and/or PELC objects (EM clusters with a track in the wire chambers, mostly electrons). In addition, a set of quality cuts were applied to remove the background events. There are two types of background:

- The **Instrumental Background** is contributed by events in which the photon, or pair of photons from a π°, is not well isolated from a significant amount of hadronic energy (i.e. the photon candidate is a jet). This background is removed by longitudinal and transverse isolation cuts. If a jet is dominated by a leading π° or γ with no nearby hadronic activity, it is a background to direct photons. However, since the response

Table 4.1: Triggers used in the photon event selection. The Level 2 filter condition, L2EM(1,E_T), only selects events with at least one electromagnetic cluster above a particular E_T. Additional E_T cuts are applied offline.

Trigger Name	Run	Level 2	E_T^{min}	E_T^{max}
GAM_LOW	Ia	L2EM(1,4,gam)	4.5 GeV	15 GeV
GAM_LOW_ISO	Ia	L2EM(1,6,gis)	7 GeV	50 GeV
GAM_MED_ISO	Ia	L2EM(1,14,gis)	15 GeV	50 GeV
GAM_HIGH_ISO	Ia	L2EM(1,30,gis)	31 GeV	900 GeV
GAM_6_ISO_GAM	Ib	L2EM(1,6,gis)	7 GeV	15 GeV
GAM_14_ISO_GAM	Ib	L2EM(1,14,gis)	15 GeV	50 GeV
GAM_20_ISO_GAM	Ib	L2EM(1,20,gis)	21 GeV	900 GeV
EM1_GIS	Ib	L2EM(1,25,gis)	26 GeV	41 GeV
EM1_GIS_HIGH	Ib	L2EM(1,40,gis)	41 GeV	900 GeV
EM1_ESC	Ib	L2EM(1,60,esc)	61 GeV	900 GeV

to this object is very close to the photon or the electron response, it is not considered background in the calibration sample.

- The **Physics Background** include Drell-Yan, $Z \rightarrow e^+e^-$, and most notably $W \rightarrow e\nu$ backgrounds, which are primarily removed by cuts on EM-clusters with a track in a road to the vertex.

To ensure that the PPHO or PELC is a well measured cluster, we apply fiducial cuts which reject candidates near detector edges. The distance of CC clusters from an azimuthal EM crack must be greater than 0.01 radians. To avoid the inter-cryostat region and the region in which the granularity of the third EM layer of the calorimeter is coarser, we require the detector pseudorapidity[1] of the EM-cluster to satisfy $|\eta_\gamma| < 1.0$ or $1.6 < |\eta_\gamma| < 2.5$.

In general, the event is rejected if the μBLANK bit is set, that is if there is main ring activity (beam in the accelerator preceding the Tevatron) at the time of the event. In addition, events with primary vertices reconstructed in the far forward region tend to be poorly measured. As a result, we require the z-coordinate of the vertex to satisfy $|z| <$70 cm. Also, the $\not\!\!E_T$ in events which were flagged during reconstruction by the AIDA routine[2] during reconstruction was significantly different than in the rest of the sample. These events tended to register lower response jets in the case a cell was incorrectly removed from a probe jet. As a result, any event with a noisy cell removed by the AIDA routine is rejected. Since these events are rare, the effect on the measured response is less than 0.2%.

In order to avoid events with photons due to bremsstrahlung from cosmic ray muons, we use the muon system as a loose veto. If the leading photon has $E_T < 30$ GeV, we require no muons to be reconstructed in the event, otherwise we require $p_{T\mu} < 100$ GeV/c.

Jet quality cuts are also applied to remove fake jets. There must be at least one reconstructed jet in the event. The leading jet detector η must satisfy $|\eta| <$0.7 in the CC and

[1] Calculated from the geometric center of the detector and not the interaction vertex.

[2] AIDA removes noisy cells if they are five times more energetic than their neighbors in the longitudinal direction.

1.8< $|\eta|$ <2.5 in the EC. We ignore the event if any jet fails the coarse hadronic fraction (CHF), hot cell fraction (HCF) or the electromagnetic fraction (EMF) cuts, defined as:

$$0.05 < \mathrm{EMF} < 0.95$$
$$\mathrm{HCF} < 10$$
$$\mathrm{CHF} < 0.5\,.$$

CHF and EMF are the fractions of the jet energy deposited in the coarse and electromagnetic sections of the calorimeter, respectively. HCF is defined as the E_T ratio between the highest and the second highest E_T cells in a jet.

4.2.1 Studies of Backgrounds to Direct Photon Events

There are several processes with electromagnetic and hadronic clusters in the final state, but only a few contribute to the desired sample from which to extract a calibration. The physics background is composed of events with at least one isolated electron or photon. Examples are W events, various Drell-Yan processes, and diphoton production. The instrumental background arises from QCD dijet events in which one or more jets fake a photon or an electron. Although these events are background to direct photon events, most of them are included in the calibration sample since they increase statistics and make little change in the measured response.

Instrumental Background

The signature of the QCD dijet event in which one jet fakes a photon is very similar to that for the direct photon. By virtue of the leading π°, the EM-jet has good response and resolution. In addition, there is no real $\not{E}_T$ in the event. In some sense, the use of this sample for calibration is superior to the photon sample because the physics processes involved give jets more representative of the inclusive jet sample, from the point of view of their gluon and quark content. Leading jets balancing high E_T photons are predominantly quarks, while for low E_T photon events the recoil is primarily gluons. Also, the fraction of the recoiling jet population which arises from gluons depends on the difference in η of the jet and photon. Combining the QCD and direct photon samples improves the statistics. The drawback is that the jet leading π° is not isolated but usually associated with hadronic activity. Therefore, the jet response measured from the combined sample may be biased high.

The following variables are used in the procedure to select a sample which contains direct photon events and QCD events with one jet with high EMF and little hadronic activity:

- EMF: fraction of the cluster E_T deposited in the EM-layers of the calorimeters. EM-clusters deposit more than 90% of their energy in the EM-layers.

- f_{iso}: the transverse isolation variable. It is defined as:

$$f_{iso} \equiv \frac{E_{tot}(\mathcal{R}=0.4) - E_{em}(\mathcal{R}=0.2)}{E_{em}(\mathcal{R}=0.2)}\,.$$

  A cut on this variable removes jets with high EM content if they also include significant hadronic activity. For low E_T EM-clusters, the cut threshold is raised to avoid inefficiencies due to the general hadronic activity in the calorimeter. iso_4 is a total energy isolation variable which is used at low E_T to complement the f_{iso} cut. It is defined as:

$$iso_4 \equiv E_{tot}(\mathcal{R}=0.4) - E_{em}(\mathcal{R}=0.2)\,.$$

- ε_t: a function of the total charge seen in the transition radiation detector (TRD) [5, 1]. Low ε_t is associated with a high charge deposition, and high ε_t with low deposition. ε_t is approximately flat for electrons, peaks near 1 for charged pions, and photon conversions tend to group around 1 and 0. For example, a cut of $\varepsilon_t < 0.1$ or $\varepsilon_t > 0.9$ rejects approximately 80% of the electrons and has a high acceptance for photon conversion.

- dE/dx: ionization in the central tracking detectors [1] in units of minimum ionizing particles (MIP). By definition, dE/dx is 1 for an electron, 2 for a photon conversion, and peaks near 0.7-0.8 for low E_T hadrons. For example, a cut such as dE/dx <0.8 or dE/dx >1.5 is a good compromise between high photon acceptance, background rejection and good statistics.

- σ_{trk}: track match significance. It measures mis-alignment between the energy cluster in the calorimeter and the track in the central detectors. Electrons have low values of σ_{trk}. In the case of photons, tracks may be associated with low energy charged hadrons which spatially overlap high p_T photons. Large values of σ_{trk} are associated with this type of photon events. σ_{trk} is defined as:

$$\sigma_{trk} = \sqrt{\left(\frac{\Delta\varphi}{\sigma_{\Delta\varphi}}\right)^2 + \left(\frac{\Delta R}{\sigma_{\Delta R}}\right)^2}.$$

Each variable was studied as to whether it was significantly correlated with the measured R_{jet}. There is little correlation between the measured response and cuts on the tracking variables, except in the case of W events, discussed below. The isolation variables like the EMF, on the other hand, were significantly correlated with R_{jet}. We use isolated electrons from $Z \to e^+e^-$ events to tune the EMF and the isolation cuts, since they represent the typical behavior of isolated electrons or photons which adhere to the EM-scale. The tracking cuts were tuned to remove electrons from background events, also using the $Z \to e^+e^-$ sample. The set of cuts shown in Table 4.2 was designed to reduce the dependence on the cut thresholds of the response measured from the EM-jet sample. In the case of the three tracking variables, the cuts are applied in an OR or in an AND basis, depending on whether a $\not{E}_T$ cut is satisfied or not. The $\not{E}_T$ cut will be discussed in the next section since it is introduced to remove physics background.

Table 4.2: Quality cuts on photon candidates to reject background.

	$E_{T\gamma} < 15$ GeV	$E_{T\gamma} > 15$ GeV
dE/dx	< 0.8 or > 1.5	< 0.6 or > 1.5
ε_t	< 0.25 or > 0.75	< 0.1 or > 0.9
σ_{trk}	> 3.0	> 3.0
EMF	> 0.9	> 0.96
f_{iso}	< 0.5	< 0.15
iso_4	< 2.0	no cut

The bias in R_{jet} due to the presence of highly electromagnetic jets in the photon sample was studied using the H-matrix χ^2 test. This matrix is constructed with transverse and longitudinal shower shape information from the cluster and then compared with a Test Beam measurement. A cut on χ^2 removes a significant number of events but it is a good discriminator between real photons and EM-jets. Figure 4.1 shows the magnitude of the instrumental background bias. As the cut on χ^2 tightens the fraction of real photons to fake photons in the sample grows, and the apparent response of the probe jet decreases very slightly. The response for CC jets is plotted for three different ranges of E'. Even very tight cuts on the sample, $\chi^2 < 50$ and no tracks pointing to the cluster, change the response of the probe jet by less than 1%.

The χ^2 cut is not applied in the selection procedure so that good statistics in the sample can be retained. The contribution of the instrumental background bias to the response uncertainty will be discussed in Chapter 6.

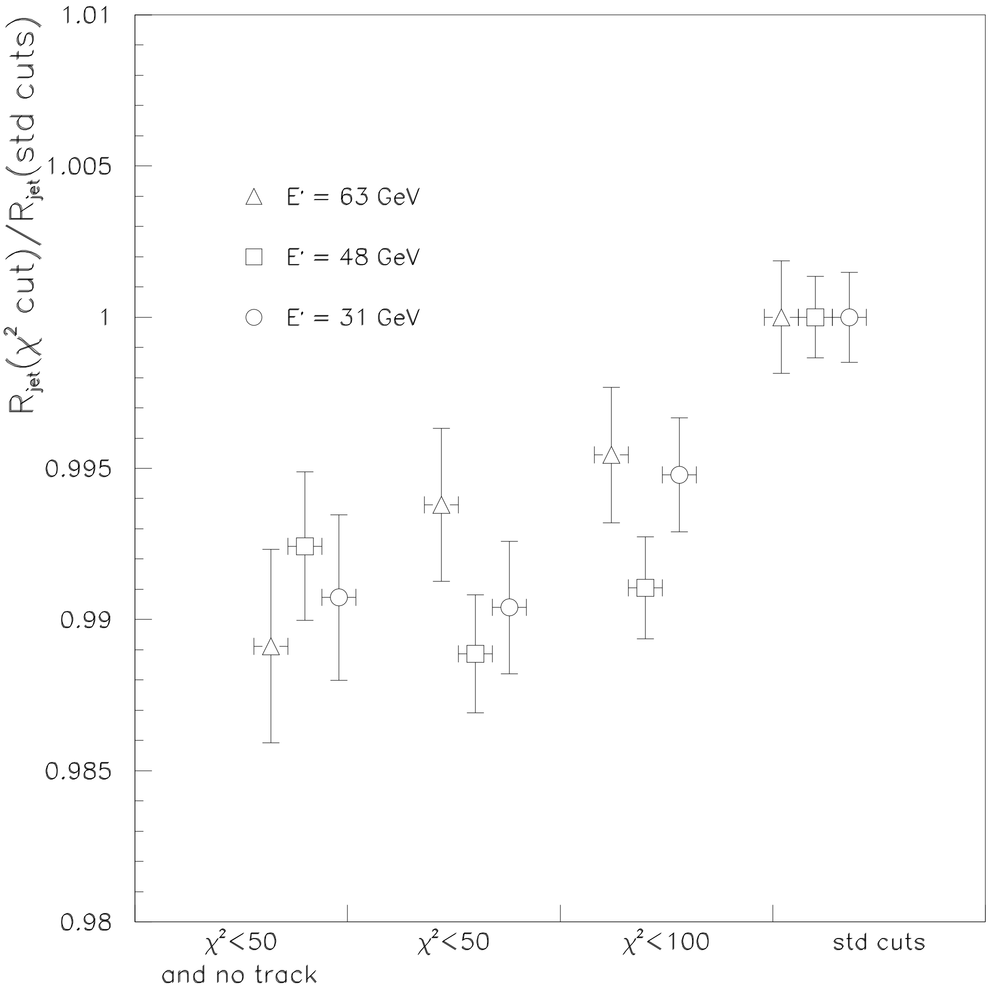

Figure 4.1: Change in the measured R_{jet} as the the χ^2 cut is tightened. R_{jet} (std cuts) is the measured response from the γ-jet sample selected with the cuts described in this chapter. An additional cut on χ^2 in the H-matrix test is applied to obtain R_{jet} (χ^2 cut).

Physics Background

The physics background consists of Drell-Yan signals such us $Z \to e^+e^-$, $W \to e\nu$ and diphoton production. In collider data, the major contribution comes from W plus jet events.

In the case of an event with two electromagnetic clusters, such as in $Z \to e^+e^-$ production, R_{jet} is approximately 1. For example, from a $Z \to e^+e^-$ ISAJET[13] sample, the measured R_{jet} is 0.95. The effect of the Z background on the R_{jet} measured from the γ-jet sample can be easily checked by applying a cut on the di-electron invariant mass. A cut on this mass, M_{ee} >105 GeV or M_{ee} <75 GeV, produces a negligible change in the measured response.

$W \to e\nu$ events have a large $\vec{\not{E}}_T$ in the direction of the neutrino. They are not useful for calibration purposes. The cuts to remove this background were developed from data and Monte Carlo samples.

First, the number of $W \to e\nu$ events was estimated from a subset of the Run Ia direct photon sample. We selected events passing the GAM_HIGH_ISO filter and applied the cuts described in the previous section. For the W estimation, we used a subset of 5000 PELC events (L=3.8 $\pm$ 0.6 pb^{-1} passing the quality cuts). In the total Run Ia W sample, there were 9800 events (L=12.8 $\pm$ 0.7 pb^{-1}). In the subset, we expect:

$$N = N^W_{totalIa} \times (\mathcal{L}_{subset}/\mathcal{L}_{totalIa}) \times \varepsilon \,.$$

The efficiency ε of W events to pass the selection relative to the Run Ia W cross section analysis cuts was estimated from a sample of ISAJET $W \to e\nu$ events. It was found to be ε =0.135. Therefore,

$$9800 \times (3.8/12.8) \times 0.135 = 393 \,.$$

A cut on $\not{E}_T$ is a good discriminator against W events, $\not{E}_T/E_{T\gamma} < 0.65$. The number of events failing this cut is 376 in the subset. Since 10% of W events in the ISAJET sample pass the $\not{E}_T$ cut, the total number of W events expected in the subset is $376 \times 1.1 = 414$ events. This number is in good agreement with the result derived in the preceding paragraph. The neutrino in W events is opposite in φ to the electron. Therefore, R_{jet} is approximately 0.1 measured from the ISAJET sample, and closer to 0.85 from real photon events. As a result, if no cut is applied to remove W events, we expect a $\sim$6% bias in the response measured from the 5000 PELC sample. For the PPHO sample, the bias is on the order of 1.5%.

The W background is reduced by requiring $\not{E}_T/E_{T\gamma}$ <0.65 for moderate to high p_T photon events. The cut on $\not{E}_T$ may introduce a bias on the R_{jet} distribution by cutting off the tail preferentially on the low side. To avoid this, we apply a weak version of the $\not{E}_T$ cut. If the event does not pass the $\not{E}_T/E_{T\gamma}$ <0.65 condition, it is kept only if the three tracking variables, dE/dx, σ_{trk}, and ε_t, are inconsistent with an electron (see Table 4.2). If $\not{E}_T/E_{T\gamma}$ <0.65, then the event is kept if at least one of the three tracking cuts is satisfied.

The residual background left in the PELC sample after the $\not{E}_T/E_{T\gamma}$ cut introduces a bias in the measured response of $0.10 \times 0.06 \approx 0.5\%$ (0.1% in the PPHO sample), since 10% of W events pass the $\not{E}_T$ cut. Therefore, after the cuts, the residual physics background uncertainty on R_{jet} is on the order of 0.5%.

4.3 Topology Cuts

The relation $R_{had} = R_{jet}$, where jet is the leading jet in the γ-jet event, is exact only in the case of a two body process. Photon events may contain more than one reconstructed jet plus a number of energy clusters which were not reconstructed by the cone algorithm. Therefore, event topology is expected to contribute a systematic error to the response measurement. Since the second leading E_T jet usually has a lower energy, the measured response for the

Table 4.3: $\not\!\!E_T$ cut on photon events to remove physics background. The cut is applied in combination with the tracking cuts in an OR or an AND basis.

	$E_{T\gamma} < 15$	$15 < E_{T\gamma} < 25$	$E_{T\gamma} > 25$
$\not\!\!E_T/E_{T\gamma}$	< 2	< 1.2	< 0.65

leading jet is expected to be biased low when additional jets are present in the event. In the case that the second leading E_T jet is very forward, its energy may be larger than the energy of the leading jet. The response measurement would then be biased high. Since forward jets are infrequent, the latter is a second order effect [12].

In order to remove the topology bias, the photon and the leading jet are required to be back-to-back within 20°, that is $\Delta\varphi \equiv |\varphi_\gamma - \varphi_{jet}| > 2.8$. This cut increases the measured response by approximately 1%, and removes most of the topological bias. A cut on the E_T ratio of the leading and second leading jets was discarded since it would bias the sample towards events where the second leading jet fluctuated low. No bias due to the $\Delta\varphi$ cut is observed in variables such us the EMF and the width of the leading jet. The residual error is investigated by studying the change in response as a function of the $\Delta\varphi$ threshold from 2.1 to 3.1 radians for different energy bins. Figure 4.2 shows the change in R_{jet} as we tighten the $\Delta\varphi$ cut for the 50< E' <60 GeV bin. The circles correspond to an integrated distribution (lower $\Delta\varphi$ bins include the events of the higher $\Delta\varphi$ bins), while the open squares are associated with a differential distribution. A cut on $\Delta\varphi > 2.8$ is a good compromise between good statistics and bias minimization. The residual error after the cut is studied from the parametrizations to the integrated (linear fit) and differential distributions (exponential fit). The fractional difference between R_{jet} at $\Delta\varphi = \pi$ and $\Delta\varphi$ >2.8 is an estimate of the remaining topology bias. This difference as a function of E' is plotted in Figure 4.3 for both the CC and the EC. Again, the circles are the result from the integrated distribution and the squares are associated with the differential distribution. The plots suggest that after a $\Delta\varphi$ >2.8 cut, the remaining bias is on the order of 0.5-1% towards a lower response and consistent with a constant dependence on E'. Note that the topology and the instrumental background biases go in opposite directions. The contribution of the topology bias to the response uncertainty will be discussed in Chapter 6.

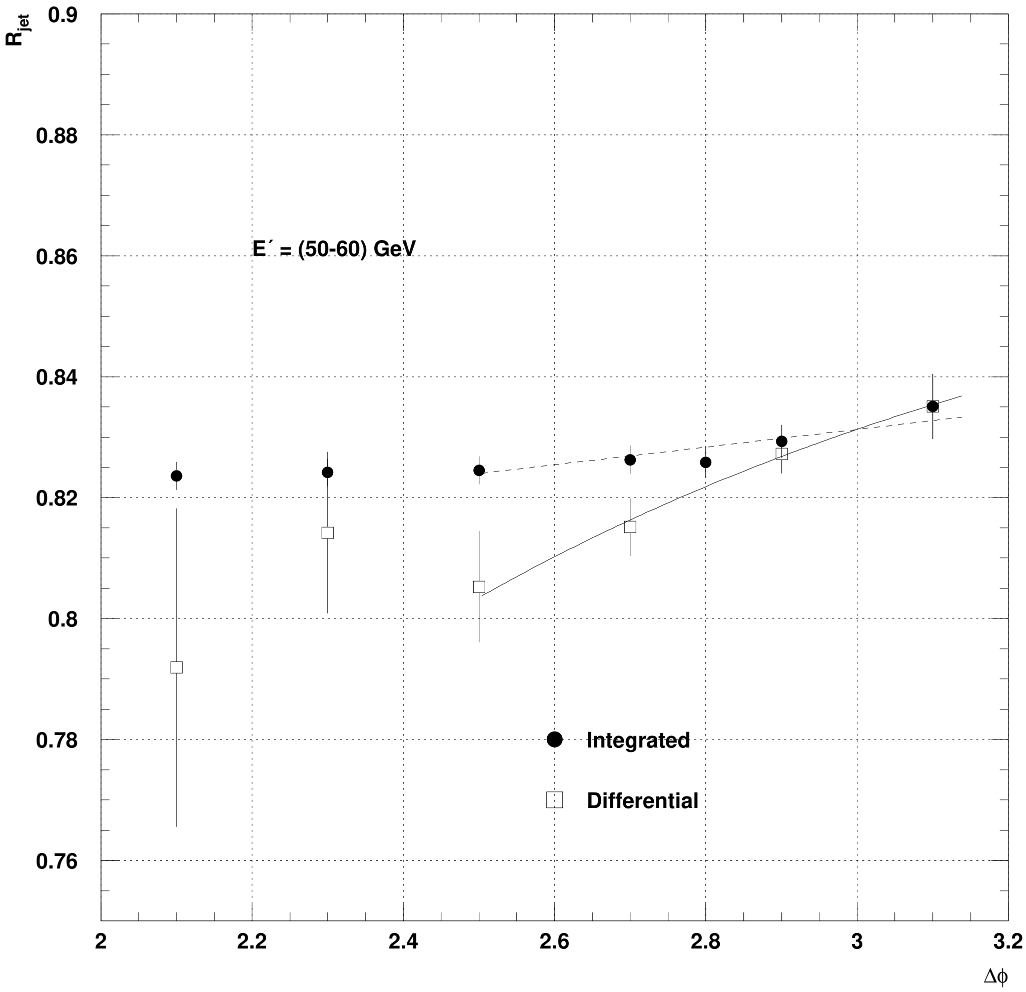

Figure 4.2: R_{jet} as a function of the $\Delta\varphi$ cut threshold for $50 < E' < 60$ GeV. The circles correspond to an integrated distribution (lower $\Delta\varphi$ bins include the events of the higher $\Delta\varphi$ bins), while the open squares are associated with a differential distribution. The solid and dashed lines are parametrizations to the integrated and differential distributions.

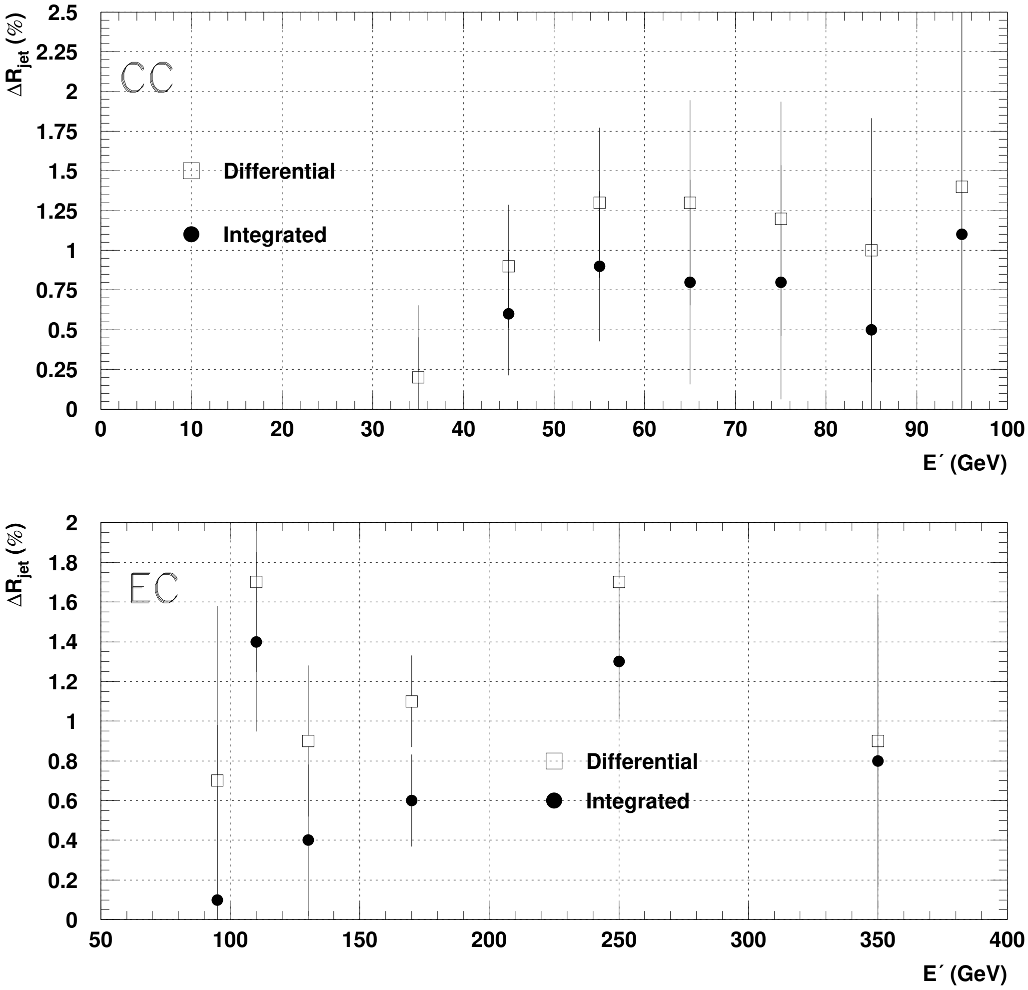

Figure 4.3: Percentage difference between R_{jet} at $\Delta\varphi = \pi$ and $\Delta\varphi$ >2.8 versus E'. The circles are the result from the integrated distribution and the squares from the differential distribution.

4.4 Multiple Interaction Cut

The limited accuracy of the vertex finding and reconstruction algorithms can produce a large shift in the measured response. On average, the effect on events reconstructed with an incorrect vertex selection is to increase the measured E' by smearing jets to higher pseudo-rapidity. This has the effect of increasing the $\not\!\!E_T$ in the direction of the jet, thus lowering the measured response. This effect grows as luminosity increases. Figure 4.4 shows R_{jet} versus E' measured from samples of low ($\mathcal{L}$ <5), medium (5< $\mathcal{L}$ <8) and high ($\mathcal{L}$ >8) luminosities. It is clear from the R_{jet} distributions in Figure 4.4 that the bias in the measurement is due to low response tails which grow as the probability of mis-vertexing increases with luminosity.

The low luminosity sample still contains a fraction of multiple interaction events. We remove them by requiring MITOOL to be 1 or 2, which means that it is very likely that the remaining events are single interactions. A cut on MITOOL uses Level Ø trigger, tracking and calorimeter information to distinguish between single and multiple interactions. It is more efficient than a cut on the number of vertices since the latter would not reject multiple interaction events for which the second vertex was not reconstructed. Another possibility is to remove the events where the most probable vertex does not give the minimum $\not\!\!H_T$, where $\not\!\!H_T$ is the $\not\!\!E_T$ recalculated using each of the other reconstructed vertices. But $\not\!\!H_T$ is only an approximation to $\not\!\!E_T$, since it is not recalculated using cell information. Figure 4.5 shows the change in the measured response from a low luminosity sample when the MITOOL cut is applied. Remaining tails in the R_{jet} distributions are removed by the cut.

To check for any residual luminosity effects in the response after the MITOOL cut, the response versus luminosity was measured as a function of luminosity for various E' bins for CC and EC jets. We chose the following exclusive luminosity intervals: [0,3],[3,5], [5,8], [8,10], [10,∞]. Then, we determined R_{jet} versus E' for each luminosity bin while requiring MITOOL to be 1 or 2. Figures 4.6 and 4.7 show the response as a function of L for different E' bins for CC and EC jets respectively. By doing a linear fit of R_{jet} versus L, we can extrapolate to zero luminosity and assume that the response at zero luminosity is the correct result. In Fig. 4.6 it is clear that the CC data shows very little sensitivity to luminosity. The EC data show a slight trend to lower response with increasing luminosity. The estimated difference in response between a luminosity of 5 and 0 is on the order of 0.5% for the EC jets. Since the sample used in this analysis is integrated over luminosities from 0 to 5, we expect any residual luminosity effect to be about half of the above 0.5%. Further, we see no evidence for an E' dependent luminosity effect in the data. After the luminosity and MITOOL cuts are applied, there is a significant reduction in the luminosity dependence of the response measurement. Therefore, it is reasonable to assume that mis-vertexing in the data contributes a small uncertainty to the response measurement, on the order of 0.25% for EC jets only.

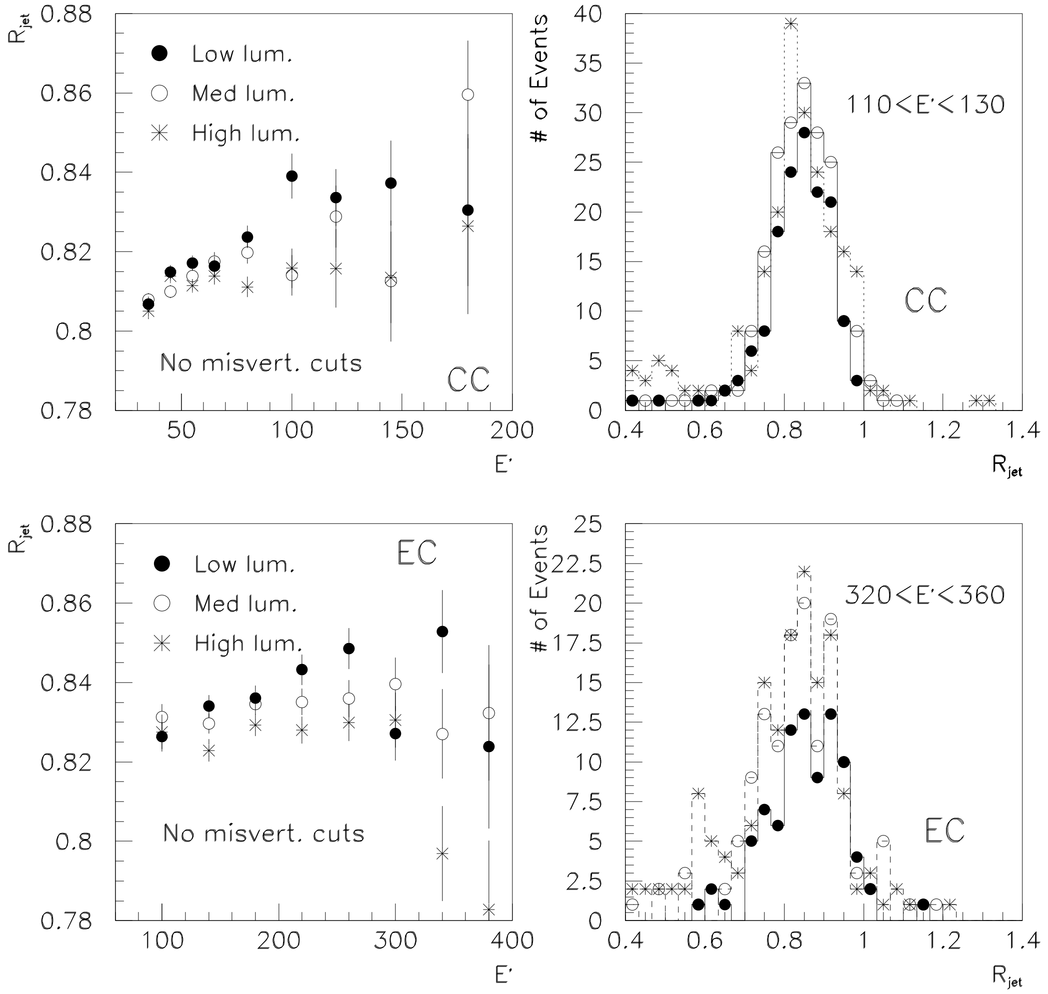

Figure 4.4: R_{jet} versus E' (in GeV) in the CC and EC measured from samples at different instantaneous luminosity. High luminosity samples give biased measurements due to misvertexing.

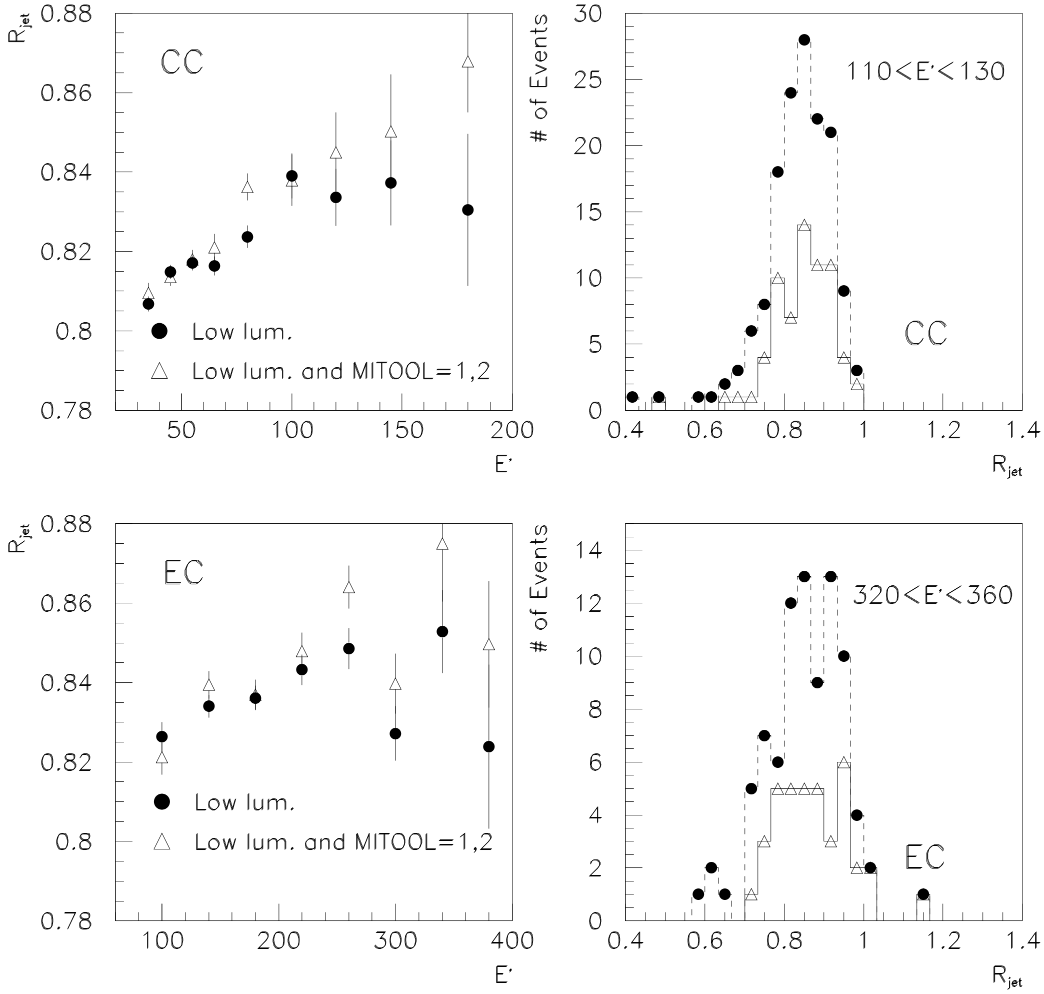

Figure 4.5: R_{jet} versus E' (in GeV) in the CC and EC measured from a low luminosity sample. The MITOOL cut removes remaining multiple interaction events.

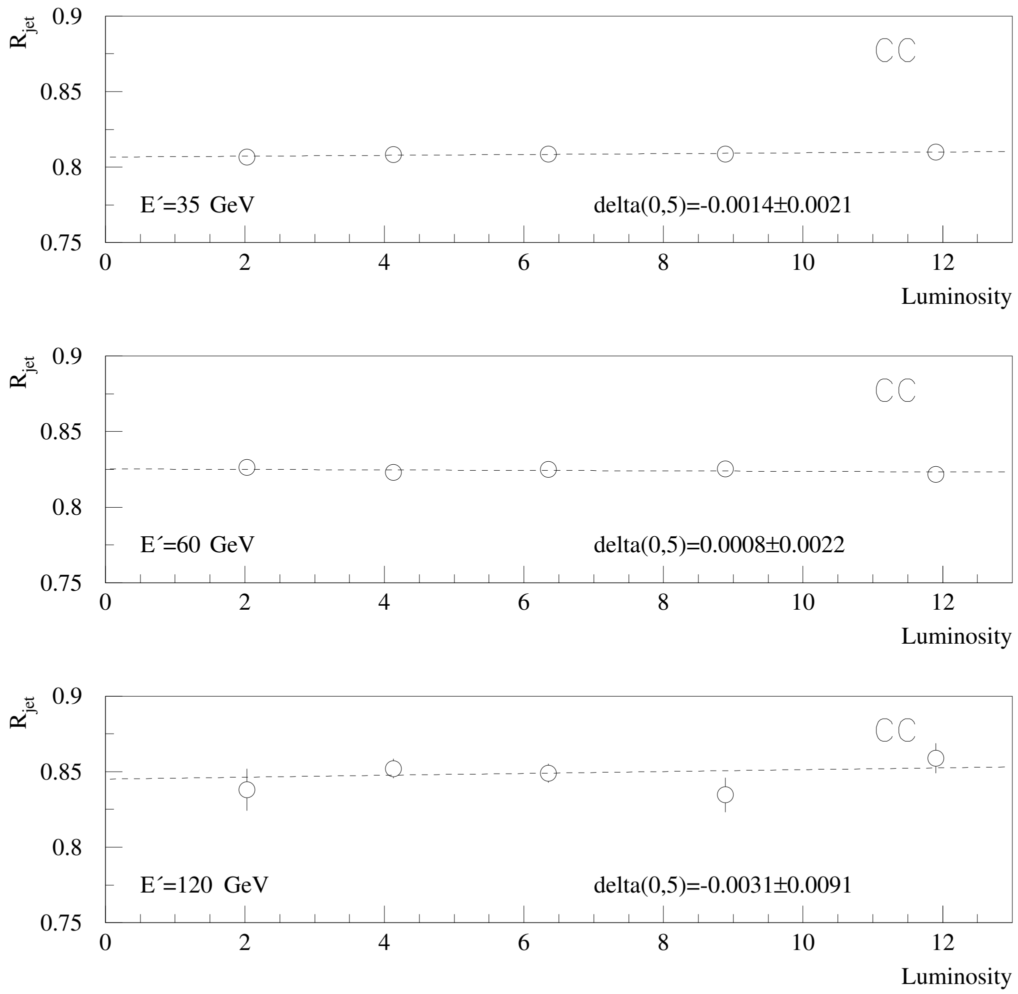

Figure 4.6: Response as a function of luminosity for CC jets with $E' = 35$, 60, and 120 GeV. The variable delta(0,5) is the difference in R_{jet} measured from samples taken at luminosities of 0 and 5.

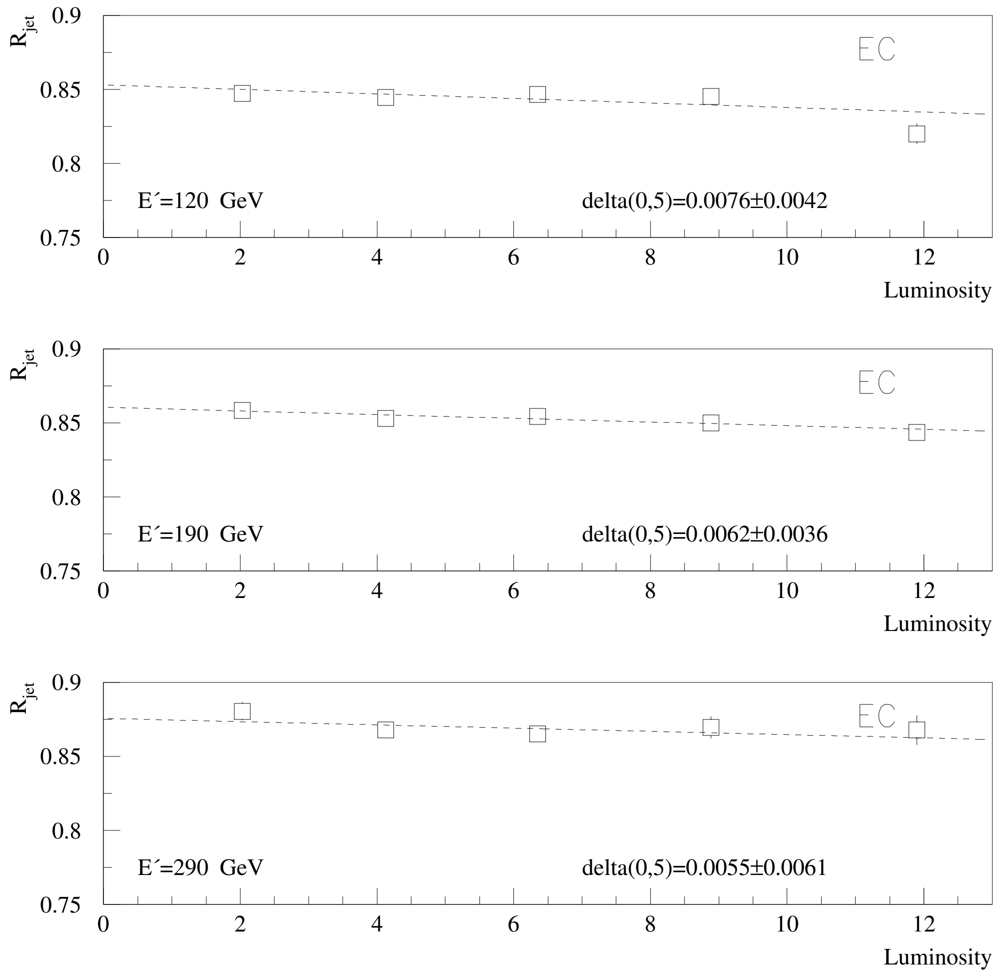

Figure 4.7: Response as a function of luminosity for EC jets with $E' = 120$, 190, and 290 GeV. The variable delta(0,5) is the difference in R_{jet} measured from samples taken at luminosities of 0 and 5.

Chapter 5

Response: Reconstruction and Rapidity dependence

The DØ calorimeter system is fairly uniform as a function of the azimuthal angle and pseudorapidity. However, since most of the physics analyses need a high level of accuracy in the jet energy scale at all rapidities, an η dependent correction is derived. No φ dependent calibration is currently implemented.

The reasons for the non-uniformities in pseudorapidity include cracks in the intercryostat region, differences between the CC and EC calorimeters and changes in sampling weights in different versions of the reconstruction program (RECO). After η dependent corrections are applied, the calorimeters are uniform in energy response to a 1% level. At that stage, R_{jet} can be described by a single curve for all φ's and pseudo-rapidities.

The reconstruction and other η dependent corrections are applied to the jet energy as multiplicative factors. The event $\not\!\!E_T$ must also be corrected since we want the R_{jet} measurement to be independent of the RECO versions and pseudorapidity. As a first step in the measurement of R_{jet}, we apply a response correction to the photons in the γ-jet sample and modify the event $\vec{\not\!\!E}_T$ accordingly. Following this step, the η dependence of R_{jet} is determined. After we apply the η dependent correction to $\vec{\not\!\!E}_T$, the detector becomes uniform in pseudorapidity and we determine the absolute response.
Given the definition of $\vec{\not\!\!E}_T$:

$$\vec{\not\!\!E}_T = -\Big(\sum_i E_x^{(i)}, \sum_i E_y^{(i)}\Big)\,,$$

we can make the approximation:

$$\vec{\not\!\!E}_T \approx -\sum_{obj} \vec{E}_T^{(obj)}\,,$$

where the sum is over the E_T of the physics objects (jets and photons in the γ-jet sample). The formula to correct the $\vec{\not\!\!E}_T$ reduces to:

$$\vec{\not\!\!E}_T^{\,corr} = \vec{\not\!\!E}_T^{\,meas} + \sum_\gamma \vec{E}_{T\gamma}^{meas} - \sum_\gamma \vec{E}_{T\gamma}^{corr} + \sum_{jet} \vec{E}_{Tjet}^{meas} - \sum_{jet} \vec{E}_{Tjet}^{corr}\,.$$

This formula is a good approximation to the corrected $\not\!\!E_T$. It depends on the jet algorithm because it is based on reconstructed physics objects instead of all the calorimeter cells. We choose a large cone algorithm, $\mathcal{R}$=0.7, to ensure a good approximation.

5.1 Reconstruction Dependent Correction

Most of the physics analyses which apply the jet energy scale correction use RECO V10, V11 or V12. The first two versions were only used for Run Ia samples, while all Run Ib samples are reconstructed with RECO V12.

RECO V11 included in the raw energy calibration the change in the calorimeter high voltage (HV) setting, from 2.5 KV to 2 KV, implemented from run 52470 during Run Ia [14]. One power supply on the calorimeter has been at 1.6 kV (PS# 92) rather than 2.0 kV because of an oscillating current. There is not any version of the reconstruction algorithm, up to 12.21 at least, that compensated for this. We do not attempt to do so here, since the effect is minor.

RECO V12 included updated sampling weights. These changes are constant for all hadronic layers in each compartment (ie. all CC FH cells get corrected by 5.1% regardless of layer), but EM cells were changed layer-by-layer. We have determined approximate corrections which average the various actual sampling weight changes by a typical longitudinal jet profile in that compartment. Since only the EM sampling weights changed layer-by-layer, this weighting only affects the correction of the EM energy of jets. For RECO V10 and V11, the energy scale includes an extra ICR correction, prior to the general ICR correction described in this chapter. This reconstruction dependent correction puts RECO V10 and V11 jets on the same footing as V12. In order to obtain these corrections, we ran RECO V11 and V12 over 400 jets with the z coordinate of the interaction vertex set to zero, to prevent the changes in the tracking code from affecting the result. From the ratios between the jet E_T clustered by RECO V11 and V12, we extracted the relative correction between the two algorithm versions for each calorimeter section (EM, FH and CH). The correction factors are applied separately to the EM, FH and CH energy fractions of the jets, depending on the jet position.

The calibration of RECO V11 and V10 to V12 is not achieved with a high level of accuracy in the ICR. Users must be aware that in the region $0.7 < |\eta| < 1.8$, the correction presented here does not necessarily correct back to the particle level within the quoted errors for RECO V10 and V11. The reason is that the general ICR correction, which is described later in this chapter, is tuned with RECO V12 data. There is also evidence that RECO V10 jets are undercorrected by $\sim$2%. This is not surprising since the corrections to the sampling weights and the response measurement were obtained from RECO V11 data.

In order to put all the RECO versions on the same footing, the jet energy for RECO V10 and V11 are corrected by the multiplicative factors shown in Table 5.1. The high voltage corrections are applied only to RECO V10. The $\vec{\not\!E}_T$ is also corrected using the corrected jet transverse energy.

Table 5.1: High voltage and sampling fractions corrections.

	Sampling (EM)	Sampling (FH)	Sampling (CH)	HV (EM)	HV (HAD)
CC	0.995 ± 0.005	1.051 ± 0.001	0.980 ± 0.001	1.015	1.023
EC	0.990 ± 0.002	0.980 ± 0.005	0.987 ± 0.001	1.016	1.019

5.2 Cryostat Factor Correction

The measured R_{jet} versus E' before any correction is shown Figure 5.1. R_{jet} is plotted in three pseudorapidity regions: CC ($|\eta| < 0.7$), ICR ($0.7 < |\eta| < 1.8$) and EC ($1.8 < |\eta| < 2.5$).

The difference in response is on the order of 2% between the EC and the CC, and 5% between the ICR and the CC.

The cryostat factor, F_{cry}, is defined as the ratio $R_{jet}^{EC}/R_{jet}^{CC}$. The CC and the EC calorimeters were constructed using the same technology. Moreover, the increase of the jet width with pseudorapidity is approximately the same in the CC and the EC. Therefore, it is reasonable to assume that F_{cry} is a constant function of E', as suggested by Figure 5.1.

The cryostat factor is obtained from the range 60 GeV$< E' <$180 GeV, where the CC and EC data overlap. In the EC, a cut on $E_{T\gamma} > 25$ GeV is added to those described in Chapter 4. Its purpose is to remove the reconstruction threshold bias due to jet finite energy resolution. Although F_{cry} should not depend on the jet algorithm, the $\mathcal{R}$=0.7 cone algorithm was used to determine the jet pseudorapidity in the CC or EC. The jet detector η was required to satisfy $|\eta| < 0.7$ in the CC and $1.8 < |\eta| < 2.5$ in the EC in order to avoid the intercryostat region. F_{cry} was also measured separately in the EC north $(-2.5 < |\eta| < -1.8)$ and the EC south $(1.8 < |\eta| < 2.5)$. The ratio, $F_{cry}^N/F_{cry}^S = 0.997 \pm 0.003$ suggests F_{cry} is the same in both EC's within errors. Figure 5.2 illustrates the determination of F_{cry} from a fit of a constant function to the measured $R_{jet}^{EC}/R_{jet}^{CC}$ versus E'.

The results from Run Ia (RECO V11) and Run Ib (RECO V12) data are:

$$F_{cry} = 0.980 \pm 0.007\,(\mathrm{stat})\ \mathrm{for\,RECO\,V11}$$
$$F_{cry} = 0.977 \pm 0.005\,(\mathrm{stat})\ \mathrm{for\,RECO\,V12}\,.$$

Figure 5.3 shows the R_{jet}^{CC} and R_{jet}^{EC} responses versus E' after the $\not{E}_T$ has been corrected with the cryostat factor in EC jet events. The EC points are allowed to float in a fit to the response, through a normalization parameter. The normalization parameter is very close to unity, 0.999 ± 0.005, proving that the object-based correction to the $\not{E}_T$ is a good approximation.

The jets and the $\not{E}_T$ in the EC are corrected first by F_{cry}, to remove the η dependence of the response before measuring the absolute calibration (R_{jet} measured in the CC). Later, we will see that this approach is a good approximation. In reality, F_{cry} is a function of the jet detector pseudorapidity, since R_{jet} depends on the jet width, which is a measure of the number of towers embraced by the jet.

The most important consequence of the constant dependence of F_{cry} on energy is the possibility of using EC data to extend the range of the CC response measurement. This is possible because, on average, forward jets have higher energies than central jets with the same E_T. As a consequence, the energy range of the response measurement can be extended from $\sim$ 150 GeV to $\sim$ 300 GeV.

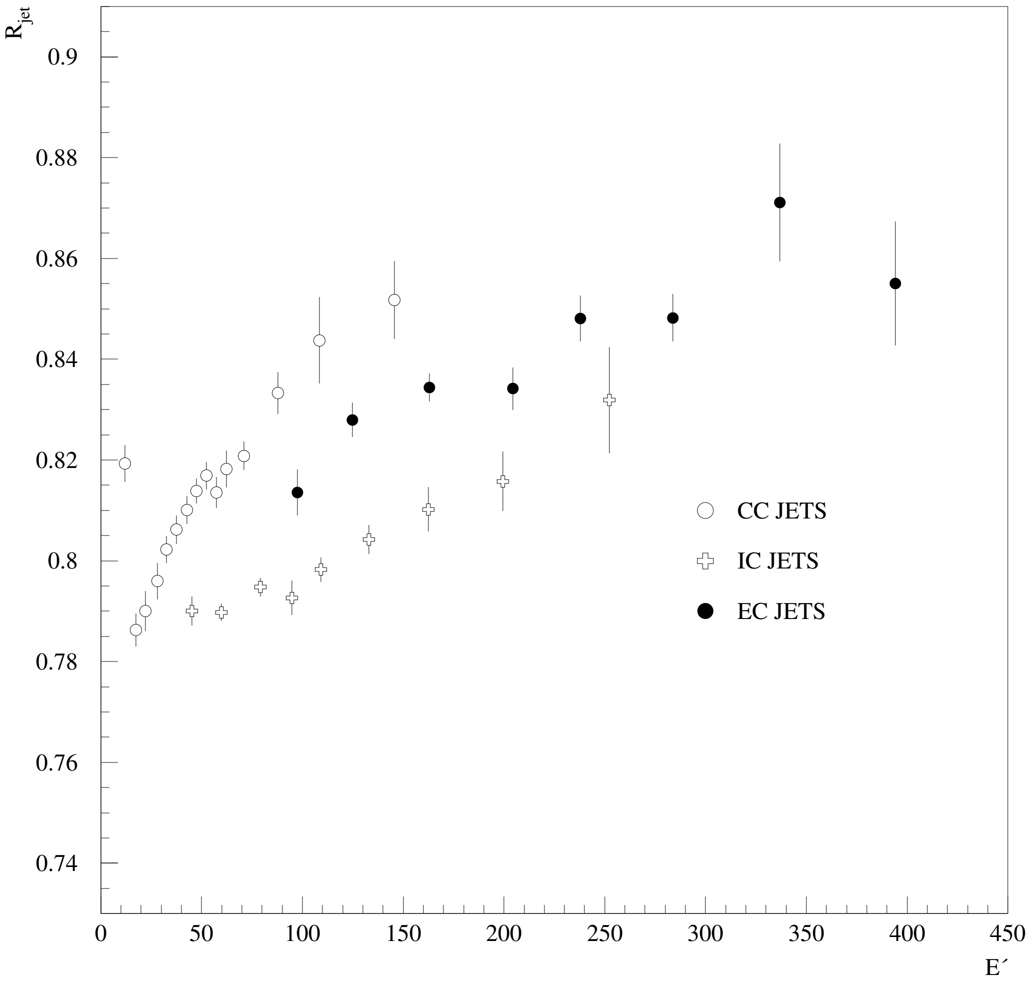

Figure 5.1: R_{jet} versus E' for a completely uncorrected sample (RECO V12). CC jets correspond to $|\eta_{jet}| < 0.7$, IC jets to $0.7 < |\eta_{jet}| < 1.8$ and EC jets to $1.8 < |\eta_{jet}| < 2.5$.

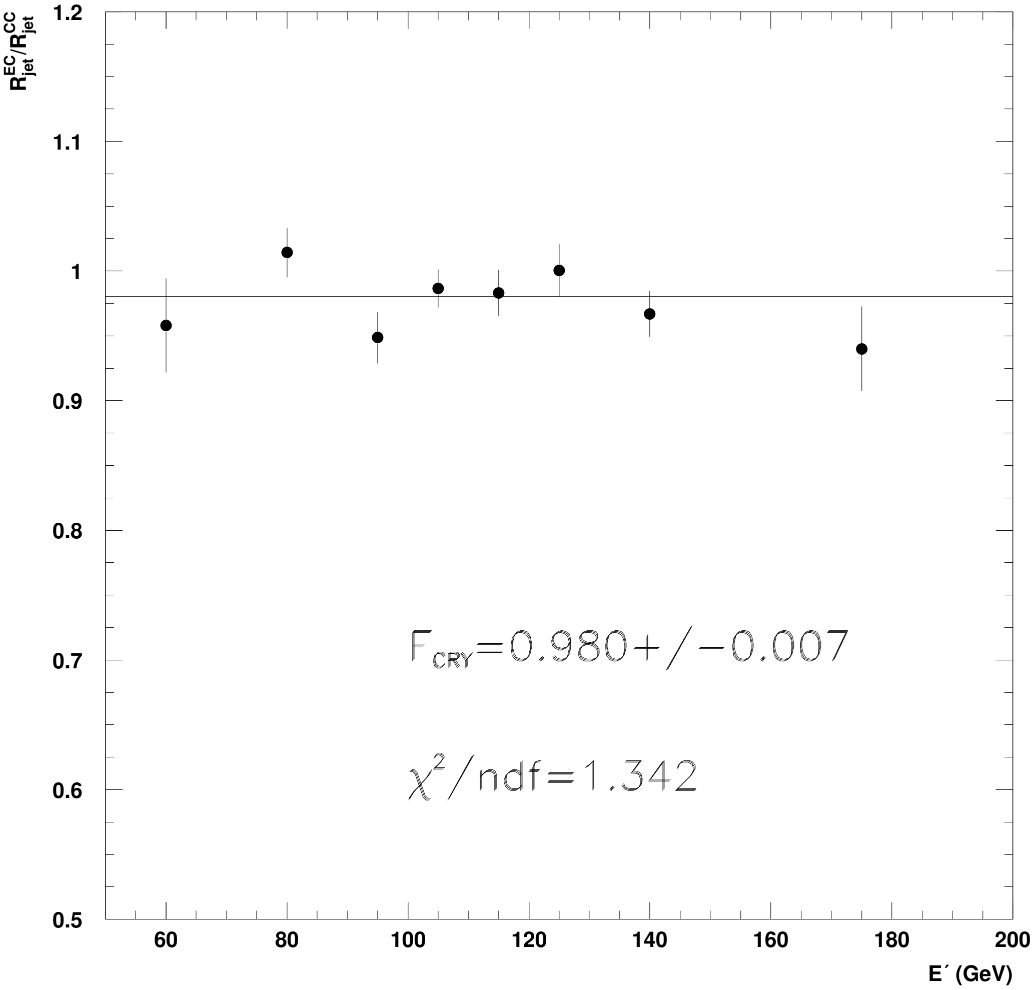

Figure 5.2: Cryostat factor as a function of E' measured on the Run Ia γ-jet data sample. The solid line is a straight line fit to the data.

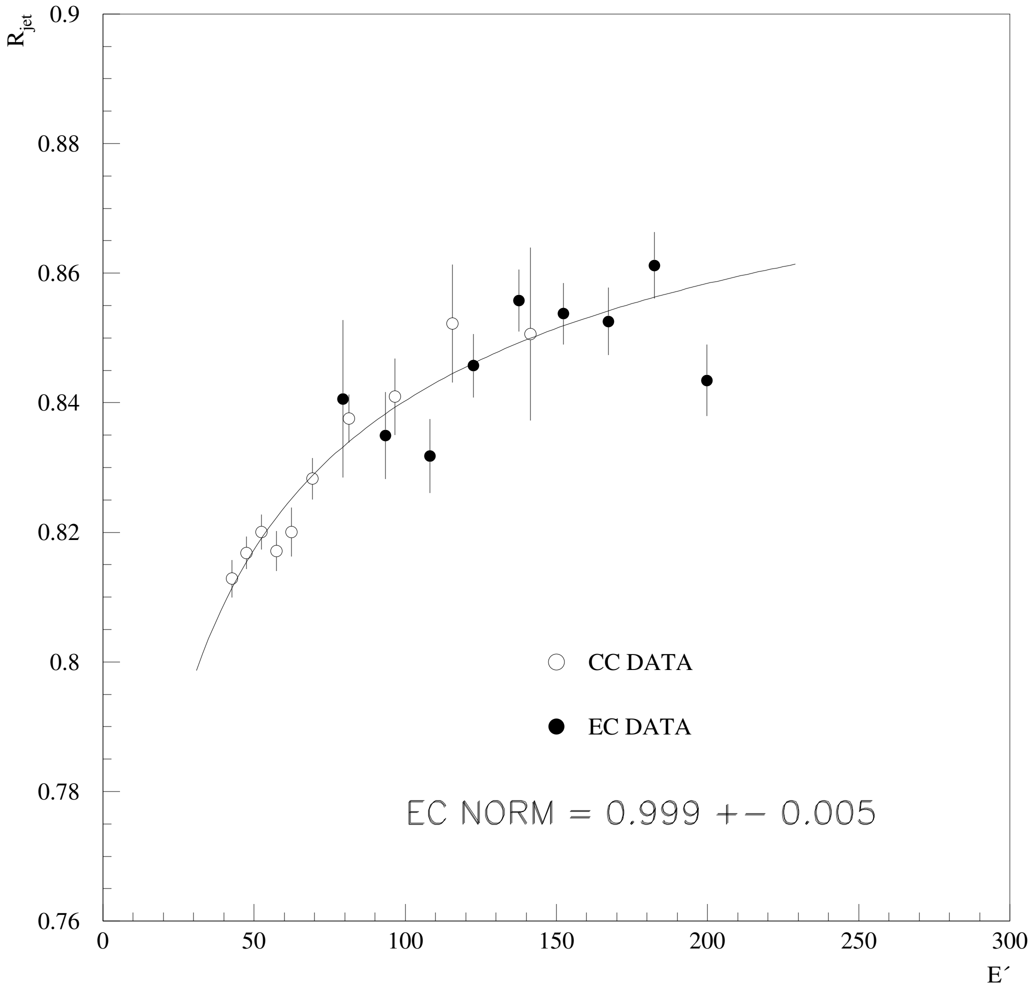

Figure 5.3: R_{jet} as a function of E' for the CC and the EC measured on the Run Ib γ-jet data sample. The R_{jet}^{EC} is measured after the F_{cry} correction on the event $\not{E}_T$. The solid line is a fit where the EC points are allowed to float, through a normalization parameter. The normalization factor that results from the fit is consistent with 1.0, proving that the approximation to correct the $\not{E}_T$ is excellent.

5.2.1 Width dependence of R_{jet} and F_{cry}

Jet width is arbitrarily defined as

$$W_{jet} = \sqrt{\left[\sum_i \frac{E_{Ti}}{E_T}(\eta_i - \eta_\circ)^2\right] + \left[\sum_i \frac{E_{Ti}}{E_T}(\varphi_i - \varphi_\circ)^2\right]},$$

where $(\eta_\circ, \varphi_\circ)$ are the coordinates of the jet centroid, (η_i, φ_i) is the position of calorimeter tower i, E_{Ti} is the total E_T in tower i, and the sum is over all the towers encompassed by the algorithm cone.

Energy response to narrow jets is better than response to wide jets of the same energy in the same calorimeter region. This is due to the fact that narrow jets are composed of fewer particles than wide jets of the same energy. The energy response to the many low energy particles in wide jets could be very poor. This simple picture gets more complex in the DØ calorimeters due to increasing segmentation towards the beam pipe. If we assume that central and forward jets of the same energy have the same width in real space, which is not true since forward jets are more boosted, the difference in their $\eta - \varphi$ width would increase as they move further apart in pseudorapidity. For a fixed cone size, the width would still increase with η, since the core of the jet will encompass more towers and those at the edge will have considerable weight. Figure 5.4 shows that the jet width increases linearly as a function of detector η_{jet} for the $\mathcal{R}$=0.7 cone algorithm. This trend is different for different cone sizes, since the smaller cone sizes embrace only the core of the jet.
The observed decrease in the EC response compared to the CC response for jets would be related to the fact that particles which belong to jets of the same E_T and width in real space traverse more cells in the forward regions than in the central region.

Figure 5.5 shows R_{jet} versus E' in the CC and EC for different width bins ($\mathcal{R}$=0.7). As expected, R_{jet} varies strongly with jet width. For jets of the same energy and width, the EC jet energy response is approximately 3% higher than the CC response. The EC provides a better intrinsic response than the CC because it contains a lower density of dead material. This result is consistent with the measured electromagnetic energy scale in both cryostats [2, 9, 10]. Photons and electrons are very narrow objects, even in the forward regions. They typically deposit most of their energy inside a $\mathcal{R}$ =0.3 cone. In summary, the cryostat factor is $\sim$ 1.03 for photons or electrons and $\sim$ 0.98 for jets. This is probably due to the larger $\eta - \varphi$ calorimeter segmentation in the forward calorimeters.

A corollary to the preceding discussion is an η dependent cryostat factor. In addition, low E' points in the response measurement would be associated with low η jets and high E' points with high η jets. Potentially, this could produce a bias in the energy dependence of the measured response, both in the CC and the EC. Figure 5.6 shows the average jet η_{jet} as a function of E' for the CC ($|\eta| < 0.7$) and the EC ($1.8 < |\eta| < 2.5$). The average η changes from 0.34 to 0.41 in the CC and from 2.09 to 2.28 in the EC. Figure 5.4 provides a mapping between η change and width change. The bias is completely negligible in the CC and on the order of 0.2% in the EC. Since only the very high E' points are biased by as much as 0.2%, the bias in the CC response measurement using both CC and normalized EC data is much less than 0.2%. This effect is negligible compared with other uncertainties. The fixed cryostat factor approximation is probably not good for jets above $|\eta|$ =2.5. The effect of the bias is accounted by the uncertainty on the η dependent corrections.

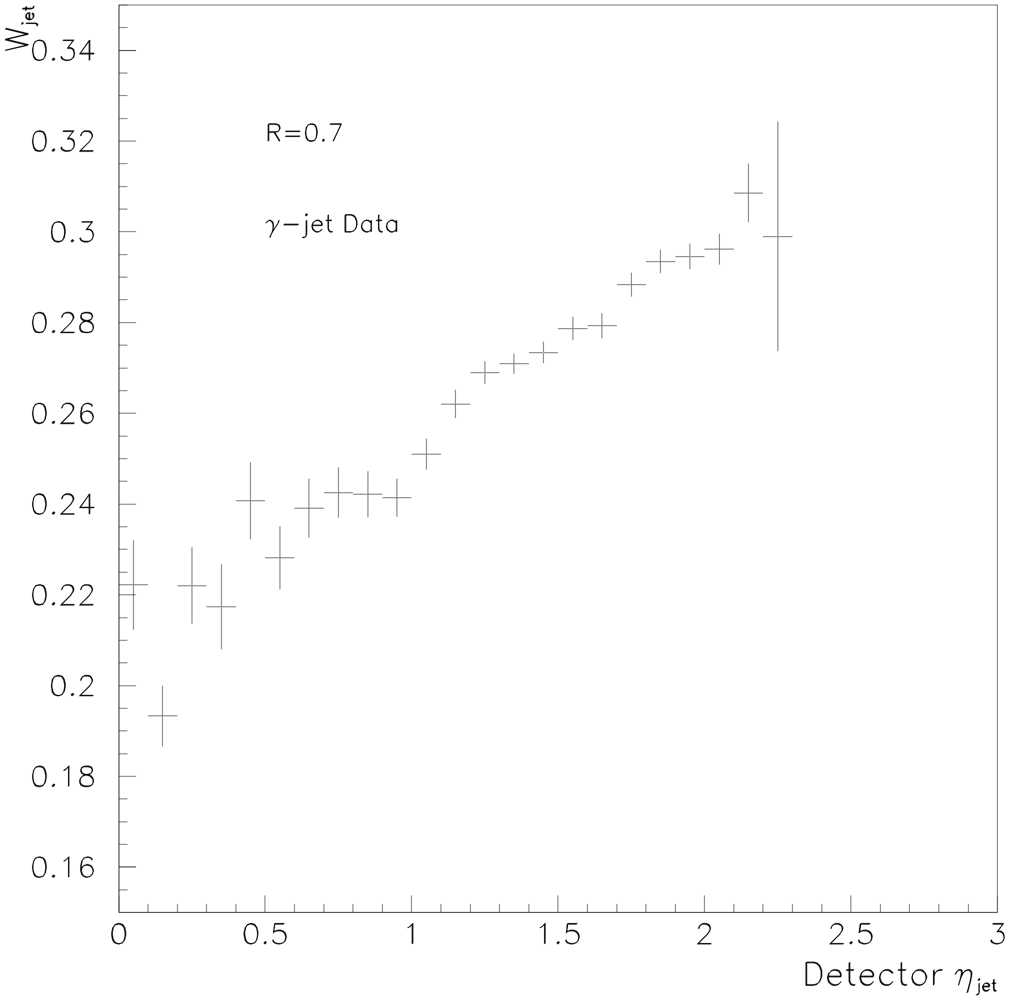

Figure 5.4: Jet width as a function of detector jet pseudorapidity for $\mathcal{R}$=0.7 cone jets.

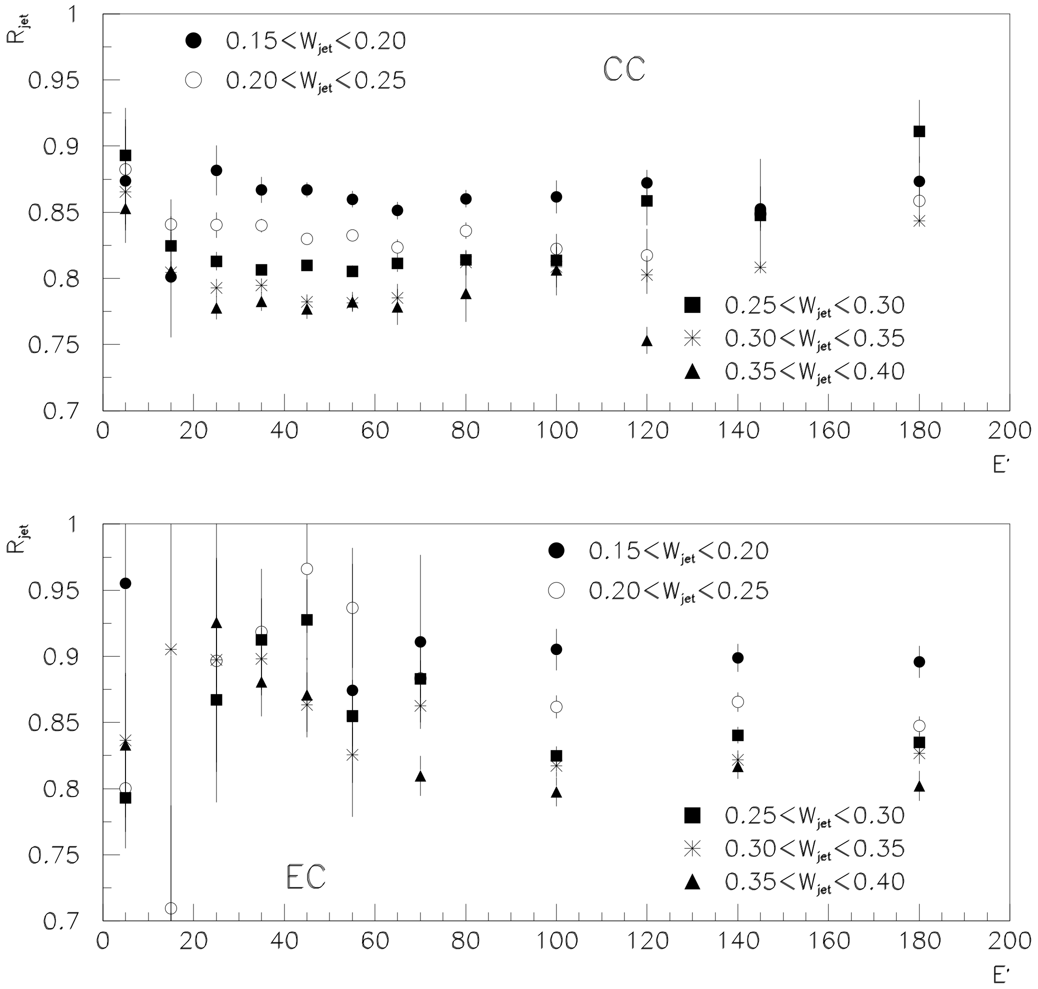

Figure 5.5: R_{jet} versus E' in the CC and EC for different width bins ($\mathcal{R}$=0.7). For jets of the same energy and width, the EC jet energy response is approximately 3% higher than the CC response. This is consistent with the measurement of the electromagnetic energy scale in both cryostats. The low jet energy response in the EC is due to width effects.

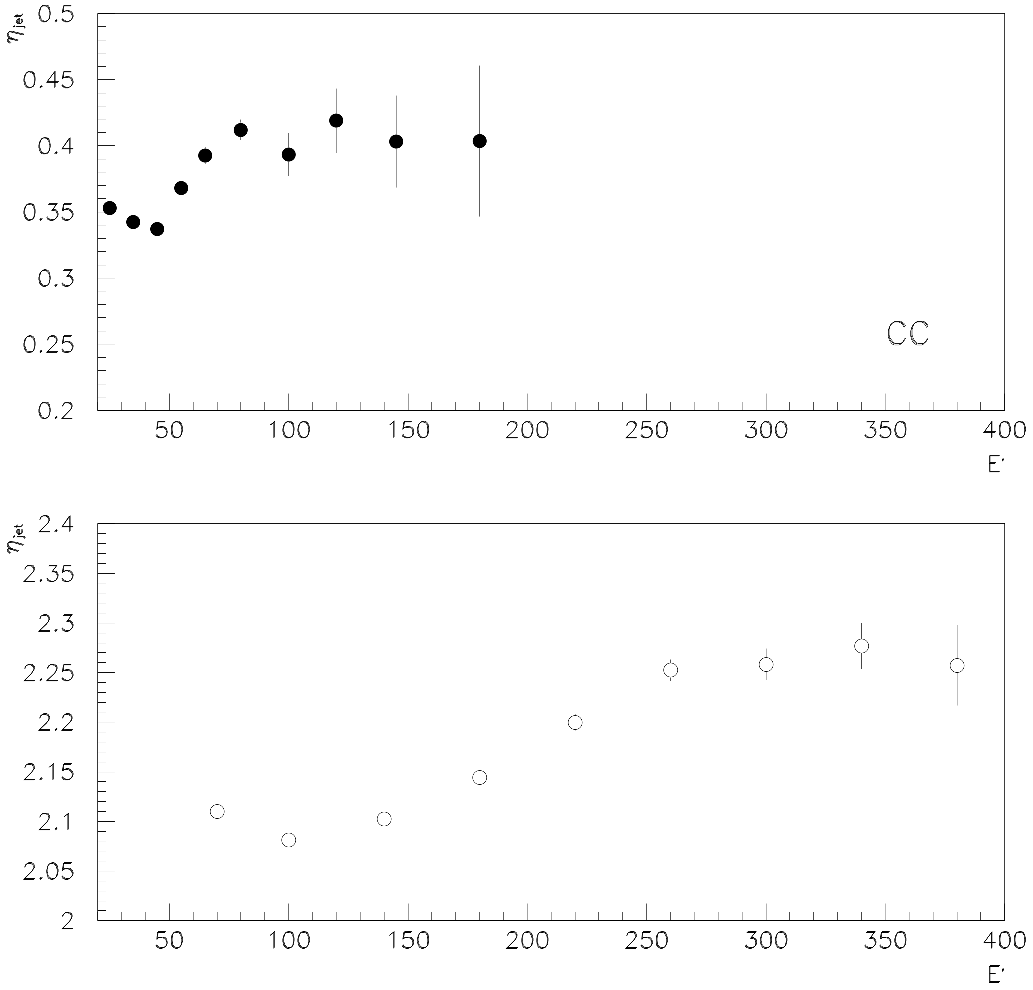

Figure 5.6: Average η_{jet} versus E' in the CC and the EC. The change in average pseudorapidity and in average jet width is small.

5.3 ICR Corrections

The intercryostat region, which covers the pseudorapidity range $0.8 < |\eta| < 1.6$, is the most poorly instrumented region of the calorimeter system. A substantial amount of energy is lost in the cryostat walls, module endplates and support structures. In the $1.2 < |\eta| < 1.4$ range, the system lacks electromagnetic calorimetry and the total depth falls slightly below 6 interaction lengths. As it was mentioned in Chapter 1, two types of detection systems were added to improve the calorimetric sampling. The intercryostat detectors (ICD) are an array of scintillator tiles located on the EC cryostat wall. The massless gaps (MG) are separate single-cell structures installed in the CC and EC calorimeters between the module endplates and the cryostat walls. Both systems are shown in Figure 5.7. The cryostat factor puts two very similar detectors, the CC and the EC, on the same footing. The ICR is a non-uniform region covered by different types of detectors. Therefore, it is reasonable to observe a residual η dependence of the response in that region, even after the cryostat factor is applied to EC jets.

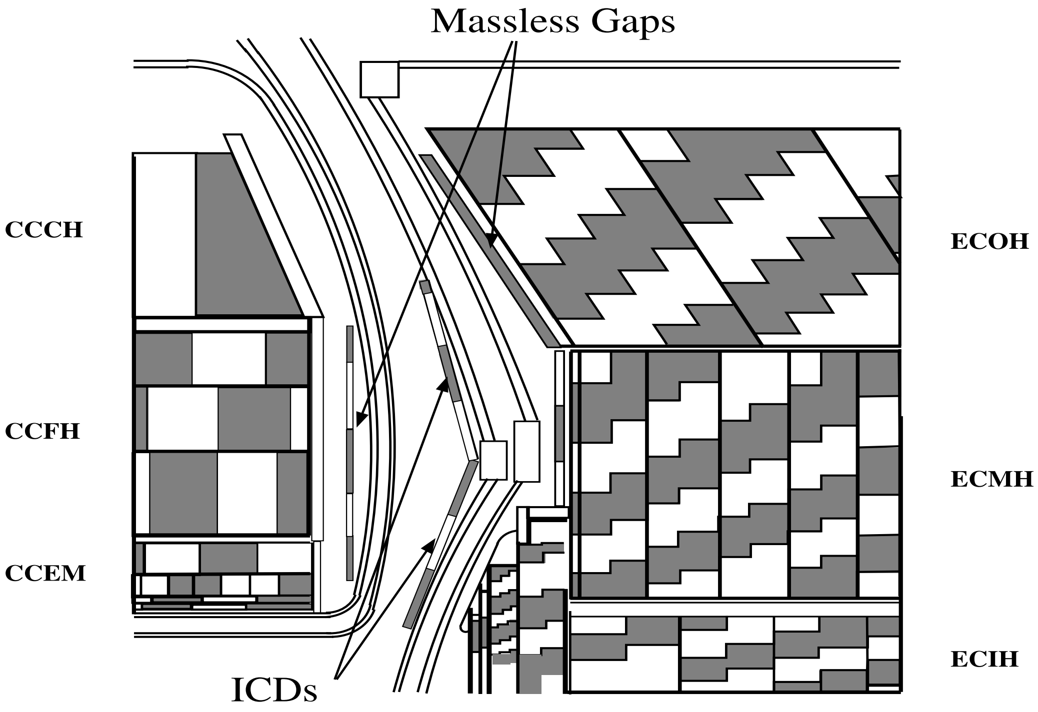

Figure 5.7: Side view of calorimeter modules, intercryostat detectors and massless gaps.

The η dependence of the response must be removed in order to have a uniform detector. This correction is performed before the energy dependent response correction. Since the energy dependence of R_{jet} is folded into R_{jet} versus η, this function should not be a constant even for a completely uniform calorimeter. However, R_{jet} as a function of η should be smooth for a uniform calorimeter. Therefore, having calibrated the EC with respect to the CC, the ICR or η dependent correction is obtained by means of a smooth interpolation through the ICR of the measured R_{jet} versus η in the CC and the EC.

1

5.3.1 Event Selection

The η dependence is measured from both γ-jet and jet-jet events. For the γ-jet sample, the photon is kept central, $|\eta| < 0.5$, and there is no restriction on the jet η. For the jet-jet sample, one of the two leading E_T jets must be central ($|\eta| < 0.5$), and there is no restriction on the η of the probe jet. Since the dependence of R_{jet} on pseudorapidity is related to detector inhomogenities, $R_{jet}(\eta)$ is measured using detector pseudorapidity. From the jet-jet sample, R_{jet} is defined as:

$$1 + \frac{\vec{\not{E}}_T \cdot \hat{n}_{\text{central jet}}}{E_{T\,\text{central jet}}}.$$

It is measured as a function of the probe jet detector η.

The γ-jet events are used to measure the η dependence only at low jet E_T, since the sample is statistically limited at high E_T. The correction for high E_T jets is determined from the jet-jet data. The jet-jet sample has two features that affect the measurement of the response: a resolution bias and the effects of the offset correction. These are not present in the γ-jet sample.

The cuts applied to determine the η dependence from the γ-jet sample are the same as those discussed in Chapter 3, with the additional requirement $E_{T\gamma} > 25$ GeV.

For the jet-jet sample the cuts are identical to those used to determine the response as a function of energy:

- Event passed a jet trigger (described in Table 5.2) and the trigger is fully efficient.
- At least one jet with $|\eta| < 0.5$.
- One and only one vertex found, with $|z| < 50$ cm.
- Two and only two reconstructed jets.
- Jets pass the quality cuts defined in Chapter 4.

Many cross checks were performed on the cuts used in the jet-jet sample. For example, the requirement on the z coordinate of the interaction vertex was removed, events in which there was a third jet with E_T less than 15 GeV were allowed, the single vertex requirement was removed. A cut on the instantaneous luminosity, $\mathcal{L} < 5\times10^{30}\text{cm}^{-1}\text{sec}^{-1}$ ($\mathcal{L} < 5$ for simplicity of notation), and the condition MITOOL=1 or 2 were also applied. None of these changes affected the ICR calibration results.

5.3.2 Resolution Bias

For two identical E_T jets, one central and one far forward, it is more likely to have the central η jet than the forward jet fluctuate to a higher measured E_T jet. This is because, for the same E_T, forward jets have higher energies and a better the resolution than forward jets. In addition, forward jets are kinematically suppressed. This causes a bias in determining the response for jets with η greater than approximately 2.

This resolution bias can be removed by means of a "mass" cut on the jets. A cut demanding that the product of $E_{T1} \cdot E_{T2}$ be greater than some threshold removes events in which one jet fluctuated very high. However, this "mass" cut causes a bias in the measurement of the response at lower η because, due to the falling cross section, it demands that both jets have nearly the same E_T. Therefore, the mass cut is only applied to determine the expected η dependence.

Complications due to the offset correction restrict the use of the jet-jet data for this study to high E_T. Therefore, γ-jet events were used at low E_T.

Data Sample	a	b
γ-jet E_T >25	0.817	0.027
γ-jet E_T >55	0.832	0.019
γ-jet E_T >80	0.832	0.019
JET_30	1.004	0.034
JET_50	1.0	0.026
JET_85	1.0	0.012
JET_MAX	1.006	0.010

Table 5.2: Fit parameters of $a + b \cdot \ln[\cosh(\eta)]$ to R_{jet} versus η. In the case of the jet-jet sample, triggers require one jet with E_T above 30, 50 and 85 GeV respectively. JET_MAX requires one jet above E_T =115 GeV.

5.3.3 Results

In order to determine the expected η dependence in the ICR, the response versus η was fit to the function $R_{jet} = a + b \cdot \ln[\cosh(\eta)]$ in the CC and the EC, since both detectors are already calibrated relative to each other. This functional form is derived from the energy dependence of the response, which is well described by:

$$R_{jet} = \alpha + \beta \cdot \ln(E) .$$

Therefore:

$$R_{jet} = \alpha + \beta \cdot \ln[E_T \cdot \cosh(\eta)] \Rightarrow$$

$$R_{jet} = \alpha + \beta \cdot \ln(E_T) + \beta \cdot \ln[\cosh(\eta)] .$$

Reordering terms, and for a fixed E_T bin:

$$R_{jet} = a + b \cdot \ln[\cosh(\eta)] .$$

For the γ-jet events, the functions were fit to the data in the range $|\eta|$ <0.5 and 2< $|\eta|$ <2.3. For the jet-jet events, the curves were fit to the data with the "mass" cut in the ranges $|\eta|$ <0.5 and 2< $|\eta|$ <2.5. Table 5.2 shows the values of a and b obtained from the different fits. We refer to these fits as the expected η dependence. By "expected" we mean the η dependence of R_{jet} in the case of a completely uniform calorimeter.

The two η regions, η >0 and η <0 were treated separately. Figures 5.8 and 5.9 show the measured η dependence with no "mass" cut for jet-jet data, along with the fit to the expected response. Figure 5.10 shows the measured η dependence for γ-jet data along with the fit to the expected response.

The correction is plotted in bins of 0.1 in detector η. The difference between the fit to the expected response and the measured value is used to obtain a correction factor F_η. Figure 5.11 shows F_η as a function of the average central jet E_T ($\mathcal{R} = 0.7$) for several η bins. Also shown is a linear fit to the data, which is used to determine the correction factor as a function of jet E_T.

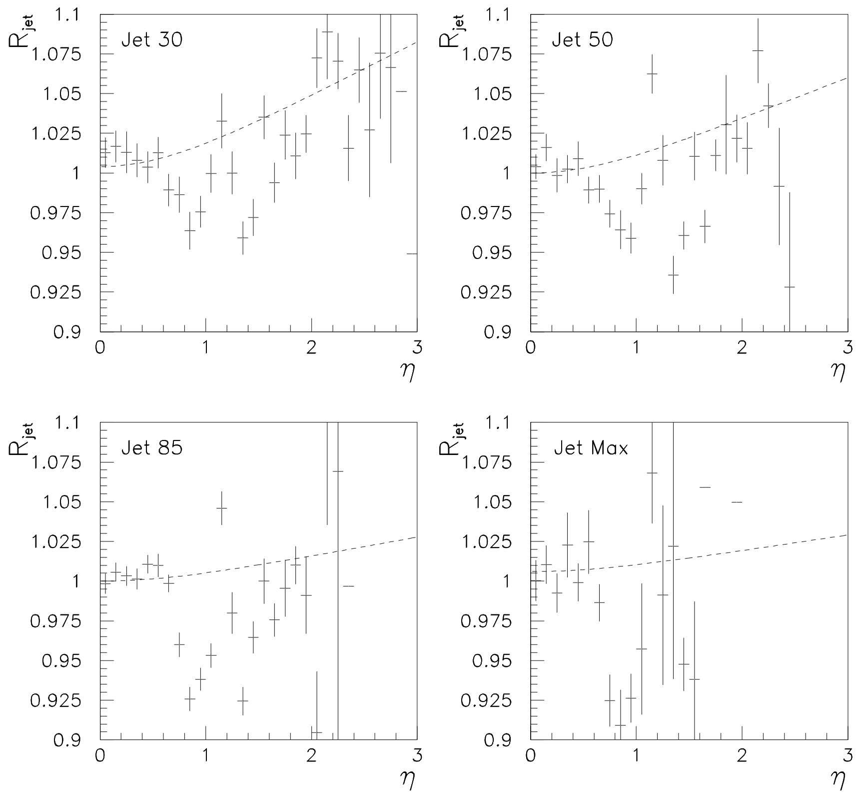

Figure 5.8: Response versus η for jet-jet data ($\eta > 0$). The dashed line is the fit to the expected η dependence.

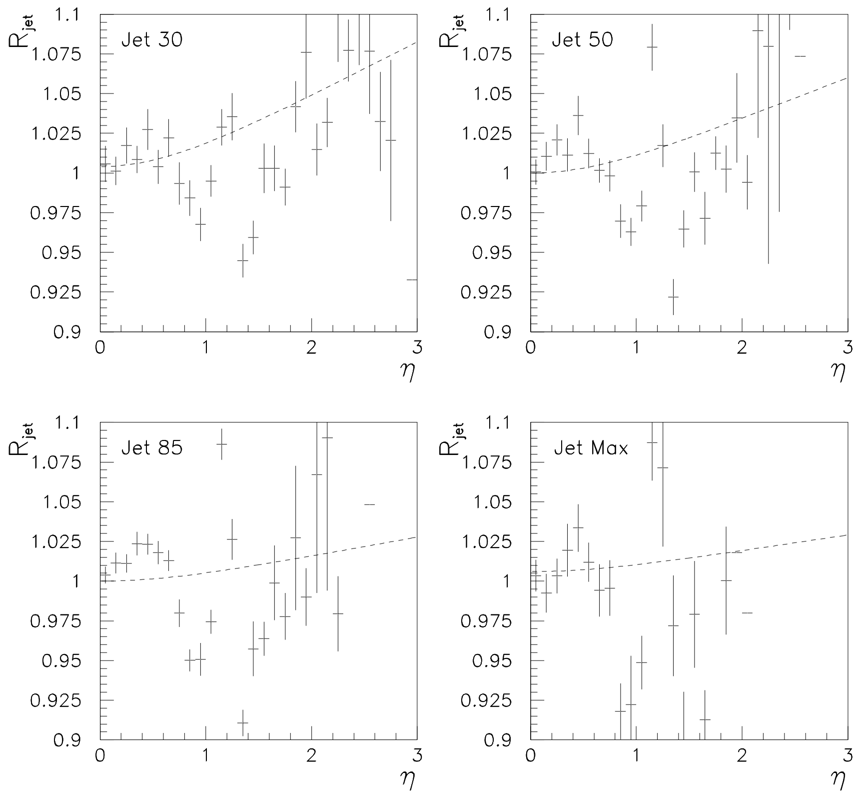

Figure 5.9: Response versus η for jet-jet data ($\eta < 0$). The dashed line is the fit to the expected η dependence.

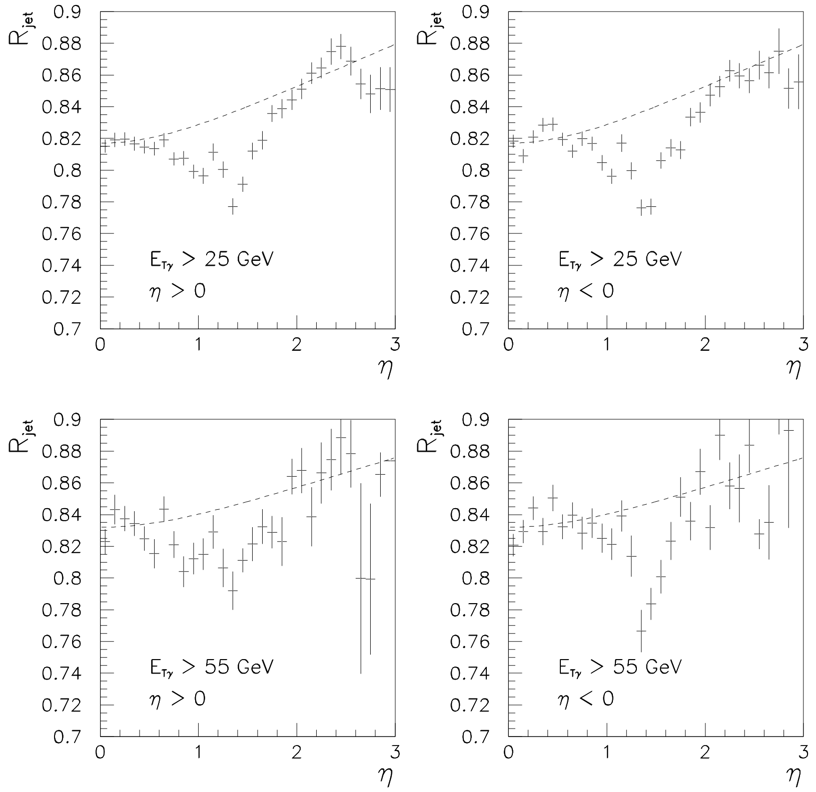

Figure 5.10: Response versus η for γ-jet data. The dashed line is the fit to the expected η dependence.

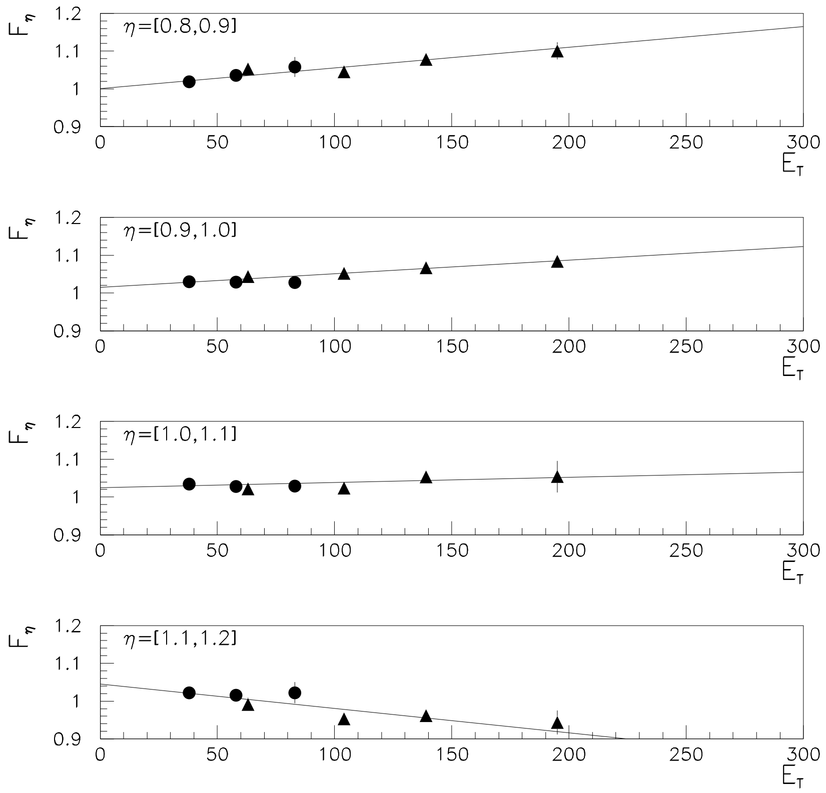

Figure 5.11: Correction factor F_η as a function of central jet E_T for positive η between 0.8 and 1.2. The circles are the γ-jet data and the triangles are the jet-jet data. The line is a fit through all of the data points.

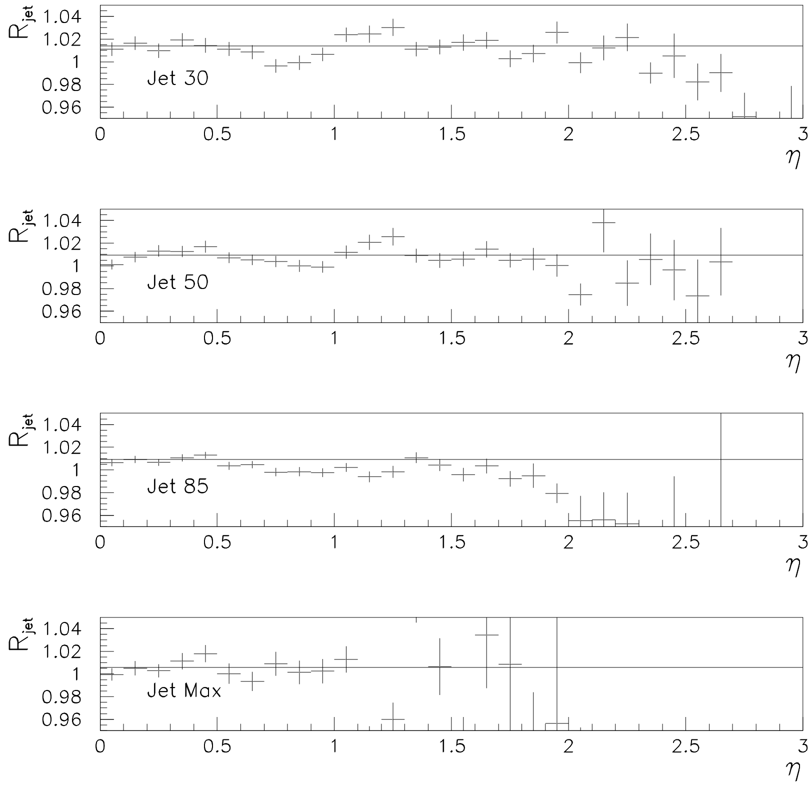

Figure 5.12: Response as a function of η for the four jet triggers after all corrections have been applied (averaged over positive and negative η. The line is the expected η dependence. The effects of the resolution bias are evident in the JET_85 distribution for $\eta > 2.0$.

5.3.4 Errors and Verification Studies

It is possible to measure the accuracy of the correction, using the fact that the response versus η should be constant after all corrections are applied. This is shown in Figure 5.12, where the corrections applied to R_{jet} are the offset, the cryostat factor, the η dependence, and the energy dependence. The η dependence is only applied to jets with $0.5 < |\eta| < 2$. It extends beyond the ICR towards the CC and the EC because a jet with a centroid near the edges of the calorimeters deposits a fraction of its energy in the ICR. Figure 5.13 also shows the response versus η after all corrections are applied. The lower limit of the plot is reduced in order to see more clearly the effects of the resolution bias.

The error on the measurement was determined from the residuals of the corrected γ-jet and jet-jet data with respect to the expected η dependence. Figure 5.14 shows the difference between the corrected data and the expected η dependence for the four jet triggers within four separate η regions.

Figure 5.14 and Table 5.3 display the means and RMS values for the residual distributions derived from jet-jet data.

The error for $|\eta| > 2$ was derived from γ-jet data, since these events are not affected

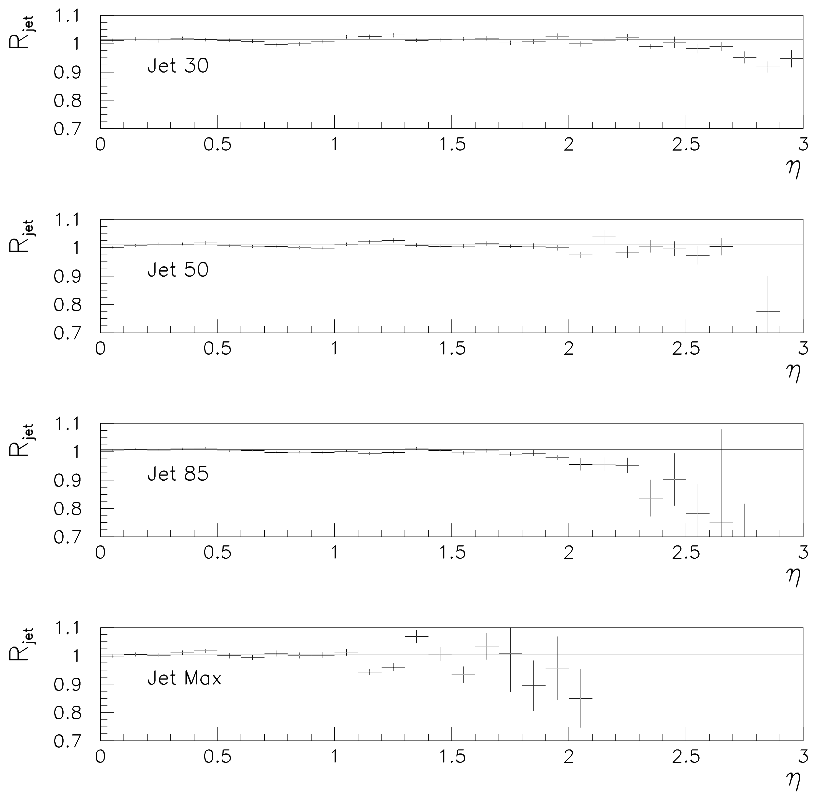

Figure 5.13: Same plot as in the previous page except that the lower limit of the response axis has been lowered. One can clearly see the response falling at high η due to the resolution bias.

η Region	Mean	RMS
$\|\eta\| < 0.5$	0.0	0.005
$0.5 < \|\eta\| < 1.0$	0.007	0.005
$1.0 < \|\eta\| < 1.5$	0.001	0.024
$1.5 < \|\eta\| < 2.0$	0.010	0.022

Table 5.3: Means and RMS values for the residual η dependence derived from jet-jet data.

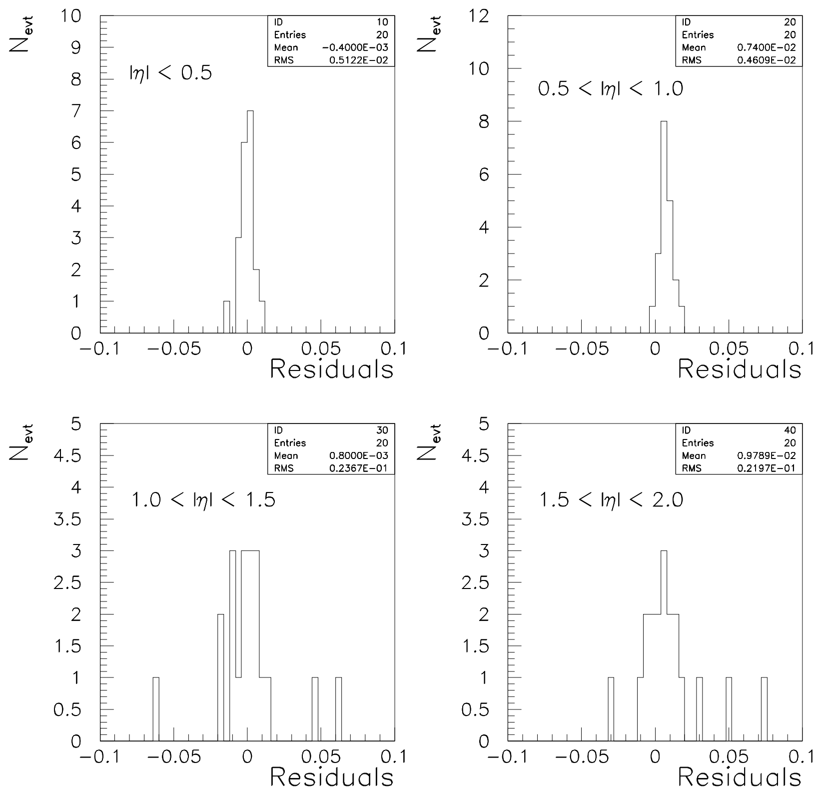

Figure 5.14: Residuals for the four jet triggers in 4 separate η regions. The large residuals at high η all come from the JET_MAX trigger, which has poor statistics.

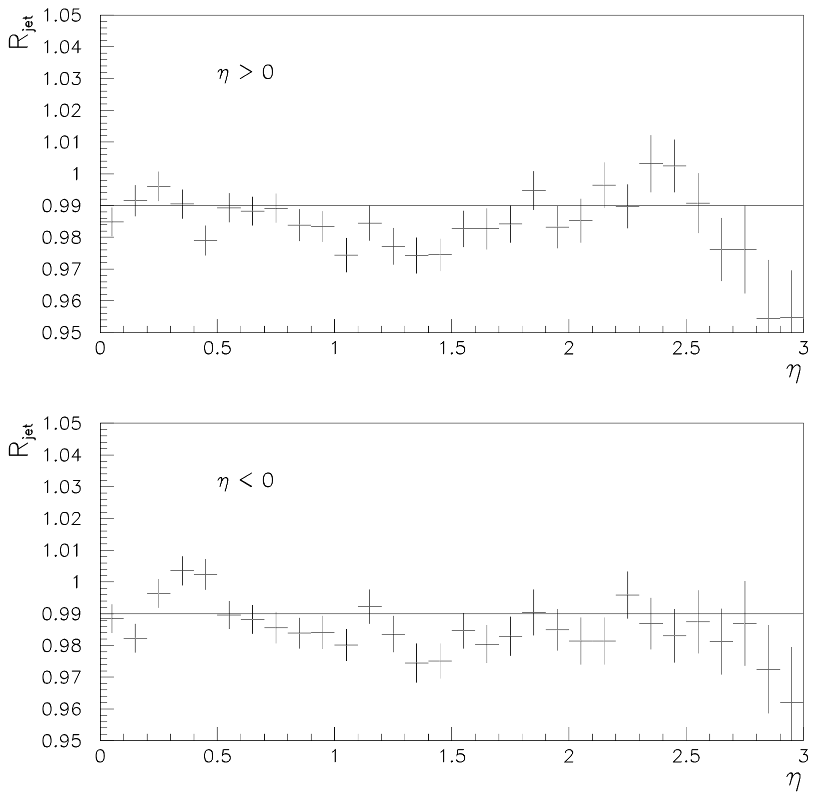

Figure 5.15: Response versus η for γ-jet events after all corrections have been applied.

by the resolution bias like the jet-jet data. Figure 5.15 shows the response versus η after all corrections have been applied to the γ-jet data. The horizontal line is the expected η dependence of R_{jet} after all corrections have been applied. After all corrections, the response is slightly less than unity. The reason is that the energy scale is applied only to reconstructed jets. The energy not associated with jets is not corrected for the calorimeter response. Therefore, since the correction to the $\not{E}_T$ is based on found objects, the measured response is less than one after all corrections. There is some evidence of a residual η dependence beyond $|\eta|$ =2.5. This bias towards a higher response may be due to the breakdown of the cryostat factor approximation at very high pseudorapidity. I could also be due to a fraction of the jet energy lost down the beam pipe. In order to account for this effect, we introduce an additional η dependent error that turns on at $|\eta|$ =2.5 and increases linearly up to a 3% at $|\eta|$ =3.

The residuals from the expected η dependence for γ-jet events are shown in Figure 5.16. Table 5.4 shows the means and RMS values for the residual distributions for γ-jet data. The residuals derived from both data samples, γ-jet and jet-jet, are in good agreement.

Since the η dependence changes dramatically with η, the effects of the binning were examined using finer bins of 0.05 in η. Figure 5.17 shows the η dependence after all corrections have been applied with the standard binning of 0.1 in η and with finer bins of 0.05 in η. A small effect can be observed in the region $1.1 < |\eta| < 1.3$.

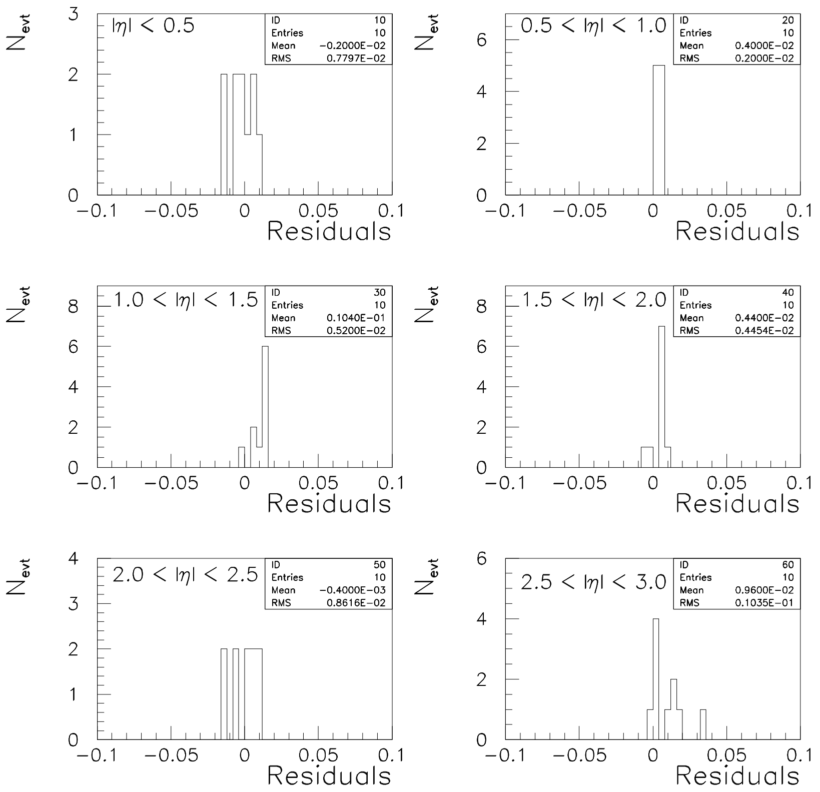

Figure 5.16: Residuals for γ-jet events.

η Region	Mean	RMS
$\|\eta\| < 0.5$	0.0	.008
$0.5 < \|\eta\| < 1.0$	0.004	0.002
$1.0 < \|\eta\| < 1.5$	0.010	0.005
$1.5 < \|\eta\| < 2.0$	0.004	0.004
$2.0 < \|\eta\| < 2.5$	0.0	0.009
$2.5 < \|\eta\| < 3.0$	0.010	0.010

Table 5.4: Means and RMS values for the residual η dependence derived from γ-jet data.

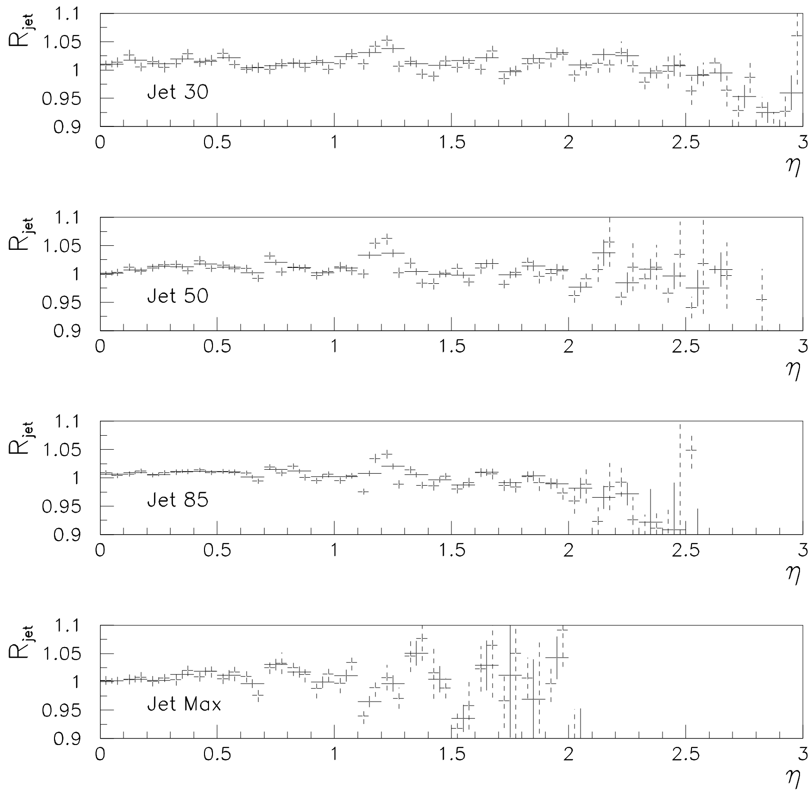

Figure 5.17: Change on the η dependence due to bin size reduction. The solid symbols are the standard 0.1 bins in η. The dashed symbols show the η dependence if the bins are reduced to 0.05 in η.

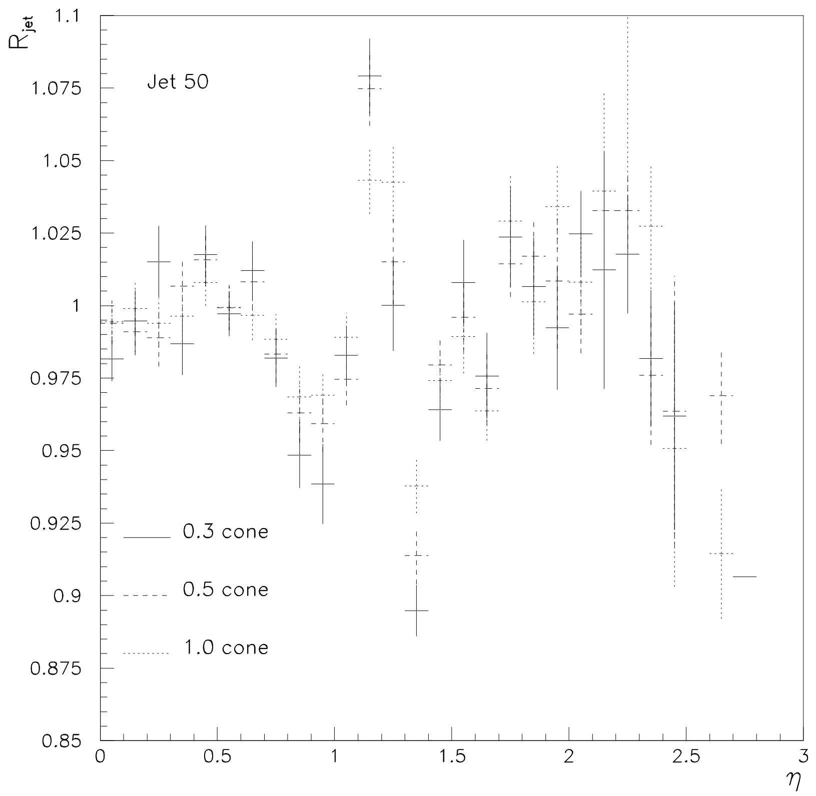

Figure 5.18: Cone size dependence of the η dependence in data. As the cone size increases, the effects of the η dependence decrease.

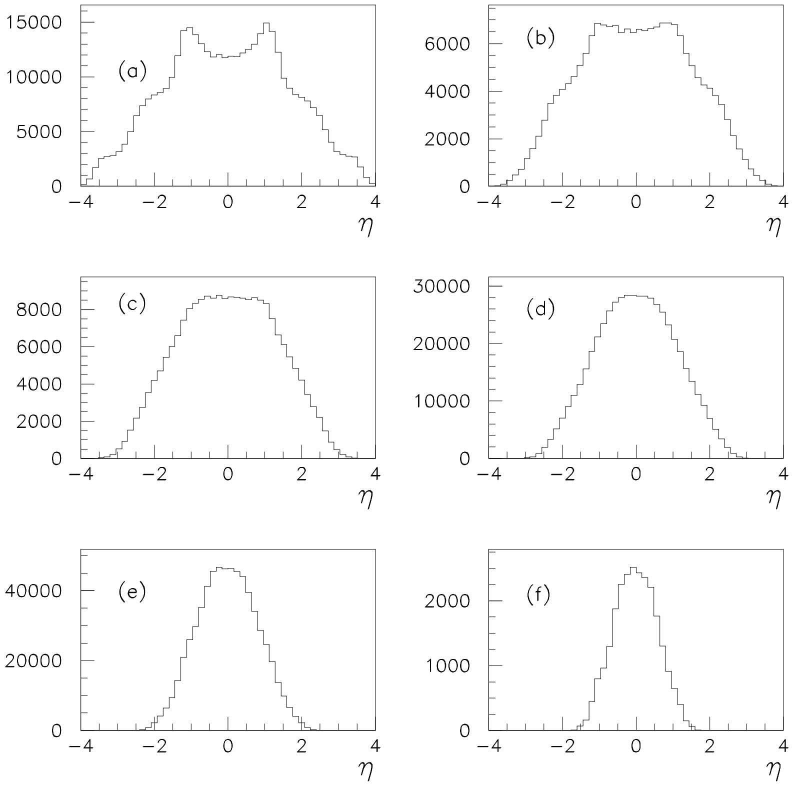

Figure 5.19: η distribution of jets ($\mathcal{R} = 0.7$) in different E_T bins before any jet energy scale corrections are applied.(a): E_T =10-20 GeV, (b): E_T =20-30 GeV, (c): E_T =30-50 GeV, (d): E_T =50-100 GeV, (e): E_T =100-200 GeV, (f): E_T =200-400 GeV.

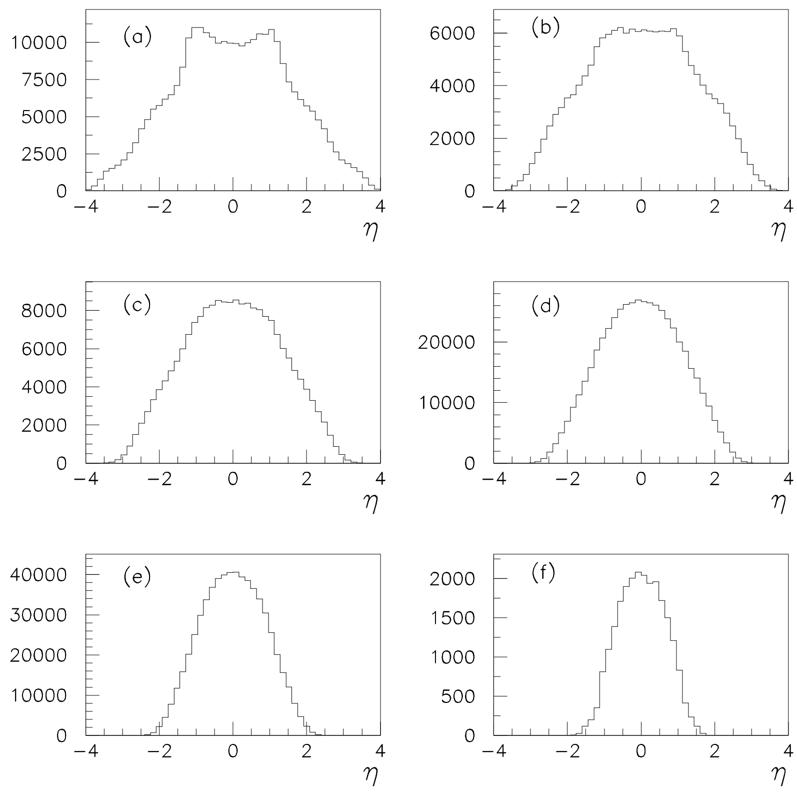

Figure 5.20: η distribution of jets ($\mathcal{R}$ = 0.7) in different E_T bins after the full jet energy scale correction is applied. (a): E_T =10-20 GeV, (b): E_T =20-30 GeV, (c): E_T =30-50 GeV, (d): E_T =50-100 GeV, (e): E_T =100-200 GeV, (f): E_T =200-400 GeV.

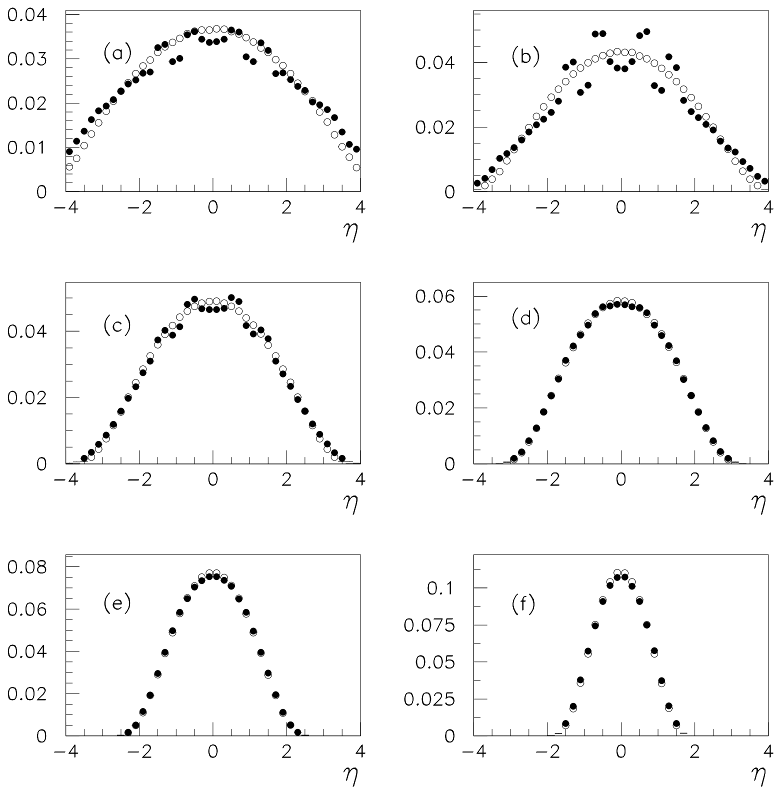

Figure 5.21: Normalized η distribution for jets using LO JETRAD. The open circles show the distribution of jets with no smearing. The solid circles show the distribution of jets after E_T and η smearing. (a): E_T =10-20 GeV (b): E_T =20-30 GeV (c): E_T =30-50 GeV (d): E_T =50-100 GeV (e): E_T =100-200 GeV (f): E_T =200-400 GeV.

Figures 5.19 and 5.20 show the η distribution for jets in different E_T bins before and after CAFIX is applied. In the two lower E_T bins, E_T <30 GeV, the distributions are not smooth. This may be due to the poorer resolution in the ICR causing jets to fluctuate to a higher E_T more often. This, coupled with the poor efficiency for reconstructing low E_T jets, will cause more jets to be reconstructed in the ICR. To check this assumption, the η distribution of jets using the leading order (LO) prediction provided by the program JETRAD [11] was generated. Figure 5.21 shows the normalized η distribution of jets before and after E_T and η smearing in the same E_T regions as in Figure 5.20. There is qualitative agreement between Figure 5.20 and the solid circles in Figure 5.21. Since the resolutions are poorly measured for jets below 20 GeV, it is unlikely to obtain quantitative agreement. The minimum E_T for jets in JETRAD before smearing is 5 GeV.

It was also observed that the η dependent correction increases for decreasing cone sizes. If there is a jet pointing to a low response region of the calorimeter, the object reconstructed with a small cone would have a lower response than the object reconstructed with a larger cone. This is because the fraction of the jet energy deposited in high response cells would be larger in the second case. Figure 5.18 shows the η dependence in jet-jet events for three different cone sizes.

A separate η correction was determined for each cone size and plotted as a function of 0.7 cone jet E_T. For each cone size, a map from that cone size E_T to the 0.7 cone E_T is used to determine the value of the correction.

The correction is then applied to the jet energy and the event $\vec{\not{E}}_T$. This η dependent calibration makes the calorimeters uniform, and the later response correction becomes a constant function of pseudorapidity.

Chapter 6

Response: Energy dependence

In this chapter, we describe the measurement of the hadronic response of the DØ calorimeters to jets. We follow the general method employed in the previous version of the jet energy scale correction [8, 16, 5]. The changes with respect to the old analysis are described in Appendix A. The response is determined directly from the DØ collider data by exploiting energy conservation in events containing a jet and a photon candidate. Photon candidate events are selected as described in Chapter 4 and the response of the hadronic recoil in the event is determined relative to the energy corrected photon cluster. At least one 0.7 cone jet is required in each event. The hadronic response is given by:

$$R_{jet}(E') = 1 + \frac{\vec{\not{E}}_T \cdot \hat{n}_{T\gamma}}{E_{T\gamma}},$$

a quantity that is independent of the reconstruction algorithm. E' is later mapped to the average reconstructed jet energies for different algorithms to derive the response as a function of jet energy.

6.1 Data Selection

The response at low to moderate E' ($E' \lesssim 100$ GeV) is determined from low E_T photons and CC jets ($|\eta| < 0.7$). At high values of E' ($E' \gtrsim 100$ GeV), EC ($1.8 < |\eta| < 2.5$) jets are used. The forward measurement is normalized to the central measurement by the value obtained for the cryostat factor[1] (see chapter 5).

In addition to the cuts described in Chapter 4, $E_{T\gamma}$ has to be greater than 6 GeV for CC jet events and greater than 25 GeV for EC jet events. The latter cut removes residual effects of the reconstruction low E_T bias, which affects jets of higher energy in the EC than in the CC. Before presenting the response determination, we will discuss this bias in detail.

6.2 The Low E_T Bias

The combination of reconstruction effects (efficiencies and E_T cutoffs) and a finite jet energy resolution produces a bias in the measured response. This bias depends on E_T, rather than energy, and occurs only near the reconstruction E_T threshold.

[1]The Run IB (RECO V12) data is consistent with a 0.5% smaller EC/CC ratio than the Run IA (RECO V10,11) data. The appropriate value was used in the determination of the response for each data sample.

At $E_T = E_T^{min}$, fixed at 8 GeV for all jet cone algorithms at DØ, the jet fractional E_T resolution is approximately 50%. Therefore, the net migration of low E_T jets to higher values is very large. Due to the reconstruction threshold, the jet E_T distribution is truncated at low E_T. This truncation may bias the average jet E_T to higher values, the $\not\!\!E_T$ to lower values and therefore the response to higher values. The jet reconstruction efficiency is not a step function that turns on sharply at E_T^{min}, but rather a small step (at threshold) followed by a slow turn on curve, that only reaches 100% at $E_T \sim 20$ GeV. This is due to the inefficiencies of the algorithm for turning seed towers into clusters and jets, even if the energy deposited in the calorimeter is greater than 8 GeV. As a consequence, the resolution bias becomes enhanced and is present until ~ 20 GeV.

The bias is η dependent, since the E_T resolution and reconstruction efficiency are η dependent. If parametrized as a function of E_{Tjet}, the bias also depends on the cone size. The curves presented here are the corrections to unbias the hadronic response and jets only if the same E_T^{min} =8 GeV threshold is applied to all jets in the sample. If the reconstruction threshold is changed or applied to a subset of any jet sample, (like the first leading or first two leading jets in each event), the size of the bias will be different. For example, consider a sample of medium E_T photon plus jet events where the photon E_T is well above the bias region for jets. In this sample, the jet E_T distributions will contain a small amount of low E_T jets. E_T conservation demands that most of the low E_T jets are high E_T jets that fluctuated low and not low E_T jets that fluctuated high. Therefore, in this particular sample, the low E_T jets are not biased. Unbiasing very low E_T jets in events with high E_T objects, where the $\not\!\!E_T$ measurement is critical, can cause a large error in the unbiasing correction which would degrade the $\not\!\!E_T$ resolution.

In all the cases described above, it is the user's responsibility to determine the unbiasing correction that will put the jets in their sample on the correct footing to use the hadronic response provided by CAFIX, which is unbiased. The package provides several choices that allow a user to turn the correction on or off, or apply it selectively to a given number of jets.

The low E_T bias was measured from the γ-jet data sample used in the response measurement. It was also studied using the parametric Monte Carlo simulation described in Chapter 3. The measurement agrees with the result from the simulation within the large errors of the latter. The data derived correction is used to unbias E_{jet}^{meas} and R_{jet}. The simulation is a very useful tool to study the systematics associated with the bias.

6.2.1 Data Measurement

The bias in the data is measured from the same sample of photon events described in Chapter 4. Since the jet energy response is determined from the event $\vec{\not\!\!E}_T$, $E_{T\gamma}$ and $\hat{n}_\gamma$, we can measure it without requiring any reconstructed jet in the event. This is simply the response to the hadronic recoil of the photon, with no reference to a jet algorithm.

In order to measure the bias, the response is plotted as a function of $E_{T\gamma}$ for those events having at least one jet reconstructed with a given algorithm. The ratio:

$$R_{bias} = \frac{R_{Jet(\geq\ 1\ jet)}}{R_{Jet(no\ jet\ required)}}$$

is the low E_T bias. R_{bias} is measured as a function of $E_{T\gamma}$, which is then mapped into the uncorrected E_{Tjet}^{meas} (using the sample in the numerator). The low E_T bias correction has to be applied first, since it depends on uncorrected quantities. The correction is the inverse of R_{bias}. Figure 6.1 includes plots of the bias as a function of $E_{T\gamma}$, the relation between $E_{T\gamma}$ and E_{Tjet}, and the bias versus E_{Tjet} for 0.7 cone jets. The data is fit to the function: $P1 + e^{(P2+P3\cdot E_T)}$. The bias is negligible above 20 GeV and is on the order of 5% at 12 GeV. There is a limitation to this method, which is given by the fact that jets are required to be central, $|\eta| < 0.7$ (numerator in R_{bias}), while the soft recoil (denominator in R_{bias}) has no η restriction. The two parts of the ratio are not equivalent as response measurements, because the numerator is determined only by jets in the CC and the denominator has no such η restriction. This is reflected in the observed deviation of R_{bias} from unity for $E_{T\gamma} > 20$ GeV. The value of R_{bias} is renormalized to one in this region before performing the conversion to E_{Tjet}.

Figure 6.2 shows the measured R_{bias} for different cone sizes, i.e. 0.3, 0.5 and 0.7. Also shown are the fits, which are in good agreement with each other.

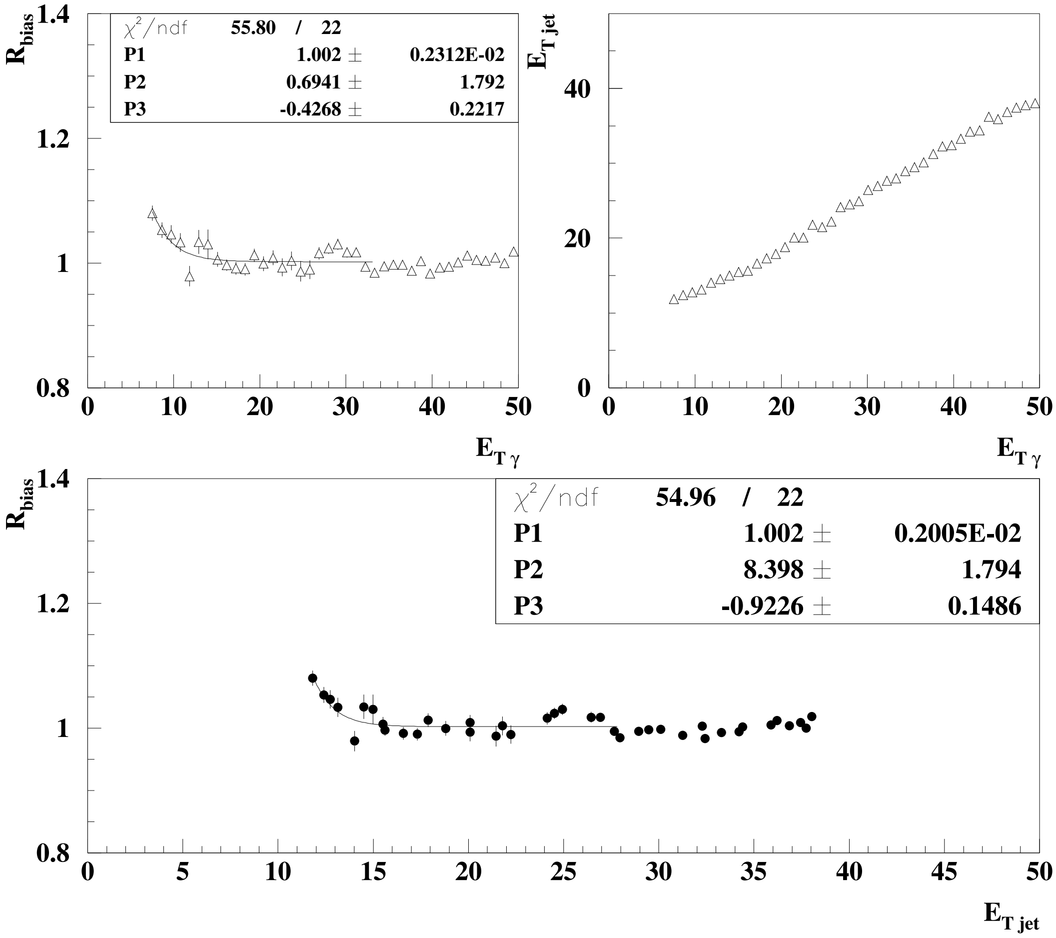

Figure 6.1: Low E_T bias measured from data: bias as a function of $E_{T\gamma}$ for 0.7 cone jets (top left), E_{Tjet} versus $E_{T\gamma}$ (top right), bias as a function of E_{Tjet} (bottom). The lines are fits to the function $P1 + e^{(P2+P3\cdot E_T)}$.

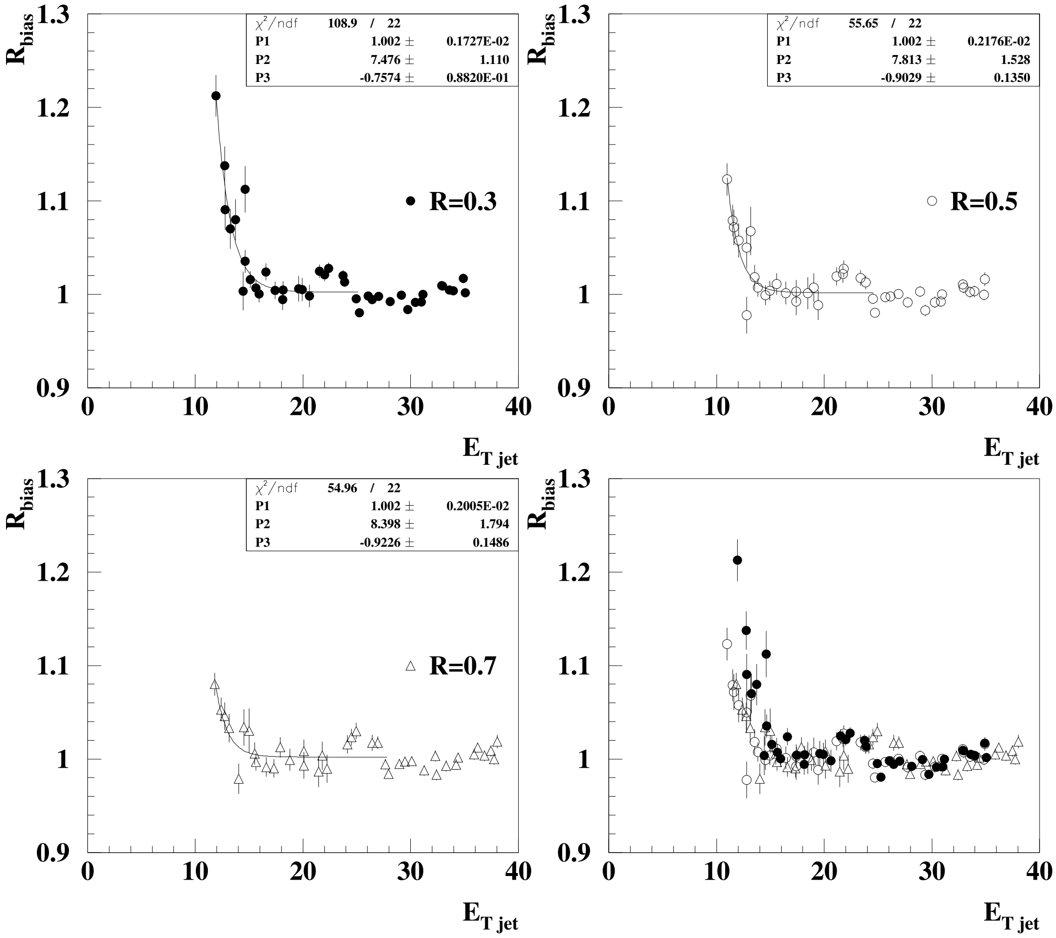

Figure 6.2: Low E_T bias from data as a function of $E_{T\,jet}$ for 0.3, 0.5, and 0.7 jet cone sizes. The results of a fit to $P1 + e^{(P2+P3\cdot E_T)}$ are indicated and the three curves compared in the last plot.

6.2.2 Parametric Monte Carlo Simulation

A description of the simulation follows:

- Parton level Leading Order γ-jet events are generated using a $1/E_T^n$ function for the direct photon cross section. The jet is back to back with the photon and is assigned the same E_T. The jet θ is generated with uniform probability in the desired interval.
- Both the photon and the jet E_T's are smeared with the measured resolutions [6].
- The jets are scaled with the measured energy response.
- The offset is added. No additional E_T smearing is introduced since the measured E_T resolutions already include the contribution of the offset.
- The effect of reconstruction efficiency is not modelled (E_{ff}^{reco} =1), since the available measurement is probably inaccurate at low E_T [17]. Our best measurement of the reconstruction efficiency provides an estimate of the associated uncertainty. A reconstruction threshold ($E_T > E_T^{min}$) cut is imposed. The new photon and jet E_T's simulate calorimeter quantities.
- $\not{E}_T$ is obtained by calculating the vector sum in the transverse plane of the photon and jet E_T's at the calorimeter level.

At this point, the hadronic response is "measured" using the MPF method. The low E_T bias is determined from the ratio of the response from a sample where the E_T^{min} cut is modeled, and the response from a sample with a very low reconstruction threshold. The uncertainty in the simulated bias is determined by adding in quadrature the effects of the variation of the simulation parameters within errors.

The simulation is performed using the offset, response and resolution parameters associated with 0.7 cone jets in the $|\eta| < 0.7$ interval. The reconstruction threshold is set at 8 GeV. The reconstruction efficiency is parametrized as:

$$E_{ff}^{reco} = A \cdot \tanh\left[B \cdot (E_{T\ jet} + C)\right] , \tag{6.1}$$

with A =0.997, B =0.257, and C =-2.89. The fractional E_T resolutions are introduced in Chapter 3 [6]. Since resolutions are measured only for $E_T \gtrsim$30 GeV, the parametrization of σ_{E_T}/E_T versus E_T is valid only in that range. For this study, we extrapolated the nominal resolution and errors down to 8 GeV. R_{jet} is parametrized with the function:

$$R_{jet} = A + B \cdot \ln(E_{jet}) + C \cdot \left[\ln(E_{jet})\right]^2 , \tag{6.2}$$

with A, B, and C being the numbers measured in the section on hadronic response below. The offset is set at 2.4 GeV (consistent with a low luminosity sample) and varied within errors to study changes of the bias with luminosity.

Figure 6.3 show the bias as a function of $E_{T\gamma}$ and E_{Tjet} (binned in terms of $E_{T\gamma}$). E_{Tjet} is uncorrected, since the bias is a function of reconstructed transverse energy. The error band in Figures 6.3c-d are the errors contributed by the uncertainties in the jet energy resolution and response. Figure 6.4a shows the effect of modelling the reconstruction efficiency in the simulation. The total error band, obtained by adding all individual errors in quadrature, is shown in Figure 6.4b. The function used to fit the simulated data is:

$$R_{bias} = 1 + e^{(P1 + P2 \cdot E_{Tjet})} ,$$

with $P1 = 7.00$, $P2 = -0.76$. The bias is primarily determined by the jet energy resolution, E_T^{min}, and the reconstruction efficiency. The offset and the E_T dependence of the photon cross section contribute very little to the total uncertainty. Figure 6.4c is a comparison between the simulated bias and the data measurement. They agree within the errors of the simulation, which are very large. The accuracy of the simulation would improve with better measurements and error estimates of the reconstruction efficiency and jet energy resolution at very low E_T's.

The CAFIX5.1 R_{bias} correction is obtained from parametrizations to the data measurement for each cone size, and the uncertainty is determined using the simulation. The quoted errors account for the η dependence of the bias.

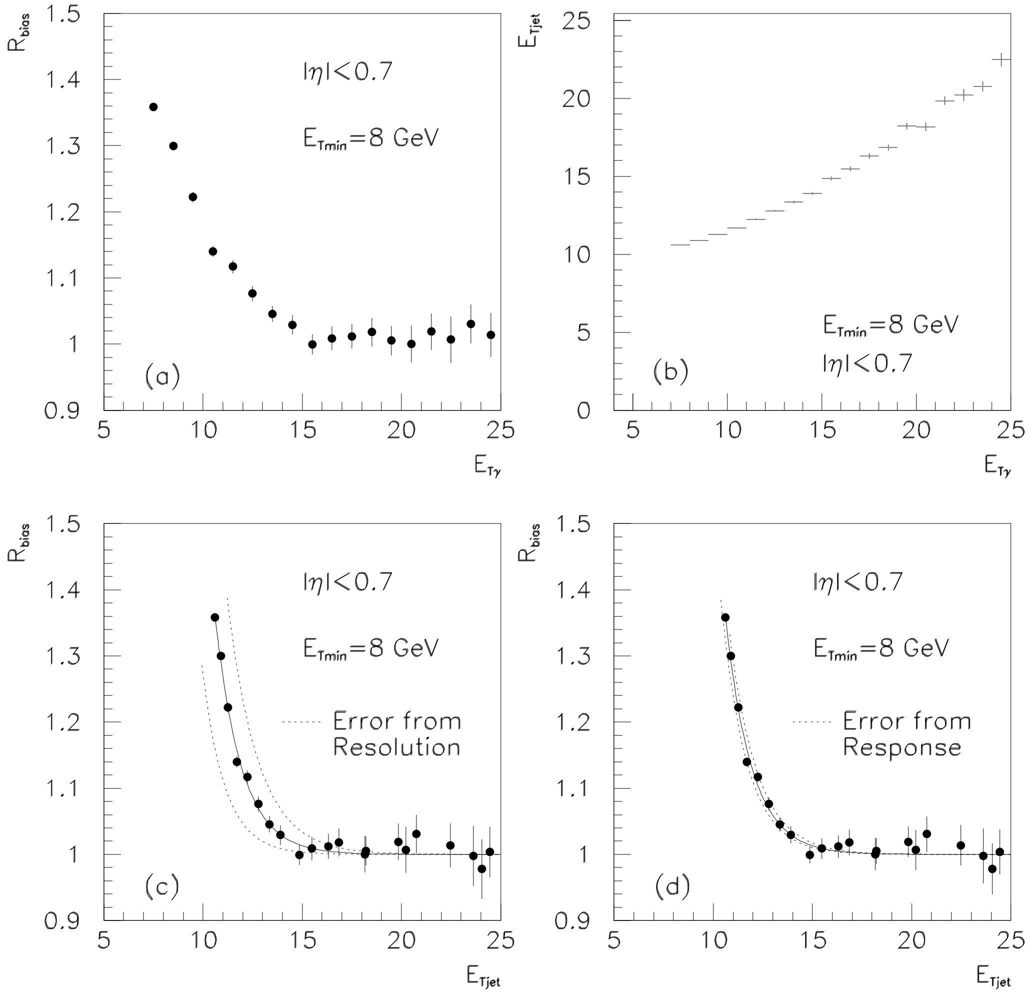

Figure 6.3: (a): R_{bias} as a function of $E_{T\gamma}$. (b) E_{Tjet} versus $E_{T\gamma}$. (c) and (d): R_{bias} versus E_{Tjet} (binned in terms of $E_{T\gamma}$). The bands in (c) and (d) are the errors contributed by the uncertainties in the jet energy resolution and response.

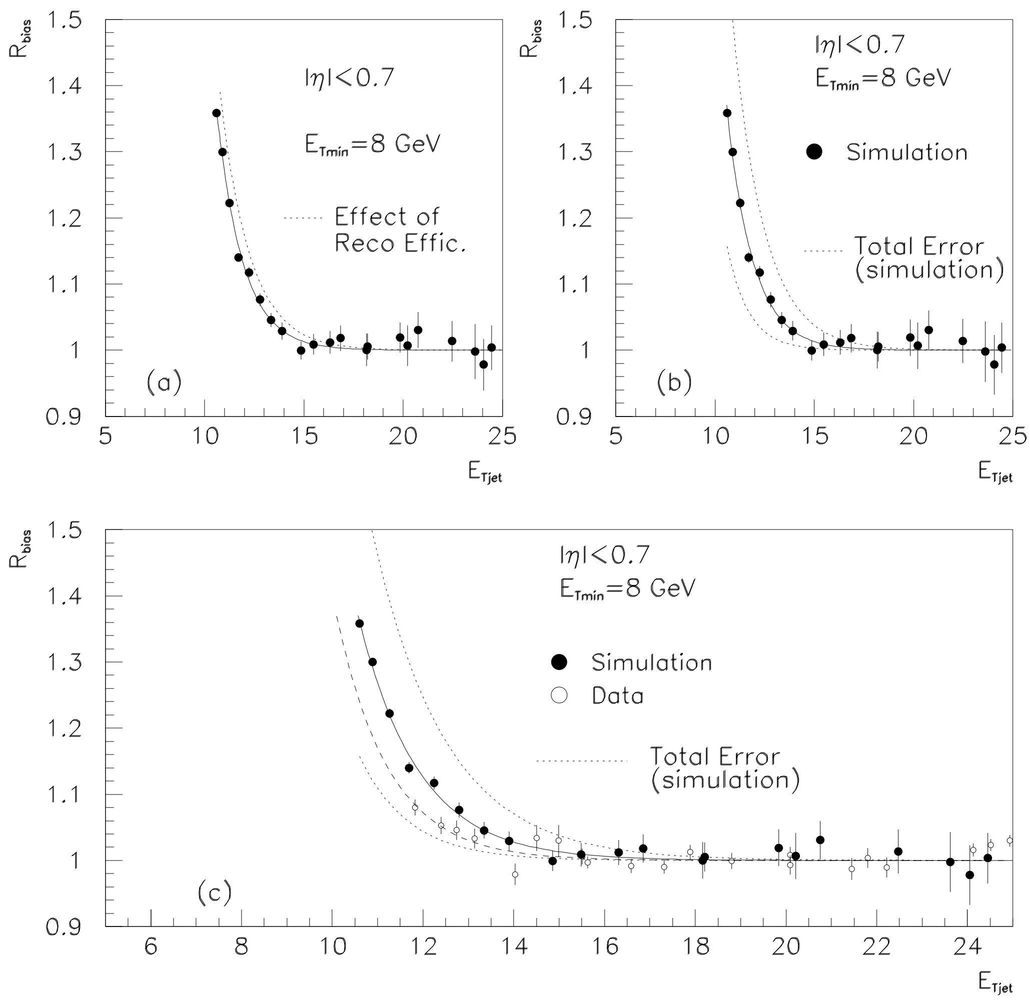

Figure 6.4: (a): R_{bias} as a function of E_{Tjet} (binned in terms of $E_{T\gamma}$). The dotted line shows the change in R_{bias} when the reconstruction efficiency is modelled in the simulation. (b): Same as (a) but the band is the total systematic uncertainty. (c): Same as (b). The measured R_{bias} is also shown.

6.3 Corrections Applied Before Response Derivation

The following corrections are applied to the data before the hadronic response is derived:

- Photon energy scale.
- The low E_T bias correction was applied to the leading 0.7 cone jet in the event. (Note: Only 0.7 cone jets are used in correcting the $\not\!\!E_T$). The correction affects events if the E_T of the leading jet is below approximately 20 GeV. It applies a correction to the $\not\!\!E_T$ which in general lowers the measured response and also adds an additional error to the energy associated with the low E_T jet.
- Jet offset correction: The total offset, including the physics underlying event was subtracted from the jet energy .
- Reconstruction and other η dependent corrections: Corrections for relative sampling fraction changes were applied to data reconstructed with RECO version 11. The appropriate cryostat factor (see Chapter 5) was applied to normalize the response in the EC to the CC, and any jets in the ICR were corrected with the η dependent correction. On average, these corrections improve the measured response by lowering the $\not\!\!E_T$ for events with jets outside the CC.

6.4 Response versus E'

Before applying any corrections to the jets, the hadronic response versus E' shows large dependencies in different pseudorapidity regions as shown in Figure 5.1 (Chapter 5). The response is observed to depend strongly on the calorimeter region. Figure 6.5 shows R_{jet} versus E' after the above jet corrections are applied. The data were reconstructed with RECO V12. The points are plotted at the average value of E' within each bin. The average response in each E' bin is determined by fitting the response distribution corresponding to that E' range with either a single or double gaussian parameterization. A single gaussian is sufficient for E' bin with less than 100 entries. The fits provide a response measurement which is less luminosity dependent that the arithmetic means of the distributions, since they are less sensitive to an occasional outlying point far from the peak of the response distributions. Such outlying points increase in frequency as luminosity increases due to mis-vertexing effects as discussed in Chapter 4.

The η dependence is dramatically reduced in Figure 6.5; however, the ICR is still observed to be about 1% low compared to the CC and EC regions. Due to this observation, only the CC and EC data will be used to derive the hadronic response. Additionally, the topological requirement on the leading jet being back-to-back with the photon effectively limits the amount of radiation that may fall in the ICR. Figure 6.6 shows the effect of applying the η dependent correction to the measured response for CC and EC jets. The average change in the response for CC and EC jets with application of the η dependent correction is less than 0.3%. Since the error on the η dependent correction is small compared to the magnitude of the correction, we may ignore any additional error in the hadronic response due to uncertainties on the η dependence.

After determining the response versus E', a mapping between E' and the average jet energy is obtained separately for each jet algorithm. The mapping for 0.7 cone jets is shown in Figure 6.7. The observed difference in the energy to E' mapping between EC and CC jets is consistent with showering effects.

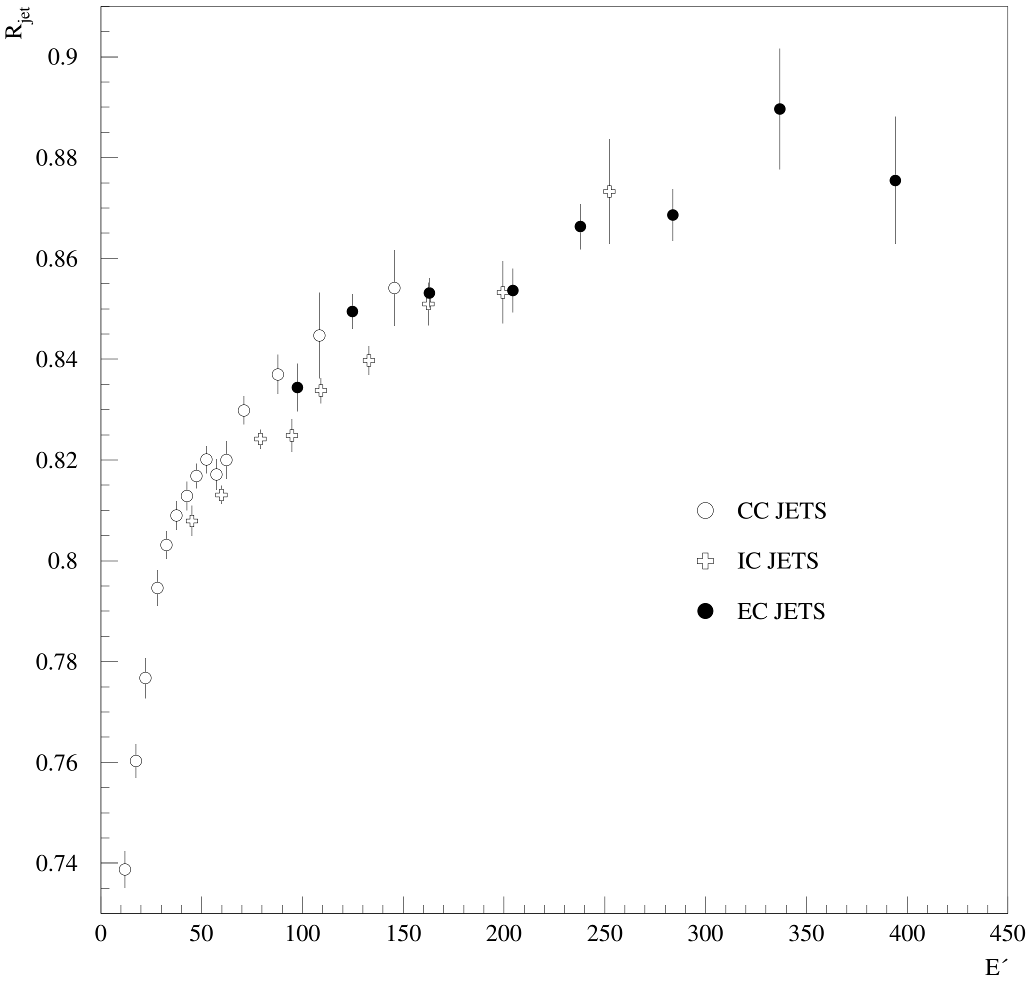

Figure 6.5: R_{jet} versus E' for the corrected sample. CC jets correspond to $|\eta_{jet}| < 0.7$, IC jets to $0.7 < |\eta_{jet}| < 1.8$ and EC jets to $1.8 < |\eta_{jet}| < 2.5$.

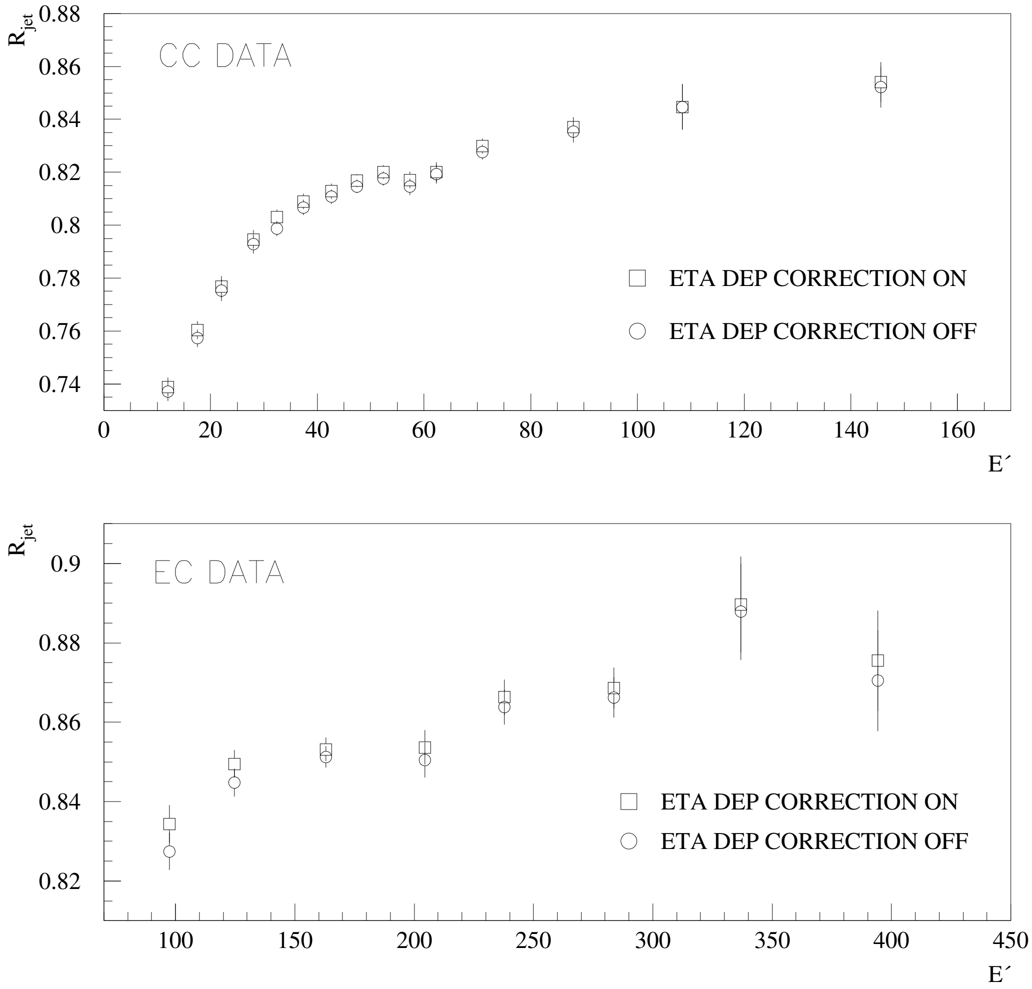

Figure 6.6: R_{jet} versus E' for CC (top) and EC jets (bottom) with and without application of the η dependent correction. This plot shows that the η dependent correction has a small effect for the hadronic response determined from central or forward jets.

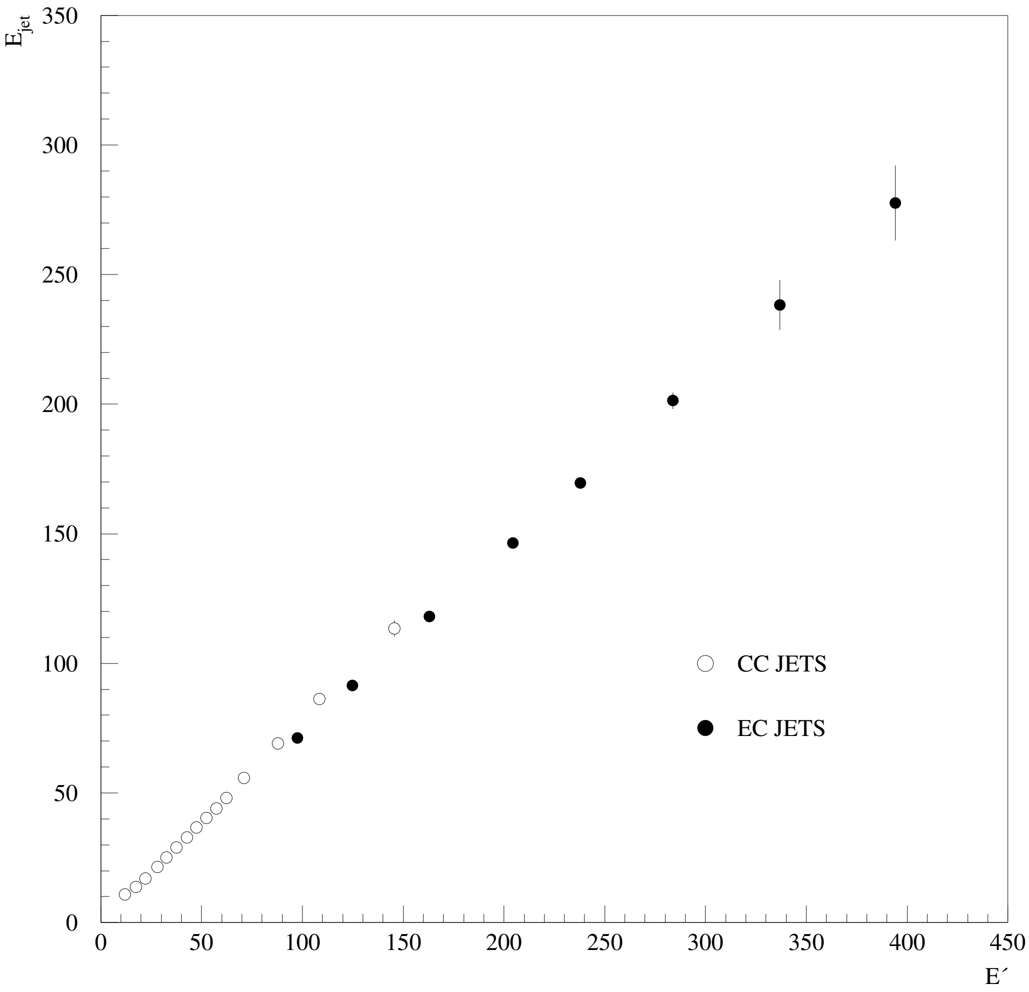

Figure 6.7: Mapping of Energy to E' for the 0.7 cone jet algorithm.

6.5 Constraining High Energy Response with Monte Carlo

Figure 6.7 shows that the hadronic response can be determined from the data for jets with energy less than 300 GeV. The highest energy jets in the DØ data reach about 600 GeV. Therefore, it is desirable to include Monte Carlo information at high energy to constrain the hadronic response where it must be extrapolated from the available data.

In Chapter 8, we will see that the hadronic response as measured from the HERWIG[18]+SHOWERLIB[19] γ-jet sample is inconsistent with the response measured in the data. In particular, the Monte Carlo response is observed to rise faster than in the data, and it reaches a plateau much sooner. We must therefore improve the Monte Carlo if we wish to use it to constrain the response in the data.

We derive a correction to the Monte Carlo response by utilizing the single particle response of the calorimeter as measured in the DØ Test Beam. Figures 6.8a-c show the fractional calorimeter response to electrons and pions as a function of particle energy from the Test Beam Particle Library [21] and from DØ SHOWERLIB (Figure 6.8d). The three versions of Test Beam plots show three different extrapolations of fractional response below 2 GeV for electrons and pions. (There are no Test Beam data below 2 GeV). We choose models where the fractional response is either extrapolated or held fixed below 2 GeV (Figure 6.8a-c). Figure 6.8d shows the single particle fractional response for electrons from SHOWERLIB and pions from plate/mixture level GEANT. Monte Carlo pion responses were determined in a Test Beam GEANT study[7], and electron responses were determined using the same HERWIG γ-jet sample that was produced for these energy scale studies (see Chapter 8).

To derive a corrected Monte Carlo sample, we convolute the single particle response with the particle level jets. Each particle in the particle jet has its energy reduced by a factor derived from the single particle response curves. Photons and electrons are corrected by the electron response factor, and π^0s are treated as two photons of half the pion energy. All other particles are reduced by the pion response factor. As a test of this method, we compare the measured hadronic response from the SHOWERLIB Monte Carlo (derived using the MPF method) to the response calculated by the above method. The result is shown in Figure 6.9. The points are derived from the MPF analysis. The solid curve is a fit to these points. The dashed curve is a fit to the jet response measured via the single particle response method. Agreement to within 1% is seen between the response from $\not\!\!E_T$ and the jet response derived from the single particle response, validating this method. This result might be improved by using a Monte Carlo single particle response from a more modern DØGEANT/RECO combination for pions and by using the Monte Carlo response to lower energies for electrons.

We repeat the derivation of the response with the various Test Beam response models and find excellent shape agreement between the second model (Figure 6.8b: extrapolated electron response, fixed pion response) and the data as shown in Figure 6.10. Here, the response derived from single particles was normalized down by 7.7% to match the jet response measured in the data[2]. This normalization is necessary as the pion response in the Test Beam particle library is higher than expected, resulting in an $\frac{e}{\pi}$ ratio of less than 1.0 for high energies. Presumably, this is the result of overestimated sampling weights applied to the pion sample. To test our sensitivity to changes in sampling weights, we rederived the response after changing $\frac{e}{\pi}$ by 5% in the single particle response functions by scaling down the pion response. An overall change in normalization was observed, but no significant shape change occurred.

[2]Note: a small normalization was also applied to match the Monte Carlo curves in Figure 6.9 – the single pion response curve used for the Monte Carlo was derived with a very early version of the reconstruction software, containing old sampling fraction corrections.

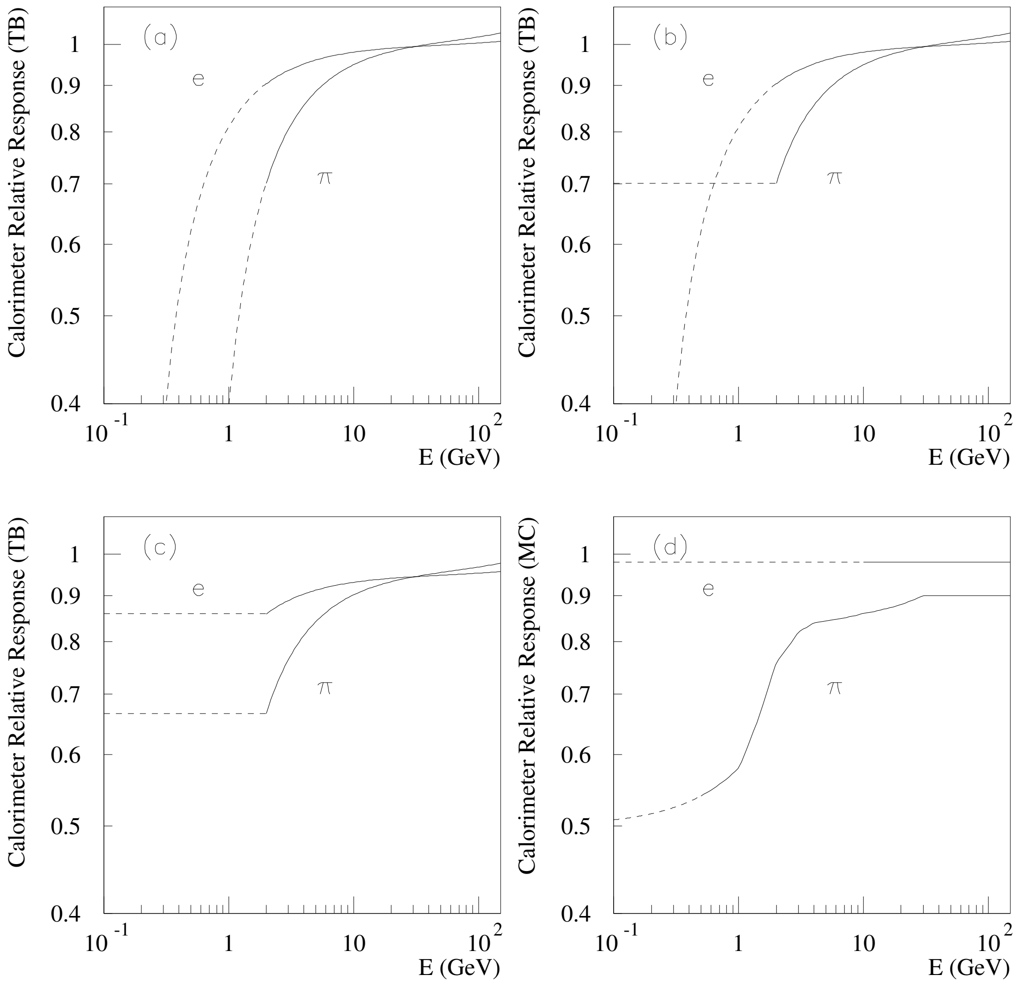

Figure 6.8: Single particle response models for electrons and pions at the Test Beam. (a-c) Single particle responses measured using the Test Beam particle library with different models for extrapolating the response below 2 GeV. (d) Single particle response for Monte Carlo.

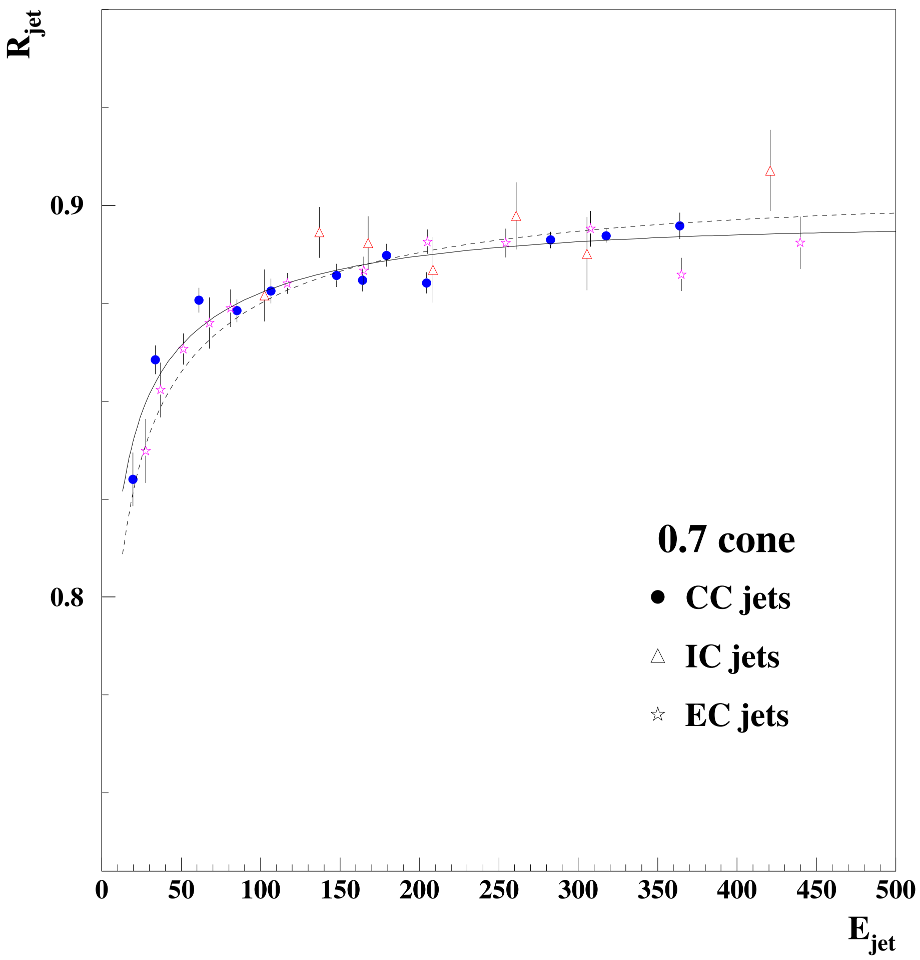

Figure 6.9: Jet energy response from SHOWERLIB Monte Carlo compared to single particle response model. The symbols show the MPF response measured for CC (circles), ICR (triangles), and EC jets (stars). The solid line shows a fit to these points. The dashed line shows the relative particle jet response after convolution with the single particle response functions derived from the Monte Carlo.

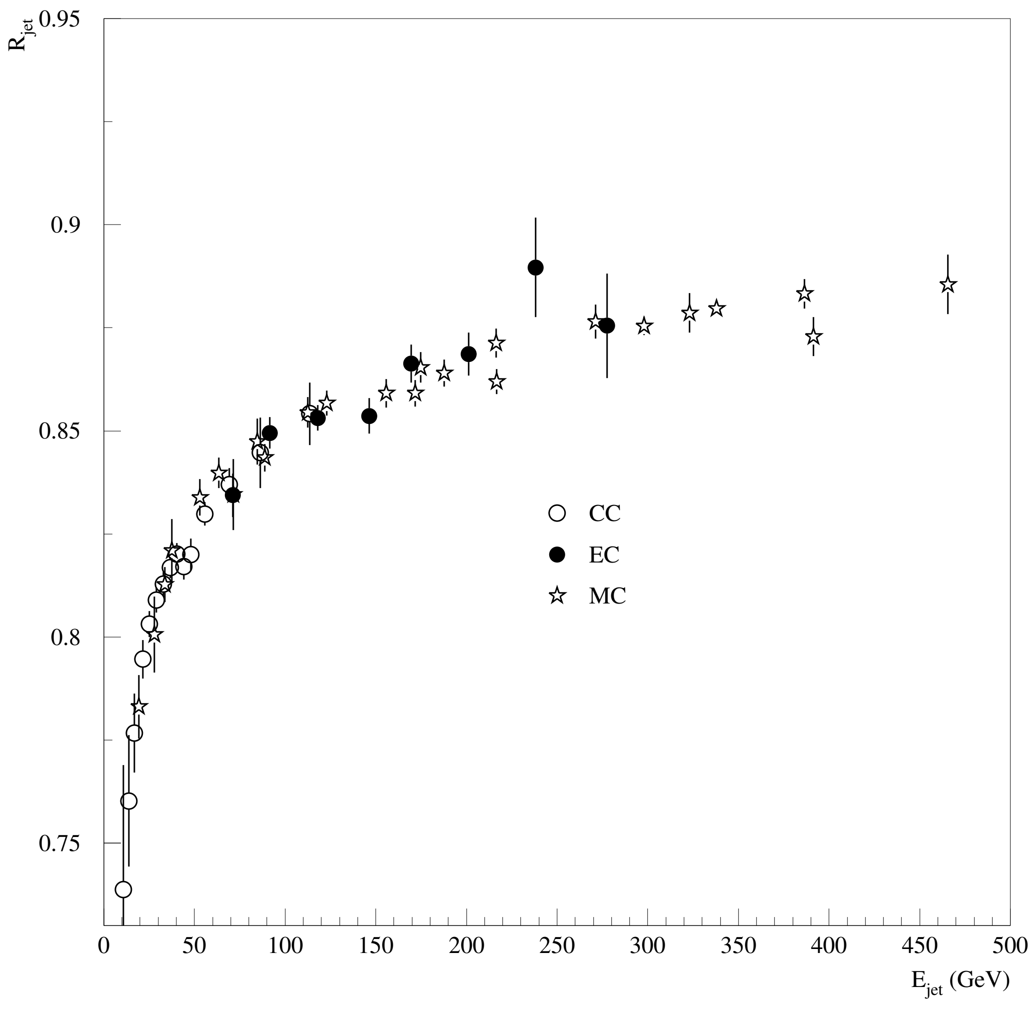

Figure 6.10: Best Monte Carlo model normalized to Data (normalization factor = 7.7%). Data are shown in circles (open in the CC and filled in the EC). Monte Carlo R_{jet} using single particle response from Test Beam is shown in stars.

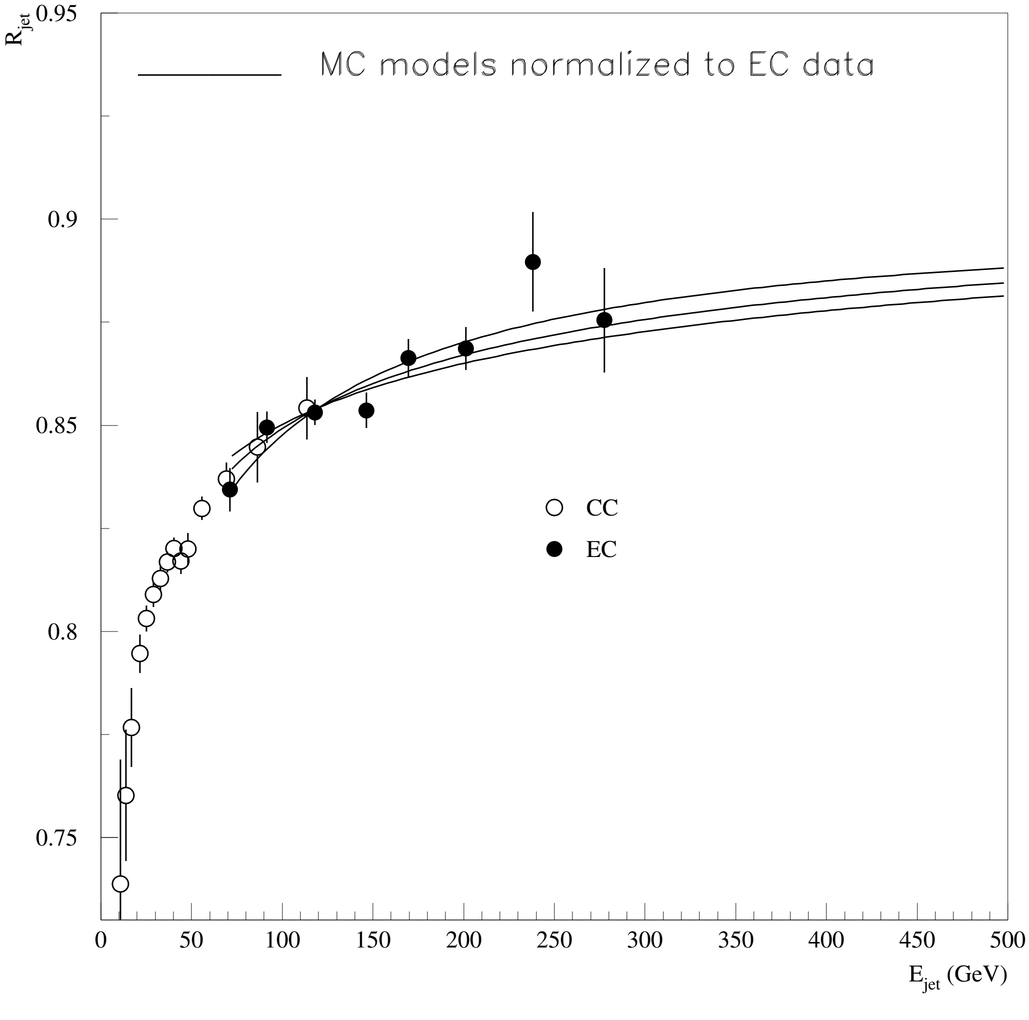

Figure 6.11: Three Test Beam Monte Carlo models normalized to EC data are shown by the solid lines. Data are shown in circles (open in the CC and filled in the EC).

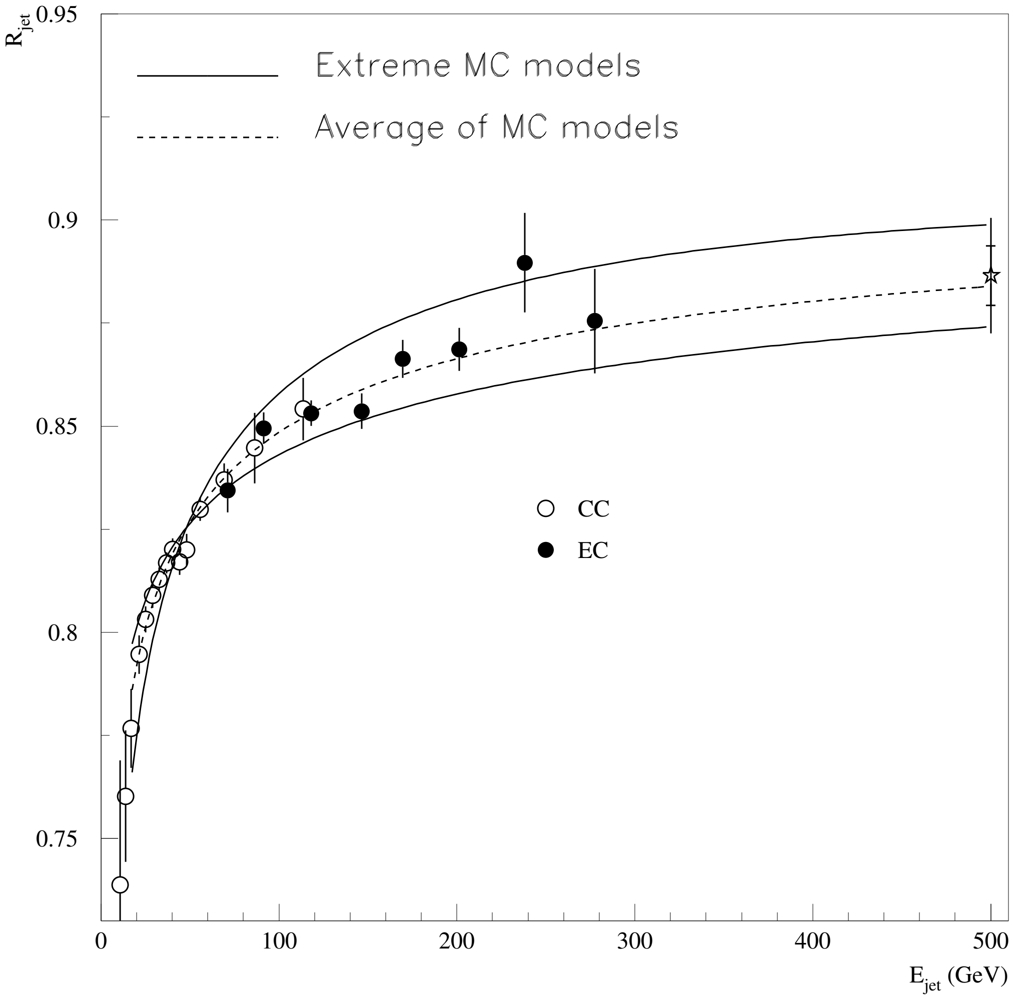

Figure 6.12: Extreme Monte Carlo models normalized to all data. The curves show the three Test Beam response models normalized to the collider data. An estimated response for 500 GeV jets is plotted with a star. The inner error bar is based on the difference between the two extreme models, the full error bar includes all errors as explained in the text.

The various single particle response models differ in shape primarily at low energy. If we normalize the models to the EC data, the extrapolation of the data to higher energy using Monte Carlo is relatively insensitive to the model chosen for the low energy single particle response (see Figure 6.11). The model-dependent error on the response at 500 GeV is $\sim$ 0.4%. This model-dependent error in the extrapolation depends upon the lower cutoff energy for normalizing to the data. We take a more conservative approach to the error in using the Monte Carlo to constrain the response fits at high energy. We take the two extreme single particle response models: the extrapolated (a) and the fixed (c) response, then we normalize the Monte Carlo curves to the entire energy range where we have data, as shown in Figure 6.12. The response for one model (a) rises more slowly than the data, and the second model (c) rises more quickly. We assume that these two extreme models bound the true response. We use the mean value of the two models at 500 GeV to estimate the response. We then use the difference divided by $\sqrt{12}$ to determine the error due to choice of model (inner error bar) [22]. This gives an error of about 0.7%. To this, we add linearly another error based on the closure test illustrated in Figure 6.9. This $\sim$ 0.6% error is based on the disagreement observed in the closure plot in the vicinity of 50 GeV, where the data constrains the normalization to the Monte Carlo curves. The negligible normalization and fit errors are also included in the full error bar shown.

6.6 Response Fits

The response versus energy for the 0.7 cone algorithm (RECO V12) is shown in Figure 6.13. The data have been fitted with the functional form:

$$R_{jet}(E) = a + b \cdot \ln(E) + c \cdot \ln(E)^2 \,. \tag{6.3}$$

A logarithmic functional form is motivated by physics arguments considering that a high energy hadronic shower becomes increasingly, but slowly, more "electromagnetic" with increasing energy. This is because in the development of a shower generated by a high energy hadron, some fraction $\langle F_{em} \rangle$ of the energy is usually spent in the production of π°'s and η's. A hadron shower, therefore, has an electromagnetic and a non-electromagnetic component. We define e as the response of the calorimeter to the EM component and h as the response to the non-EM component of a hadron shower. We also define π as the response to charged pions. We may write [23]:

$$\frac{e}{\pi} = \frac{1}{\frac{e}{h} - \langle F_{em} \rangle (\frac{h}{e} - 1)},$$

where $\langle F_{em} \rangle = 0.1 \cdot \ln(E(GeV))$ is a reasonable approximation. If the calorimeter is compensating, $\frac{e}{h}$=1, and the ratio $\frac{e}{\pi}$ is one for all energies. However, if $\frac{e}{h} \neq 1$, the ratio $\frac{e}{\pi}$ tends to one at high energies but grows exponentially as we move to lower energies. If we approximate e =1, then π may be written as $a + b \cdot \ln(E)$.

Therefore, since the DØ calorimeter is not completely compensating, the hadronic response depends logarithmically on energy. This functional form is suggested by the Test Beam measured e/π ratio as a function of beam energy [2], and also directly by R_{jet} measured from Collider data using the MPF method. The inclusion of the $\ln(E)^2$ term improves the agreement of the fit with the data in the quickly varying low energy region, while preventing the slope of the function from rising faster than the data at high energies. Other functional forms will be described below.

The three sets of points shown in Figure 6.13 correspond to CC jet data (open circles), EC jet data (filled circles), and Monte Carlo data (star). Monte Carlo data were used to derive a response point at 500 GeV in energy in order to constrain the fit where Collider

Jet Response parameters								
Cone	0.7(11)	0.7(12)	0.5(11)	0.5(12)	0.3(11)	0.3(12)	1.0(11)	1.0(12)
a	0.6380	0.6802	0.6398	0.6807	0.5240	0.6822	0.6692	0.6739
(error)	0.0527	0.0515	0.0524	0.0506	0.0737	0.0555	0.0469	0.0485
b	0.0620	0.0422	0.0625	0.0429	0.1156	0.0439	0.0466	0.0433
(error)	0.0244	0.0236	0.0246	0.0235	0.0342	0.0263	0.0218	0.0221
c	-0.0033	-0.0013	-0.0033	-0.0014	-0.0091	-0.0015	-0.0016	-0.0013
(error)	0.0028	0.0027	0.0028	0.0027	0.0039	0.0031	0.0025	0.0025

Table 6.1: Fit parameters for hadronic response correction. Parameters are shown for all jet cone sizes and RECO versions 11 and 12.

data are unavailable. The result of the fit is shown in Figure 6.13. The resulting χ^2 is 10 for 15 degrees of freedom for RECO V12 data and 20.2 for 15 d.o.f for RECO V11. A fit to the latter data set reconstructed with the 0.7 cone algorithm is shown in Figure 6.14. (Note that the large errors in the three lowest energy points are dominated by the low E_T bias correction and are nearly 100% correlated).

The best fit parameters for the various cone algorithms are shown in Table 6.1. The single parameter errors show one standard deviation uncertainties as calculated from the $\chi^2 = \chi^2_{min} + 1$ surface in the parameter space.

6.6.1 Errors from Response Fits

We wish to assign an error to the response function which corresponds to a 68% confidence region for parameter fluctuations. The probability for all parameters to simultaneously take on values within the one standard deviation ($\chi^2 = \chi^2_{min} + 1$) region is significantly less than 68% [24]. The error on the response is estimated in the following way. A surface is mapped out in parameter space containing a region with a 68% probability for parameter fluctuations. For three parameters this corresponds to a surface defined by $\chi^2 = \chi^2_{min} + 3.5$ [24, 25]. The points lying on this surface are then mapped back onto the response versus energy plane. At each energy, the error is determined by the parameter set giving the greatest derivation from nominal response. The result for the 0.7 cone algorithm is shown in Figures 6.13-6.14. The outer band represents the error on the fit to the response.

The size of the error band and the nominal fit value were determined by starting the fit above various energy thresholds, namely: 0, 25, 30, 35, 40, 50, and 60 GeV. The error band at large energy was found to be weakly dependent on the energy threshold, and nearly constant above 30 GeV. We therefore use a 30 GeV threshold in all the response fits. The low energy response remains well constrained by this choice.

Two other functional forms were also used to fit the data:

$$R_{jet}(E) = a + b \cdot \ln(E) + c \cdot \sqrt{E} \tag{6.4}$$

$$R_{jet}(E) = a + b \cdot \ln(E) + c \cdot E \tag{6.5}$$

Functional forms with higher powers of energy in the third term tended to cause the response to start falling at high energies in the extrapolation region which is an unphysical result. The above two forms were fitted to the data above 30 GeV and the error bands were again calculated as described above. The final fit error used in the CAFIX package is the maximum of the three bands at each energy. Errors from the $\sqrt{E}$ form were smaller than the errors using the nominal function. The linear function produced slightly larger errors for highest energies ($\sim 0.1\% - 0.3\%$ larger from 400-500 GeV).

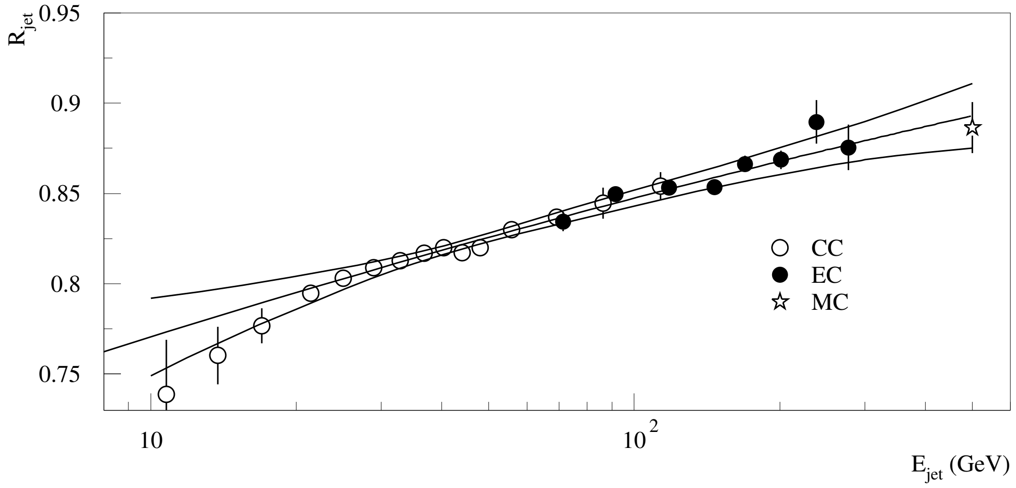

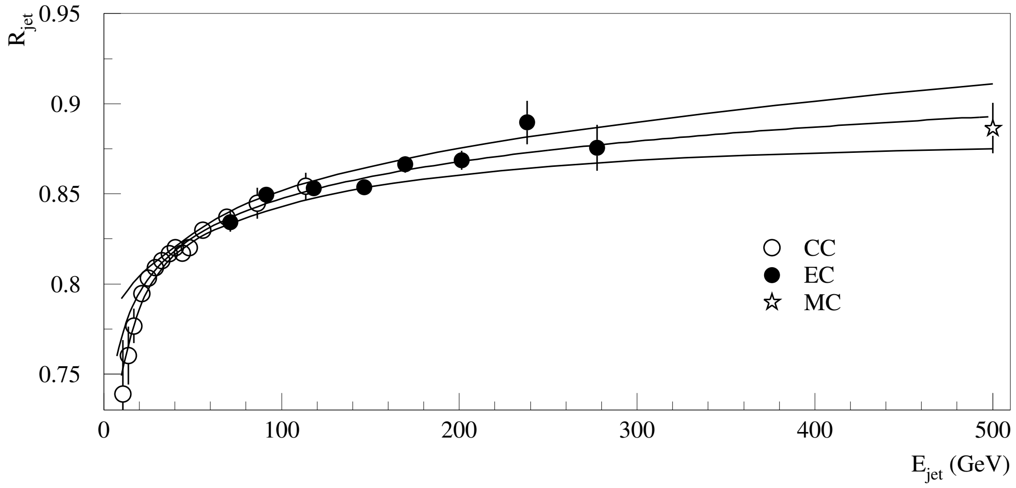

Figure 6.13: R_{jet} versus energy for the 0.7 cone jet algorithm (RECO V12). The outer band shows limits on the measured response for high energy jets based on the region in parameter space defined by the $\chi^2 = \chi^2_{min} + 3.5$ surface. This region corresponds to the 68% confidence region of parameter fluctuations from the nominal values.

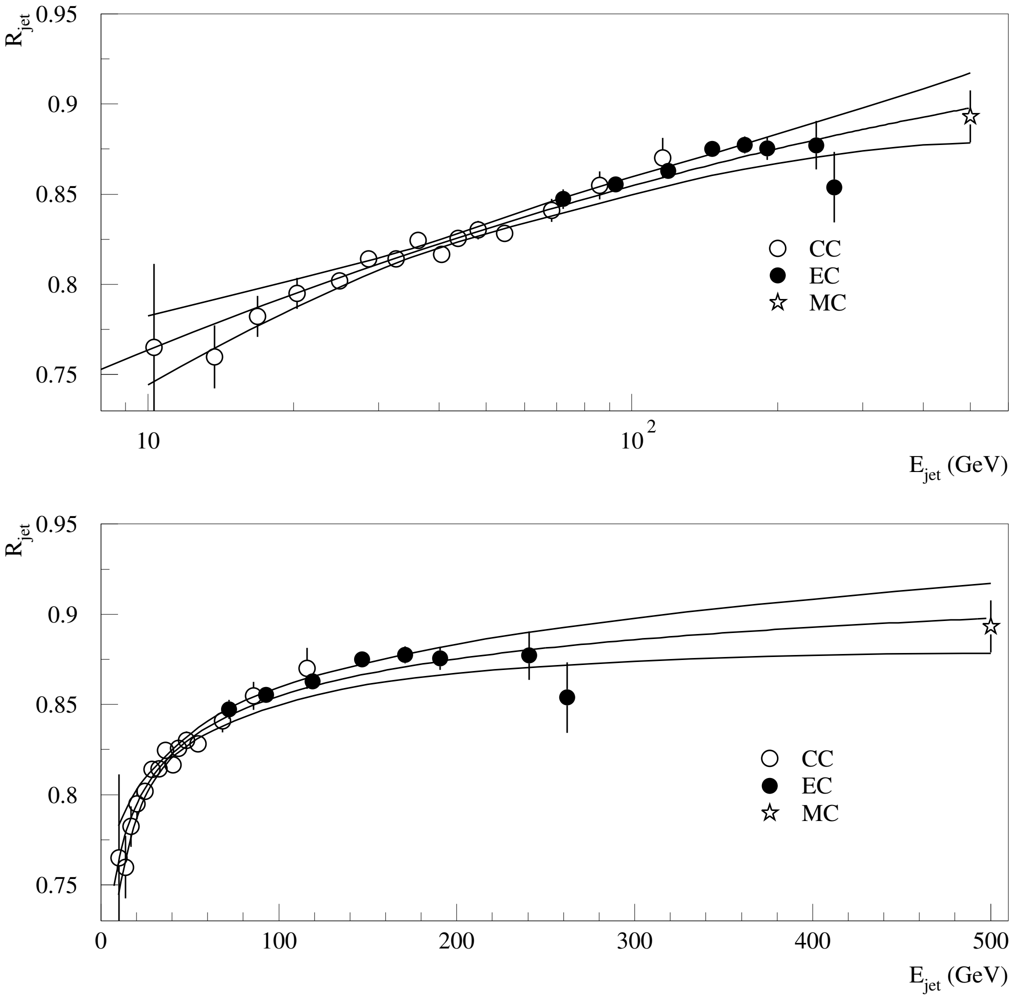

Figure 6.14: R_{jet} versus energy for the 0.7 cone jet algorithm (RECO V11). The outer band shows limits on the measured response for high energy jets based on the region in parameter space defined by the $\chi^2 = \chi^2_{min} + 3.5$ surface. This region corresponds to the 68% confidence region of parameter fluctuations from the nominal values.

6.6.2 Error Correlations in Response Fit

The error on the hadronic response measurement is the dominant systematic uncertainty over large regions of jet energy and pseudorapidity. In this section, we describe the point-to-point correlations in jet energy for the fit errors described above. As we show below, the response errors for the largest energy jets are highly correlated.

The error bands shown in Figures 6.13-6.14 represent the extreme response variation at each energy value based on fluctuations of all fit parameters. However, the parameter set that produces a given variation at one energy need not produce the same variation at any other energy in either magnitude or sign. And, in general, no single set of fit parameters may exist to produce the extreme curves. However, it is reasonable to expect that errors for two points close in energy should be largely correlated. We calculate the energy correlations in the fit error in the following way:

- We generate a grid of parameter sets (N_{grid}) to define the $\chi^2 \leq \chi^2_{min} + 3.5$ volume. This volume contains all fit parameter set fluctuations corresponding to a 68% probability. Each parameter set defines a response function contained within the bands shown in Figures 6.13-6.14.

- We loop through all the parameter sets, noting the variation in response at eleven values of uncorrected jet energy[3] between 10 and 500 GeV. The correlations in response for each pair of energy values are calculated from the parameter sets in the grid and these are used to define a correlation matrix for the eleven energy values. Each element of the matrix ($r(i,j)$) is just the standard correlation coefficient between the responses measured at each energy value. $r(i,j)$ is defined as:

$$r(i,j) = \frac{\sum_{n=1}^{N_{grid}}(R_n(i) - \overline{R(i)})(R_n(j) - \overline{R(j)})}{[\sum_{n=1}^{N_{grid}}(R_n(i) - \overline{R(i)})^2 \sum_{n=1}^{N_{grid}}(R_n(j) - \overline{R(j)})^2]^{\frac{1}{2}}}, \tag{6.6}$$

  where $R(i)$ is the response for the i^{th} energy bin.

The correlation matrix for the response fit to 0.7 cone jets in RECO V12 is shown in Table 6.2. Correlations are illustrated graphically in Figure 6.15 where four rows of the matrix are plotted showing the error correlations relative to the errors at 20, 50, 100, and 500 GeV respectively. The correlations for fits to other cone sizes and for the RECO V11 fits are provided in Tables 6.3-6.9.

[3]In this context uncorrected energy means energy uncorrected for the hadronic response correction. The jet energy has already been corrected for low E_T bias, offset, sampling fractions (RECO V11 only), and any η dependent corrections.

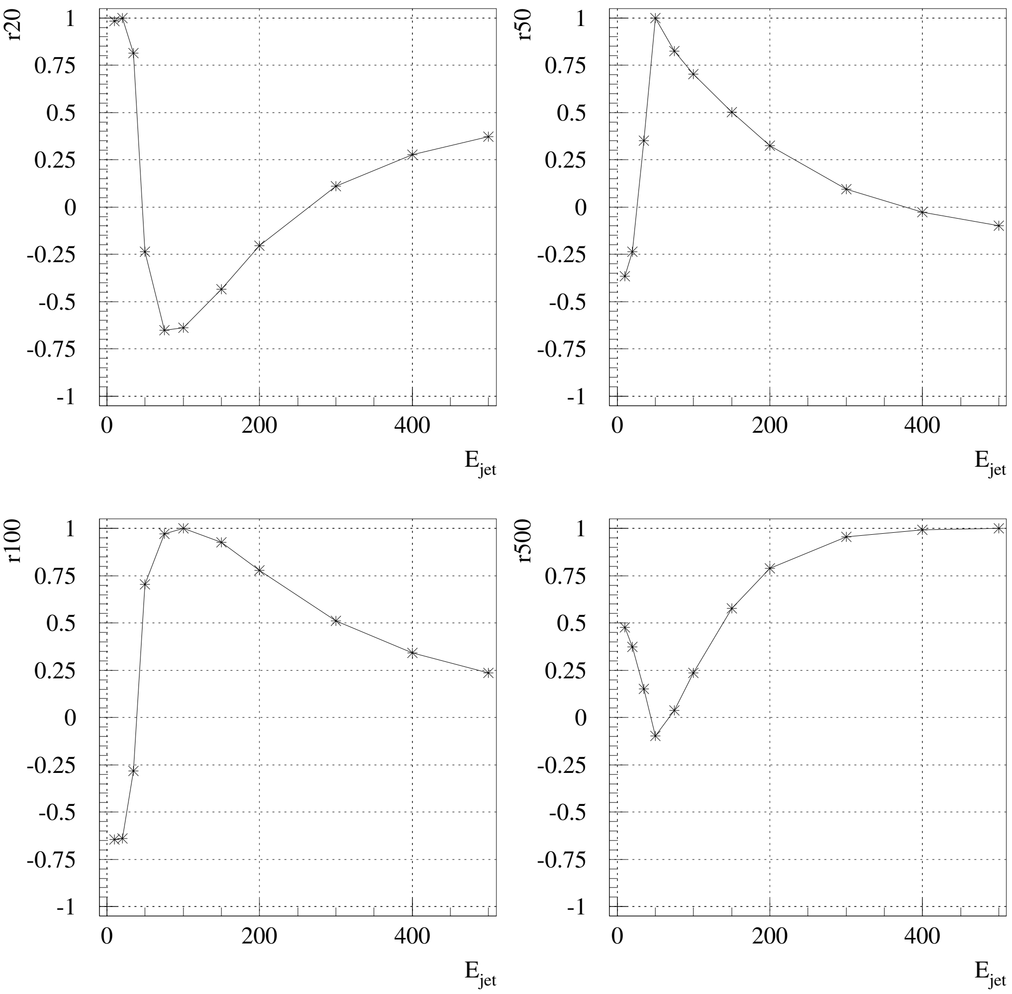

Figure 6.15: Error correlations for 0.7 cone (RECO V12) response fit. Error correlations are shown in four slices from the full correlation matrix. The four curves show the point-to-point correlation of fit errors relative to energy values of 20, 50, 100, and 500 GeV respectively.

Correlations for Fit Error, 0.7 Cone, Reco 12											
E(GeV)	10	20	35	50	75	100	150	200	300	400	500
10	1.00	0.98	0.71	-0.37	-0.70	-0.65	-0.39	-0.13	0.21	0.38	0.48
20	0.98	1.00	0.81	-0.24	-0.65	-0.64	-0.43	-0.20	0.11	0.28	0.37
35	0.71	0.81	1.00	0.35	-0.19	-0.28	-0.25	-0.15	0.00	0.10	0.15
50	-0.37	-0.24	0.35	1.00	0.83	0.70	0.50	0.33	0.09	-0.03	-0.10
75	-0.70	-0.65	-0.19	0.83	1.00	0.97	0.82	0.62	0.32	0.14	0.04
100	-0.65	-0.64	-0.28	0.70	0.97	1.00	0.93	0.78	0.51	0.34	0.24
150	-0.39	-0.43	-0.25	0.50	0.82	0.93	1.00	0.96	0.79	0.67	0.58
200	-0.13	-0.20	-0.15	0.33	0.62	0.78	0.96	1.00	0.94	0.85	0.79
300	0.21	0.11	0.00	0.09	0.32	0.51	0.79	0.94	1.00	0.98	0.95
400	0.38	0.28	0.10	-0.03	0.14	0.34	0.67	0.85	0.98	1.00	0.99
500	0.48	0.37	0.15	-0.10	0.04	0.24	0.58	0.79	0.95	0.99	1.00

Table 6.2: Correlation matrix for error band in hadronic response correction (0.7 cone jets, RECO version 12).

Correlations for Fit Error, 0.5 Cone, Reco 12											
E(GeV)	10	20	35	50	75	100	150	200	300	400	500
10	1.00	0.98	0.58	-0.48	-0.70	-0.62	-0.33	-0.07	0.25	0.41	0.50
20	0.98	1.00	0.72	-0.35	-0.65	-0.61	-0.38	-0.15	0.14	0.29	0.38
35	0.58	0.72	1.00	0.38	-0.07	-0.16	-0.15	-0.10	0.00	0.06	0.10
50	-0.48	-0.35	0.38	1.00	0.87	0.76	0.53	0.32	0.07	-0.06	-0.13
75	-0.70	-0.65	-0.07	0.87	1.00	0.97	0.80	0.60	0.31	0.14	0.04
100	-0.62	-0.61	-0.16	0.76	0.97	1.00	0.92	0.77	0.51	0.36	0.26
150	-0.33	-0.38	-0.15	0.53	0.80	0.92	1.00	0.96	0.81	0.69	0.61
200	-0.07	-0.15	-0.10	0.32	0.60	0.77	0.96	1.00	0.94	0.87	0.81
300	0.25	0.14	0.00	0.07	0.31	0.51	0.81	0.94	1.00	0.98	0.96
400	0.41	0.29	0.06	-0.06	0.14	0.36	0.69	0.87	0.98	1.00	0.99
500	0.50	0.38	0.10	-0.13	0.04	0.26	0.61	0.81	0.96	0.99	1.00

Table 6.3: Correlation matrix for error band in hadronic response correction (0.5 cone jets, RECO version 12).

Correlations for Fit Error, 0.3 Cone, Reco 12											
E(GeV)	10	20	35	50	75	100	150	200	300	400	500
10	1.00	0.98	0.44	-0.57	-0.68	-0.57	-0.23	0.04	0.35	0.49	0.56
20	0.98	1.00	0.60	-0.44	-0.64	-0.57	-0.29	-0.04	0.24	0.37	0.45
35	0.44	0.60	1.00	0.42	0.08	0.00	-0.01	0.01	0.06	0.08	0.10
50	-0.57	-0.44	0.42	1.00	0.91	0.80	0.54	0.32	0.05	-0.08	-0.16
75	-0.68	-0.64	0.08	0.91	1.00	0.97	0.78	0.56	0.27	0.12	0.03
100	-0.57	-0.57	0.00	0.80	0.97	1.00	0.91	0.75	0.50	0.35	0.27
150	-0.23	-0.29	-0.01	0.54	0.78	0.91	1.00	0.96	0.81	0.71	0.64
200	0.04	-0.04	0.01	0.32	0.56	0.75	0.96	1.00	0.95	0.88	0.84
300	0.35	0.24	0.06	0.05	0.27	0.50	0.81	0.95	1.00	0.99	0.97
400	0.49	0.37	0.08	-0.08	0.12	0.35	0.71	0.88	0.99	1.00	1.00
500	0.56	0.45	0.10	-0.16	0.03	0.27	0.64	0.84	0.97	1.00	1.00

Table 6.4: Correlation matrix for error band in hadronic response correction (0.3 cone jets, RECO version 12).

Correlations for Fit Error, 1.0 Cone, Reco 12											
E(GeV)	10	20	35	50	75	100	150	200	300	400	500
10	1.00	0.98	0.74	-0.29	-0.68	-0.63	-0.36	-0.11	0.21	0.38	0.47
20	0.98	1.00	0.84	-0.15	-0.64	-0.63	-0.42	-0.19	0.10	0.26	0.35
35	0.74	0.84	1.00	0.39	-0.23	-0.33	-0.29	-0.19	-0.03	0.07	0.13
50	-0.29	-0.15	0.39	1.00	0.78	0.64	0.42	0.25	0.05	-0.05	-0.11
75	-0.68	-0.64	-0.23	0.78	1.00	0.97	0.80	0.60	0.32	0.15	0.05
100	-0.63	-0.63	-0.33	0.64	0.97	1.00	0.92	0.78	0.52	0.36	0.26
150	-0.36	-0.42	-0.29	0.42	0.80	0.92	1.00	0.96	0.81	0.69	0.61
200	-0.11	-0.19	-0.19	0.25	0.60	0.78	0.96	1.00	0.94	0.87	0.81
300	0.21	0.10	-0.03	0.05	0.32	0.52	0.81	0.94	1.00	0.98	0.96
400	0.38	0.26	0.07	-0.05	0.15	0.36	0.69	0.87	0.98	1.00	0.99
500	0.47	0.35	0.13	-0.11	0.05	0.26	0.61	0.81	0.96	0.99	1.00

Table 6.5: Correlation matrix for error band in hadronic response correction (1.0 cone jets, RECO version 12).

Correlations for Fit Error, 0.7 Cone, Reco 11											
E(GeV)	10	20	35	50	75	100	150	200	300	400	500
10	1.00	0.98	0.55	-0.55	-0.73	-0.66	-0.40	-0.13	0.21	0.39	0.49
20	0.98	1.00	0.69	-0.43	-0.68	-0.65	-0.43	-0.20	0.12	0.29	0.39
35	0.55	0.69	1.00	0.34	-0.05	-0.12	-0.12	-0.06	0.04	0.10	0.13
50	-0.55	-0.43	0.34	1.00	0.90	0.81	0.61	0.41	0.13	-0.03	-0.12
75	-0.73	-0.68	-0.05	0.90	1.00	0.98	0.83	0.63	0.32	0.14	0.03
100	-0.66	-0.65	-0.12	0.81	0.98	1.00	0.93	0.78	0.51	0.33	0.22
150	-0.40	-0.43	-0.12	0.61	0.83	0.93	1.00	0.96	0.79	0.66	0.56
200	-0.13	-0.20	-0.06	0.41	0.63	0.78	0.96	1.00	0.93	0.85	0.78
300	0.21	0.12	0.04	0.13	0.32	0.51	0.79	0.93	1.00	0.98	0.95
400	0.39	0.29	0.10	-0.03	0.14	0.33	0.66	0.85	0.98	1.00	0.99
500	0.49	0.39	0.13	-0.12	0.03	0.22	0.56	0.78	0.95	0.99	1.00

Table 6.6: Correlation matrix for error band in hadronic response correction (0.7 cone jets, RECO version 11).

Correlations for Fit Error, 0.5 Cone, Reco 11											
E(GeV)	10	20	35	50	75	100	150	200	300	400	500
10	1.00	0.98	0.35	-0.62	-0.72	-0.63	-0.33	-0.05	0.27	0.43	0.52
20	0.98	1.00	0.52	-0.50	-0.67	-0.61	-0.37	-0.13	0.18	0.33	0.41
35	0.35	0.52	1.00	0.45	0.14	0.06	0.02	0.02	0.04	0.05	0.06
50	-0.62	-0.50	0.45	1.00	0.93	0.83	0.60	0.38	0.09	-0.06	-0.15
75	-0.72	-0.67	0.14	0.93	1.00	0.97	0.81	0.60	0.30	0.13	0.03
100	-0.63	-0.61	0.06	0.83	0.97	1.00	0.92	0.76	0.50	0.34	0.24
150	-0.33	-0.37	0.02	0.60	0.81	0.92	1.00	0.96	0.80	0.68	0.60
200	-0.05	-0.13	0.02	0.38	0.60	0.76	0.96	1.00	0.94	0.86	0.81
300	0.27	0.18	0.04	0.09	0.30	0.50	0.80	0.94	1.00	0.98	0.96
400	0.43	0.33	0.05	-0.06	0.13	0.34	0.68	0.86	0.98	1.00	0.99
500	0.52	0.41	0.06	-0.15	0.03	0.24	0.60	0.81	0.96	0.99	1.00

Table 6.7: Correlation matrix for error band in hadronic response correction (0.5 cone jets, RECO version 11).

Correlations for Fit Error, 0.3 Cone, Reco 11											
E(GeV)	10	20	35	50	75	100	150	200	300	400	500
10	1.00	0.98	0.58	-0.47	-0.70	-0.62	-0.32	-0.03	0.32	0.48	0.57
20	0.98	1.00	0.71	-0.34	-0.63	-0.60	-0.36	-0.09	0.23	0.39	0.47
35	0.58	0.71	1.00	0.40	-0.02	-0.10	-0.08	-0.01	0.09	0.15	0.18
50	-0.47	-0.34	0.40	1.00	0.89	0.78	0.56	0.34	0.05	-0.09	-0.16
75	-0.70	-0.63	-0.02	0.89	1.00	0.97	0.79	0.56	0.23	0.05	-0.05
100	-0.62	-0.60	-0.10	0.78	0.97	1.00	0.91	0.73	0.43	0.26	0.16
150	-0.32	-0.36	-0.08	0.56	0.79	0.91	1.00	0.95	0.76	0.63	0.54
200	-0.03	-0.09	-0.01	0.34	0.56	0.73	0.95	1.00	0.93	0.85	0.78
300	0.32	0.23	0.09	0.05	0.23	0.43	0.76	0.93	1.00	0.98	0.96
400	0.48	0.39	0.15	-0.09	0.05	0.26	0.63	0.85	0.98	1.00	0.99
500	0.57	0.47	0.18	-0.16	-0.05	0.16	0.54	0.78	0.96	0.99	1.00

Table 6.8: Correlation matrix for error band in hadronic response correction (0.3 cone jets, RECO version 11).

Correlations for Fit Error, 1.0 Cone, Reco 11											
E(GeV)	10	20	35	50	75	100	150	200	300	400	500
10	1.00	0.98	0.54	-0.55	-0.72	-0.63	-0.35	-0.10	0.21	0.37	0.46
20	0.98	1.00	0.69	-0.42	-0.68	-0.63	-0.41	-0.19	0.10	0.25	0.34
35	0.54	0.69	1.00	0.34	-0.07	-0.16	-0.17	-0.12	-0.04	0.02	0.05
50	-0.55	-0.42	0.34	1.00	0.89	0.77	0.55	0.35	0.10	-0.04	-0.12
75	-0.72	-0.68	-0.07	0.89	1.00	0.97	0.81	0.62	0.35	0.19	0.09
100	-0.63	-0.63	-0.16	0.77	0.97	1.00	0.93	0.79	0.55	0.40	0.30
150	-0.35	-0.41	-0.17	0.55	0.81	0.93	1.00	0.96	0.82	0.71	0.64
200	-0.10	-0.19	-0.12	0.35	0.62	0.79	0.96	1.00	0.95	0.88	0.82
300	0.21	0.10	-0.04	0.10	0.35	0.55	0.82	0.95	1.00	0.99	0.96
400	0.37	0.25	0.02	-0.04	0.19	0.40	0.71	0.88	0.99	1.00	0.99
500	0.46	0.34	0.05	-0.12	0.09	0.30	0.64	0.82	0.96	0.99	1.00

Table 6.9: Correlation matrix for error band in hadronic response correction (1.0 cone jets, RECO version 11).

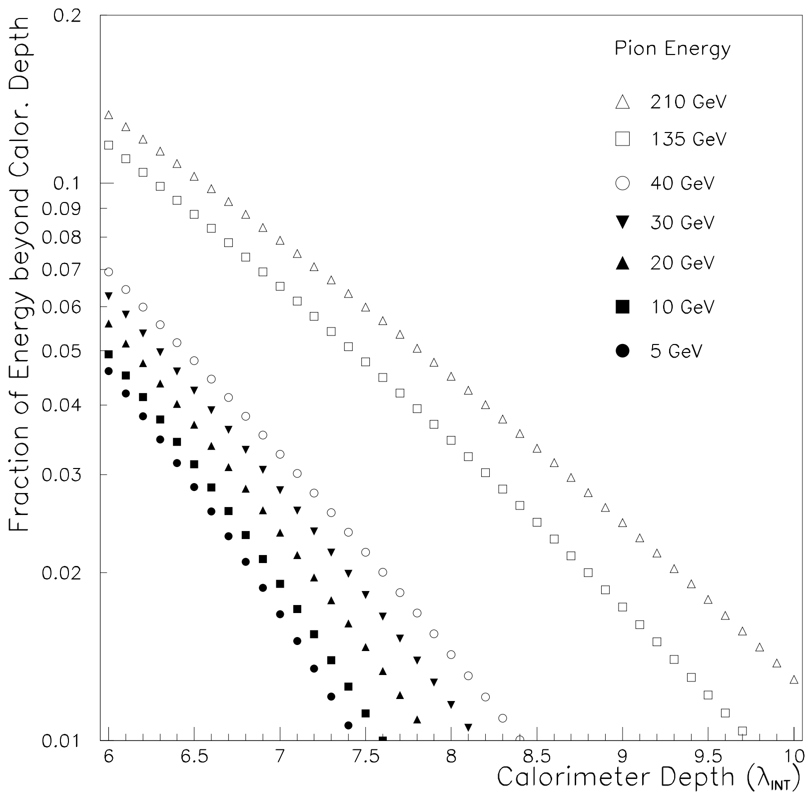

Figure 6.16: Fraction of pion energy contained by the NuTeV calorimeter as a function of depth in units of interaction lengths.

6.7 Shower Containment

The DØ central calorimeter is more than 7.2 interaction lengths (λ_{INT}) thick and the end calorimeters are more than $8\lambda_{INT}$ thick. Although the depth of the EC assures full hermeticity, there is still a probability of the central calorimeter not containing the entire shower from very high energy jets.

The fraction of energy lost as a function of the number of absorption lengths for pions was obtained from the NuTeV collaboration. The NuTeV calorimeter consists of stainless steel (absorber) and scintillator (active medium), however the energy loss as a function of λ_{INT} does not depend on the absorber to first order. Therefore, we use the NuTeV data for this study despite the difference in the calorimeters. Figure 6.16 shows the fraction of energy beyond a certain calorimeter depth as a function of calorimeter depth in units of λ_{INT} [26]. Even after 7 interaction lengths there is still a significant amount of energy not contained for very high energy pions. Since high energy jets contain many low energy particles, the effects of containment is much smaller for jets.

The thickness of the DØ central calorimeter was determined from a GEANT simulation of the DØ detector. Figure 6.17 shows the depth of the CC as a function of λ_{INT}. By definition, the length of one λ_{INT} depends on the proton cross section with the absorption material. For the DØ calorimeter, the uncertainty in this cross section gives the different results displayed in figure 6.17. GEISHA and FLUKA are different simulations of physics processes implemented in GEANT [27, 28, 29].

The energy containment of jets was determined using HERWIG jets with $|\eta| < 0.7$. The η of each particle within a jet and Figure 6.17 were used to determine the number of interaction lengths each particle traversed. Using the parameterization shown in Figure 6.16, the containment of each particle was measured. All hadronic particles were treated as pions. The electromagnetic particles (π^o,e^-,γ) deposited all of their energy within the calorimeter. The energy contained within a jet was compared to the total particle level jet energy in order to measure the fraction of energy lost out the back of the calorimeter.

In the central calorimeter, any energy not contained within the calorimeter is measured as $\not\!\!E_T$. Therefore, the measured response corrects for containment. The response of jets with energy less than 100 GeV is measured using the CC and therefore it includes the containment correction. However, for jets with E $>$ 100 GeV, the response is determined from EC data. The EC is normalized to the CC using the cryostat factor. Since the EC's are over 8 interaction lengths thick, they contain the entire jet shower. By measuring the high energy response in the end cap calorimeter, where the containment is 100%, and applying it to the central calorimeter, where the containment is less than 100%, we are ignoring the containment contribution to the response at high energies. Since the cryostat factor is measured for jets with energy $\sim$ 100 GeV, we need to evaluate the effect of containment for jets with energy greater than 100 GeV in order to obtain an estimate of the containment bias in the measured response.

Figure 6.18 shows a Monte Carlo simulation of the fraction of the jet energy contained within the DØ central calorimeter ($|\eta| < 0.7$) as a function of jet particle level energy. The most conservative of the CC depth estimates (7.2 λ_{INT} at η=0) was used in the simulation. The data have been normalized to 1.0 at 100 GeV to evaluate only the energy loss with respect to 100 GeV jets. The effect on the measured response due to energy lost out the back of the CC is less than 0.5% for $E_T \lesssim 400$ GeV, given the assumptions in our simulation.

Since the absolute number of interaction lengths in the central calorimeter is not known precisely, differing thicknesses were modeled. The absolute energy contained varied between the different models but the relative change as a function of jet energy was constant. The simulation was also repeated using a parameterization of pion energy loss as a function of λ_{INT} from Fabjan and Wigmans[3]. The latter gave results which were consistent with those obtained from the NuTeV parametrization. From these studies, we conclude that the effects on the measured response at high energy due to energy not contained within the calorimeter is less than 0.5% in the kinematic range covered by DØ.

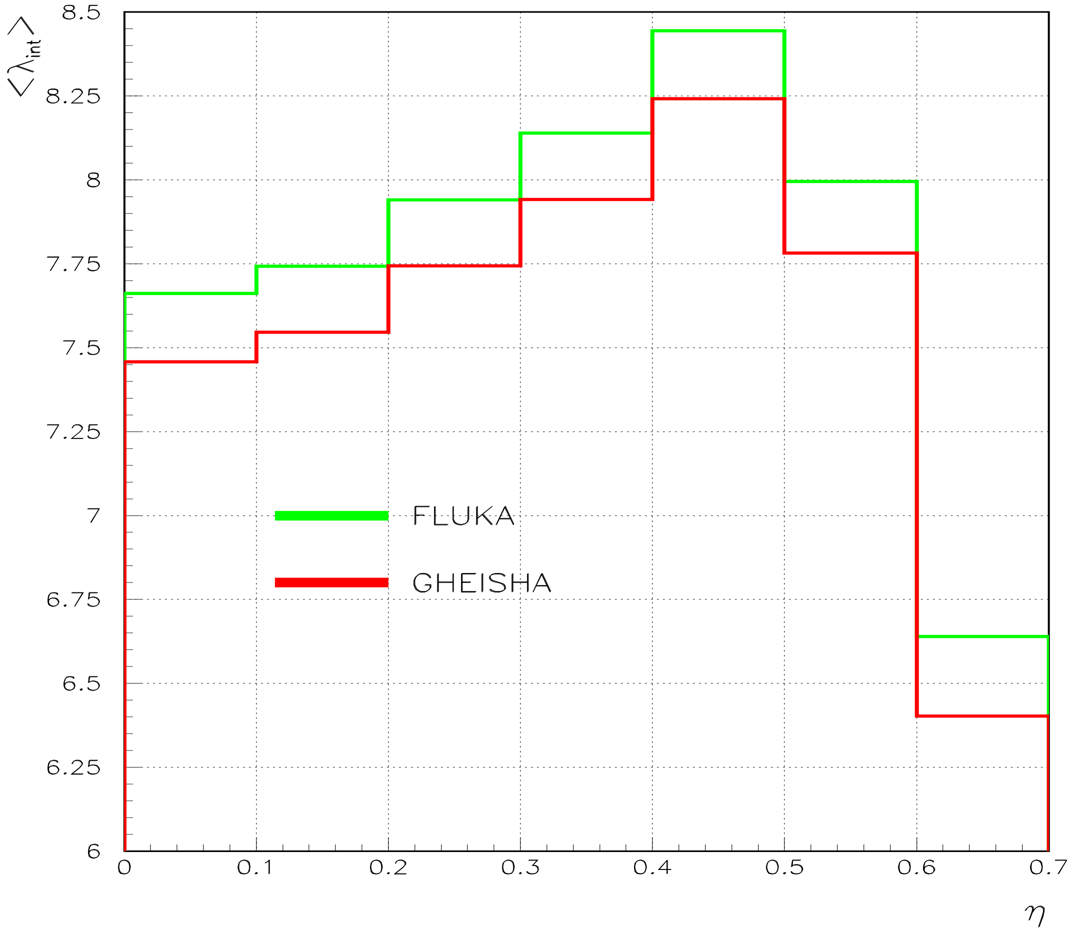

Figure 6.17: Depth of the DØ central calorimeter in units of interaction lengths.

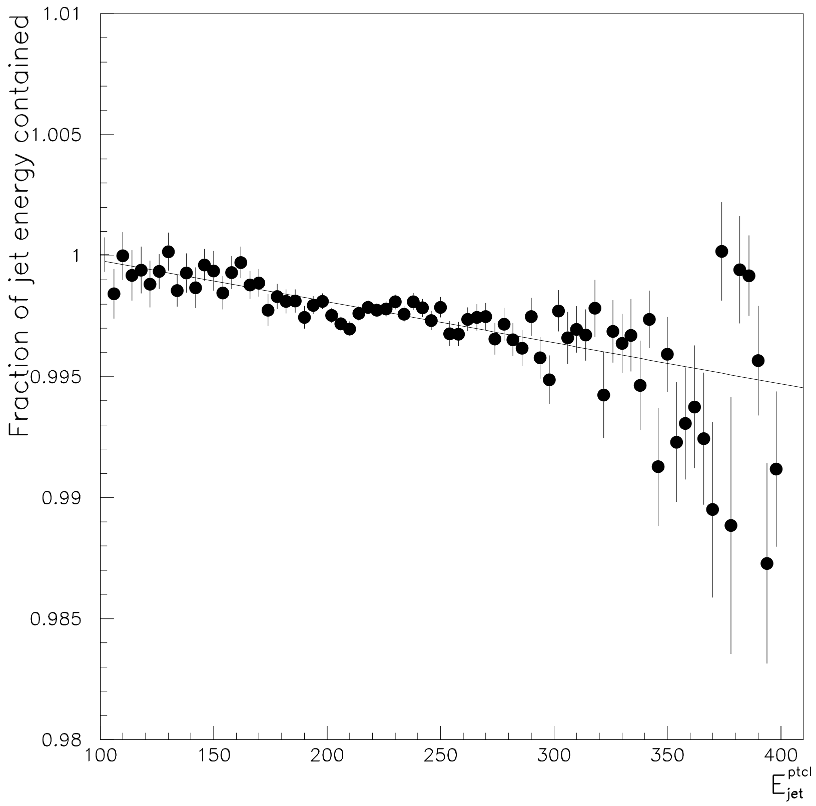

Figure 6.18: Fraction of the jet energy contained within the DØ central calorimeter ($|\eta| < 0.7$) as a function of jet energy. The data is normalized to 1.0 at 100 GeV.

6.8 Effects of $\not\!\!E_T$ Acceptance

The event $\not\!\!E_T$ is measured from energy deposited in the individual calorimeter cells. The sum is done over all cells within the range $|\eta| < \eta_{lim}$ with η_{lim} =4.5, which is equivalent to the range θ <1° in terms of the polar angle. To study the effects on R_{jet} of the large but limited acceptance in the $\not\!\!E_T$ measurement, we recalculated $\not\!\!E_T$ as a function of η_{lim} in a γ-jet Monte Carlo sample (HERWIG-SHOWERLIB). From the measured R_{jet} versus η_{lim}, it is possible to extract the effect of the limited $\not\!\!E_T$ acceptance by extrapolation to $\eta_{lim} \to \infty$. The process is repeated for different E_{jet} bins.

Figures 6.19-6.21 show clearly that the $\not\!\!E_T$ acceptance bias is negligible above $E_{jet} \gtrsim 50$ GeV, since R_{jet} is a constant function of η_{lim} above 4. Below this threshold, the bias is very small and no larger than 0.5%. To be conservative, we include a 0.5% error below E_{Tjet} =15 GeV, which decreases linearly to zero at 50 GeV.

This $\not\!\!E_T$ acceptance bias is likely to come from soft initial state radiation emitted at small angles. This energy would not be detected by the calorimeter and would be responsible for a "K_T kick" of the parton-parton system. The event $\vec{\not\!\!E}_T$ would not be zero and the response determined with the MPF method would be biased low, since initial state radiation is mostly correlated with the direction of the leading jet.

6.9 Systematic Errors in R_{jet}

In addition to the error of the fit, there is a 0.5% physics background error on R_{jet}, as discussed in Chapter 4. The $\not\!\!E_T$ acceptance error is 0.5% below 15 GeV and decreases linearly to zero at 50 GeV. At very low E_T's, below about 20 GeV, the low E_T bias error quickly becomes the dominant uncertainty. Above E_T =100 in the CC, we include an error that increases linearly from zero to a 0.5% at 400 GeV. This uncertainty accounts for the possible bias in R_{jet} due to energy not contained inside the calorimeter limits.

There are two biases present in the response measurement: the topology bias and the instrumental background bias (see Chapter 4). The topology bias causes the measured response to be between 0.5%-1% low and is constant as a function of jet energy (Figure 4.3).

The instrumental background bias is measured by comparing the nominal response to the response derived after applying tighter photon selection criteria. Figure 6.22 shows the nominal response divided by the response curve after applying the tighter H-matrix χ^2 cut. Figure 6.22 shows a constant bias of approximately 0.7% towards a higher response due to instrumental background.

It is difficult to accurately measure and apply a correction to each bias. Since the two effects approximately cancel each other, we do not correct but incorporate a 0.5% error to account for the residual bias.

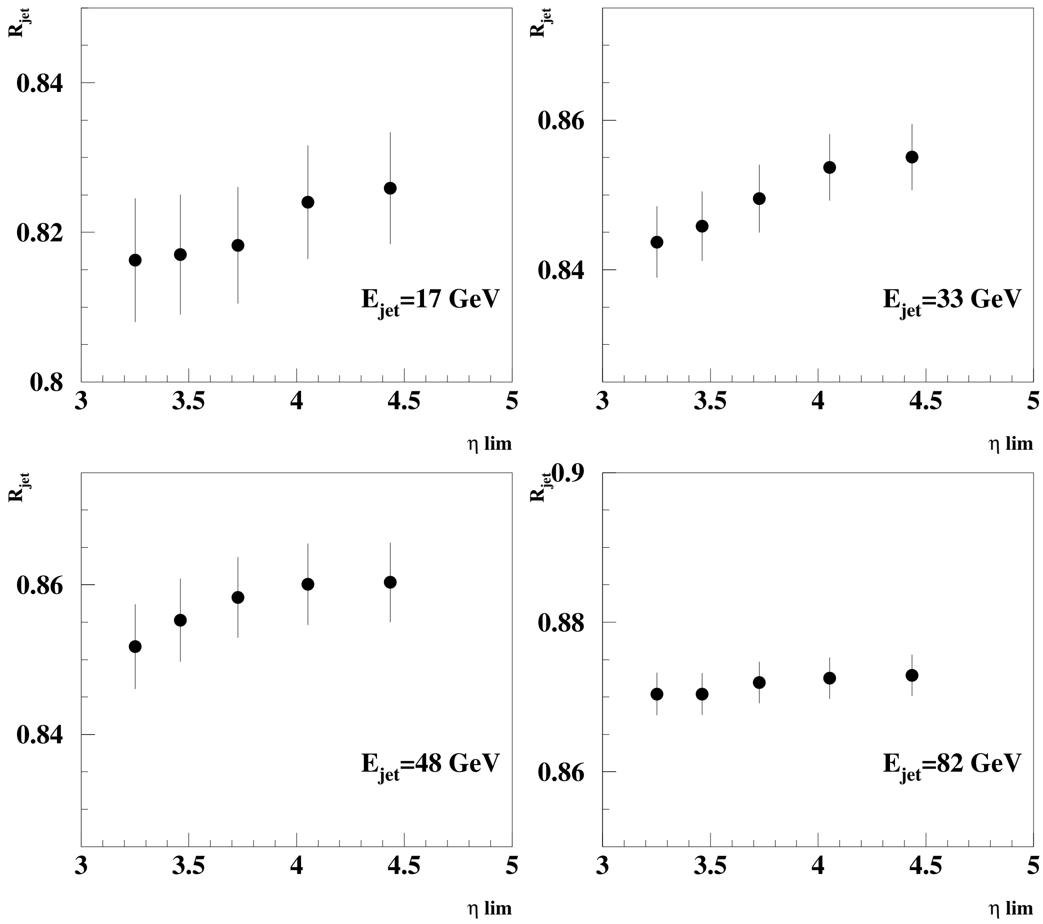

Figure 6.19: R_{jet} in the CC as a function of $\eta_{\rm lim}$.

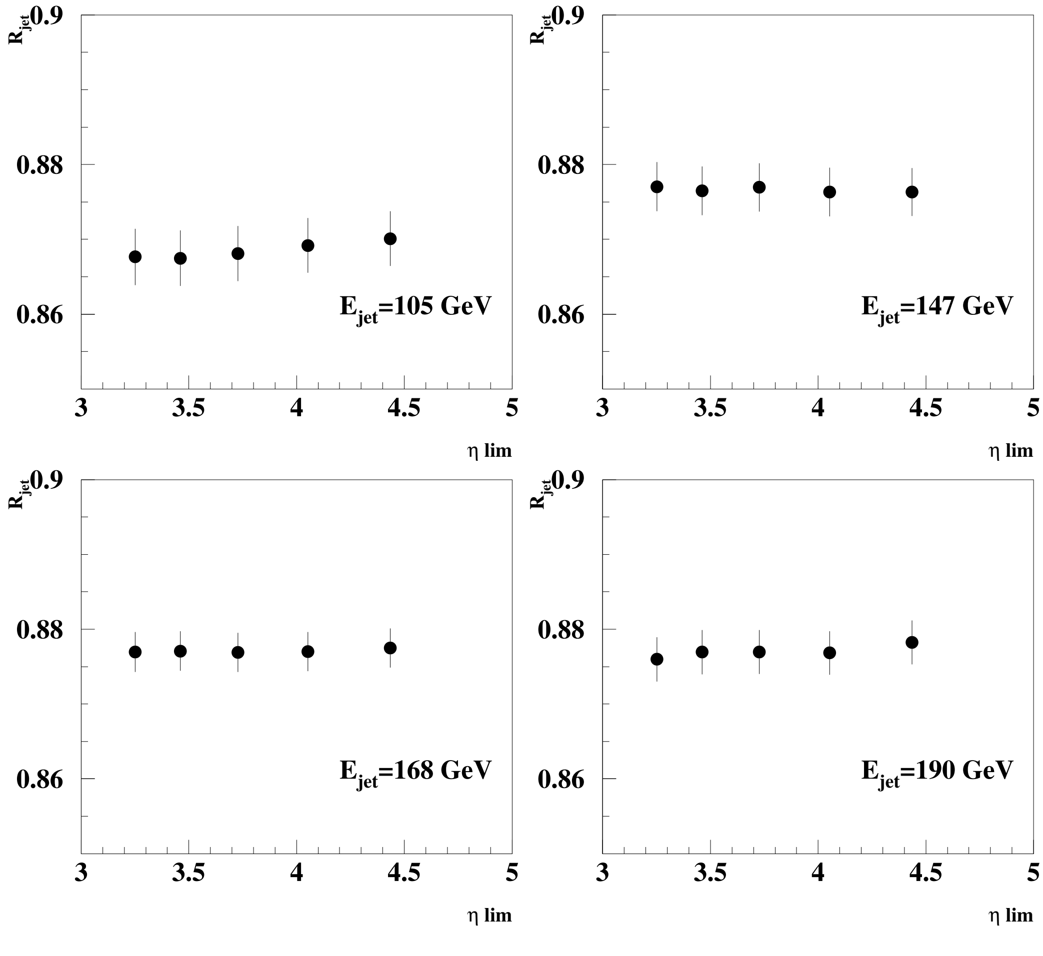

Figure 6.20: R_{jet} in the CC as a function of $\eta_{\rm lim}$.

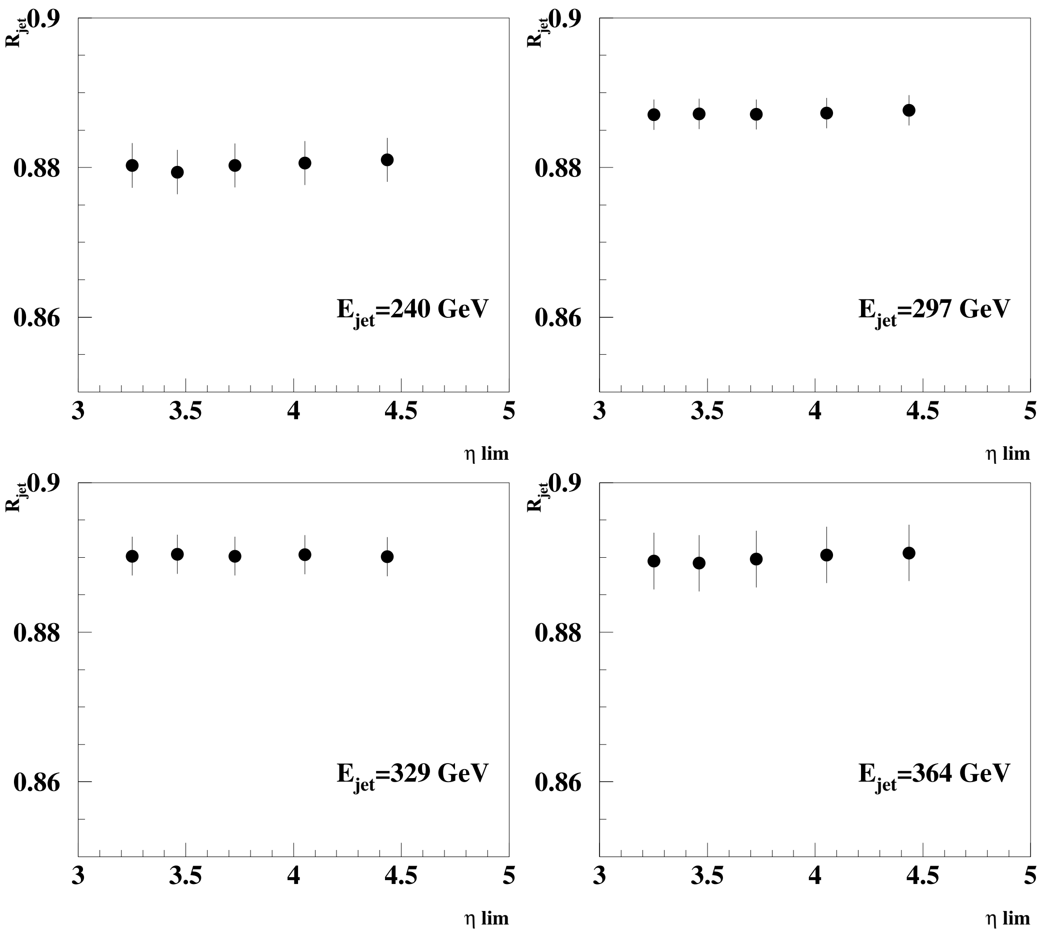

Figure 6.21: R_{jet} in the CC as a function of $\eta_{\rm lim}$.

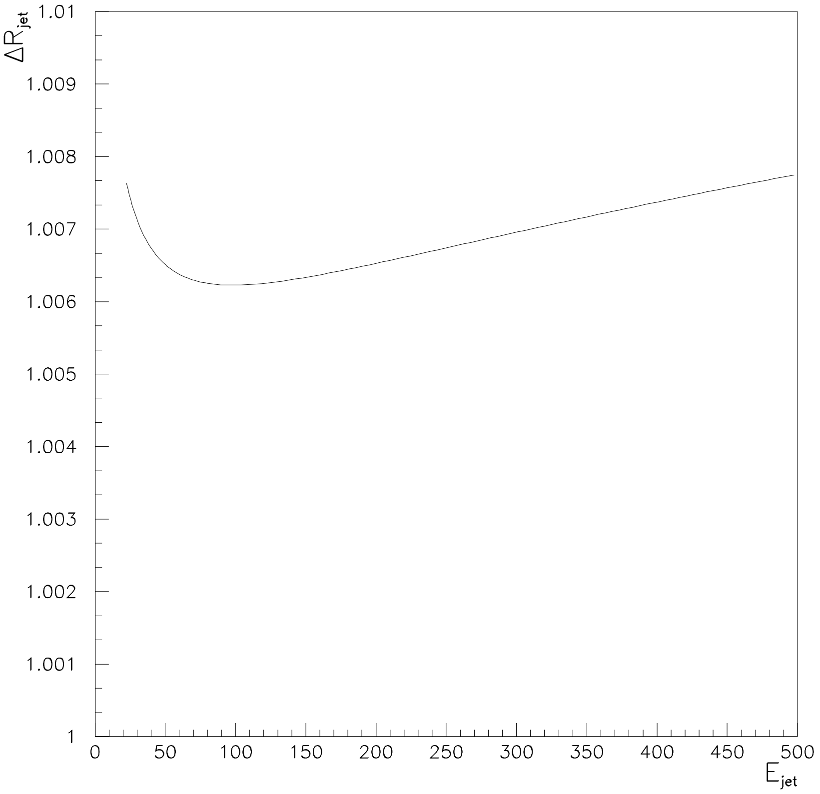

Figure 6.22: Energy dependence of the ratio of the nominal response to the response after applying tighter photon quality cuts.

6.10 Jet Width in γ-jet and Inclusive Jet Samples

The jet energy response is strongly dependent on the jet width, W_{jet}, as mentioned in Chapter 5. The average jet width, as well as its dependence on energy, is virtually identical in the γ-jet sample and in the inclusive jet sample. Therefore, the response measured from the former sample is quite representative for an average jet at DØ. However, before using the jet scale correction on a particular sub-sample, it is important to check its average jet width against the same quantity in the γ-jet sample. Additional corrections might be needed if there were significant differences.

The average width of 0.7 cone jets in the γ-jet sample is binned in terms of E', mapped onto E_{jet}^{meas} and plotted for both the CC and the EC in Figure 6.23a. There is an increase of W_{jet} with η due to finer segmentation in physical space. Since we want to compare the average width of the CC jets in the jets sample with the same quantity in the sample used for the R_{jet} measurement, we need to normalize the EC width to the CC width before verification against the jet sample. Figure 6.23b shows the same quantities as Figure 6.23a after the EC points are normalized to the CC points. Figure 6.23c also includes W_{jet} versus E_{jet}^{meas} from the Run Ia 0.7 cone jet sample. Above 70 GeV, the jet data were obtained from the different jet triggers above the threshold of full efficiency and show that W_{jet} in the inclusive jet sample is in excellent agreement with W_{jet} in the γ-jet sample. For energies below 70 GeV, we used width information from the highest threshold triggers, which are all in agreement with each other and the γ-jet data. High E_T threshold triggers populate the low energy range with soft jets, which are not biased. It is the width of the leading jets that could be biased, since these jets are likely to have fired the trigger. The only fully efficient trigger in that low energy range is JET_MIN, which gives average jet widths greater than those from the γ-jet sample. This is because JET_MIN has a low jet E_T threshold (20 GeV) and is more likely to fire on events that fluctuated to noise levels higher than average. The current definition of W_{jet} (see Chapter 5) allows a small amount of energy in the edge of the jet to produce a large change in the width. On the other hand, the shift in the energy scale would be small. The effect of the offset in the jet width has been studied using different cone size algorithms. The width differences observed between the γ-jet and jet samples vanish for smaller cones, which are less sensitive to noise fluctuations. Triggers other than JET_MIN give excellent agreement with each other above and well below the trigger efficiency threshold. A small bias towards a higher width is observed in the vicinity below the thresholds.

Figure 6.24a compares the width in the γ-jet sample with the width in the Run Ib inclusive jet sample with no luminosity or multiple interaction cuts. A significant deviation towards higher values is observed in the jet sample at low energies, even if only non-leading jets from high E_T threshold triggers are included. The difference between Run Ia and Run Ib results is due to the higher instantaneous luminosity average in the Ib data, as is clearly illustrated in Figure 6.24b, which includes cuts on instantaneous luminosity and MITOOL. This increase in the width for high luminosity events does not affect the jet energy scale, since it comes from energy deposited by extra interactions, which is subtracted.

The raw jet width as defined in the current DØ reconstruction algorithm is not a good variable to be used to parametrize the jet energy response, since not all contributions to the width are associated with a change in the energy scale. Jet width should be corrected for spurious contributions before doing any quantitative study of the response dependence on this variable. The alternative would be to change the definition of jet width. For example, the σ of a gaussian fit to the jet energy density profile would be a better definition. In any case, the plots included in this section and Chapter 5 are a reasonable guide to estimate response changes in samples with average widths significantly different from the average in the γ-jet sample.

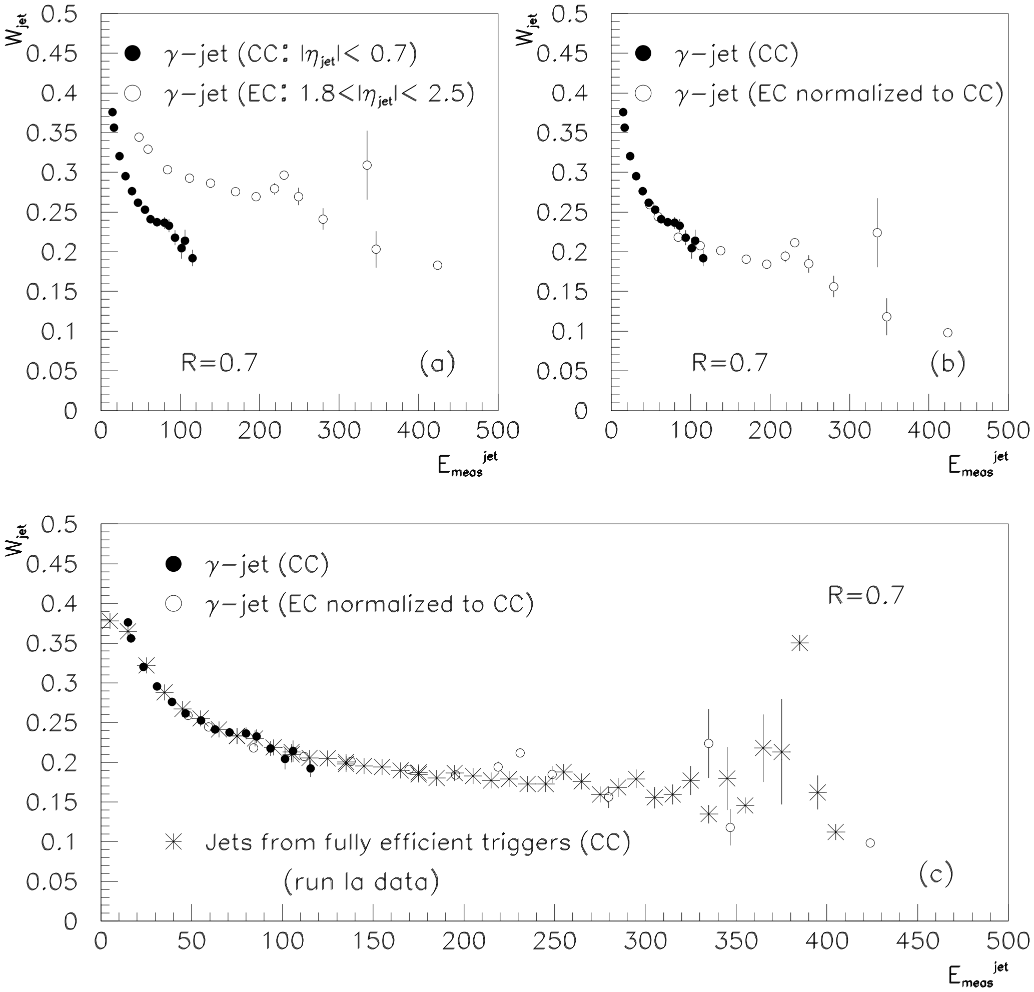

Figure 6.23: a) Average jet width in the CC and the EC in the γ-jet sample. b) Same as top left but EC width is normalized to CC. c) Jet width in the γ-jet sample compared with the same quantity in the Run Ia inclusive jet sample.

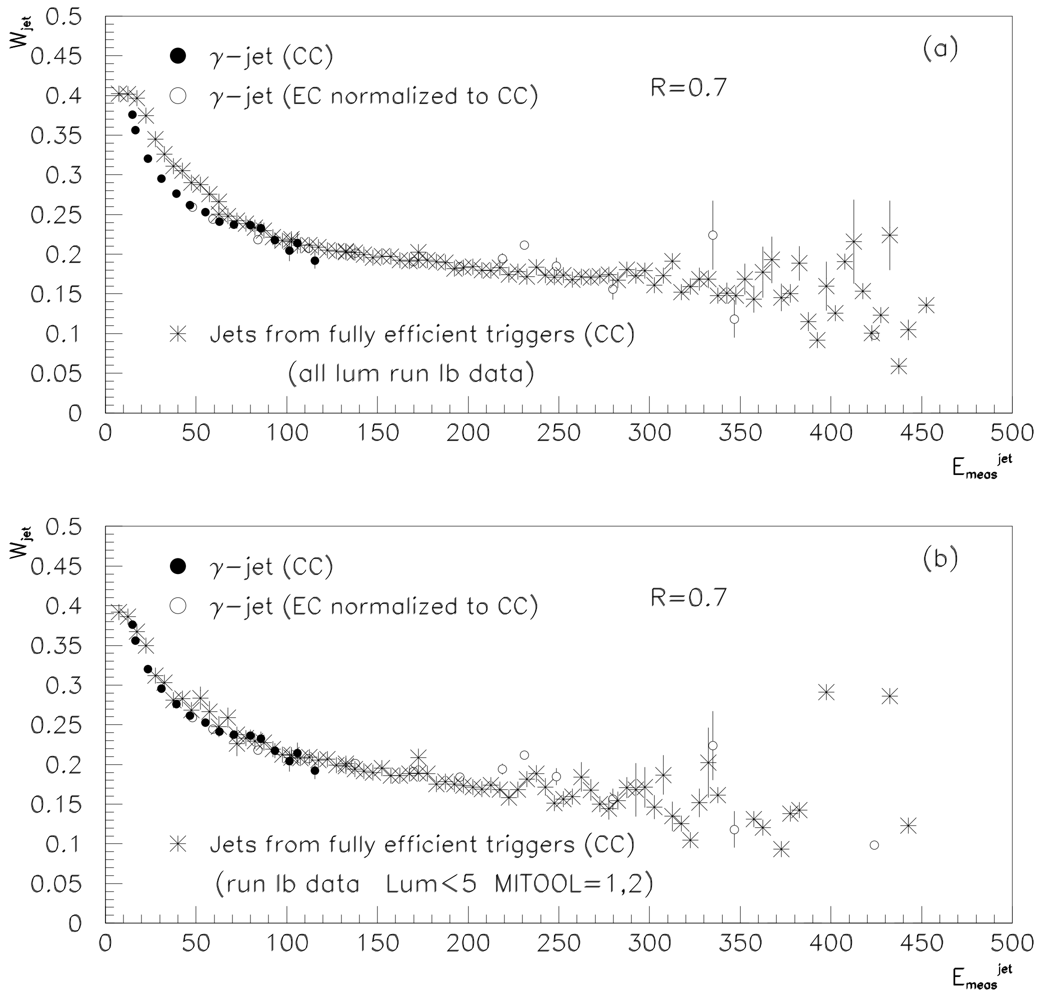

Figure 6.24: a) Average jet width in the γ-jet sample compared with the same quantity in the Run Ib inclusive jet sample. b) Same as top plot with the addition of luminosity and MITOOL cuts.

Chapter 7

Showering Correction

The jet energy correction ideally should scale the jet energy from the reconstruction level to the particle level. As the collimated beam of particles strikes the detector, it interacts with the calorimeter material producing a wide shower of more particles. Some particles produced inside (outside) the cone deposit a fraction of their energy outside (inside) the cone as the shower develops inside the calorimeter. The showering correction is the last correction applied and compensates for the net energy flow through the cone boundary during calorimeter showering.

The correction is derived using jet energy density profiles from data and particle level HERWIG [18] Monte Carlo. In principle, it is not possible to determine the showering effect directly from calorimeter data by measuring the amount of energy left outside the cone that defines the jet. That energy may be associated with gluon emission or fragmentation outside the cone at the particle level ("physics out-of-cone"). The energy may not even be related to the hard scattering but to the underlying event, noise or pile-up. A large fraction of the spurious energy may be removed by applying cuts on the number of jets and luminosity, and applying a physics out-of-cone correction based on particle level Monte Carlo. Thus, the showering correction can be determined by subtracting the physics out-of-cone (particle level Monte Carlo) from the total out-of-cone (data).

7.1 Sample Selection

The data are events from QCD jet triggers reconstructed with RECO V12.13 or higher. Other RECO versions did not include the necessary cell information in the DST (Data Summary Tape) data files. Most of the sample is associated with the low E_T triggers (JET_30). Its average instantaneous luminosity is $\mathcal{L} \sim 4 \times 10^{30}$ cm^{-1} sec^{-1}. The correction is derived in different pseudorapidity regions for the four cone sizes: 1.0, 0.7, 0.5, 0.3. Several cuts are applied to remove spurious energy:

- Events are rejected if the beam of the Main Ring accelerator passes DØ in coincidence with a Tevatron crossing.
- Events flagged by the AIDA routine are vetoed.
- One and only one vertex is required.
- The z coordinate of the interaction vertex must satisfy $|z| < 100$ cm.
- Two and only two jets are required in the event.

- The standard jet quality cuts described in Chapter 4, and the $\not{E}_T/E_T^{lead}$ <0.7 cut are applied (E_T^{lead} corresponds to the highest E_T jet in the event). The event is vetoed if at least one jet does not pass at least one of the cuts.

- Split and merged jets are removed.

7.2 Method

The description that follows is based on $\mathcal{R}$ =0.7 jets with $|\eta|$ <0.4. We define sub-jets of increasing cone sizes (0.1 steps) centered around the $(\eta_\circ, \varphi_\circ)$ axis reconstructed with the fixed cone algorithm (see Figure 7.1). The total energy of the sub-jets, $E_{jet}(r)$, is determined as the sum over all cells contained within a sub-cone of radius r, with $r = 0.1, ..., 0.9, 1, ..., 2$. The contribution from the underlying event, uranium noise and pile-up is subtracted.

The total out-of-cone fraction is defined as the fraction of the energy of the cluster deposited outside the algorithm cone and inside a larger cone taken as the limits of the cluster. From data, we measure F_{tot}, which is the ratio of the total energy of the cluster and the energy contained in the algorithm cone:

$$F_{tot} = \frac{E_{jet}(r < 1)}{E_{jet}(r < 0.7)}\,.$$

This definition assumes the cluster does not extend beyond the $r = 1$ limit. The angular area covered by the shower is approximately constant as we move forward. However, η space shrinks towards the beam pipe. Therefore, the cluster boundary is not the same for all pseudorapidity bins. For $|\eta| < 0.4$, we choose the limit at $r = 1$; for $0.4 < |\eta| < 0.8$ and $0.8 < |\eta| < 1.2$, the limit is $r = 1.2$; for $1.2 < |\eta| < 1.6$ and $1.6 < |\eta| < 2$, $r = 1.4$; for $2 < |\eta| < 2.5$ and $2.5 < |\eta| < 3$, $r = 1.6$. In the central region, Test Beam single hadron measurements show that hadrons deposit more than 99.5% of their energy inside a 0.4 cone, equivalent to $\sim 20^\circ$ in the polar direction. A 0.3 cone contains approximately 90% of the total jet energy. Therefore, a 0.7 cone should contain the total energy associated with particles emitted inside a 0.3 cone. That means that outside a 0.7 cone we would find less than 10% of the showering loss of a 0.7 cone jet. A limit of $r = 1$ is a reasonable choice for a central jet. As we move forward, the limit is chosen using the latter criteria or at the r point where the energy density becomes constant, whichever comes first.

The F_{tot} factor includes both the showering loss and the physics out-of-cone. The latter, expressed as F_{phy}, is obtained in the same way as F_{tot} from a HERWIG particle level jet sample reconstructed with the 0.7 cone algorithm. The number of jets required is two and only two per event and no split or merged jets are allowed. The events are generated at the geometrical center of the detector, and the underlying event is not modelled.

The showering correction factor F_{sho} is a multiplicative factor defined as:

$$F_{sho} = \frac{E_{jet}(r < 0.7) + E_{sho}}{E_{jet}(r < 0.7)}\,,$$

where E_{sho} is the amount of energy associated with particles emitted inside the cone at the particle level, but deposited outside the cone in an annulus defined by r >0.7 and r <1 at the calorimeter level. In the same way, we can write F_{tot} and F_{phy} as:

$$F_{tot} = \frac{E_{jet}(r < 0.7) + E_{phy}(r > 0.7) + E_{sho}}{E_{jet}(r < 0.7)}\,,$$

$$F_{phy} = \frac{E_{jet}(r < 0.7) + E_{phy}(r > 0.7)}{E_{jet}(r < 0.7)}\,,$$

where E_{phy} is the energy associated with the "physics" out-of-cone. If we add and subtract both $E_{jet}(r < 0.7)$ and $E_{phy}(r > 0.7)$ in the numerator of the expression for F_{sho}, we can express this factor in terms of F_{tot} and F_{phy}:

$$F_{sho} = F_{tot} - F_{phy} + 1 .$$

In this analysis, we measure $R_{cone} = \frac{1}{F_{sho}}$, which is the fraction of the shower contained in the $\mathcal{R}$=0.7 cone. This quantity is parametrized as a function of E_{jet}, where E_{jet} includes the offset, η dependent and response corrections.

This method can be used in every pseudorapidity region and for every cone size. Furthermore, it relies, at least in part, upon the real data jet shapes. Among the drawbacks of the method is the fact that it is sensitive to the difference between the data and the Monte Carlo energy density profiles. HERWIG jets are narrower than real jets [30], and this biases the measurement towards a larger F_{sho}. In addition, the ratio is measured from uncorrected energy because the response correction is not performed at the cell level. Since the average energy of single particles is higher in the core of the jet than at the edge, the calorimeter response to E_{sho} is lower than to $E_{jet}(r < 0.7)$. Therefore, F_{sho} is biased towards a lower value. The cuts also remove split and merged jets, which are present in most of the jet samples used in physics analyses. Additional jets in the event (more than two), could also leak energy inside the two leading jets, compensating a fraction of their showering loss.

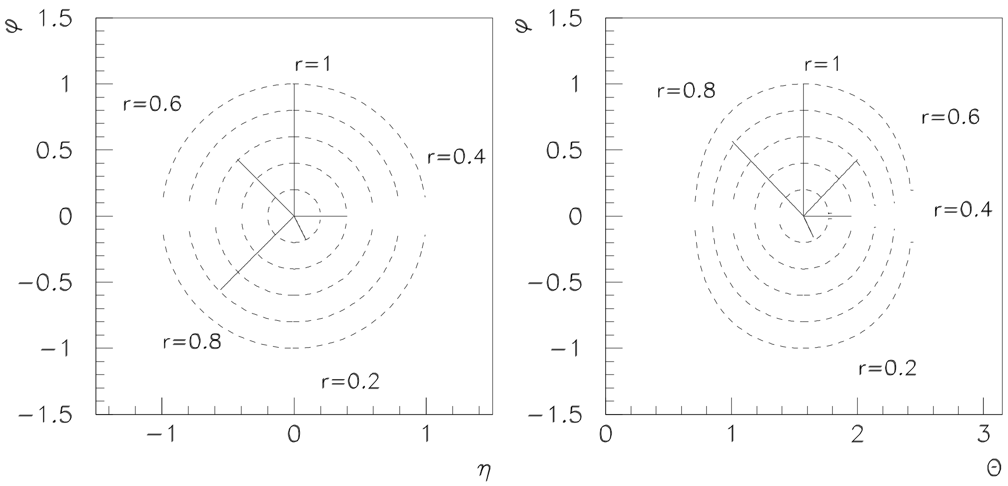

Figure 7.1: Illustration on jet cones in $\eta - \varphi$ and $\theta - \varphi$ space. The jet area is constant and limited by a circumference in $\eta - \varphi$ space, but it is θ dependent in $\theta - \varphi$ space (it shrinks towards the beam direction, $\theta \to 0$).

7.3 Results and Discussion

One of the most important sources of uncertainty is the difference in jet shapes between the data and the Monte Carlo. This effect is studied using HERWIG jet events processed through GEANT (mixture level). The energy density versus the $\eta - \varphi$ distance to the jet centroid is determined for this Monte Carlo sample and compared with the data measurement. In both samples, jets are reconstructed with a $\mathcal{R}$ =1 cone algorithm. Fiducial cuts are applied on the jet pseudorapidity ($|\eta|$ <0.2) and corrected transverse energy (45< E_T <70 GeV). The average jet energy inside the $\mathcal{R}$ =1 cone is 44.2 GeV for the Monte Carlo and 44.6 GeV for the data. These averages are less than 45 GeV because they are obtained by integration of the energy density plots, which are not corrected for jet scale.

Figure 7.2 shows a comparison between data and Monte Carlo energy density profiles. Underlying event or noise are not modelled in the Monte Carlo sample. Instead, the data includes the contributions of underlying event, noise, pile-up and extra $p\bar{p}$ interactions. There is an energy baseline ("physics baseline") that remains in the Monte Carlo, even far from the jet centroid. These particles in between the two jets are presumably a manifestation of the color interaction between two leading E_T outgoing partons. Figure 7.3 shows the same comparison as Figure 7.2 after the data density profile is normalized to the Monte Carlo profile. This normalization is only an approximation to the offset correction, since the latest is an η dependent subtraction. After the normalization, the two samples are on the same footing, except that the average jet energy is lower in the data. In Figure 7.4, both the Monte Carlo and data distributions are normalized to zero at r =1 in order to facilitate a shape comparison of the density profiles. The resulting average energies are 35.2 GeV in the data and 40.1 GeV in the Monte Carlo, and the shape of the distributions are in good agreement as shown in Table 7.1.

Table 7.1: Percentage of the jet energy inside a sub-cone of radius r, for jets reconstructed with a $\mathcal{R}$ =1 cone algorithm. Both the data and the Monte Carlo densities are normalized to zero at r =1.

	r <1	r <0.7	r <0.5	r <0.3
Data	100%	96.7%	91.2%	77.6%
MC	100%	97.2%	91.4%	75.1%

The fraction of the energy inside a sub-cone of radius r depends on the algorithm cone size. Table 7.1 shows that, after the baseline is subtracted, a 3.3% of the cluster energy is outside an r =1 cone measured from the jet centroid. However, this fraction is smaller for jets reconstructed with smaller algorithm cones. This is illustrated in Figure 7.5, which shows a comparison of jet energy density profiles measured with respect to the jet centroids obtained from the different algorithms.

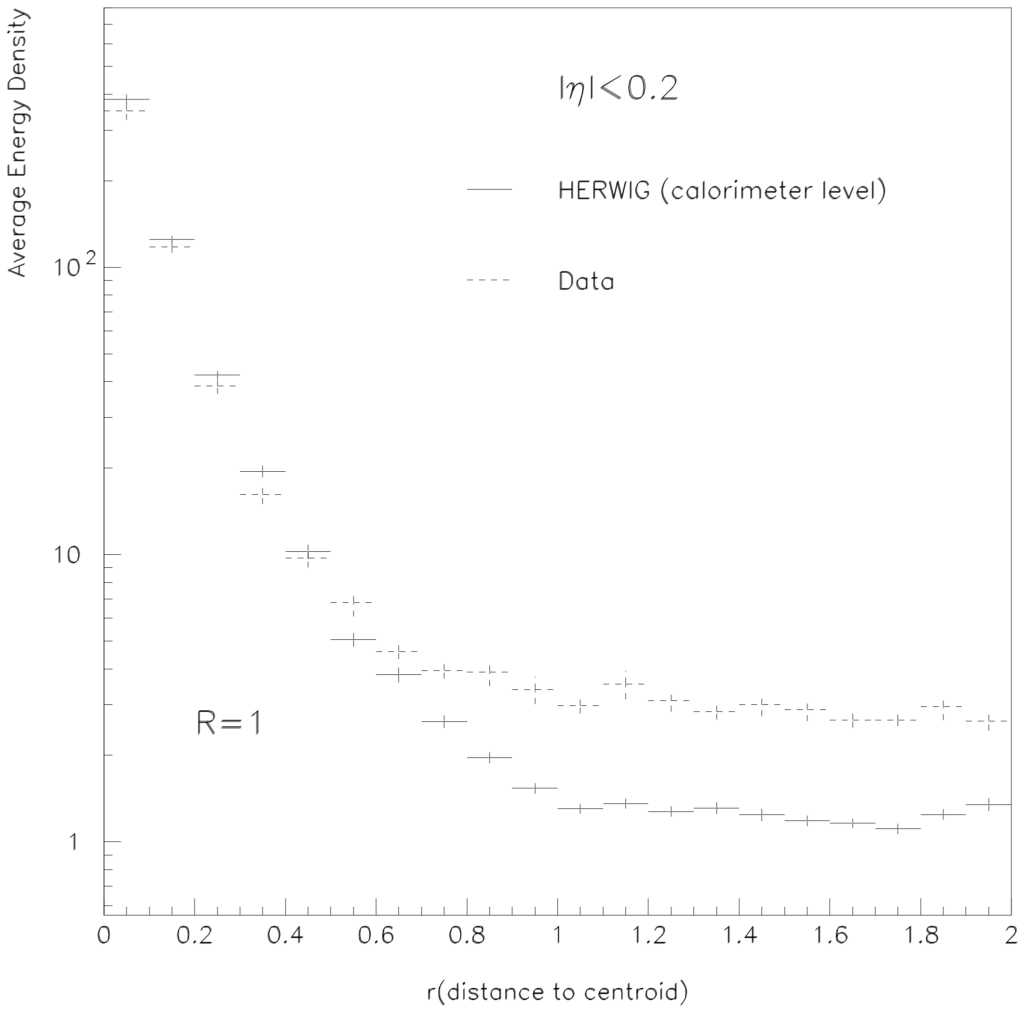

Figure 7.2: Comparison between data and Monte Carlo energy density profiles. Underlying event or noise are not modelled in the Monte Carlo sample.

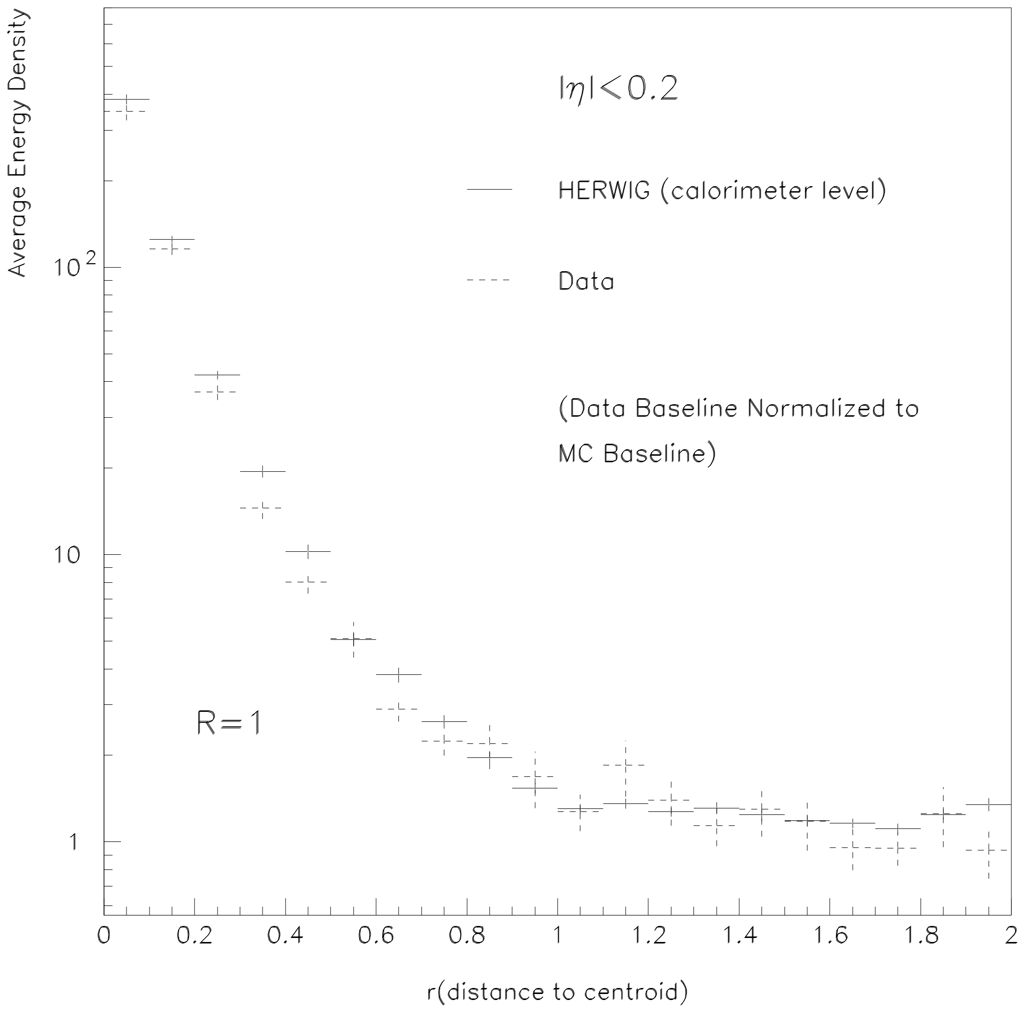

Figure 7.3: Comparison between data and Monte Carlo energy density profiles. The data profile is normalized to the Monte Carlo profile at r =1.

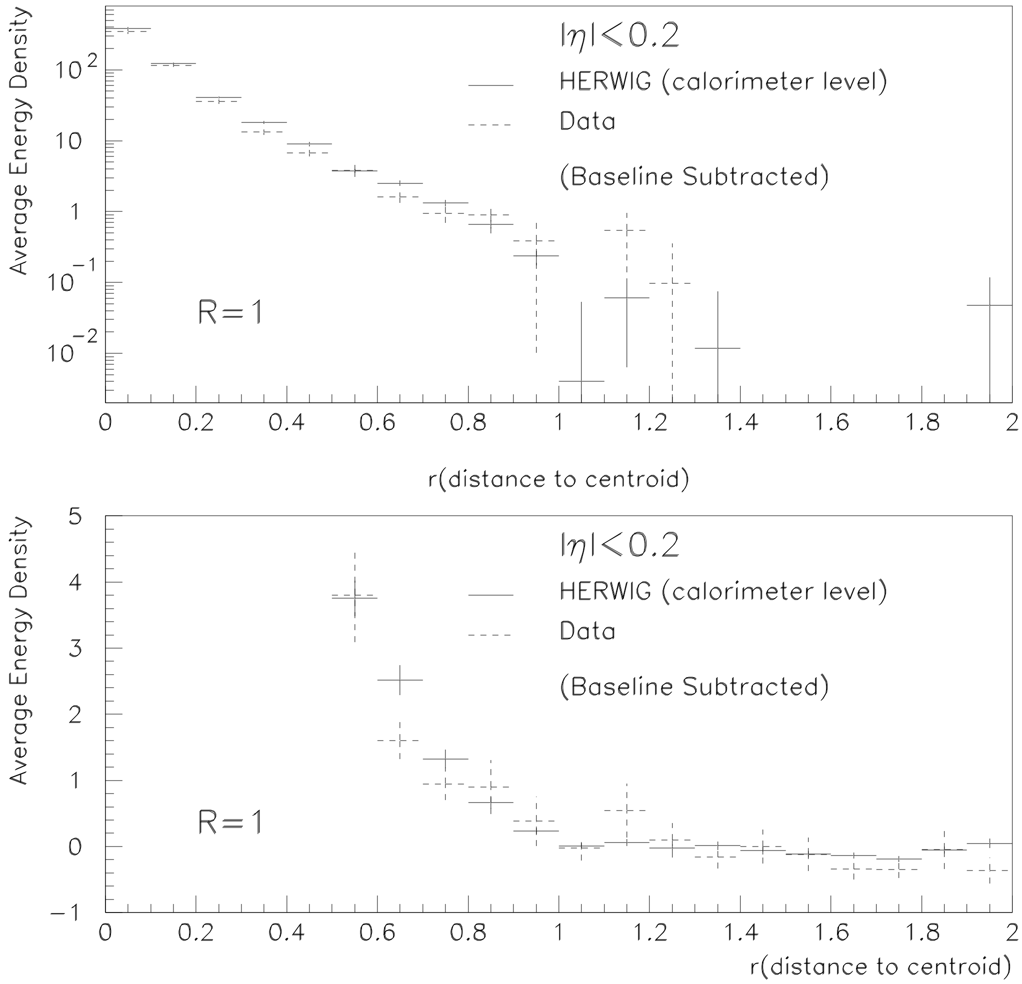

Figure 7.4: Comparison between data and Monte Carlo energy density profiles. Both distributions are normalized to zero at r =1.

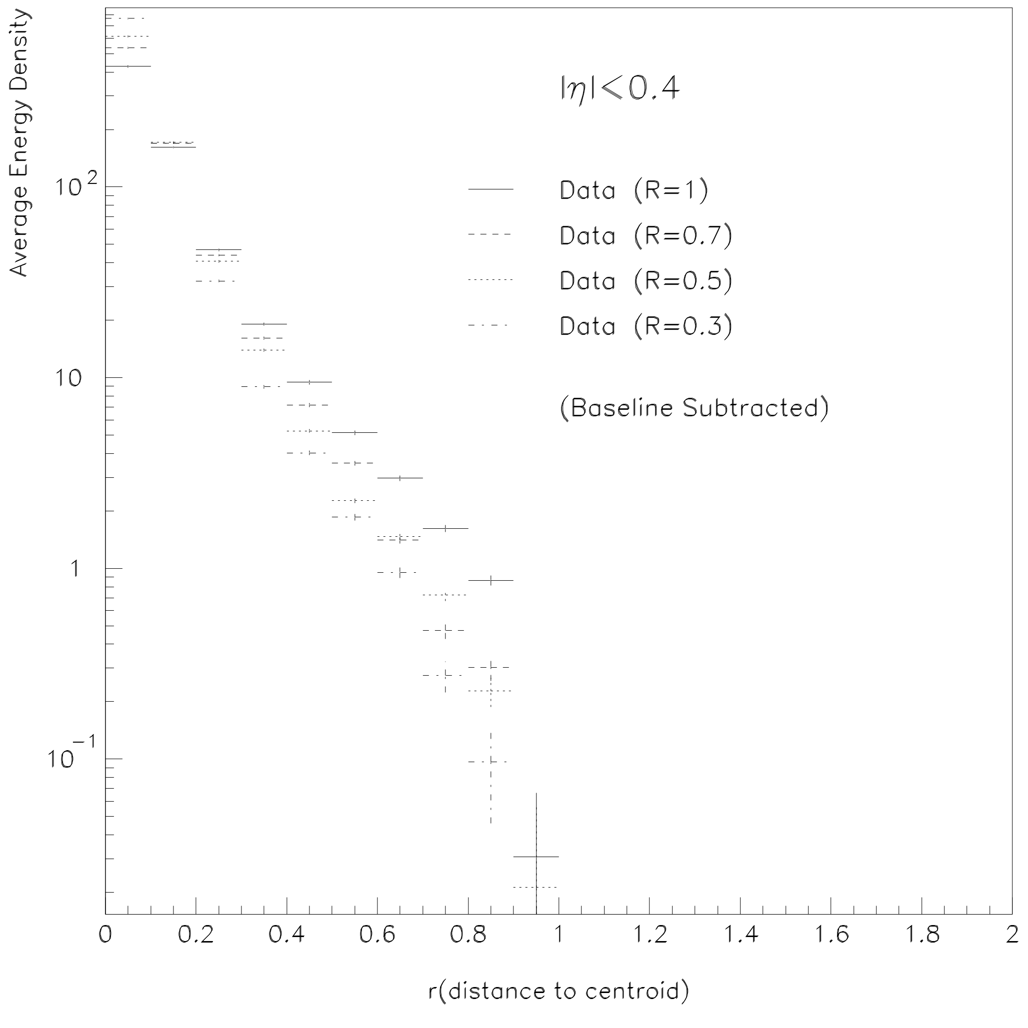

Figure 7.5: Comparison of jet energy density profiles measured with respect to the jet centroids reconstructed with the fixed cone algorithm but different cone sizes.

In order to derive the showering correction, the η dependent offset is subtracted from the data profiles. The remaining "physics baseline" constitutes one of the most important sources of systematic uncertainty at low energies, where even small differences between the data and the Monte Carlo can give a large bias. As the best solution to avoid this bias, we have subtracted, both in the data and in the particle level Monte Carlo, a uniform energy density measured at the jet limit. This subtraction plus the offset correction are still a source of error that affects the low energy range in the case of large cone algorithms and very forward regions. The energy of the "physics baseline" within the algorithm cone is part of the jet, since it is associated with the hadronization process following the hard collision. Therefore, we can subtract this energy in the showering correction derivation to minimize systematic biases, but it must not be subtracted in a jet shapes analysis involving comparisons with theory.

Figure 7.6 shows F_{tot} and F_{phy} separately and R_{cone} for 0.7 cone jets in the first central region $|\eta| < 0.4$. Figures 7.7- 7.14 show R_{cone} versus E_{jet} for all cone sizes and rapidities. The solid curves are fits to the data and the dashed lines are parametrizations to R_{cone} versus E_{Tjet} (replace E_{jet} by E_{Tjet} in the abscissa). The dotted error bands account for the different systematics, as well as for the choice of the fit function and energy range. At high energies, the total uncertainty is 1%-3.5% (2.5%-5%) in the central-forward regions for 0.7 (0.3) cone jets. At low energies, the errors increase to 1%-5% (2.5%-10%) in the central-forward regions for 0.7 (0.3) cone jets. The errors at low energy are dominated by the offset and baseline subtraction, and at high energy by poor statistics. Therefore, points below $\sim$ 70 GeV are not generally used in the fits, especially in the case of large cone sizes and large rapidities. Depending on the trend of the data points, R_{cone} versus E_{jet} was fit to a linear $a + b \cdot E_{jet}$, or a logarithmic $a + b \cdot \ln(E_{jet})$ function. All the plots show a trend towards a constant function of E_{jet} at high energies. Therefore, a straight line was fit to the high energy points to determine the high energy correction.

The showering correction is also measured in a HERWIG plus SHOWERLIB γ-jet sample (see Chapter 8). In most of the cases, the Monte Carlo result is consistent with the data measurement. However, the Monte Carlo corrections are systematically smaller than the data corrections, and provide a lower limit to the latter. This is primarily because there is an approximation in SHOWERLIB that truncates the shower development at 95% of the particle energy. Although the energy is then scaled up to compensate for the missing 5%, SHOWERLIB produces narrower jets with a smaller showering loss.

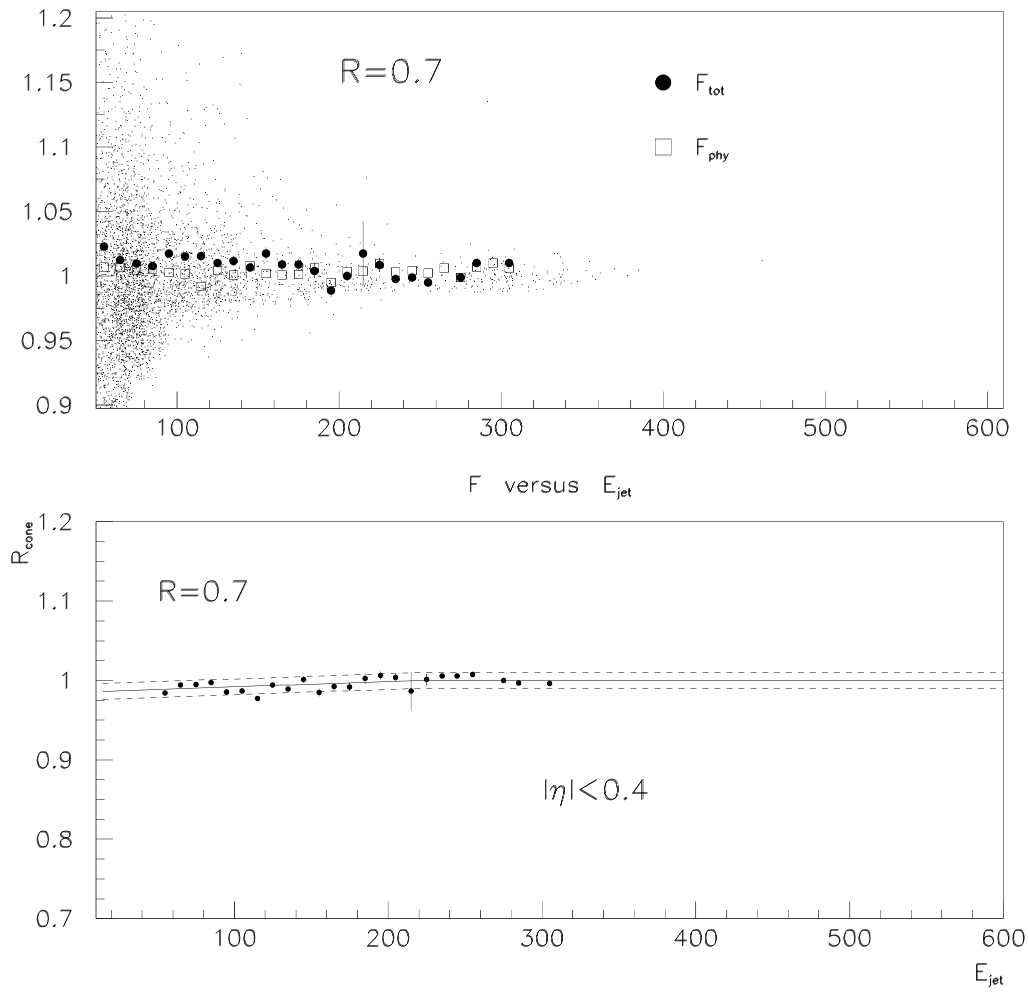

Figure 7.6: Top: F_{tot} and F_{phy} as a function of jet energy (baseline subtracted). Bottom: R_{cone} as a function of jet energy (baseline subtracted).

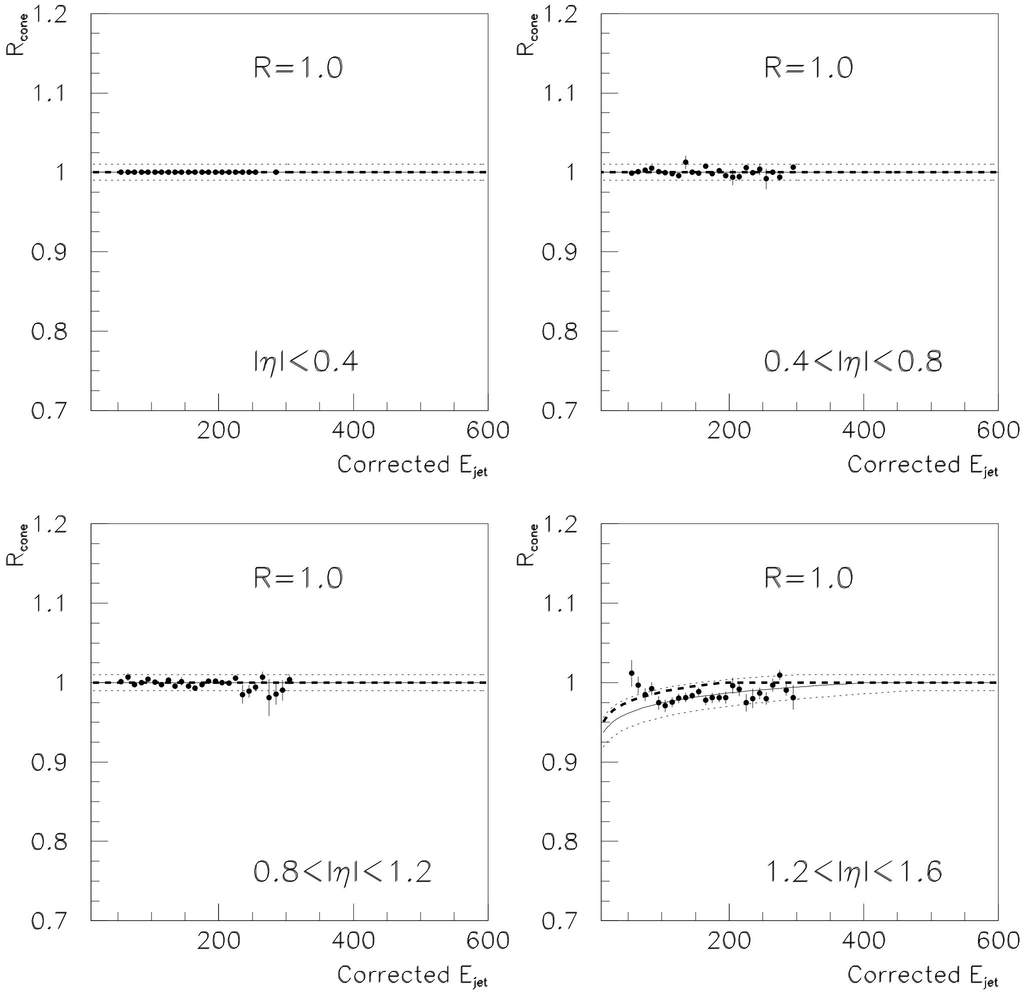

Figure 7.7: R_{cone} versus E_{jet} ($\mathcal{R}$ =1). E_{jet} is corrected by offset and response. The solid line is a fit to the data. The dotted lines show the systematic uncertainty. The dashed line is R_{cone} versus E_{Tjet} (replace E_{jet} by E_{Tjet} in the abscissa).

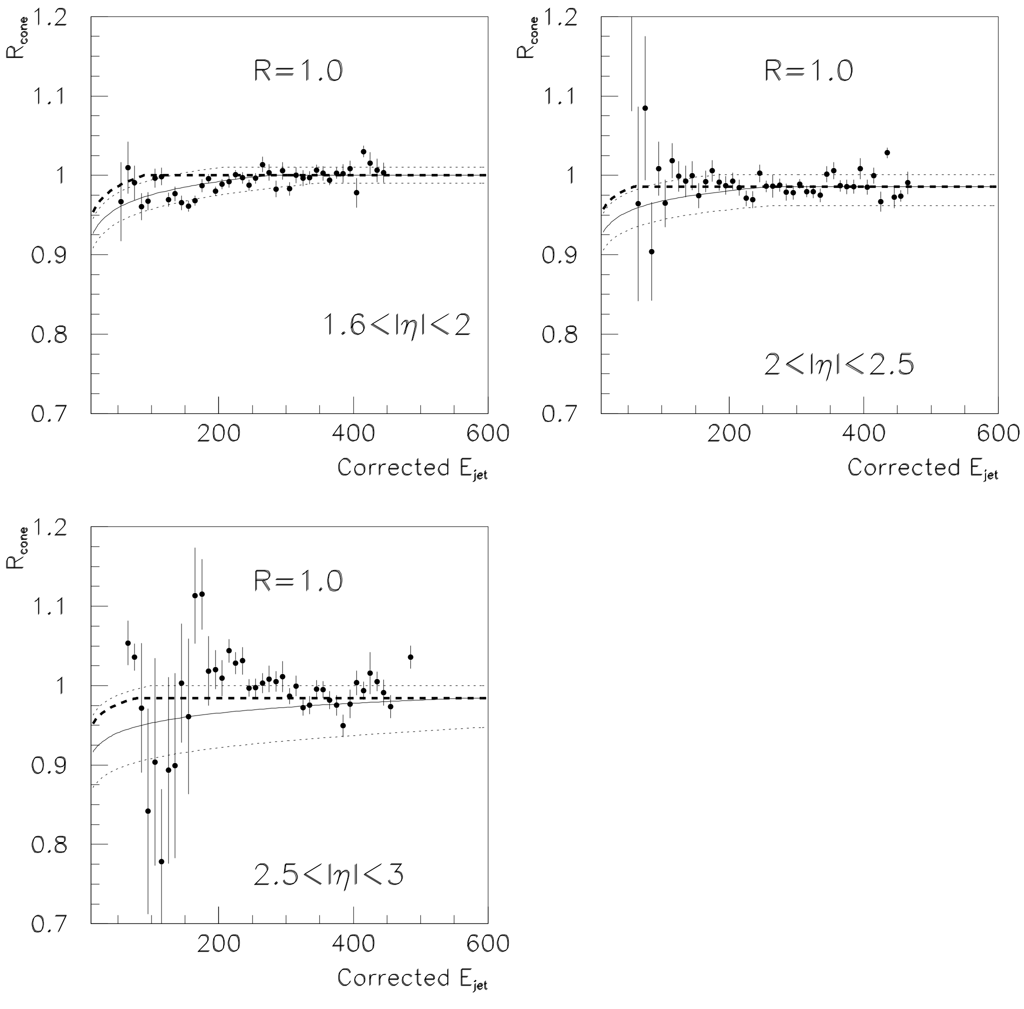

Figure 7.8: R_{cone} versus E_{jet} ($\mathcal{R}$ =1). E_{jet} is corrected by offset and response. The solid line is a fit to the data. The dotted lines show the systematic uncertainty. The dashed line is R_{cone} versus E_{Tjet} (replace E_{jet} by E_{Tjet} in the abscissa).

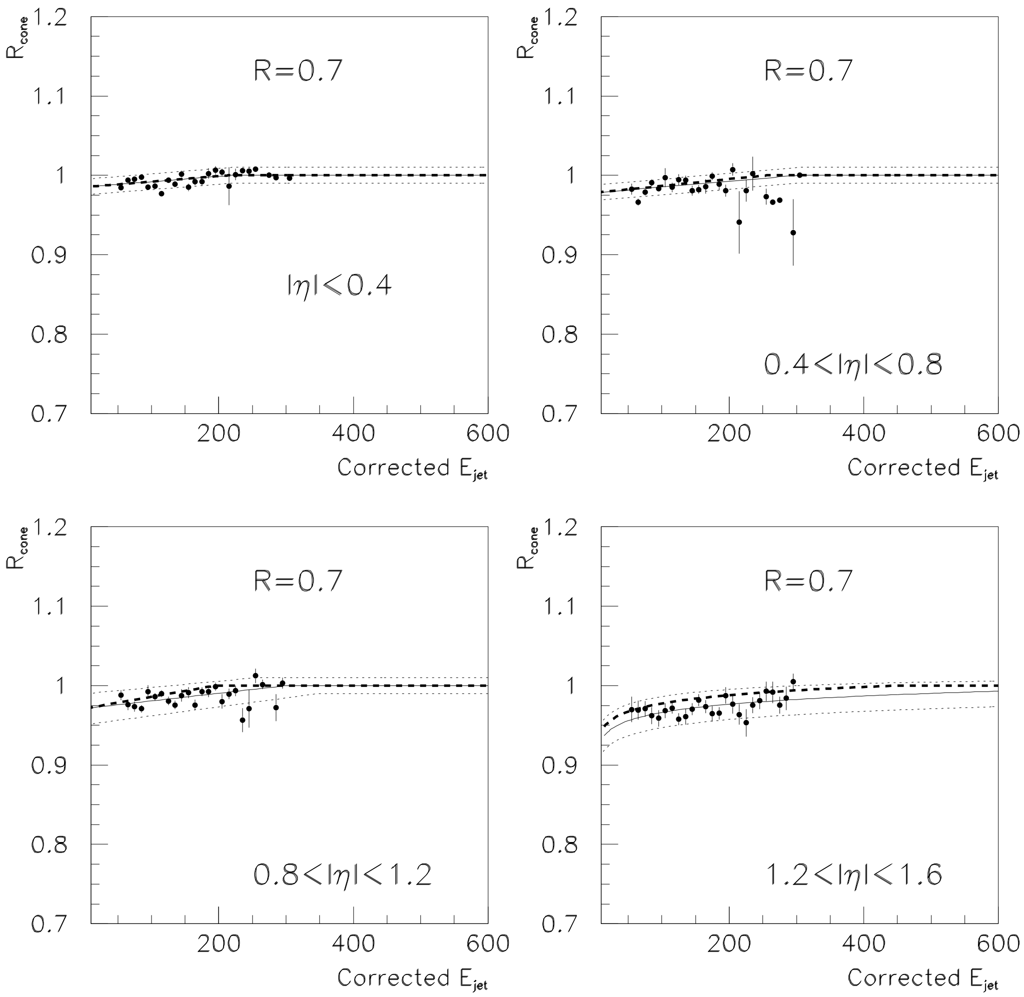

Figure 7.9: R_{cone} versus E_{jet} ($\mathcal{R}$ =0.7). E_{jet} is corrected by offset and response. The solid line is a fit to the data. The dotted lines show the systematic uncertainty. The dashed line is R_{cone} versus E_{Tjet} (replace E_{jet} by E_{Tjet} in the abscissa).

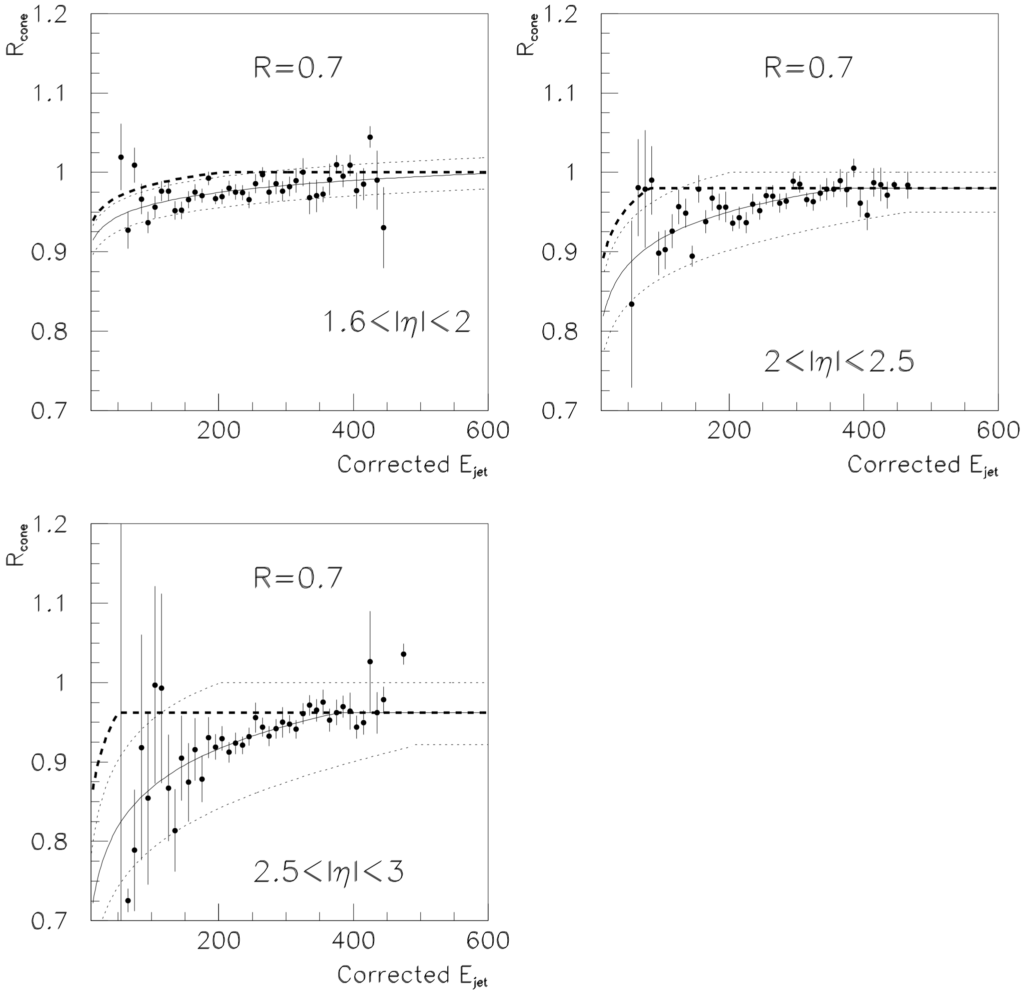

Figure 7.10: R_{cone} versus E_{jet} ($\mathcal{R}$ =0.7). E_{jet} is corrected by offset and response. The solid line is a fit to the data. The dotted lines show the systematic uncertainty. The dashed line is R_{cone} versus E_{Tjet} (replace E_{jet} by E_{Tjet} in the abscissa).

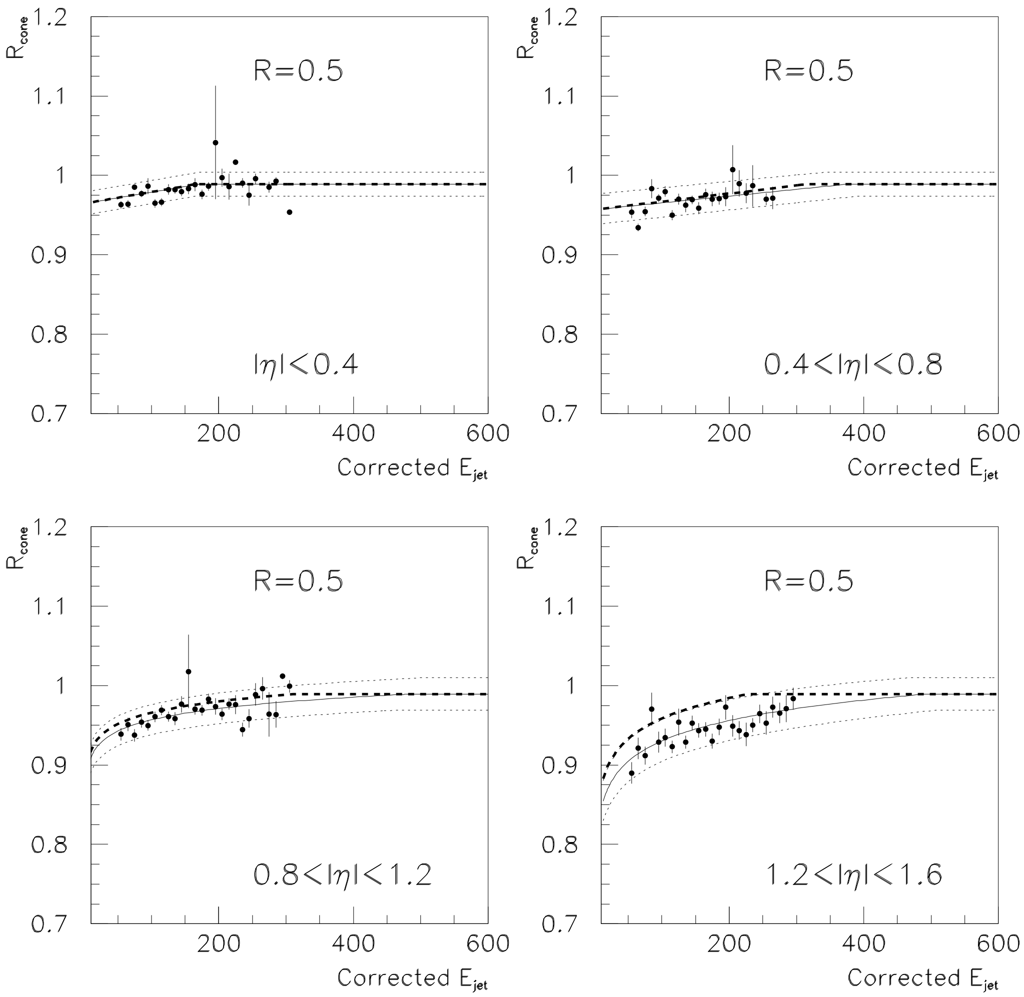

Figure 7.11: R_{cone} versus E_{jet} ($\mathcal{R}$ =0.5). E_{jet} is corrected by offset and response. The solid line is a fit to the data. The dotted lines show the systematic uncertainty. The dashed line is R_{cone} versus $E_{T\,jet}$ (replace E_{jet} by $E_{T\,jet}$ in the abscissa).

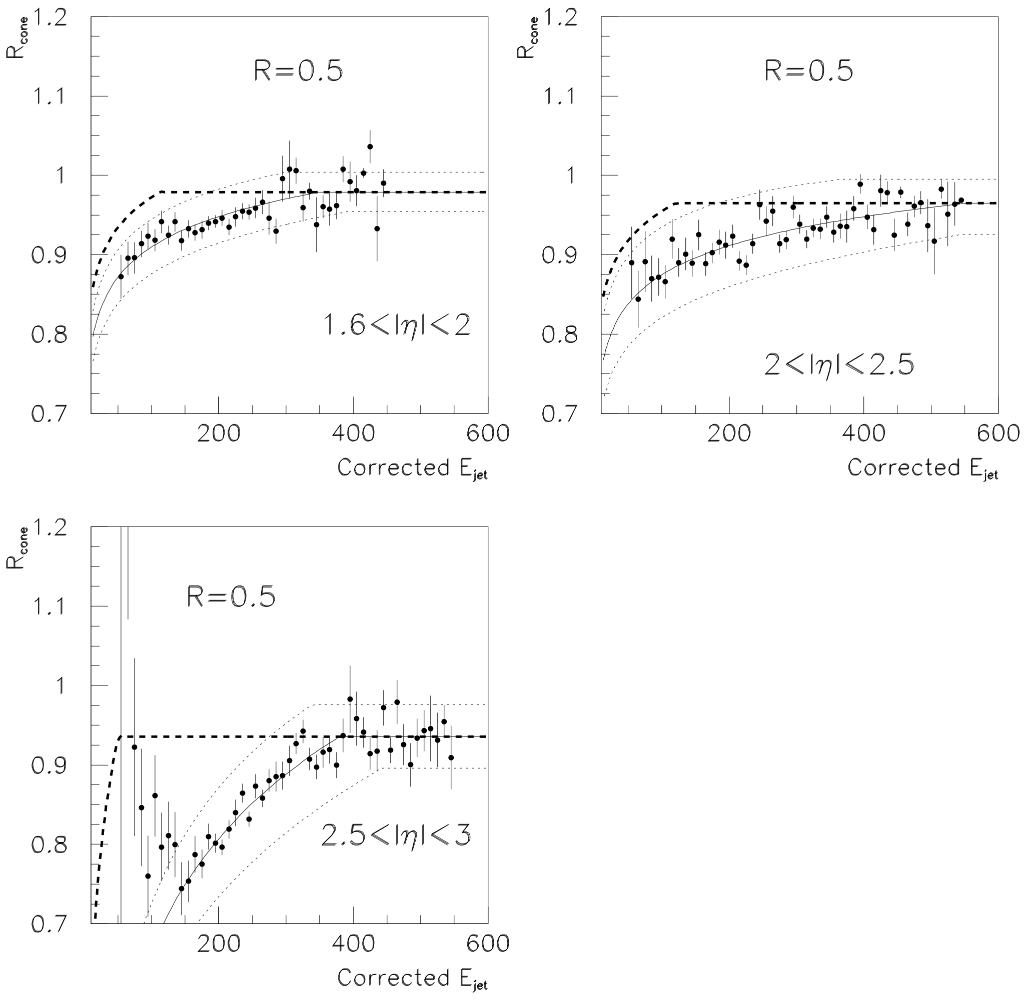

Figure 7.12: R_{cone} versus E_{jet} ($\mathcal{R}$ =0.5). E_{jet} is corrected by offset and response. The solid line is a fit to the data. The dotted lines show the systematic uncertainty. The dashed line is R_{cone} versus E_{Tjet} (replace E_{jet} by E_{Tjet} in the abscissa).

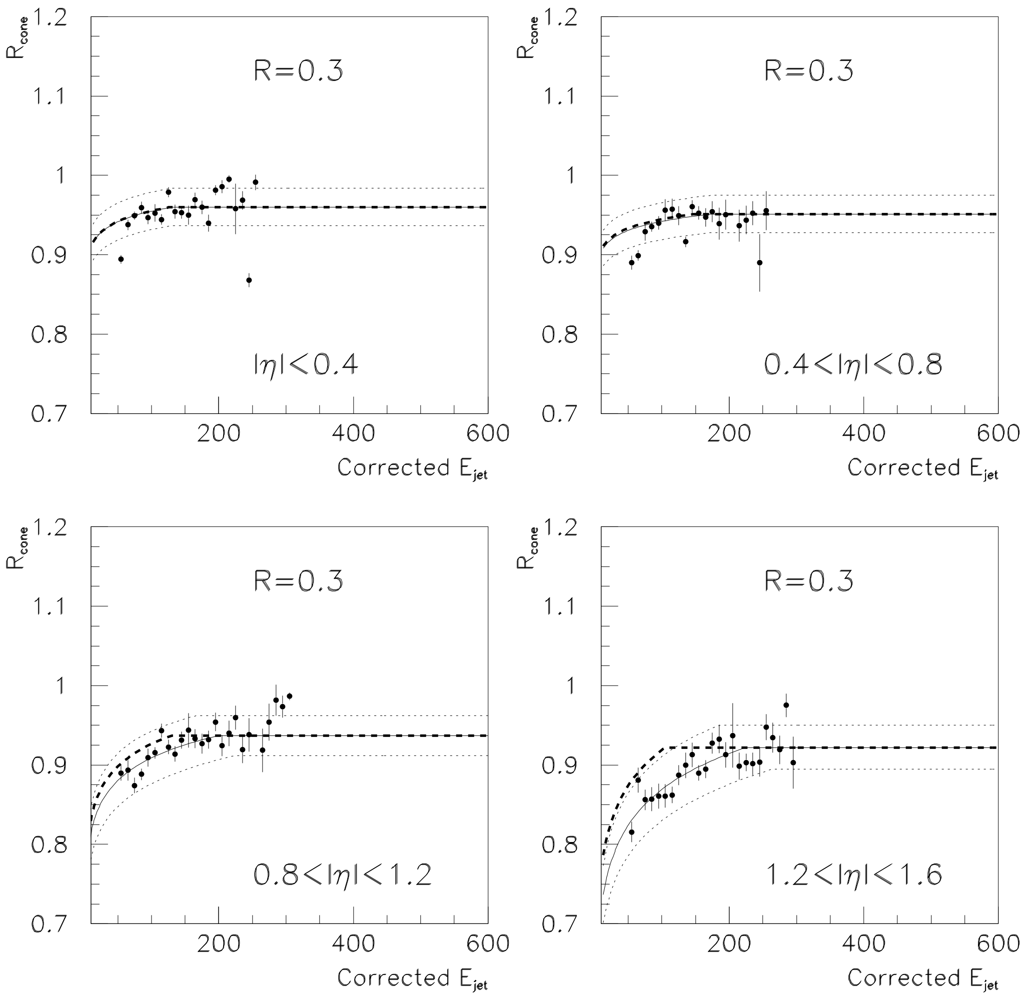

Figure 7.13: R_{cone} versus E_{jet} ($\mathcal{R}$ =0.3). E_{jet} is corrected by offset and response. The solid line is a fit to the data. The dotted lines show the systematic uncertainty. The dashed line is R_{cone} versus $E_{T\,jet}$ (replace E_{jet} by $E_{T\,jet}$ in the abscissa).

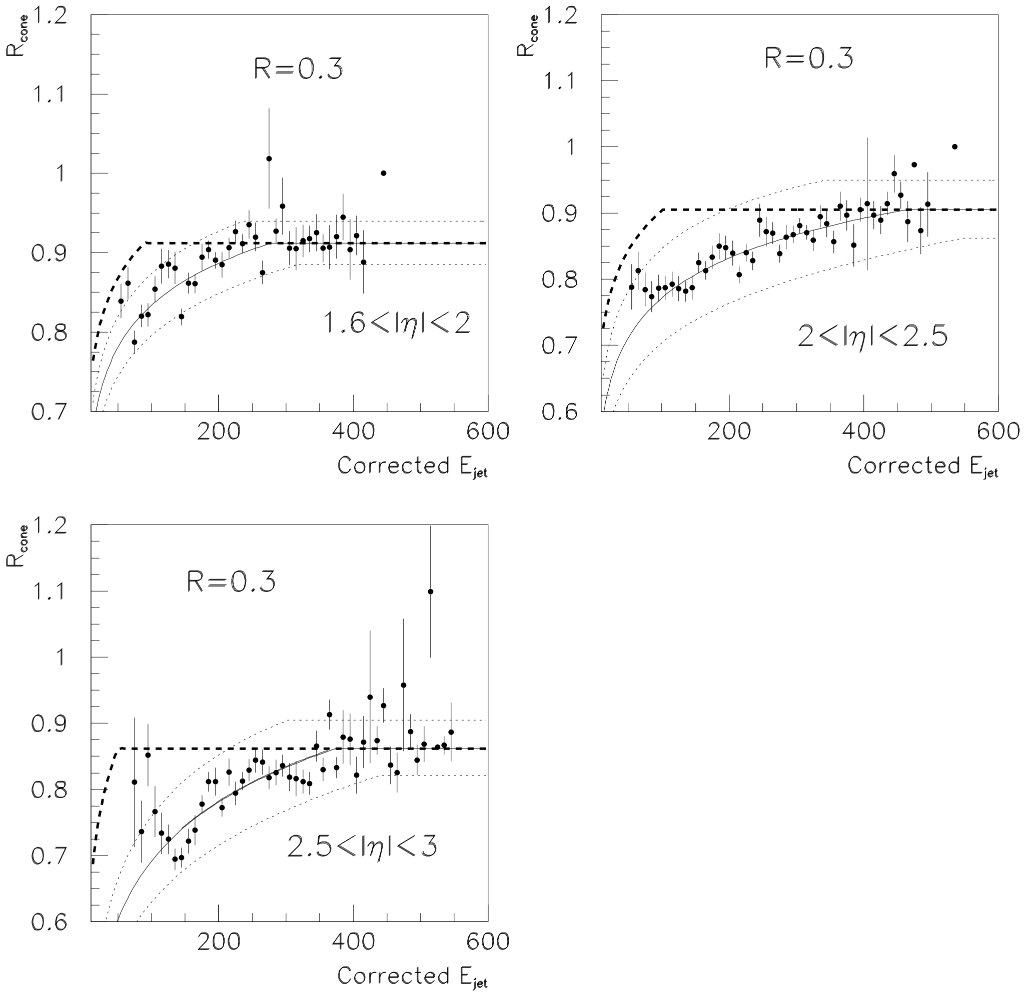

Figure 7.14: R_{cone} versus E_{jet} ($\mathcal{R}$ =0.3). E_{jet} is corrected by offset and response. The solid line is a fit to the data. The dotted lines show the systematic uncertainty. The dashed line is R_{cone} versus E_{Tjet} (replace E_{jet} by E_{Tjet} in the abscissa).

Chapter 8

Jet Energy Scale for Monte Carlo Samples

The Monte Carlo analysis described in this chapter serves two purposes. First, it provides the jet energy scale to correct Monte Carlo jets processed through SHOWERLIB[19]. Second, it proves that the method used to derive the correction achieves its purpose within errors. The first part of the chapter is dedicated to the correction for the Monte Carlo, which is derived following the same basic procedure used in the data. At the end, we include several verification tests of the method.

The analysis is primarily based on a sample of HERWIG direct photon events generated with different $E_{T\gamma}$ thresholds (7, 15, 30, 75, 150, 300, 500, and 700 GeV) to adequately populate the energy spectrum measured in the data. It was later processed through SHOWERLIB for simulation of particle showers and reconstructed with RECO V12. The methods used to obtain the corrections will not be detailed whenever they match those already described in previous chapters for the data correction.

8.1 Photon Response Correction

The photon response, R_γ, can be determined as the ratio of the measured to the generated photon energy. It is observed to be less than unity and to depend on $E_{T\gamma}$. Figure 8.1 shows R_γ versus E_γ for photons reconstructed in the CC region ($|\eta_\gamma| < 1$), and photons reconstructed in the EC region ($1.6 < |\eta_\gamma| < 2.5$).

The measured photon energy can be compared to the energy of the final state parton or to the energy of a particle jet reconstructed before the calorimeter simulation. In the latter case, the jet cone size is small, $\mathcal{R} = 0.3$, since the photon is a narrow object. Figure 8.1 shows R_γ calculated with respect to parton (full circles) and particle (open circles) level E_γ as a function of parton (particle) E_γ, for both the CC and the EC. The difference between the full and open circles is on the order of $\sim$1% at low energies ($\lesssim$150 GeV). Good agreement is observed at higher energies. The photon energy is corrected by the inverse of the R_γ parametrization which is obtained from a fit to a second order polynomial. The choice between the two possible corrections has been driven by the necessity to provide equivalent corrections for the data and the Monte Carlo. The EM scale was determined from the DØ $Z \to e^+e^-$ sample, selected with a set of quality cuts (CLEANEM package). The electron energy was corrected for underlying event and then used to measure the Z mass. The difference between this result and the LEP measurement at CERN gives the EM response of the calorimeter to collider data jets. This procedure is equivalent to deriving the scale from

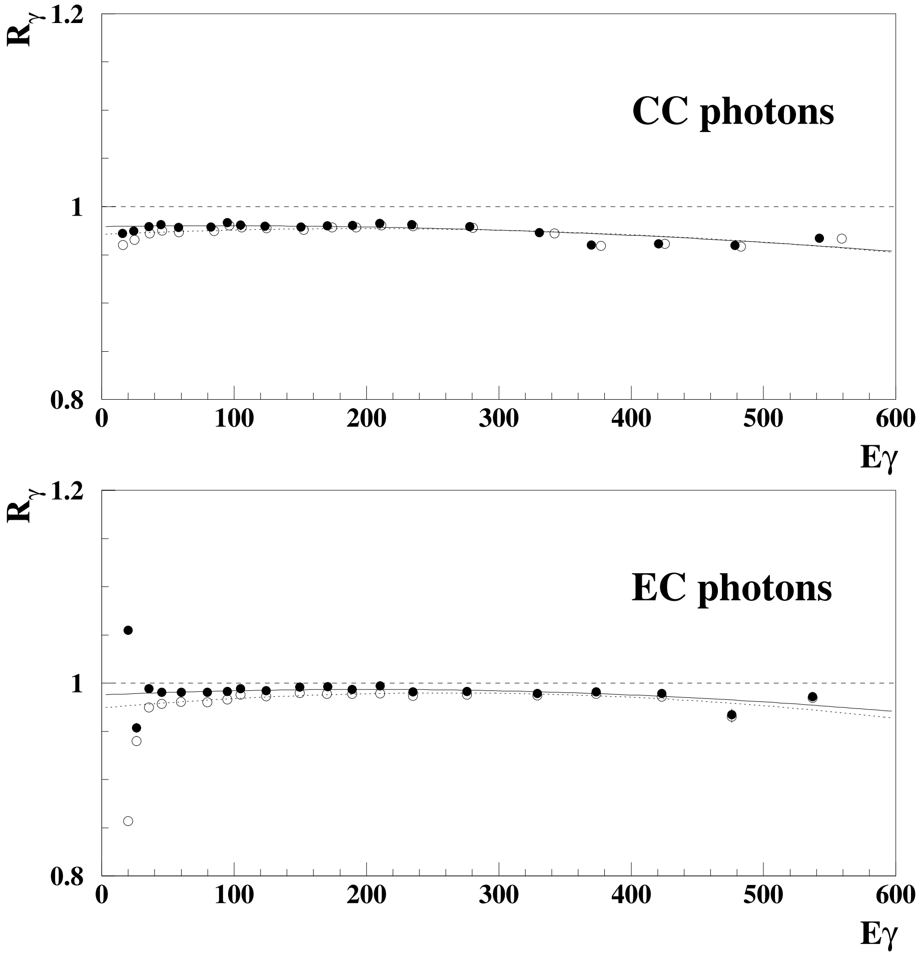

Figure 8.1: Ratio of measured E_γ to parton (particle) energy in full (empty) circles as a function of parton (particle) energy (HERWIG-SHOWERLIB).

the true parton level electron energy. Therefore, we chose R_γ obtained with respect to the parton level photon in order to put the data and the Monte Carlo corrections on the same footing. Finally, $\not\!\!E_T$ is recalculated using the corrected $E_{T\gamma}$.

8.2 Offset Subtraction

In the Monte Carlo simulation, uranium noise, pile-up and multiple $p\overline{p}$ interactions are not modelled. The only contribution to the offset is the physics underlying event, which was derived from HERWIG dijet sample. The difference between the E_T density distributions from samples generated with and without underlying event provided a measurement of the underlying event modelled in HERWIG. The result is $0.4 \pm 0.2\ \frac{\text{GeV}}{\eta\varphi}$, with no significant dependence on E_T or pseudorapidity.

The offset correction provided by CAFIX should not be applied blindly to any Monte Carlo sample. Additional corrections might be needed if the simulation includes noise, multiple $p\overline{p}$ interactions, or other features.

8.3 Selection of the γ-jet Sample

The γ-jet sample was selected with the same criteria used for the data sample. Note that the background in the Monte Carlo sample is limited to diphoton events, which have a negligible effect on the response measurement. In addition, luminosity or multiple interaction cuts are not needed.

Since there is no instrumental background but there is a topology bias in the Monte Carlo sample, we cannot say that the two effects combine into a small residual bias and introduce a 0.5% error to account for it. Therefore, we determine a topology correction which goes into R_{jet} in the Monte Carlo. Figure 8.2 shows the topology bias versus E' measured as the percentage difference between R_{jet} with a cut on $\varphi_\gamma - \varphi_{jet} \equiv \Delta\varphi$ >2.8 and the unbiased response. The latter was obtained using an extrapolation to π of the differential plot R_{jet} versus $\Delta\varphi$ (see Chapter 4). The bias is on the order of 1% at 30 GeV and becomes negligible above $\sim$ 200 GeV. In Chapter 4, we said that the topology bias in the CC response for data was approximately a constant function of E'. This is true because the effect of topology is E_T dependent and we always use relatively low E_T jets over the whole E' range (CC data up to E' $\sim$100 GeV and EC data between $\sim$100 GeV and $\sim$ 250 GeV).

8.4 Cryostat Factor Determination

The cryostat factor as a function of E' is determined by taking the ratio of R_{jet}^{EC} and R_{jet}^{CC} in the region where the CC and the EC overlap, 100< E' < 600 GeV. Figure 8.3 shows F_{cryo} fitted to a straight line. The result of the fit is:

$$F_{cryo} = 1.037 \pm 0.004\,(\text{stat})\,,$$

which is larger than the value measured from the data ($F_{cryo} \sim 0.98$). This may be due to different jet shapes in the data and the SHOWERLIB HERWIG Monte Carlo, or limitations of the calorimeter simulation model.

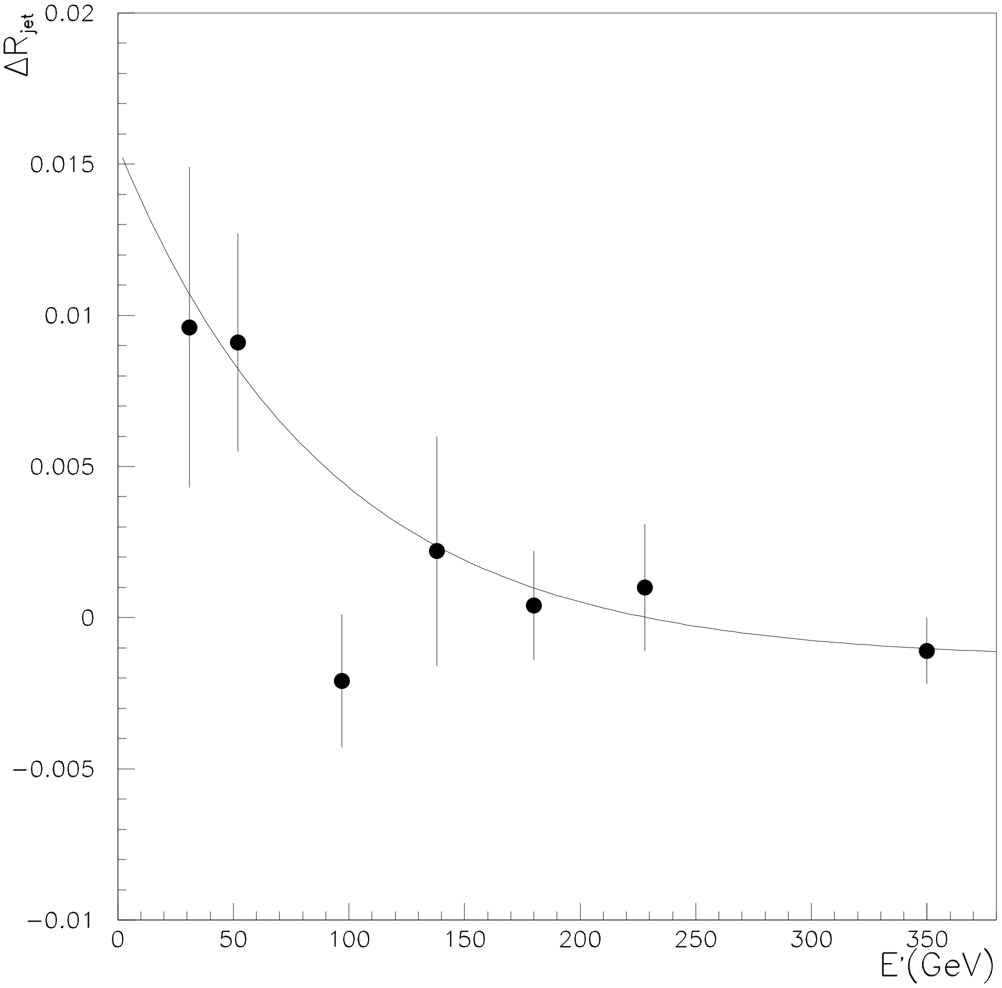

Figure 8.2: Topology bias measured as the percentage difference between R_{jet} at $\Delta\varphi = \pi$ and $\Delta\varphi > 2.8$ (HERWIG-SHOWERLIB).

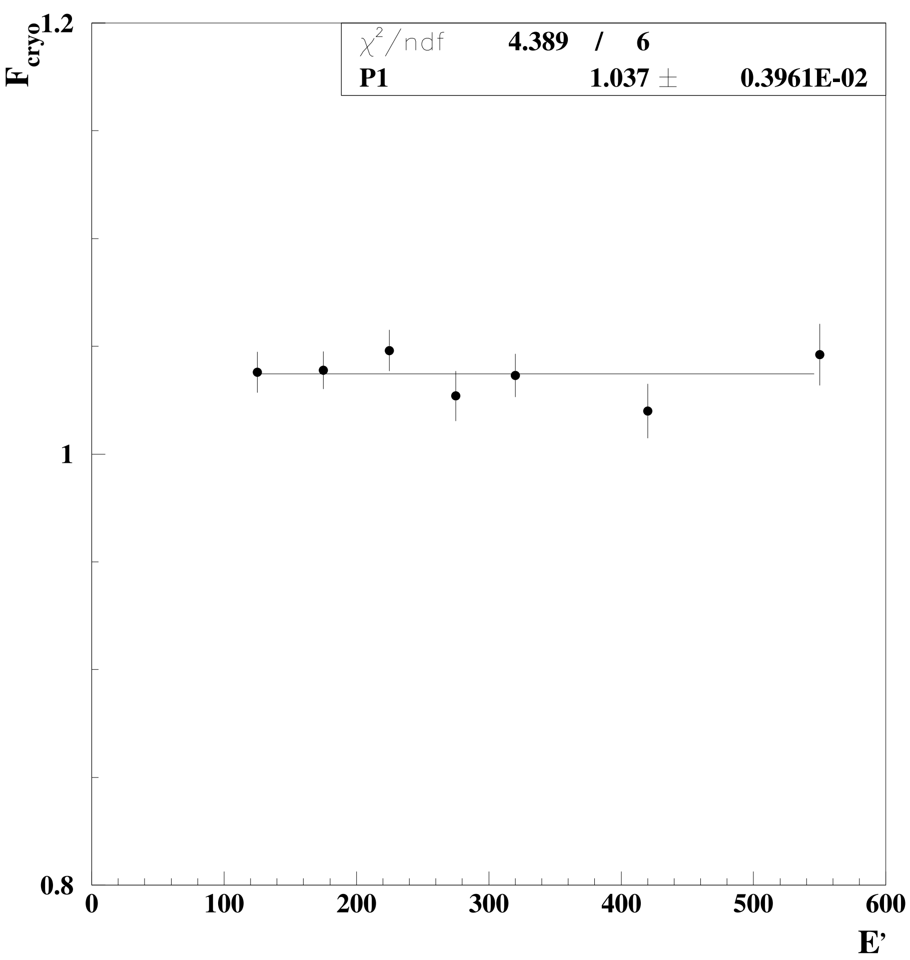

Figure 8.3: Cryostat factor as a function of E' (HERWIG-SHOWERLIB).

Data Sample	a	b
$25 < E_T < 55$	0.880	0.008
$55 < E_T < 100$	0.900	0.004
$100 < E_T < 200$	0.900	0.003
$200 < E_T < 500$	0.915	0.001

Table 8.1: Parameters from the fit of R_{jet} to the function $a + b \cdot \ln[\cosh(\eta)]$ (HERWIG-SHOWERLIB).

η region	mean	RMS
$\lvert\eta\rvert < 0.5$	0.000	0.008
$0.5 < \lvert\eta\rvert < 1.0$	0.000	0.008
$1.0 < \lvert\eta\rvert < 1.5$	-0.004	0.013
$1.5 < \lvert\eta\rvert < 2.0$	-0.005	0.013
$2.0 < \lvert\eta\rvert < 2.5$	-0.021	0.030
$2.5 < \lvert\eta\rvert < 3.0$	-0.012	0.031

Table 8.2: Means and RMS values for the residual η dependence in the Monte Carlo.

8.5 ICR Correction

There is also a residual η dependence of the response in the Monte Carlo which is different from that measured in the data. In principle, we use the same method as for the data to obtain the η dependent correction, with a few caveats. Since the Monte Carlo γ-jet sample is highly populated at high E_T's, it is not necessary to use jet-jet data. There is also no evidence of E_T or cone size dependence of the η correction in the Monte Carlo, as illustrated in Figures 8.4 and 8.5. Therefore, there is only one correction for all cone sizes.

Figure 8.4 shows the response, R_{jet}, versus η obtained from the γ-jet Monte Carlo sample after the cryostat factor correction. As in the case of the real data, the CC and EC Monte Carlo points were fit to a function of the form $R_{jet} = a + b \cdot \ln[\cosh(\eta)]$, which represents the "expected" η dependence if the calorimeter were uniform. Table 8.1 shows the fit parameters a and b, for the expected η dependence in the Monte Carlo. After all jets and the $\not\!\!E_T$ are corrected for the η dependence, the response R_{jet} was recalculated. The results, which are shown in Figure 8.6, are consistent with R_{jet} being a constant function of η. Figure 8.7 shows the residuals of R_{jet} with respect to the expected η dependence in six different pseudorapidity bins (HERWIG-SHOWERLIB). Table 8.2 contains the means of the R_{jet} residuals and their RMS values after all corrections have been applied. We assign an error to the Monte Carlo based on the mean residuals in each η region (Table 8.2), i.e. 0% for $|\eta| < 1$, 2% for $|\eta| > 2$.

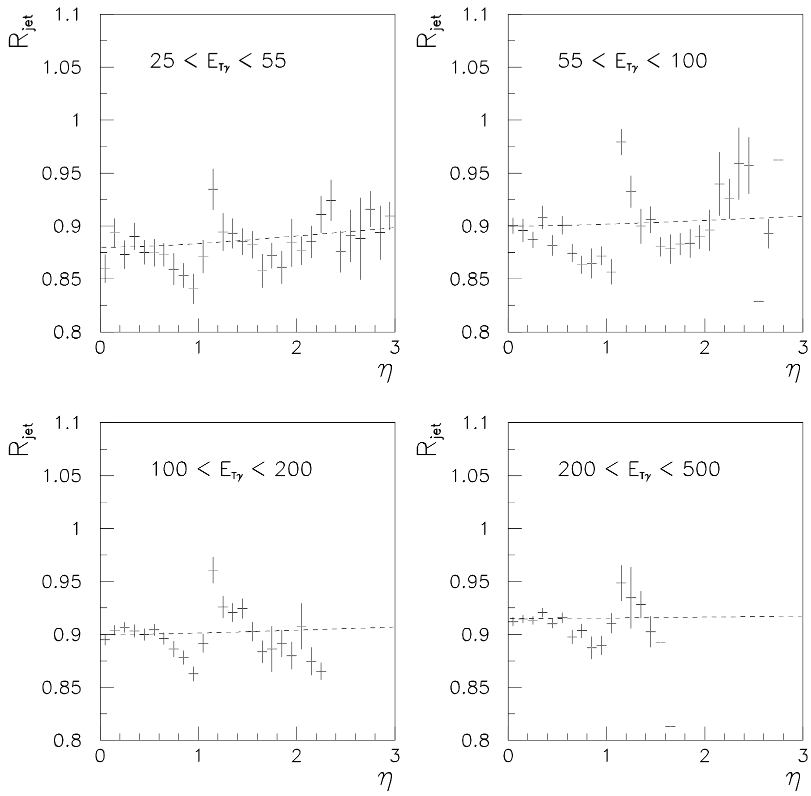

Figure 8.4: R_{jet} in the Monte Carlo as a function of η. The dashed line is a fit to the CC and EC points, i.e. the "expected" η dependence (HERWIG-SHOWERLIB).

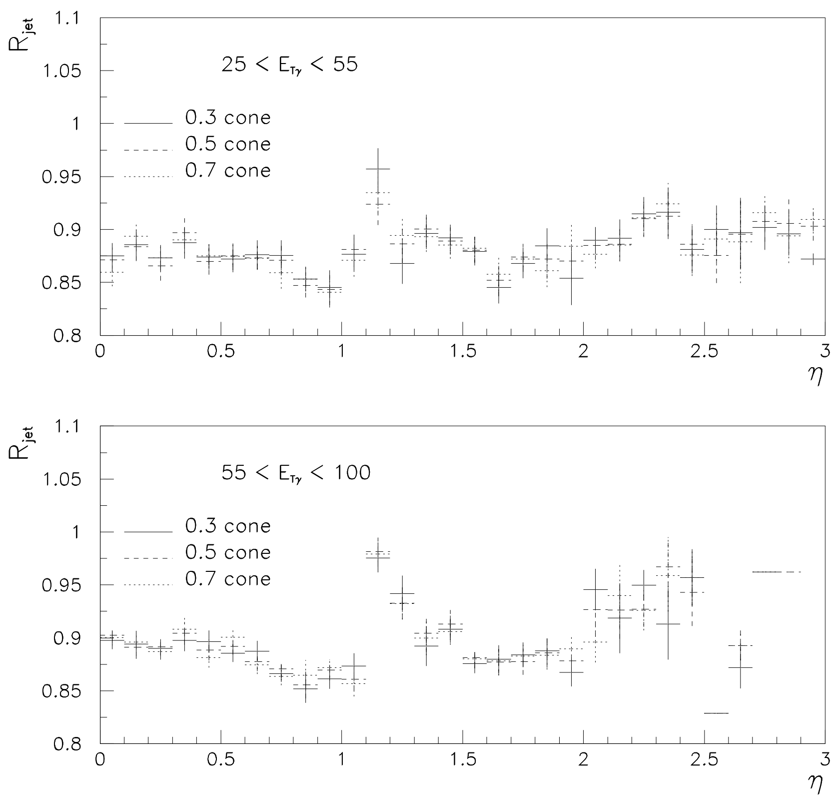

Figure 8.5: R_{jet} versus η for different cone sizes (HERWIG-SHOWERLIB).

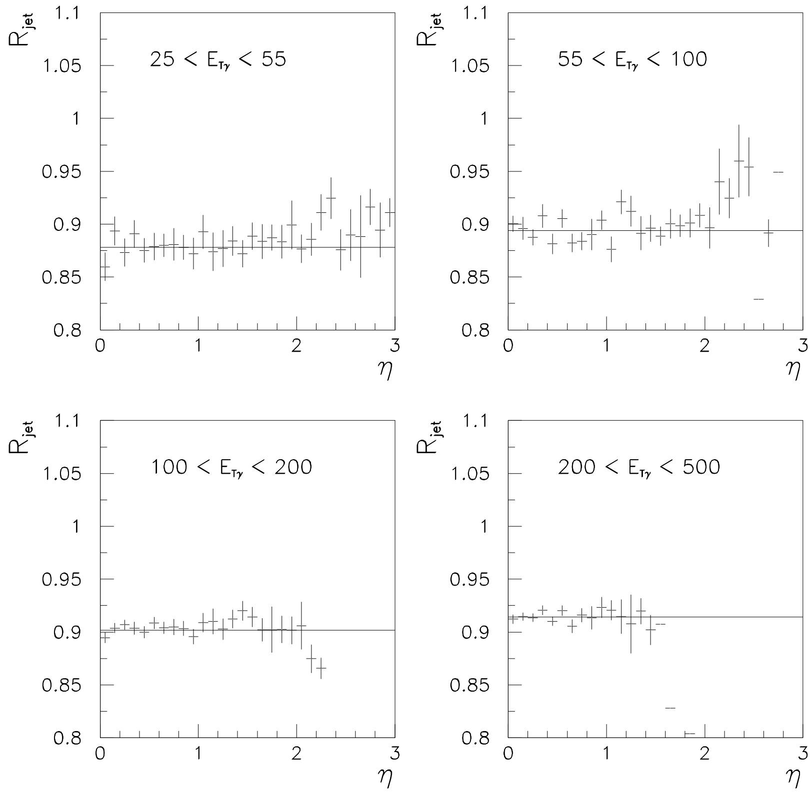

Figure 8.6: R_{jet} versus η after all corrections are applied (HERWIG-SHOWERLIB).

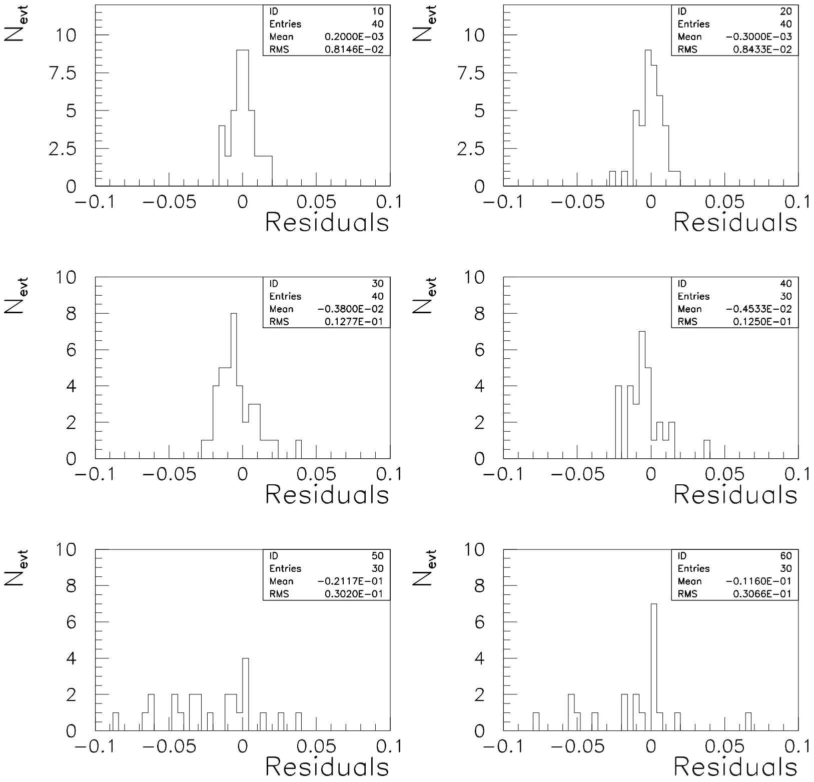

Figure 8.7: Residuals of R_{jet} with respect to the expected η dependence in six different pseudorapidity bins (HERWIG-SHOWERLIB).

Cone size	a	b	$\chi^2/ndof$
0.7	0.812 ± 0.010	0.014 ± 0.002	40/29
0.5	0.818 ± 0.010	0.013 ± 0.002	28/29
0.3	0.828 ± 0.010	0.011 ± 0.002	17/29

Table 8.3: Parameters from the fit of $a + b \cdot \ln(E)$ to R_{jet} for the three cone sizes (HERWIG-SHOWERLIB).

Cone size	a	b	c	$\chi^2/ndof$
0.7	0.738 ± 0.006	0.046 ± 0.002	-0.0033 ± 0.0002	33/30
0.5	0.765 ± 0.005	0.036 ± 0.002	-0.0024 ± 0.0002	25/30
0.3	0.841 ± 0.054	0.005 ± 0.023	0.0006 ± 0.0025	16/30

Table 8.4: Parameters from the fit of $a + b \cdot \ln(E) + c \cdot [\ln(E)]^2$ to R_{jet} for the three cone sizes (HERWIG-SHOWERLIB).

8.6 Energy dependence of R_{jet}

After the η dependent corrections were applied, the Monte Carlo response in the CC was determined in the same way as for the data (see Chapter 6). Figure 8.8 shows R_{jet} versus E_{jet} for jets reconstructed with the 0.7 cone algorithm. The response is now uniform over the whole detector, as the curves associated with the three η regions (CC, ICR, EC) agree very well with each other.

The shape of the response obtained from a HERWIG sample processed through SHOWERLIB is different from the R_{jet} measured from the data, as discussed in Chapter 6 (see Figure 8.9). Besides an overall normalization factor (R_{jet} is $\sim$ 2% to 3% the Monte Carlo response flattens out more rapidly and is nearly constant above 150 GeV. In contrast, the shape of the data curve is not well constrained at high energies due to limited statistics. A sample of particle level Monte Carlo jets convoluted with the single particle response measured in the Test Beam gives a response which reproduces the data R_{jet} much better than that derived from a GEANT simulation (see Chapter 6).

The low E_T bias correction has been derived for the three jet cone sizes (0.3, 0.5 and 0.7) used to reconstruct the HERWIG sample. Figure 8.10 shows the bias correction versus $E_{T jet}$ for 0.7 cone jets.

Both a linear and quadratic parametrization in $\ln(E)$ have been used to fit the response. The results are shown in Tables 8.3 and 8.4, for the different cone sizes.

A comparison between the χ^2 values of the two fits favors the form that includes the quadratic term, which is used to obtain the nominal response. The error of the fit has been derived in the same way as in Chapter 6 for the data. Figure 8.11 shows the fit to R_{jet} and the associated error band, for the case of jets reconstructed with the 0.7 cone algorithm. The limited $\not\!\!E_T$ acceptance contributes a small error to R_{jet}, as discussed in Chapter 6. On the other hand, since the full jet shower is contained within the calorimeter in the SHOWERLIB approximation, the shower containment error assigned to the data measurement of R_{jet} does not contribute in the case of the Monte Carlo correction.

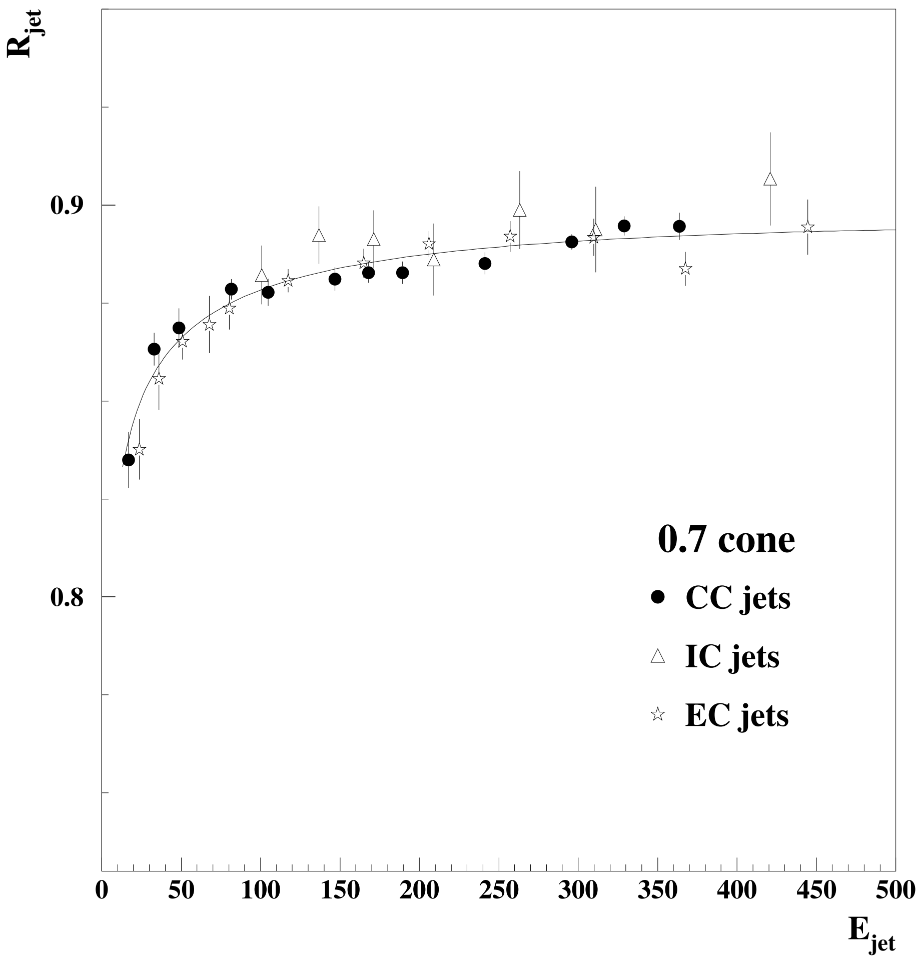

Figure 8.8: R_{jet} as a function of jet energy for jets reconstructed with the 0.7 cone algorithm. Full circles indicate CC jets, triangles EC jets and stars IC jets. The line is a fit of the form $a + b \cdot \ln(E) + c \cdot [\ln(E)]^2$ (HERWIG-SHOWERLIB).

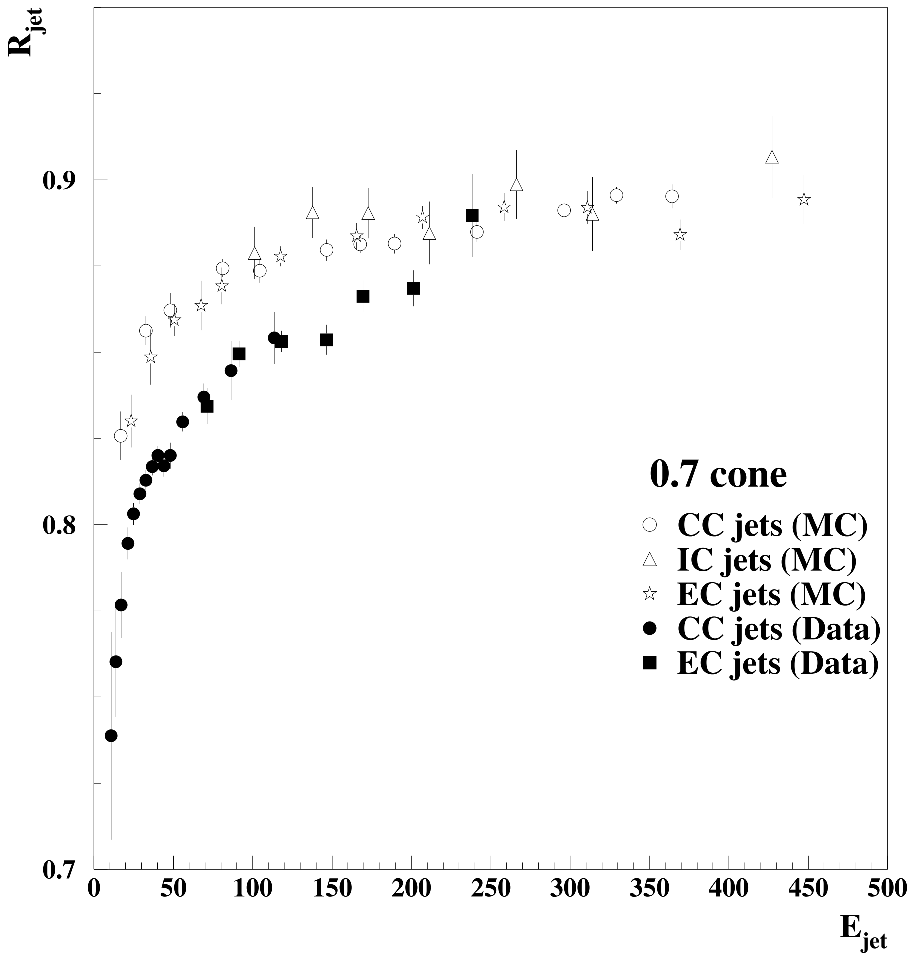

Figure 8.9: Comparison between R_{jet} measured from data and R_{jet} determined from a HERWIG-SHOWERLIB sample ($\mathcal{R}$ =0.7). The Monte Carlo response flattens out more rapidly and is nearly constant above 150 GeV.

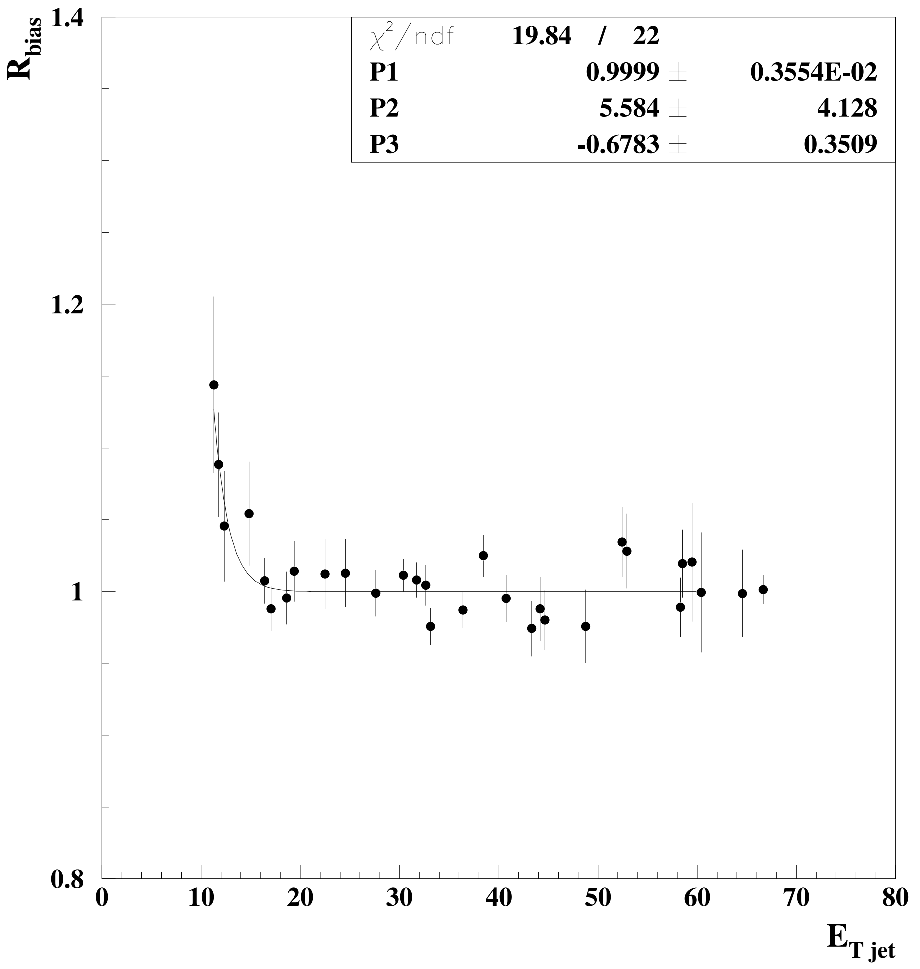

Figure 8.10: The low E_T bias as a function of E_{Tjet} measured from HERWIG-SHOWERLIB events ($\mathcal{R}$ =0.7) with the same procedure used for data. The solid line indicates the result of the fit to a $P1 + e^{(P2+P3\cdot E_T)}$.

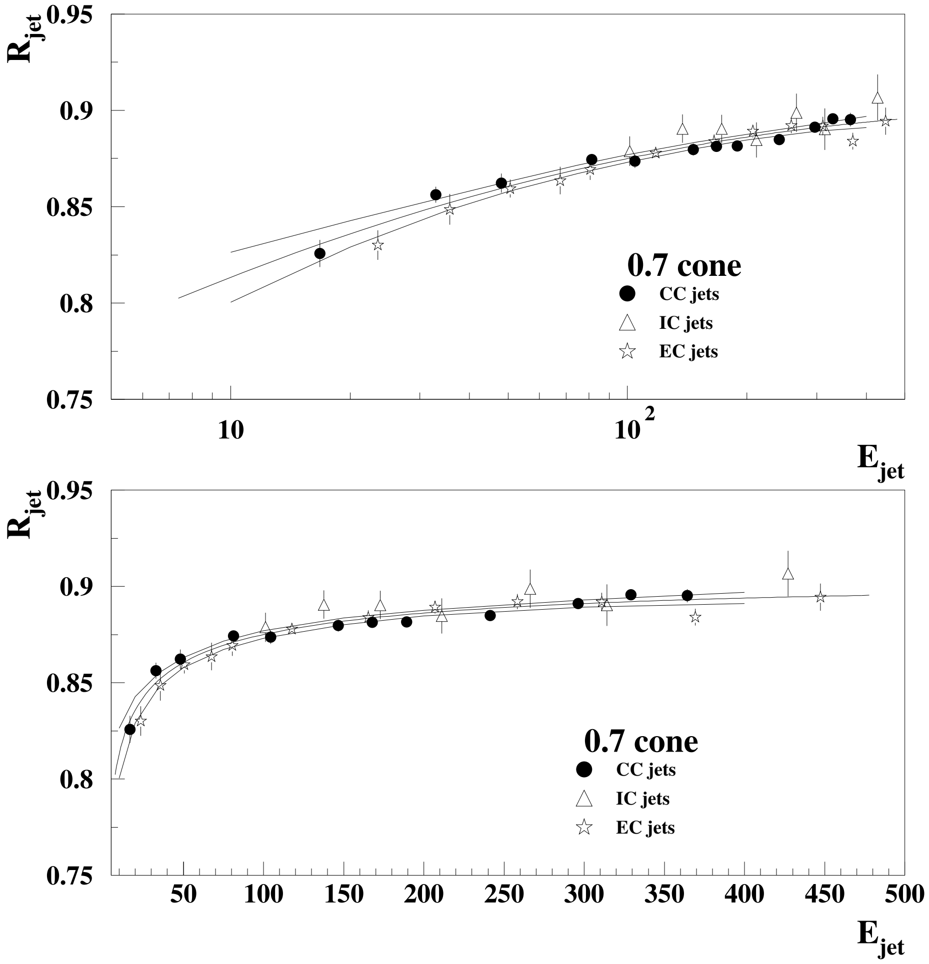

Figure 8.11: R_{jet} values for 0.7 jets (full dots are CC jets, triangles EC jets and stars IC jets) together with the result of nominal quadratic fit and the upper and lower error bands (HERWIG-SHOWERLIB).

8.7 Showering Correction

The fraction of the parent particle jet energy contained in the algorithm cone at the calorimeter level, R_{cone}, is determined with the same method used for the data correction, as described in Chapter 7. The total out-of-cone ratio, F_{tot}, is obtained from the γ-jet Monte Carlo sample by measuring the energy density in the calorimeter as a function of the angular distance to the jet centroid. The physics out-of-cone ratio, F_{phy}, is determined from the jet-jet HERWIG sample using the jet energy densities at the particle level. The underlying event and the remaining energy baseline are subtracted from both samples and the showering correction is obtained as $F_{sho} = F_{tot} - F_{phy} + 1$.

Figures 8.12-8.17 show $R_{cone} = \frac{1}{F_{sho}}$ versus E_{jet} for different pseudorapidity regions and cone sizes. As expected, the correction is smaller than in the case of the data. This is primarily due to the truncation of the single particle showers at 95% of their energy. In most of the cases, the results are consistent with R_{cone} being a constant function of E_{jet}. For very forward jets ($|\eta| \gtrsim 1.6$) reconstructed with a 0.3 cone algorithm, it becomes clear that R_{cone} drops for low E_{jet}. This is illustrated in Figure 8.17, where a logarithmic function $a + b \cdot \ln(E_{jet})$ was used to fit the points.

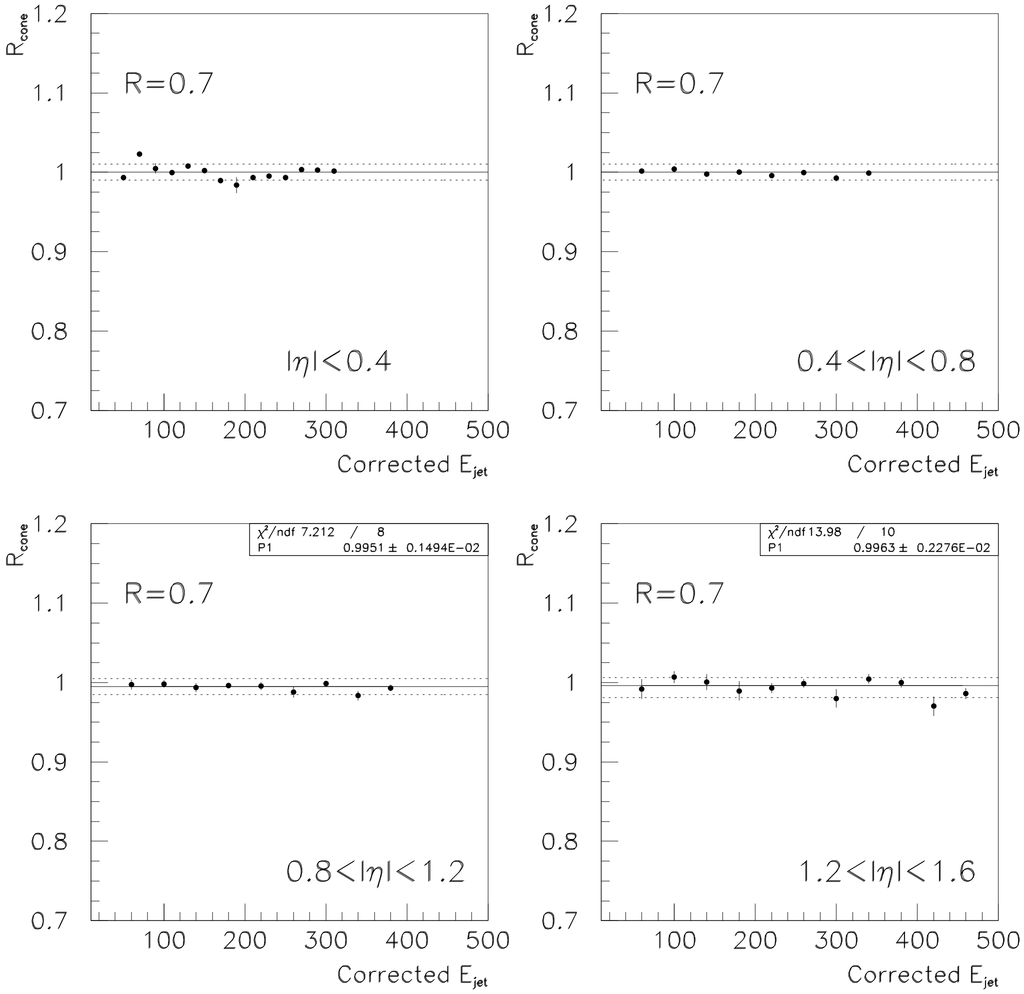

Figure 8.12: R_{cone} versus E_{jet} for $\mathcal{R}$ =0.7 cone jets (HERWIG-SHOWERLIB). E_{jet} is corrected by offset and response. The solid line is a fit to the points. The dotted lines show the systematic error.

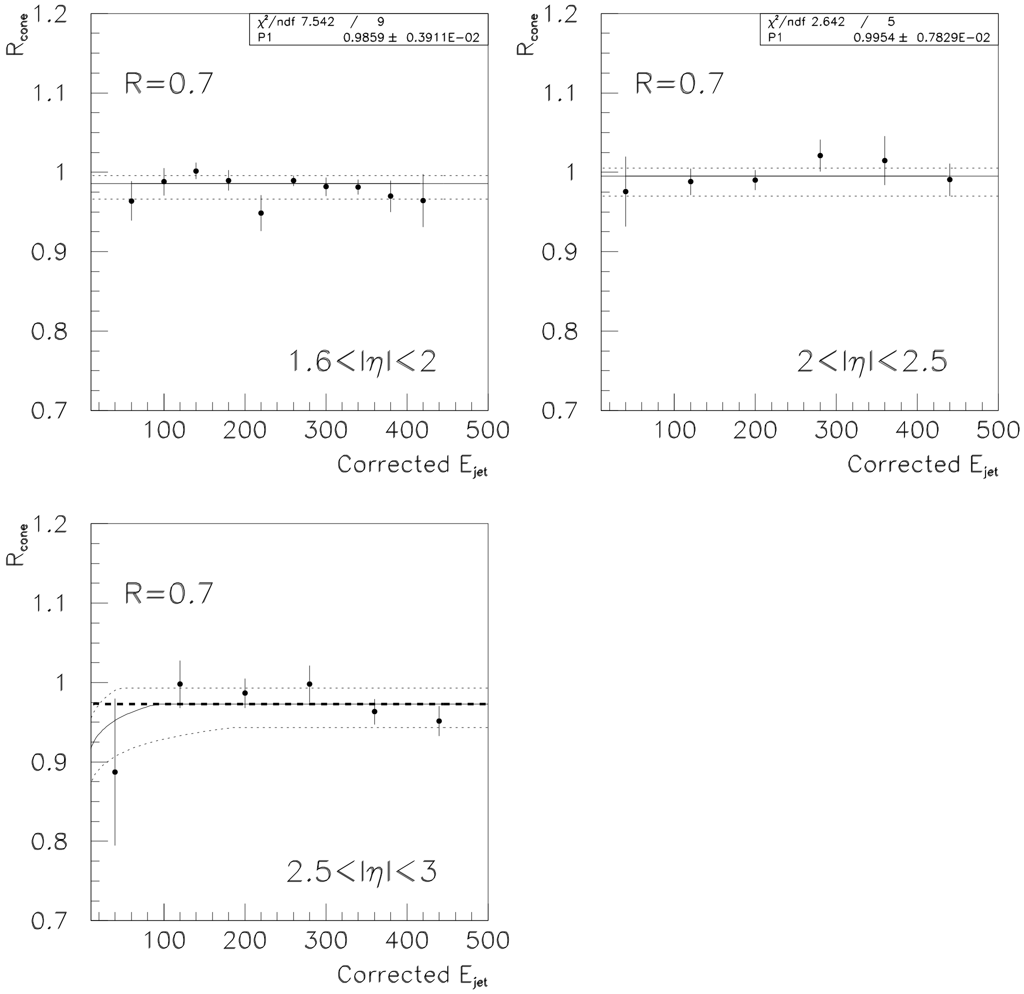

Figure 8.13: R_{cone} versus E_{jet} for $\mathcal{R}$ =0.7 cone jets (HERWIG-SHOWERLIB). E_{jet} is corrected by offset and response. The solid line is a fit to the points. The dotted lines show the systematic error.

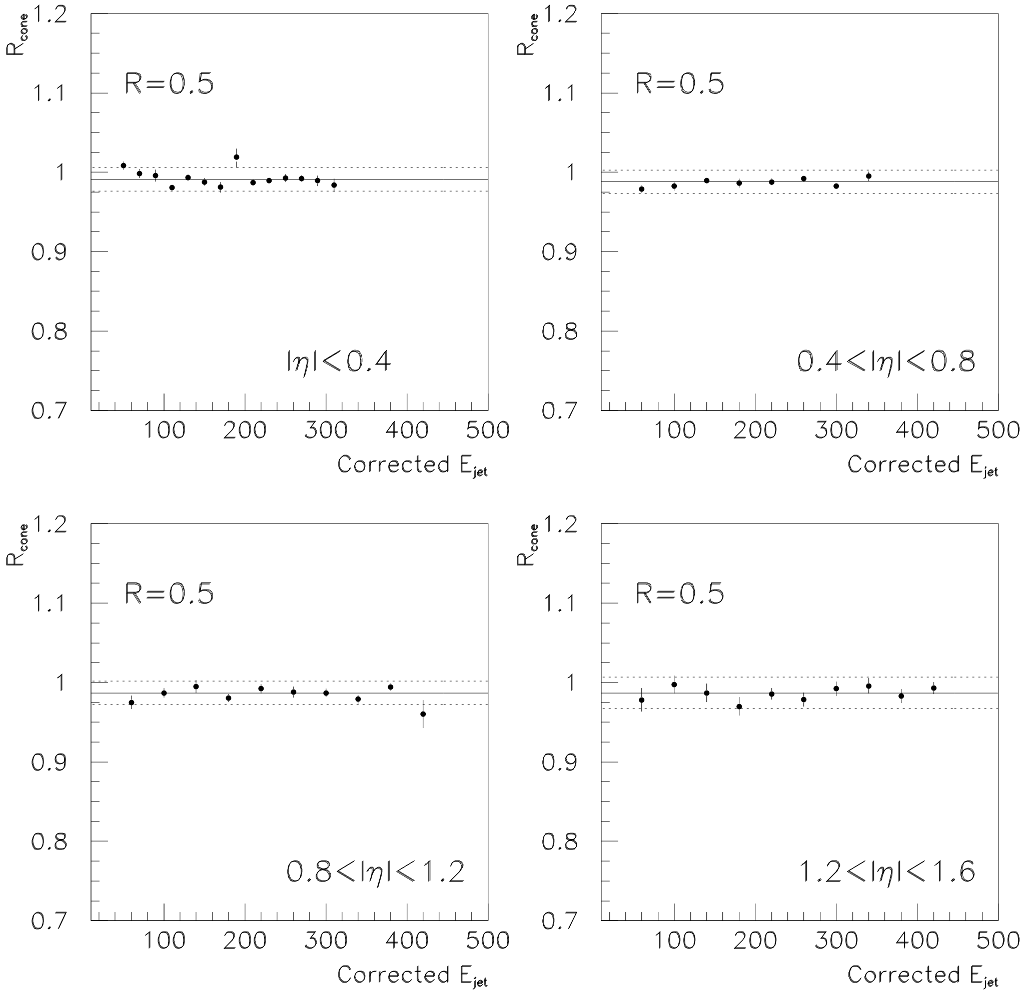

Figure 8.14: R_{cone} versus E_{jet} for $\mathcal{R}$ =0.5 cone jets (HERWIG-SHOWERLIB). E_{jet} is corrected by offset and response. The solid line is a fit to the points. The dotted lines show the systematic error.

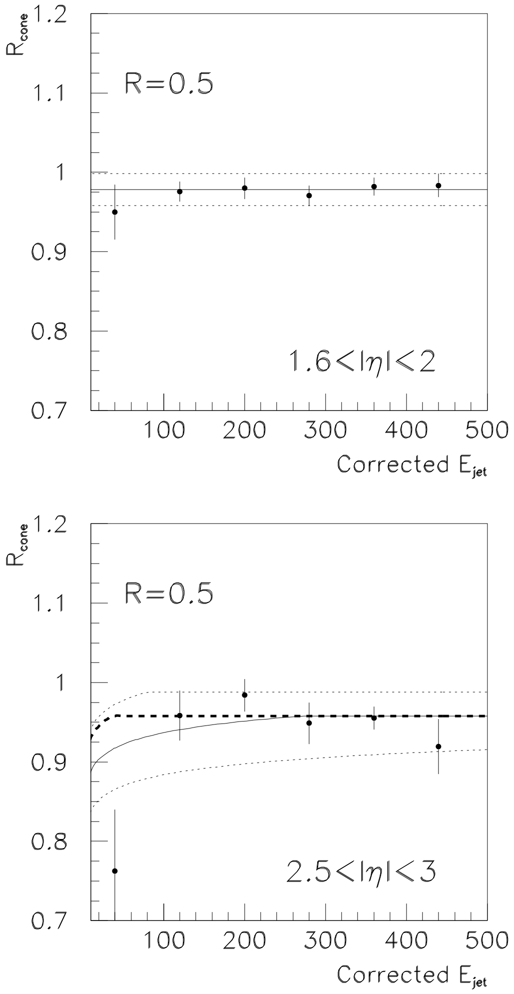

Figure 8.15: R_{cone} versus E_{jet} for $\mathcal{R}$ =0.5 cone jets (HERWIG-SHOWERLIB). E_{jet} is corrected by offset and response. The solid line is a fit to the points. The dotted lines show the systematic error.

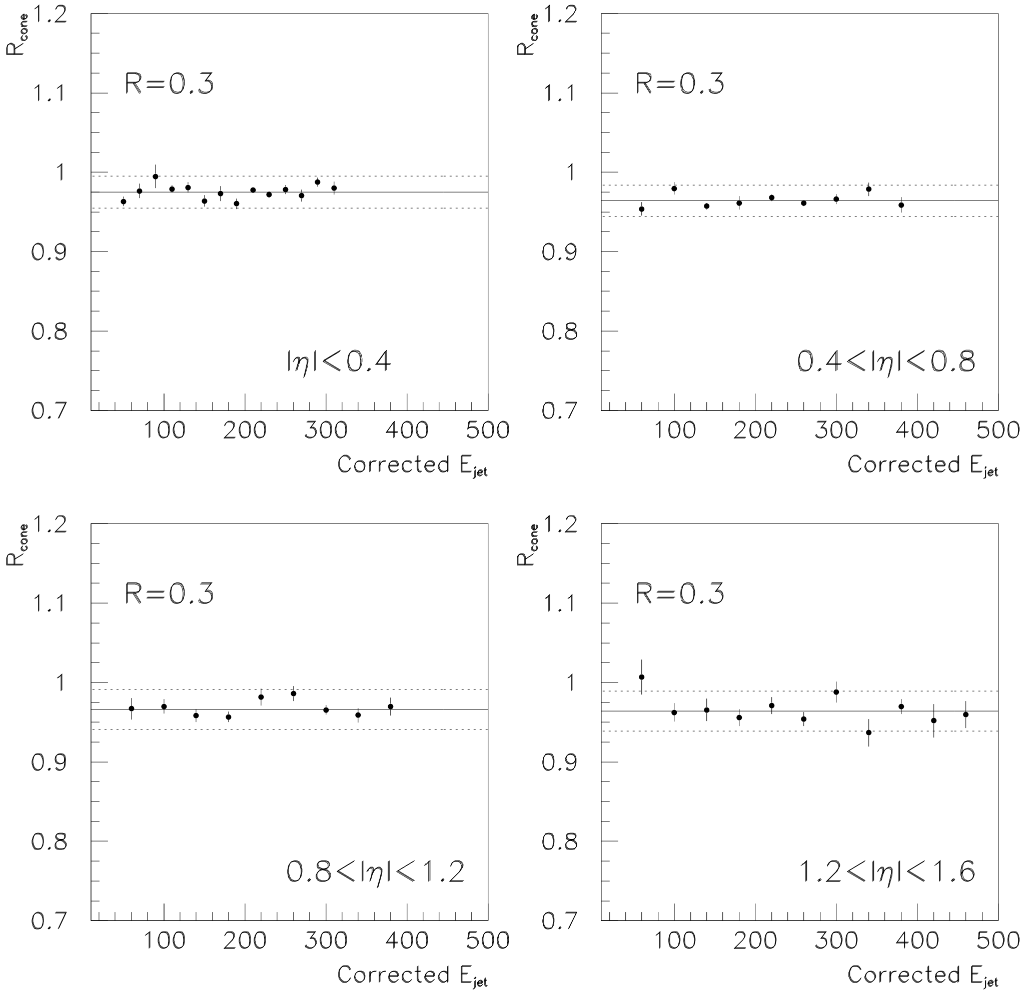

Figure 8.16: R_{cone} versus E_{jet} for $\mathcal{R}$ =0.3 cone jets (HERWIG-SHOWERLIB). E_{jet} is corrected by offset and response. The solid line is a fit to the points. The dotted lines show the systematic error.

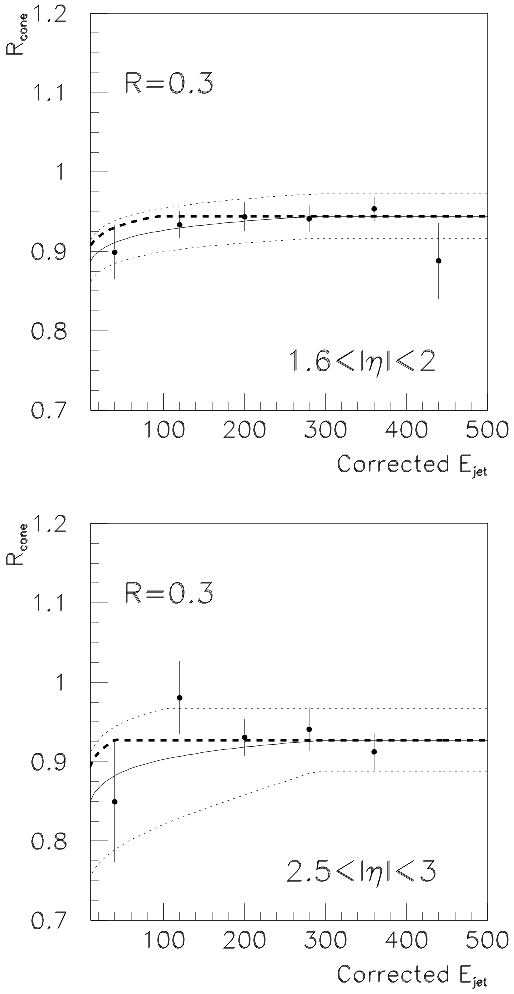

Figure 8.17: R_{cone} versus E_{jet} for $\mathcal{R}$ =0.3 cone jets (HERWIG-SHOWERLIB). E_{jet} is corrected by offset and response. The solid line is a fit to the points. The dotted lines show the systematic error.

8.8 Closure Tests

The Monte Carlo sample gives us the opportunity to verify the accuracy of the method used to derive the jet energy scale correction. This "closure" test directly compares the corrected jet energy with the energy of the associated particle jet. The ratio of these two quantities must be one for all E_{jet}^{ptcl}'s and pseudorapidities. Different particle jet algorithms have been tested, leading to comparable results. For the closure test, the underlying event contribution was subtracted from both calorimeter and particle jets. In addition, split and merged jets were removed from the sample, since splitting and merging is not implemented in the particle level algorithms.

Figures 8.18 and 8.19 show the ratio of calorimeter and particle jet energy before (open circles) and after (full circles) the CAFIX correction is applied. $\frac{E_{jet}^{meas}}{E_{jet}^{ptcl}}$ is plotted as a function of E_{jet}^{ptcl} and η_{jet}^{ptcl} for jets reconstructed with the 0.7 cone algorithm ($|\eta| < 0.5$). Statistical and systematic uncertainties are also shown. Within errors, the ratio is consistent with unity after all corrections. On average, the correction is scaling the energy of a jet reconstructed with a 0.7 cone algorithm to the energy of the associated particle jet within $\sim$0.5% for $|\eta| < 0.5$.

The closure test is also performed for the other cones and pseudorapidity bins. Figures 8.20, 8.21, and 8.22 show the $\frac{E_{jet}^{meas}}{E_{jet}^{ptcl}}$ ratio versus E_{Tjet} calculated for the 0.7, 0.5 and 0.3 cone sizes in seven η bins within the range $|\eta| <3$. The ratios are consistent with one within the total systematic uncertainties.

A second consistency check can be performed by recalculating the response, once the $\not\!\!E_T$ and the jet energies have been corrected. As mentioned in Chapter 5, this result does not necessarily have to be consistent with one, since $\vec{\not\!\!E}_T$ is not corrected for the response of unreconstructed clusters in the event. Figure 8.23 shows a plot of R_{jet} versus E_{Tjet} in the case of jets reconstructed with a 0.7 cone algorithm after the event $\not\!\!E_T$ and E_{Tjet} have been corrected. The result is consistent with one over the whole E_T and pseudorapidity range.

8.9 Comments on Monte Carlo Simulations

Monte Carlo simulations are essential tools in the derivation of jet corrections. The most difficult and limiting problem faced in the determination of the jet energy scale is the absence of a simulation that matches the data. It is crucial to tune the Monte Carlo generators and the detector simulations to reproduce the jet shape, response and resolution observed in the data. Until this is achieved, physics results will be dominated by large systematic errors at low E_T's and high pseudorapidities.

Once the Monte Carlo simulation matches the data, the errors will be further reduced and corrections to small jet samples with characteristics different from the average will be more accurate.

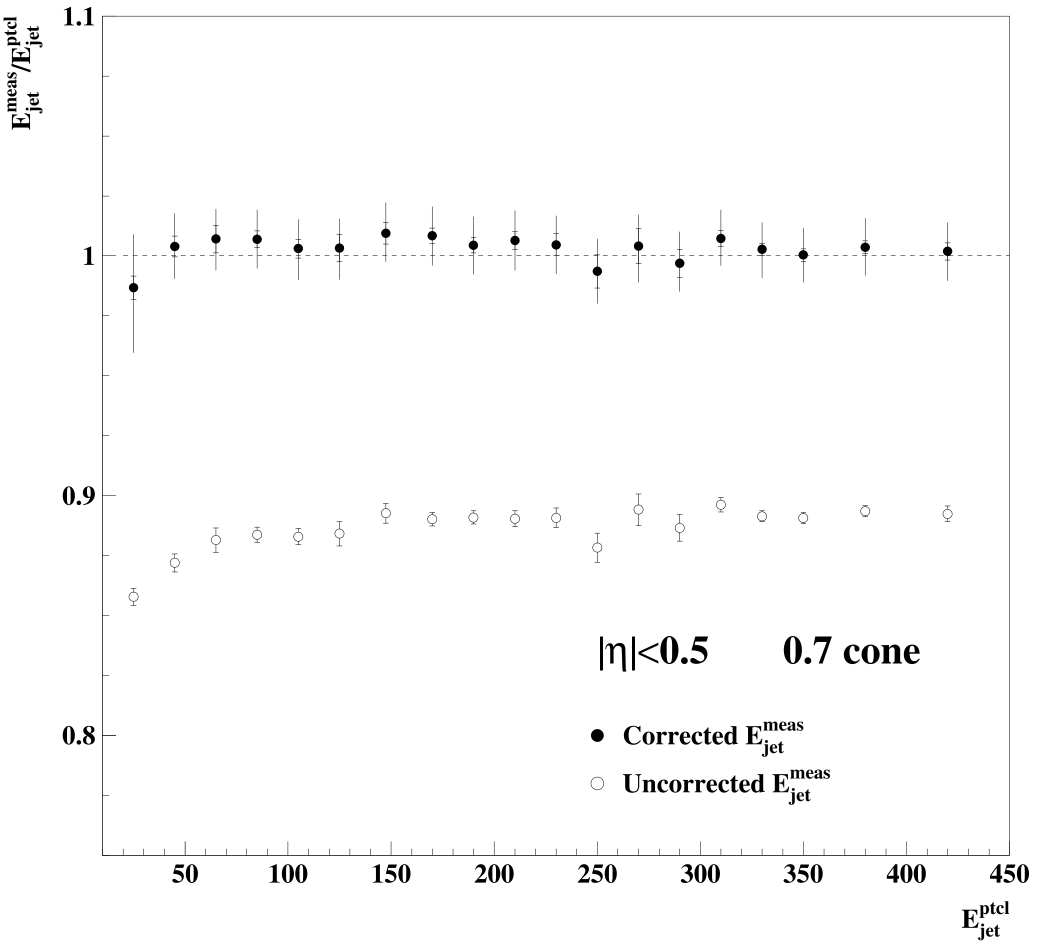

Figure 8.18: Ratio of calorimeter and particle jet energy before (open circles) and after (full circles) CAFIX is applied (HERWIG-SHOWERLIB). The ratio is plotted as a function of E_{jet}^{ptcl} for $\mathcal{R}$ =0.7 jets. Inner bars are statistical errors, and outer bars are statistical and systematic errors added in quadrature.

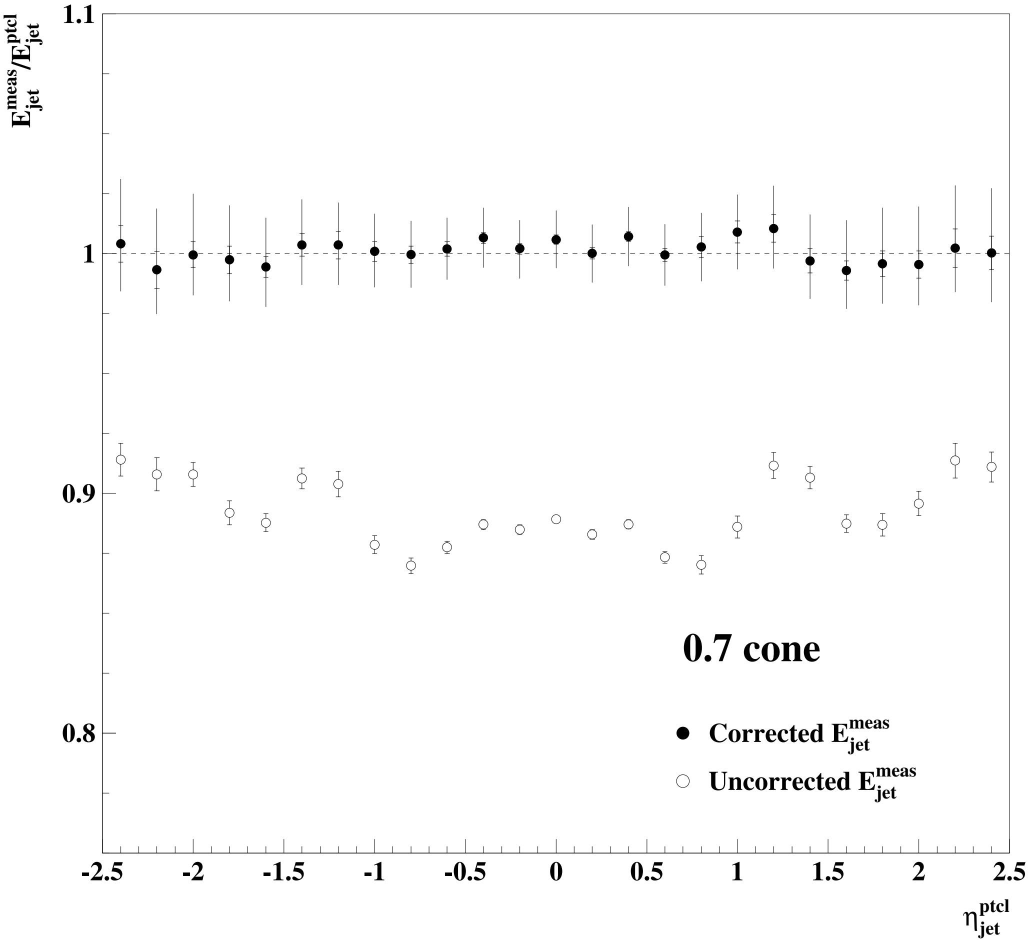

Figure 8.19: Ratio of calorimeter and particle jet energy before (open circles) and after (full circles) CAFIX is applied (HERWIG-SHOWERLIB). The ratio is plotted as a function of η_{jet}^{ptcl} for $\mathcal{R}$ =0.7 jets. A E_T > 15 GeV cut is applied to remove the region where showering losses and low E_T bias effects dominate. Inner bars are statistical errors, and outer bars are statistical and systematic errors added in quadrature.

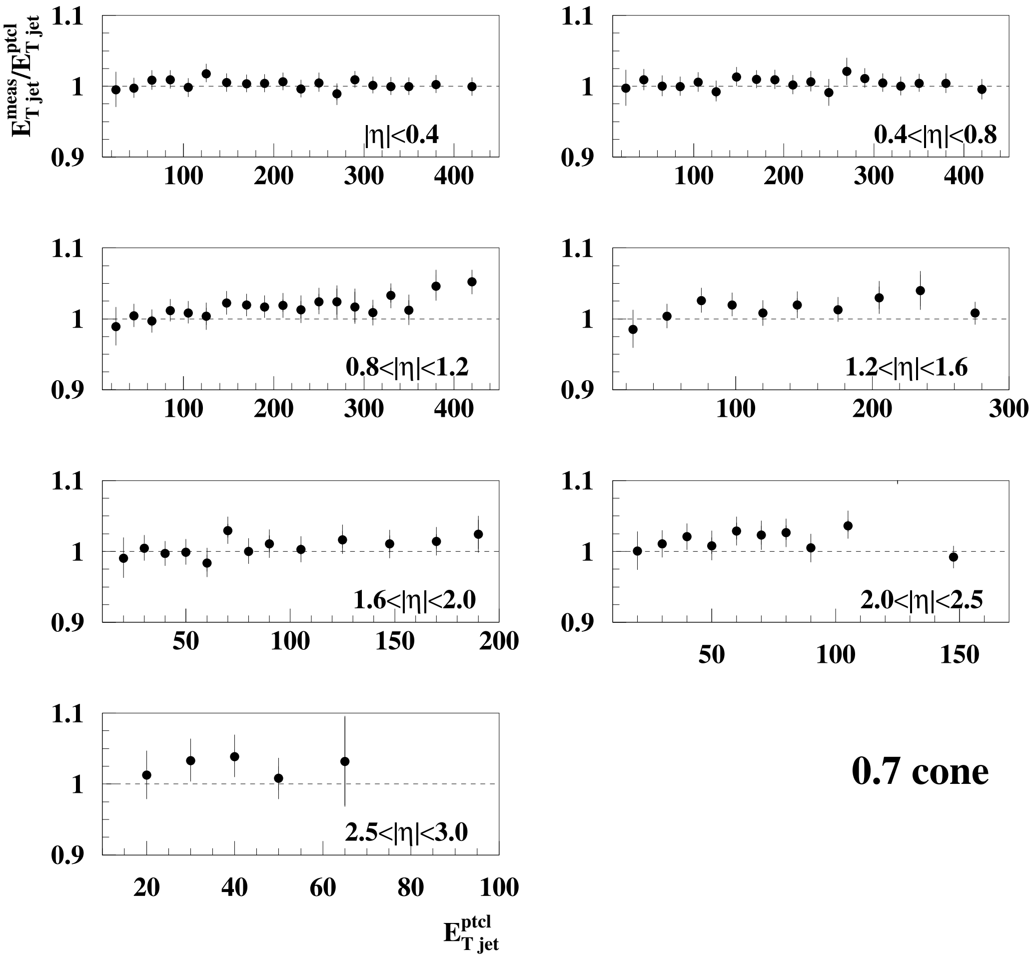

Figure 8.20: Ratio of calorimeter and particle jet energy after CAFIX is applied (HERWIG-SHOWERLIB). The ratio is plotted as a function of $E_{T jet}^{ptcl}$ for $\mathcal{R}$ =0.7 jets. Inner bars are statistical errors, and outer bars are statistical and systematic errors added in quadrature.

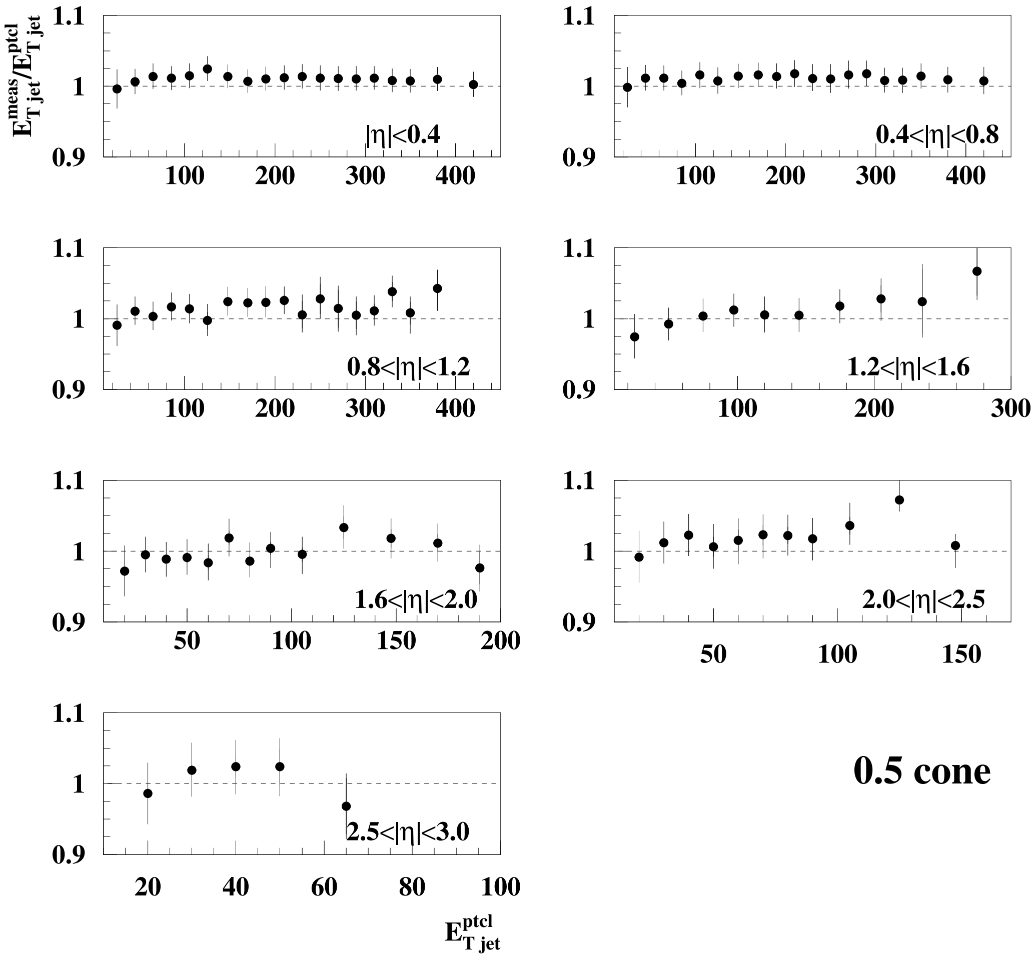

Figure 8.21: Ratio of calorimeter and particle jet energy after CAFIX is applied (HERWIG-SHOWERLIB). The ratio is plotted as a function of $E_{T\,jet}^{ptcl}$ for $\mathcal{R}$ =0.5 jets. Inner bars are statistical errors, and outer bars are statistical and systematic errors added in quadrature.

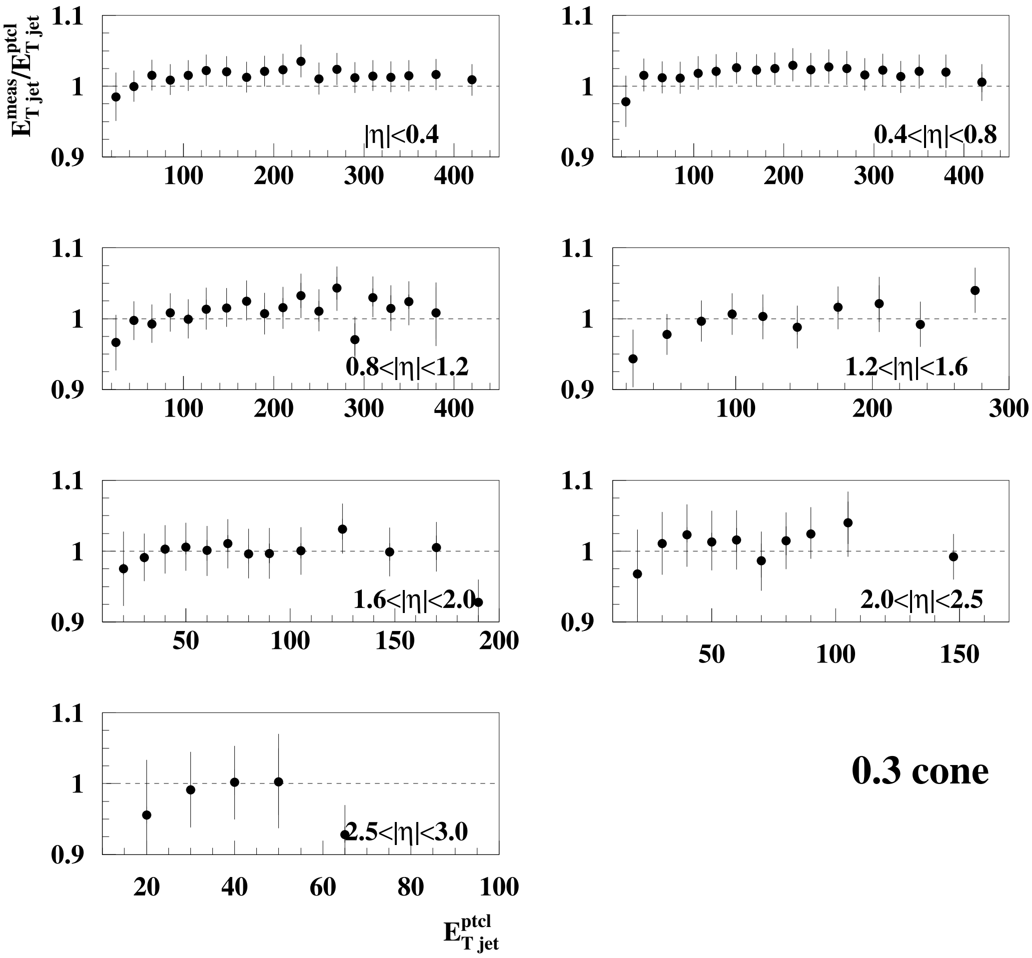

Figure 8.22: Ratio of calorimeter and particle jet energy after CAFIX is applied (HERWIG-SHOWERLIB). The ratio is plotted as a function of E^{ptcl}_{Tjet} for $\mathcal{R}$ =0.3 jets. Inner bars are statistical errors, and outer bars are statistical and systematic errors added in quadrature.

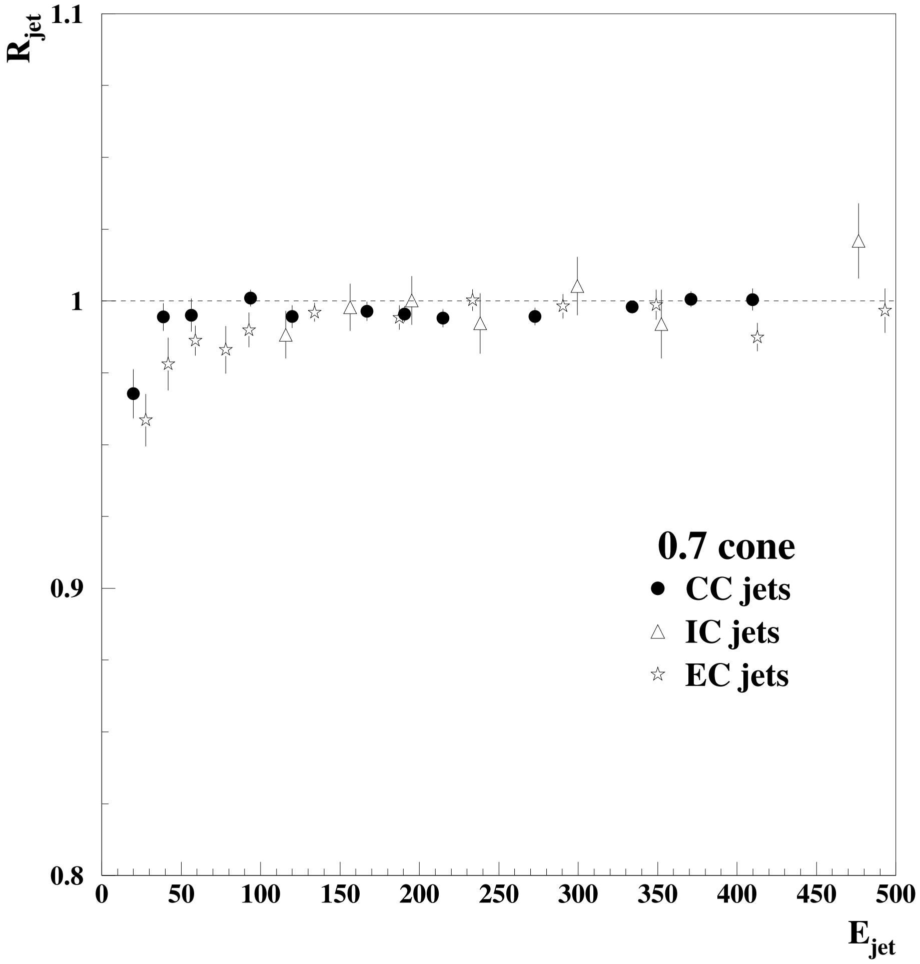

Figure 8.23: R_{jet} versus E_{Tjet} in the CC, IC and EC regions after CAFIX is applied ($\mathcal{R} = 0.7$). (HERWIG-SHOWERLIB).

Chapter 9

Summary

In this chapter, we include a description of the CAFIX package with emphasis on the computer code that performs the jet energy scale correction. We also include an illustration of the individual corrections and errors involved in the jet energy scale calibration. We conclude with a list of usage recommendations and limitations of the current CAFIX package.

9.1 The CAFIX (version 5.1) Package

All of the corrections discussed in this document are performed by individual routines within the CAFIX package; all jet operations are performed by calls from QCD_JET_CORRECTION.FOR. Two RCP files are required by CAFIX: CAFIX.RCP and QCD_JET_CORRECTION.RCP. Four flavors of QCD_JET_CORRECTION.RCP are provided in the version 5.1 release:

- QCD_JET_CORRECTION51.RCP: intended for use with all data from Run Ia and Run Ib reconstructed with RECO version $\geq$V11.
- MC_QCD_JET_CORRECTION51.RCP: intended for use with SHOWERLIB[19] Monte Carlo events reconstructed with RECO Version 12.
- QCD_JET_CORRECTION51_1C_LOWET.RCP: intended for use with data from Run Ic. Note: the η dependence correction is E_T dependent. In the case of Run Ic, the correction was measured only for jets with E_T less than $\sim$150 GeV.
- QCD_JET_CORRECTION51_630.RCP: intended for use with data from the $\sqrt{s}$ =630 GeV running reconstructed with RECO Version $\geq$V11.

The CAFIX package serves a dual purpose. The energies of clustered physics objects are corrected for detector response and these energy corrections along with measured muon P_T's and main ring losses are applied to correct the calorimeter $\not{E}_T$ by vectorial addition of raw calorimeter $\not{E}_T$ to correction vectors in VCOR banks generated by CAFIX. Switches in CAFIX.RCP specify which objects are corrected and whether these corrections will be included in the $\not{E}_T$ calculation. The general structure of CAFIX is the following:

- Correct all PELC and PPHO clusters with electromagnetic energy scale by calling CORRECTEM.FOR. By default, all clusters are now corrected instead of just those satisfying an isolation cut. This correction is controlled by toggling DO_EM_CORRECTION [default=.true.][1]. DO_MET_CORRECTION [T] allows the

[1] For the remainder of this section, default rcp parameter values will be designated by square brackets in the text. ie .true. = [T], .false. = [F], etc.

propagation of the EM-scale changes into the $\not\!\!E_T$.

- For each jet algorithm, loop over all jets. Any matching PELC or PPHO clusters are removed from each JETS bank by CORRECT_JETS_EM_REMOVE.FOR. At most two matching EM-cluster banks are removed currently because the micro-DST file only stores two such links. The PELC or PPHO clusters are removed from the JETS bank vectorially instead of using the JNEP banks. If CORRECT_EM_JETS is toggled on [T], then the remaining JETS bank energy is corrected by QCD_JET_CORRECTION.FOR.

- Apply jet corrections. The jet corrections are usually applied in twice in independent passes through the JETS banks. The first pass, used to correct the $\not\!\!E_T$, is controlled by the USE_JET_CORRECTION flag [T]. In this pass only 0.7 cone jets are considered and the showering correction is disabled. A VCOR bank is generated for each corrected jet. The second pass, controlled by the DO_JET_CORRECTION flag [T], loops over all cone jet algorithms and overwrites all JETS banks with the corrected quantities.

  Jets are corrected as follows (the relevant switches are set in QCD_JET_CORRECTION.RCP unless stated otherwise):

  – The bias correction is performed by the routine MPF_LOW_ET_BIAS_CORR.FOR. This correction is controlled by the switches: DO_BIAS_CORRECTION [T], UNBIAS_ALL_JETS [T], NJETS_TO_UNBIAS [20]. If UNBIAS_ALL_JETS=.false., then only the first 'NJETS_TO_UNBIAS' jets for each algorithm will be corrected. CAFIX.RCP contains an additional flag, MET_USE_JETBIAS [F], which disables application of this correction only for the $\not\!\!E_T$ pass through the jet corrections.

  – The offset correction is performed by CORRECT_JETS_NOISEU.FOR. This correction has two pieces: physics underlying event and the rest of the jet offset (contribution of multiple interactions, uranium noise and pile up). One can control the application of each component by toggling DO_UND_CORRECTION [T] and DO_ZSP_CORRECTION [T] in CAFIX.RCP. Either of these corrections may be turned off while retaining the consistency of the following corrections. The user should however note that this amounts to a change in jet definition. Two further controls are provided in QCD_JET_CORRECTION.RCP: USE_LUM_AND_MI [T] and USE_RECO_AREA [F]. USE_LUM_AND_MI causes the correction to be based on the measured luminosity and MITOOL value; otherwise, the correction is based on luminosity only. A run number check is used to choose the $\sqrt{s}$ =1800 GeV or $\sqrt{s}$ =630 GeV MITOOL version. For corrections to Monte Carlo, the MC_LUMIN variable [-1.0] allows the user to subtract calorimeter noise or energy from additional events if ZEROBIAS on MINBIAS events were added after GEANTing the sample. If the USE_RECO_AREA flag is .true. then the jet offset correction is modified for split or merged jets. The correction is scaled by the actual jet area in $\eta \times \phi$ space compared with the area contained in a simple jet cone. This information is available in RECO V12 DST and STA files and in DST and μDST files for DØFIX data. The area scaling request is ignored if jet area information is unavailable.

  – The routine CORRECT_JETS_SCALE_FACTORS.FOR performs corrections for sampling fractions (necessary for RECO versions prior to V12), cryostat factors, and η dependence. It is toggled by the DO_DET_SCALE_CORRECTION [T] switch. The ICR correction is performed through the ETA_DEPENDENCE.FOR routine and is controlled by the flag DO_ETA_CORRECTION [T].

  – The absolute scale correction is applied by MPF_JETCORR.FOR. This correction can be toggled by the switch DO_RESPONSE_CORRECTION [T].

- The showering correction is applied by CORRECT_JETS_OOC.FOR and is controlled by the DO_CONE_CORRECTION [T] switch in CAFIX.RCP.
- Detailed information on all corrections factors and errors for each jet is now available in the new JQUAN bank. After running CAFIX_51, the new jets bank will contain a pointer to a JQUAN bank as well as a pointer to a copy of itself before application of the corrections. See JQUAN.ZEB and JETS.ZEB for more information.

- Next the $\not{E}_T$ corrections are applied:
  - Loop over PELC, PPHO, and main ring VCOR banks and apply corrections to the $\not{E}_T$. Loop over the $R = 0.7$ cone algorithm VCOR banks and apply these response corrections to the $\not{E}_T$. The above corrections are used to create the PNUT(4) corrected $\not{E}_T$ bank. All $\not{E}_T$ corrections may be turned off by toggling DO_MET_CORRECTION in CAFIX.RCP.
  - Loop over PMUO banks and add those passing a quality mask into the muon corrected $\not{E}_T$ (PNUT(5)) bank. The quality mask used is defined by GOOD_MUON_MASK in CAFIX.RCP.

9.2 Usage Recommendations and Limitations

In this section we give a few general comments on using the CAFIX package.

9.2.1 $\not{E}_T$ Correction

The default $\not{E}_T$ correction does not include the low E_T bias jet correction. We do not recommend using this correction in the $\not{E}_T$ in physics analyses. This functionality is mainly intended for energy scale derivation studies.

9.2.2 Jet Corrections

CAFIX5.1 provides a correction to scale the measured jet energy to the energy of the associated particle level jet. The calibration is an average correction, integrated over all jet quantities except energy and pseudorapidity. Jets pointing to φ cracks, or with average characteristics different from those in the γ-jet sample, may need a different correction. The correction is accurate for jets with E_T >15 GeV and $|\eta|$ <3. The poor knowledge of the calibration in the range E_T <15 GeV is taken into account with a rapidly increasing error below this threshold. CAFIX5.1 works on data processed through RECO V10, 11 and 12. The nearest neighbor algorithm is not supported in CAFIX5.1. The jet cone algorithms, with cone sizes 1.0, 0.7, 0.5 and 0.3 are all supported, except for the 1.0 cone algorithm in the Monte Carlo correction.

The calibration is based on Run Ia and Run Ib data taken in $p\overline{p}$ collisions at $\sqrt{s}$ = 1.8 TeV. Run Ic data is also supported in the case of low E_T jets (E_T <150 GeV) produced in $p\overline{p}$ collisions at $\sqrt{s}$ =630 GeV [32]. In the case of the low center of mass energy run, the underlying event is smaller. In addition, the η dependent correction is different in Run Ic due to a change in the ICD running parameters. Those analyses using Run Ic data taken at $\sqrt{s}$=1.8 TeV should be cautious when using the correction in the IC region.

DØ angle and Snowmass angle definitions (from DØ FIX) receive the same correction, which was derived using the cone algorithm with the DØ angle definition.

- **Offset:** the underlying event density is derived from minimum bias data. In those analyses that depend strongly on this correction, the offset might need to be evaluated for that particular sample. Since the energy scale corrections were derived without jet area scaling for split/merged jets, we recommend that this feature be used cautiously or only for systematic studies.

- **Response (η dependence):** they were derived for Run 1b data using RECO V12 for E_T's and for Run Ic data using RECO V12 for jets up to $\sim$ 150 GeV in E_T. Although correction factors were included to put RECO V10 and V11 on the same footing as RECO V12, there could be a residual η-dependence if the data are not covered by the above categories. For example, the user should be cautious with the results in the ICR (0.8< $|\eta|$ <1.6) on RECO 10 and 11 data. Above $|\eta|$ =2.5, the cryostat factor approximation starts to break down. Although it is included in the errors, we expect the nominal correction to be biased towards a low correction by up to $\sim$3% at $\eta = 3$. This bias might also be related to energy lost down the beam pipe and increases as a function of pseudorapidity.

- **Response (energy dependence:** the response is known to be dependent on the jet width. Several plots with the average jet width in the γ-jet and inclusive jet samples are included in Chapters 5 and 6 for comparison with the average jet widths with the particular samples used in physics analysis. The user must be aware that there is not always a fixed relation between a change in the width and a change in the response. The response is not affected when the width increases due to noise, pile-up or extra interactions.

- **Showering:** this correction is not measured for pseudorapidities beyond $\sim$ 3. Although the showering loss is supposed to increase exponentially as a function of pseudorapidity, CAFIX5.1 applies a constant correction and error above $\eta = 2.7$.

- **Monte Carlo:** The correction is derived from a HERWIG sample processed through SHOWERLIB and reconstructed with RECO V12. The correction cannot not be applied to samples processed through GEANT, since the response and the showering losses are expected to be different. The correction is the same for ISAJET and HERWIG samples, since it primarily depends on the detector simulation and reconstruction parameters.

9.3 Summary Plots of Corrections and Errors

In this section we provide some summary plots to illustrate the size of the jet corrections and errors as a function of jet E_T and pseudorapidity. The following plots were generated by calling QCD_JET_CORRECTION.FOR using the entry point QCD_JET_CORRECTION_2.FOR to input various jet parameters for running the corrections. The entry point QCD_JET_CORRECTION_QUANS was then called to retrieve the correction factors and errors for each individual jet. Any CAFIX user may perform a similar procedure to determine the energy scale errors for a particular analysis if care is taken to average over all the relevant jet parameters. For the following plots, luminosity was set to 5×10^{30} cm^{-1}sec^{-1}, the MITOOL value was set to 1, and the jet cone size to 0.7.

In the case of the Monte Carlo correction there are a few sources of uncertainty which are absent. There is no contribution from the offset correction since noise and extra interactions are not modelled in our sample. Physics background errors are absent in the γ-jet sample. There is no instrumental background bias since the photon purity is exactly one (no contamination from highly electromagnetic jets). There is also full jet shower containment even for high energy jets in the Monte Carlo sample used in this analysis (SHOWERLIB). A topology bias correction is applied to the response in the Monte Carlo correction with a 0.5%

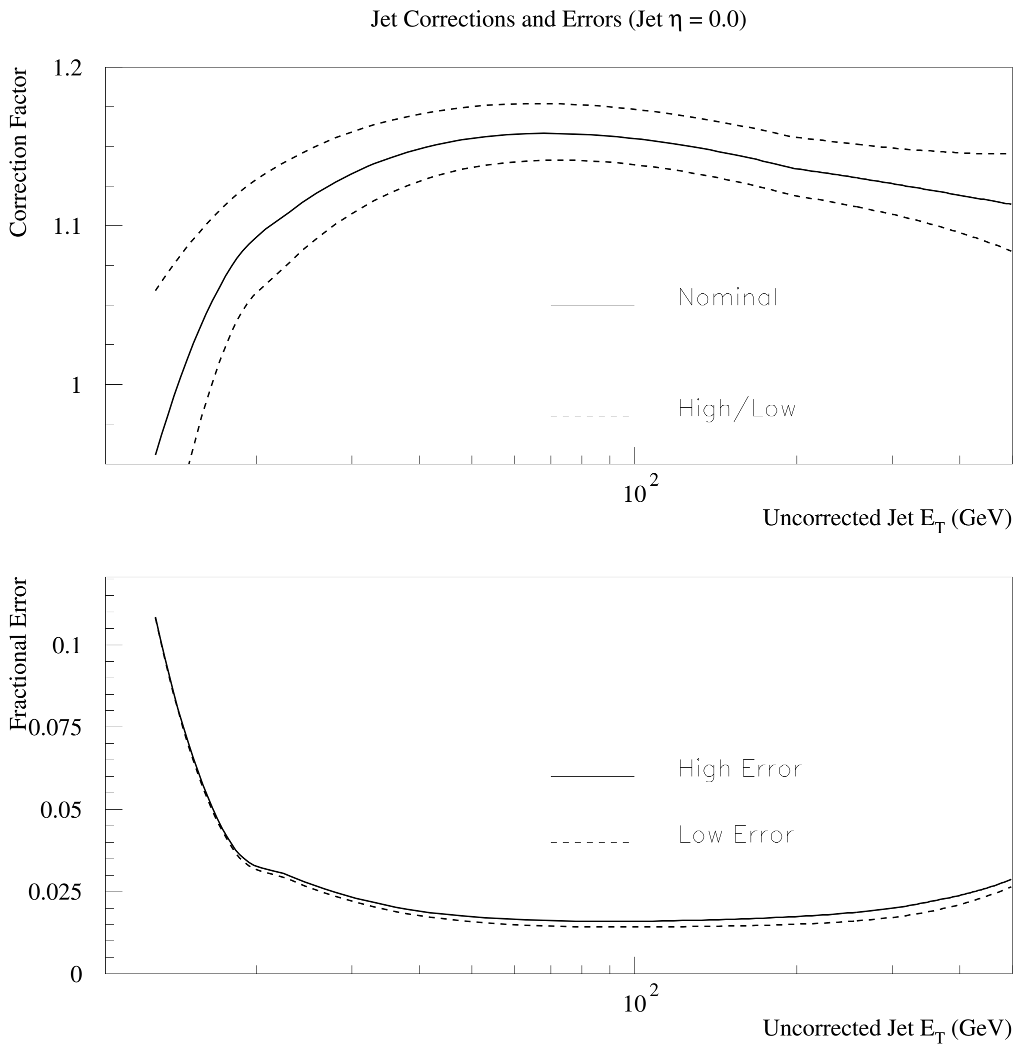

Figure 9.1: Corrections and Errors for η_{jet} =0.0, $\mathcal{R}$ =0.7. Top: Nominal, high, and low correction factors. Bottom: high and low fractional errors.

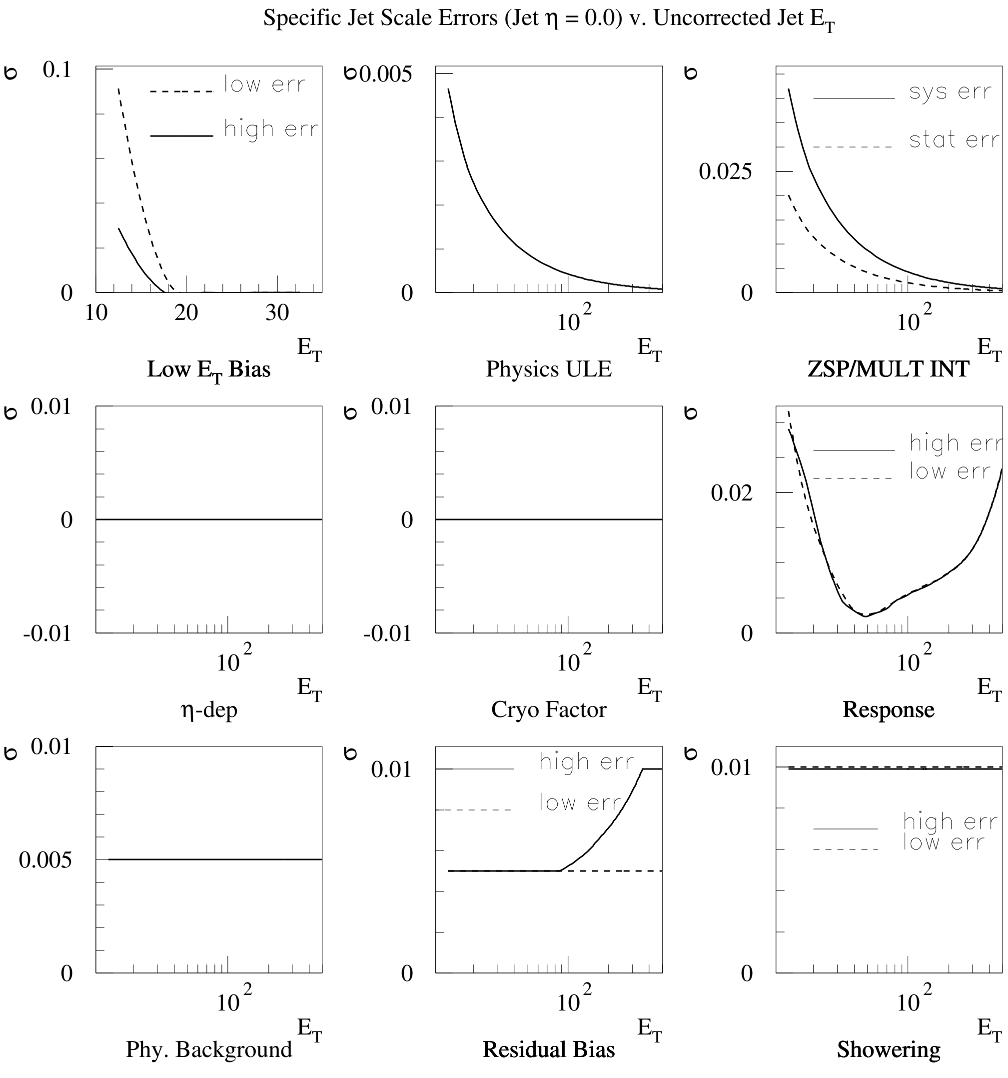

Figure 9.2: Individual components of the jet scale error plotted versus uncorrected jet E_T for η_{jet} =0.0, $\mathcal{R}$ =0.7.

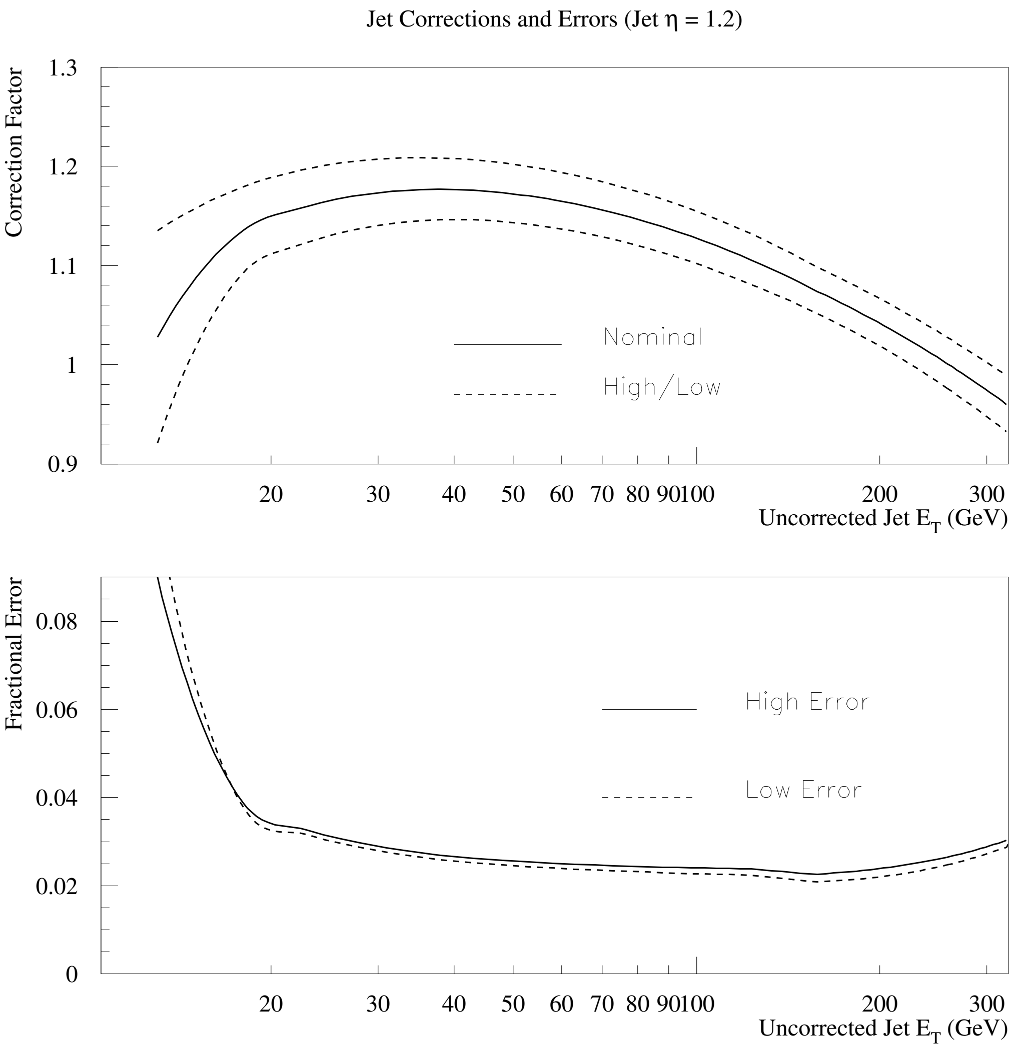

Figure 9.3: Corrections and Errors for η_{jet} =1.2, $\mathcal{R}$ =0.7. Top: Nominal, high, and low correction factors. Bottom: high and low fractional errors.

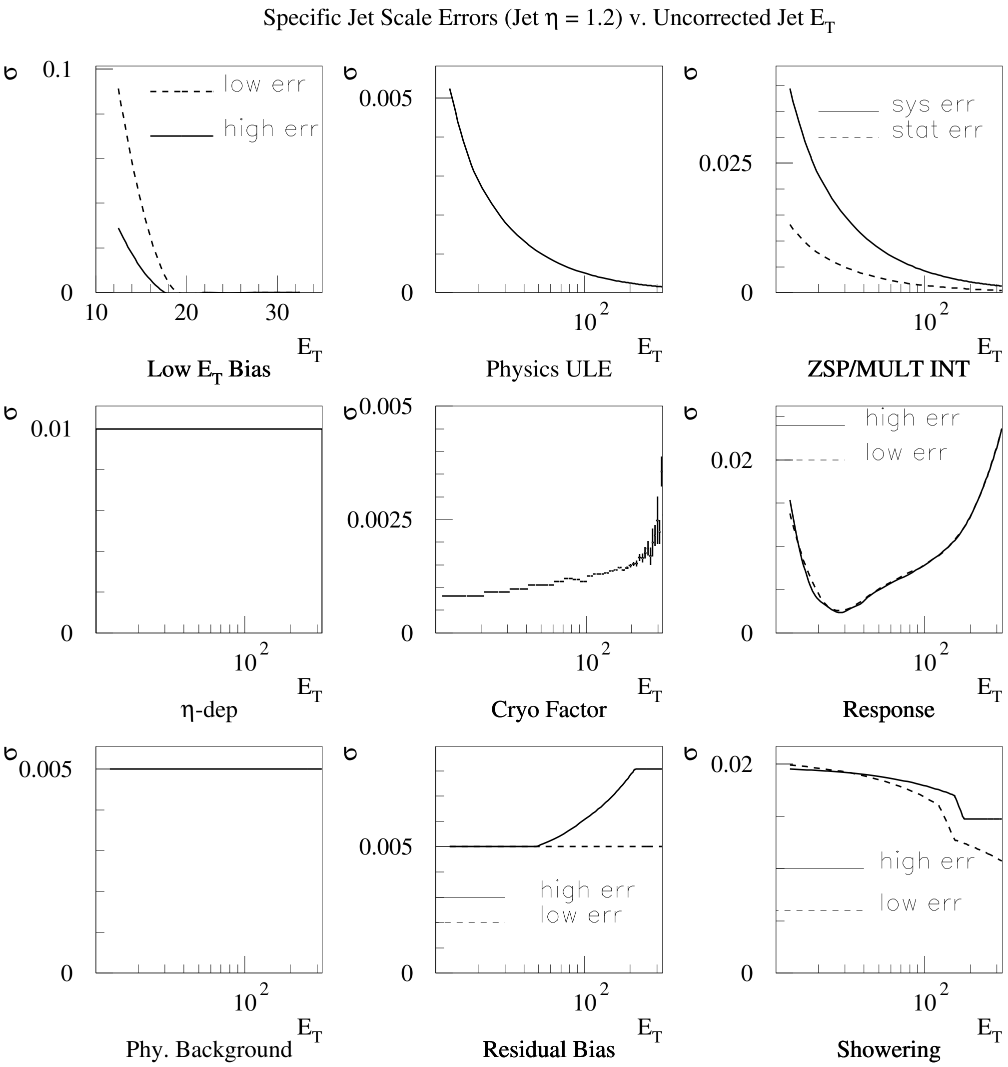

Figure 9.4: Individual components of the jet scale error plotted versus uncorrected jet E_T for η_{jet} =1.2, $\mathcal{R}$ =0.7.

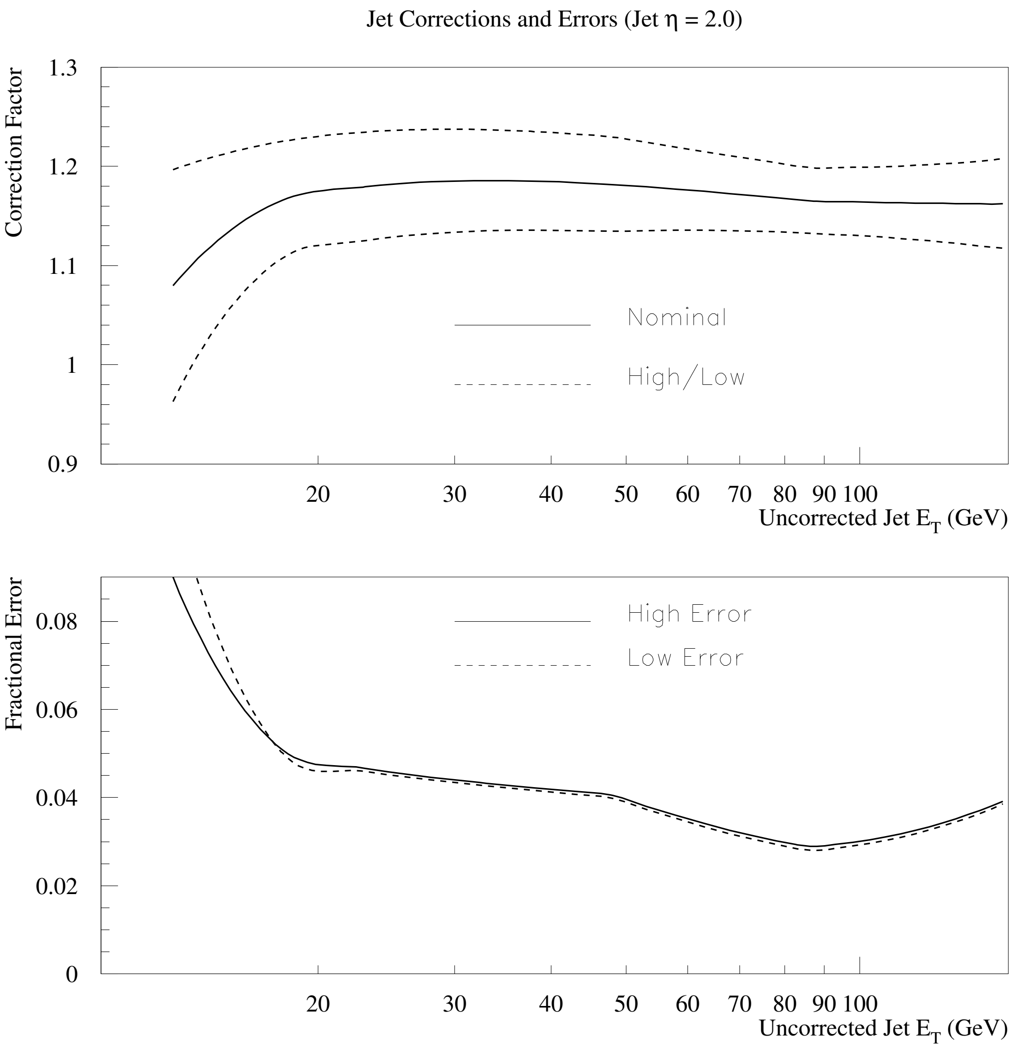

Figure 9.5: Corrections and Errors for η_{jet} =2.0, $\mathcal{R}$ =0.7. Top: Nominal, high, and low correction factors. Bottom: high and low fractional errors.

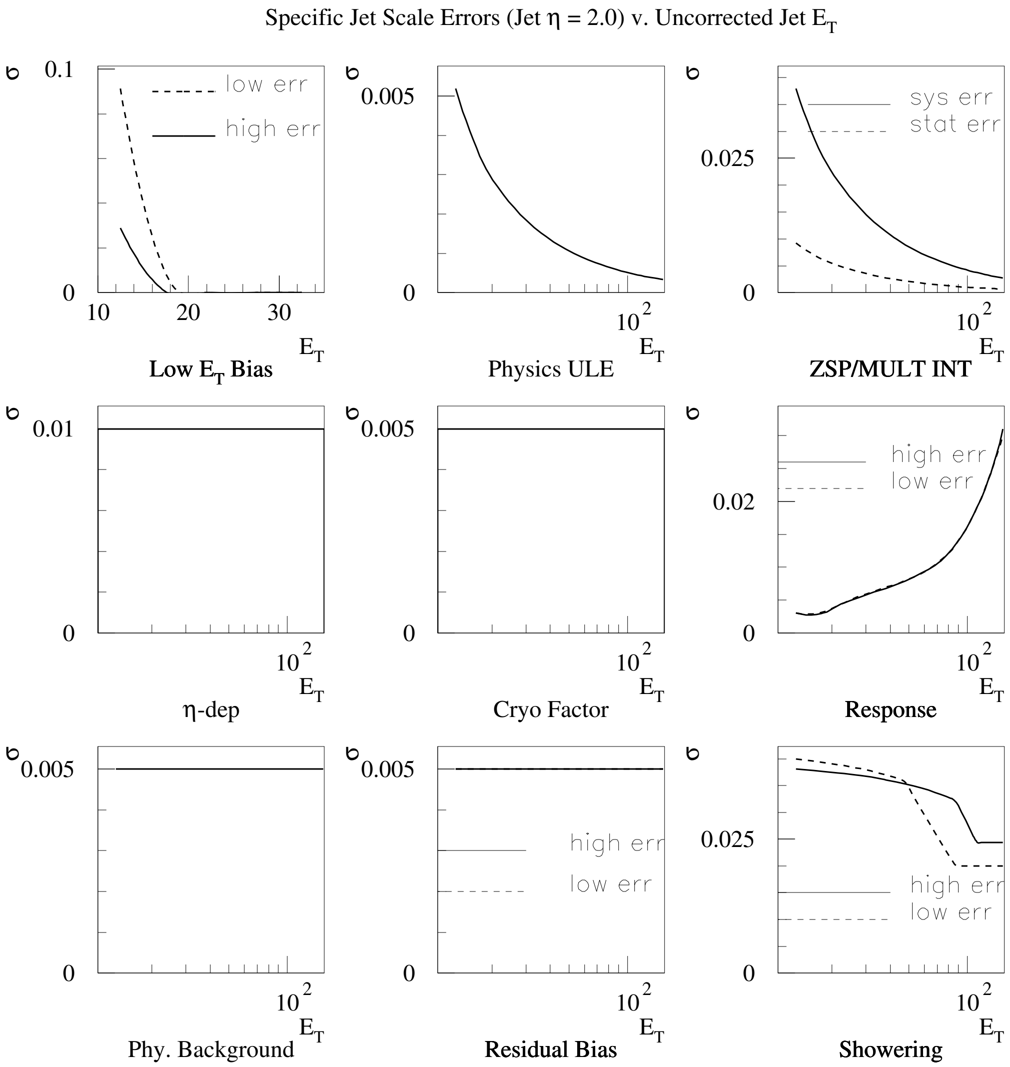

Figure 9.6: Individual components of the jet scale error plotted versus uncorrected jet E_T for η_{jet} =2.0, $\mathcal{R}$ =0.7.

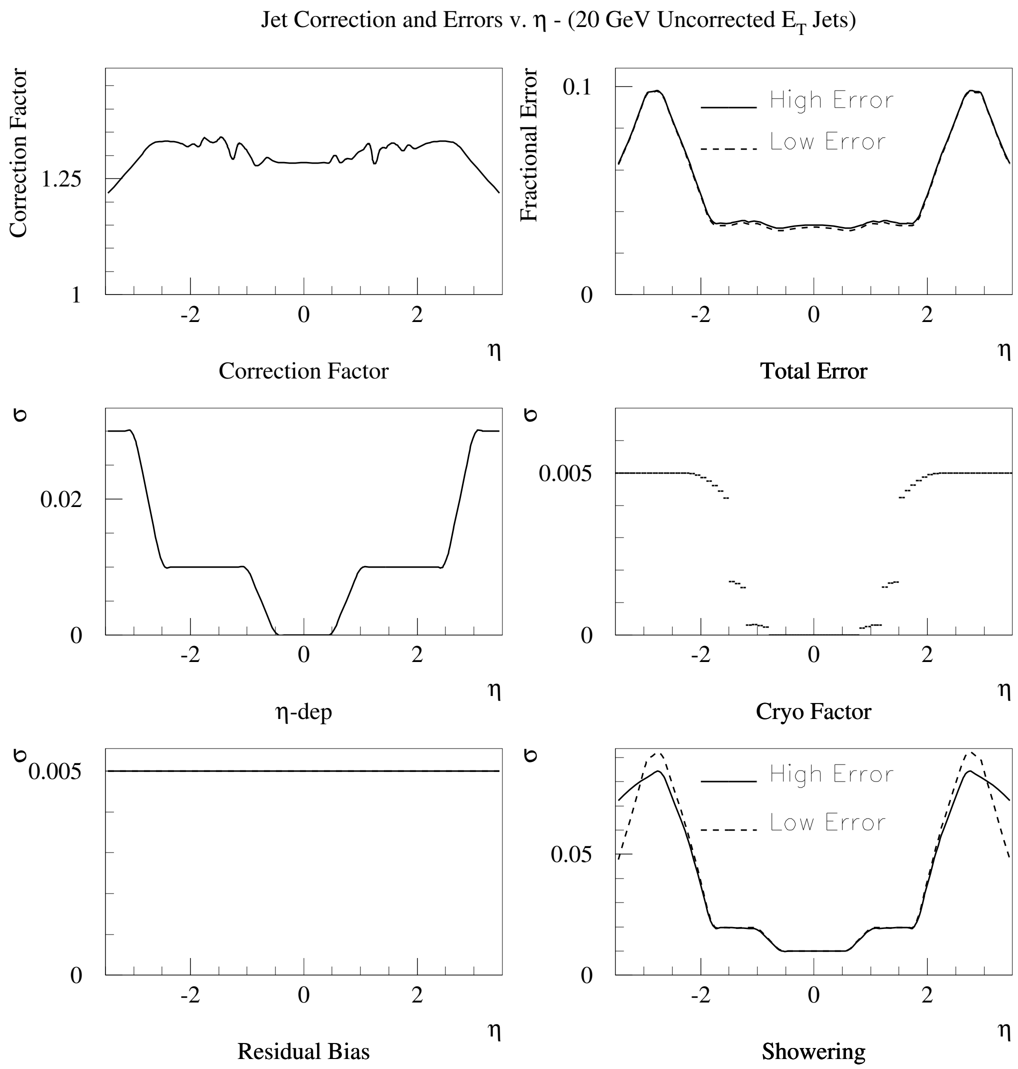

Figure 9.7: Corrections and Errors versus η_{jet}, Jet $E_T = 20$ GeV, $R_{cone} = 0.7$. The total correction and error are both shown as well as the eta dependence of several individual components of the jet scale error.

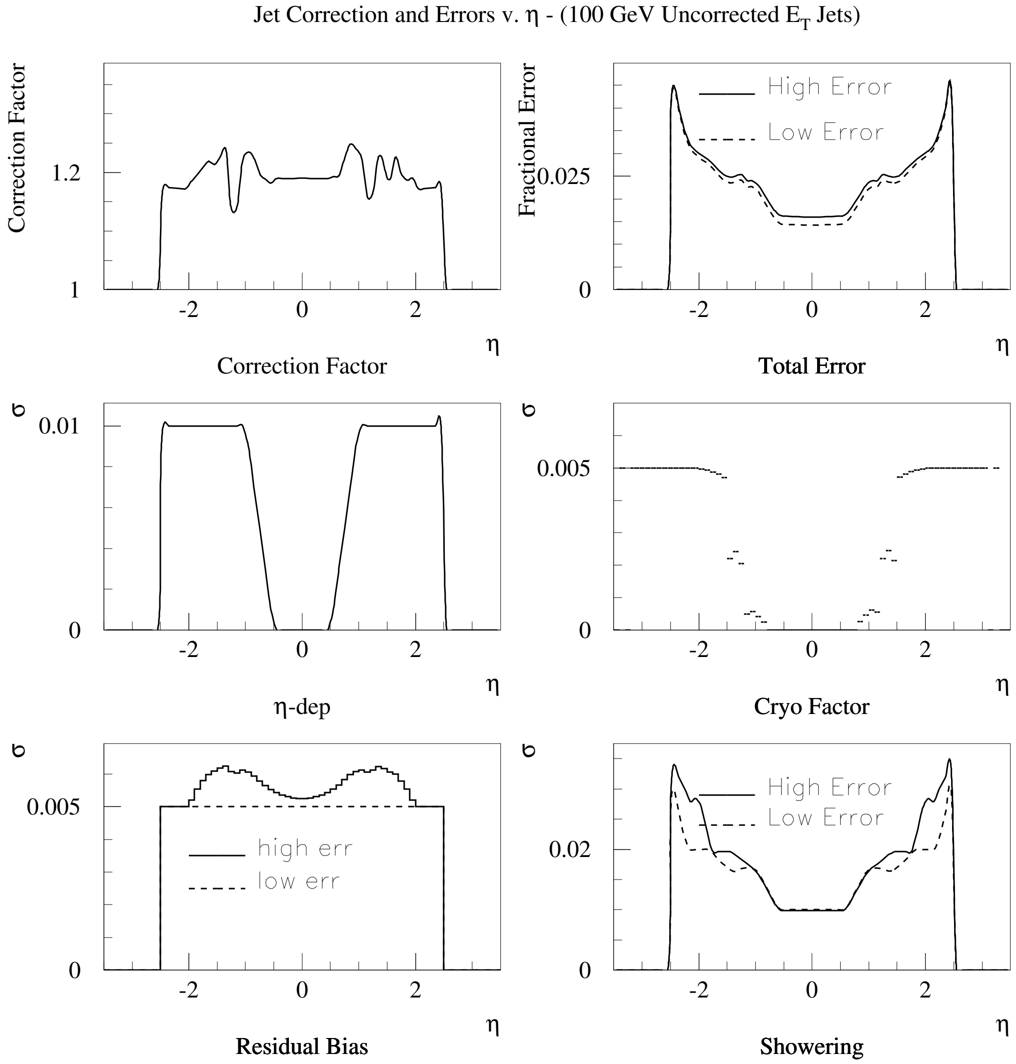

Figure 9.8: Corrections and Errors versus η_{jet}, Jet $E_T = 100$ GeV, $R_{cone} = 0.7$. The total correction and error are both shown as well as the eta dependence of several individual components of the jet scale error.

residual uncertainty. The response fit error is smaller, since there are more statistics at large energies. The showering correction is smaller in the Monte Carlo because of the truncation in SHOWERLIB.

9.4 Ideas for Future Efforts

This section contains ideas to improve the jet energy scale analysis. Some improvements can probably be implemented in the near future (width dependent correction and new showering correction). Others will have to wait until Run II.

The limiting factor in the determination of the Run I jet energy scale is the lack of a Monte Carlo simulation which mimics the data. In particular, the hadronic response measured in the Test Beam differs from the response obtained using GEANT by $\sim$10% in the CC. Since only a few calorimeter modules were studied in the Test Beam, the use of these data for calibration is restricted. With a Monte Carlo simulation which accurately models the detector response, DØ should be able to reduce the error in the jet energy scale to the 1-2% level over the whole kinematic range currently supported by CAFIX5.1 ($E_T \gtrsim$10 GeV and $|\eta| \lesssim$3). A better understanding of the jet energy resolution and reconstruction efficiency would help to reduce the errors at low E_T. A generator tuned to describe correctly the particle multiplicity, energy spectrum and width of jets would help to reduce the error in the showering correction and to derive different response corrections for jets composed of different particles. Hopefully, the availability of a central magnetic field will allow DØ to achieve these goals in Run II.

The methods described in this note will probably be used during the first stages of Run II. At the same time, the Monte Carlo will be calibrated *in-situ* using single particle information provided by the central magnetic field. One method will complement and verify the other. We do not attempt in this section to develop a strategy for Run II. However, we think it is important to mention a few ideas to improve the current analysis in the near future and in Run II.

- **Offset:** This correction needs large samples of zero bias (ZB) and min bias (MB) data, both zero suppressed (ZS) and non-zero suppressed (non-ZS) events. There must be data available at all luminosities. In particular, low luminosity non-ZS-MB and low luminosity non-ZS-ZB data are needed for the measurement of D_{ue}. ZS-ZB, non-ZS-ZB, ZS-MB, and non-ZS-MB samples are needed at all luminosities (including very low luminosity) for the measurement of D_{Θ}. The efficiency of MITOOL might be improved in Run II using the new tracking detectors. It would also be interesting to determine the underlying event for different kind of processes (measured only from MB data in CAFIX5.1). The correlation between jet E_T and underlying event density should also be investigated.

- **Response (η dependence):** The ICR corrections should be minimized by adjusting the ICD and MG sampling weights. This would avoid the possibility of large biases in the correction associated with high E_T jets in the ICR, where there is not enough statistics to derive a correction. The η dependent correction is currently measured only in the ICR. In the future, it should also be implemented in the 2.5$<|\eta|<$3 bin.

- **Response (φ dependence):** Currently a correction that makes the calorimeters uniform in φ is not implemented. A cell by cell correction of this kind is currently available [33] and it should certainly be implemented at the reconstruction level for Run II.

- **Response (energy dependence):** In Run I, the highest E_T photon trigger was prescaled by a factor of two. We need an unprescaled high E_T photon trigger in Run II to extend the reach of the response measurement as high in energy as possible. In Run II, the good vertex resolution will allow the use of high luminosity γ-jet events for the R_{jet} measurement. Currently, luminosity and single interaction cuts are applied to avoid a mis-vertexing bias. Unprescaled triggers and good tracking would give us at least a factor of four more statistics for the same integrated luminosity taken by DØ during Run I. If 2 fb^{-1} are collected in Run II, we would have $\sim$80 times more events in the γ-jet sample. This may allow us to apply tighter cuts to reduce the instrumental bias and extend the energy reach of the response measurement. Since R_{jet} depends logarithmically on jet energy, the increase in statistics will result in a dramatic reduction of the error at high E_T (even without the help of the Monte Carlo). Although the intrinsic calorimeter response is not expected to be luminosity dependent in Run II (this may be a problem in Run III), it will be necessary to take special photon runs at several values of $\mathcal{L}$ to study the possibility that R_{jet} depends on $\mathcal{L}$ due to induced current in a high luminosity environment. Another important issue is the effect of containment, which should be studied in detail in order to derive a correction, if needed, for Run II.

- **Response (width dependence):** The current definition of width (see Chapter 5) is not useful to derive a width dependent response correction. The reason is that W_{jet} is very sensitive to the contribution of the underlying event, noise, pile-up and extra $p\overline{p}$ interactions. Spurious energy in the edge of the jet produces a big change in the width without affecting the jet response. A definition based on a gaussian fit to the jet energy density profile in $\eta - \varphi$ space might be a good alternative to the current definition.

- **Showering:** Some new results using HERWIG events processed through GEANT (mixture level) suggest that jet energy density profiles in the data and the Monte Carlo are in good agreement after they are normalized to zero at the edge of the jet. This opens the possibility of deriving the showering correction from the Monte Carlo by keeping track of the energy deposited in the calorimeter by particles emitted inside or outside the jet cone at the particle level.

We Thank Paul Rubinov for his contribution to the γ-jet sample selection study, and Chip Stewart for input on various issues involved in the response measurement. We also thank Yuri Fisyak, Dan Owens and John Womersley for helping with the estimates of the calorimeter depth. We are grateful to Heidi Schellman for providing the NuTeV data used for the containment studies, and to Rich Partridge who played a very important role in the development of the method to measure the offset correction. Hugh Montgomery and Nikos Varelas deserve a special thank for their useful comments and suggestions. We extend our appreciation to the non-author members of the editorial board (Mark Strovink, Ashutosh Kotwal, Jon Kotcher, Scott Snyder and Daria Zieminska) for their corrections and ideas to improve this work. Finally, we would like to thank Rich Astur and Andy Milder who preceded us in the effort to perform the energy calibration for jets.

Chapter 10

Appendix A: Summary of Changes from CAFIX5.0 to CAFIX5.1

The structure of the CAFIX5.0 package was preserved in CAFIX5.1. The new version includes new corrections, both in the data and the Monte Carlo. New methods were developed and some studies improved to achieve a significant reduction in the systematic errors.

10.1 Offset Correction

A new model of a high p_T event is used to derive the offset correction. In CAFIX5.0, the physics underlying event was measured from a minimum bias sample as the difference in the E_T densities obtained when applying a cut MIFLAG=1,2 or MIFLAG=3,4. MIFLAG is an early version of MITOOL.

The offset correction should not change the event $\not\!\!E_T$ since it is symmetric in φ. This energy is subtracted from the clustered jet energy in correcting the energy of the jet, but no net E_T is added to the event by this correction. Therefore, the offset correction should not affect the $\not\!\!E_T$. This was not quite true in practice due to a mistake in the code [31].

10.2 Response Correction

The method essentially the same used in CAFIX 5.0. The most important improvements included in the current analysis are: a fix in the implementation of the cryostat factor, removal of the width correction, ICR correction based on MPF measurement versus η, better use of the multiple interactions information (MITOOL instead of MIFLAG) in the event selection, tighter collinearity cuts on the photon-jet system, use of Monte Carlo data from a convolution of particle level jets and Test Beam single particle response, use of the full Run Ib and Run Ia data sets, low E_T bias correction from the parametric simulation, new and smaller errors.

In the previous analysis, the cryostat factor was inadvertently mis-applied to the EC jets. The response was therefore underestimated by approximately 3% at large energies ($> 100\,\mathrm{GeV}$). This effect was partially compensated (almost exactly compensated for 0.7 cone jets) by a bias related to the width correction which tended to overestimate the response of high energy jets. The width correction has been dropped from this analysis, since the current definition of width is very dependent on spurious energy (see Chapters 5 and 6). In addition, the ICR corrections included in CAFIX5.0 were not tuned to RECO V12, resulting in biases of up to 7% in the jet energy. γ-jet and jet-jet data are used in CAFIX5.1 to remove the η dependence in the ICR.

After all these fixes and improvements, the nominal hadronic response in the CC is observed to be higher than in the previous derivation by less than one standard deviation, based on the CAFIX 5.0 error.

10.3 Showering Correction

The CAFIX5.0 showering correction was based on a Monte Carlo simulation using HERWIG particle level jets and Test Beam single particle response. The measurement was done only in the CC, using Test Beam data at $\eta = 0$. The η dependence of the showering loss was obtained by assuming that the width of the jet in real space did not change with η. The effective cone size in real space for a particular forward η was compared with a linear parametrization of the effective cone size as a function of cone size in the central region. Extrapolations were done when the forward effective cone was smaller than the smallest cone size measured in the central region ($\mathcal{R}$ =0.3). The effect of the cone shrinking in $\theta - \varphi$ space was not correctly modeled. The correction was not reliable for pseudorapidities > 1.5, where the real space cone size of a $\mathcal{R}$ =0.7 jet was equivalent to the $R = 0.3$ cone size in the central η region.

CAFIX5.1 uses collider data to extract energy density profiles of calorimeter jets and subtracts the energy of particles emitted outside the cone using particle level Monte Carlo HERWIG jets.

10.4 Monte Carlo Correction and Verification

A full Monte Carlo correction for all rapidities was added in CAFIX5.1. The CAFIX5.0 version included a width correction based on a data measurement, which was incorrect for Monte Carlo and is now removed. In addition, it did not include a cryostat factor correction, or an ICR correction. This resulted in a 4% bias towards a lower forward response. There was also a mistake in the code that prevented the offset from being subtracted when requested from the RCP file. The current analysis also includes a closure test of the method for three cone sizes.

Bibliography

[1] The DØ Collaboration, "The DØ Detector", Nucl. Instr. and Methods **A 338** issue 2/3, 185-253 (1994).

[2] J. Kotcher, "Design, performance, and upgrade of the DØ calorimeter", FERMILAB-CONF-95-007-E, Jan 1995. 15pp. Published in the proceedings of 1994 Beijing Calorimetry Symposium, Beijing, P.R. China, 25-27 Oct 1994.

[3] "Energy Measurement of Elementary Particles", C. Fabjan and R. Wigmans, Rep. Prog. Phys. 52 (1989).

[4] "Fixed Cone Jet Definitions in DØ and R_{sep}", B. Abbott et al., DØNote # 2885.

[5] Robert Kehoe, "Search for the Top Quark in Dielectron Final States at $\sqrt{s}$ =1.8 TeV and Measurement of the Response of the D0 U/LAr Calorimeter to Jets", PhD. Thesis, University of Notre Dame.

[6] M. Bhattacharjee et al., "Jet Energy Resolutions", DØNote # 2887.

[7] J. Womersley, private communication.

[8] R. Kehoe, R. Astur, "Determination of the Hadronic Energy Scale of DØ Calorimetry", DØNote # 2908.

[9] U. Heintz, "A Measurement of the Calorimeter Response Using π° Decays", DØNote # 2268, 8/94.

[10] M. Demarteau et al., "Measurement of the W mass", DØNote # 2929, 4/96.

[11] W. Giele, E. Glover and D. Kosower, Nucl. Phys. B, 403, 633 (1993).

[12] S. Grinstein, D. Elvira, "Effect of Event Topology in the jet Response Measurement", DØNote # 3075, 9/96.

[13] F. Paige, S. Protopopescu, ISAJET, BNL-31987.

[14] Chip Stewart, CSF_HV.RCP, 11/92.

[15] Rich Partridge, private communications.

[16] R. Kehoe, "Resolution Bias in Jet Response Measurement", DØNote # 2052.

[17] Z. Casilum, B. Hirosky, private communication.

[18] G. Marchesini and B. Webber, Nucl. Phys. B 310 (1988).

[19] "Shower Libraries for DØ GEANT Monte Carlo", W.Womersley, R. Raja, A. Jonckheere, DØ internal publication # 650, 1987.

[20] R. Brun and F. Carminati, "GEANT Detector Description and Simulation Tool", CERN Program Library Long Writeup $W5013$ (1993).

[21] J. Borders, PhD thesis, University of Rochester (1994).

[22] see any statistics text.

[23] Experimental Techniques in High-Energy Nuclear and particle physics, edited by Thomas Ferbel, World Scientific, 1991.

[24] Minuit Reference Manual, CERN Program Library Long Writeup D506.

[25] Numerical Methods in FORTRAN.

[26] Private communication from Heidi Schellman.

[27] R. Brun and F. Carminati, "GEANT Detector Description and Simulation Tool", CERN Program Library Long Writeup $W5013$ (1993).

[28] CERN Program Library, Long Writeup W5013, CERN Geneva, Switzerland, 1993.

[29] A. Fasso, A. Ferrari, J. Ranft, P. Sala, G. Stevenson and J. Zazula. FLUKA92. In Proceedings of the Workshop on Simulating Accelerator Radiation Environments, Santa Fe, USA, 11-15 January 1993.

[30] S. Abachi *et al.* (D0 Collaboration), Phys. Lett. **B357**, 500 (1995).

[31] R. Hirosky, http://d0wop.fnal.gov/~ d0qcd/d0_private/energy_scale/offset_fix.ps also see: http://d0wop.fnal.gov/~ d0qcd/d0_private/energy_scale/offset_coding.txt

[32] "Jet Energy Scale at DØ ($\sqrt{s}$ =630 GeV)", A. Goussiou and J. Krane, DØNote # 3288.

[33] R. Raja, DØNote in preparation.